Design and Implementation of BLDC Motor Drive Controller for Electric Vehicle Application

A thesis submitted in fulfilment of the requirements of the degree of Doctor of Philosophy

submitted by

ARVIND GOSWAMI

(2K19/PhDEE/01)

Under the Supervision of

Prof. Mini Sreejeth

Professor

Department of Electrical Engineering

Delhi Technological University

and

Prof. Madhusudan Singh

Professor

Department of Electrical Engineering

Delhi Technological University

Electrical Engineering Department

Delhi Technological University

Delhi-110042, India

2024

CANDIDATE'S DECLARATION

I, Arvind Goswami, hereby certify that the work which is being presented in this thesis entitled **"Design and Implementation of BLDC Motor Drive Controller for Electric Vehicle Application"** in partial fulfilment of the requirements for the award of the Degree of Doctor of Philosophy and, submitted in the Department of Electrical Engineering of Delhi Technological University, Delhi, is an authentic record of my own research work carried out during the period from Aug. 2019 to June 2024 under the supervision of Prof. Mini Sreejeth and Prof. Madhusudan Singh, Professors, Department of Electrical Engineering, Delhi Technological University, Delhi, India.

The matter embodied in this thesis has not been submitted by me for the award of any other degree of this or any other institution. This report contains no material which has been accepted for the award of any other degree or diploma, except where due reference is made.

ARVIND GOSWAMI
(2K19/PhDEE/01)
Department of Electrical Engineering
Delhi Technological University, Delhi

CERTIFICATE BY THE SUPERVISORS

Certified that Arvind Goswami (2K19/PhDEE/01) has carried out the research work presented in this thesis entitled **"Design and Implementation of BLDC Motor Drive Controller for Electric Vehicle Application"** for the award of Doctor of Philosophy from Department of Electrical Engineering, Delhi Technological University, Delhi under our supervision. The thesis embodies results of original work, and studies are carried out by the student himself and, the contents of the thesis do not form the basis for the award of any other degree to the candidate or to anybody else from this or any other University/ Institution.

Supervisor:

Prof. Mini Sreejeth
Professor
Department of Electrical Engineering
Delhi Technological University, Delhi

Supervisor:

Prof. Madhusudan Singh
Professor
Department of Electrical Engineering
Delhi Technological University, Delhi

ACKNOWLEDGEMENT

It has been a pleasure for me to work on this thesis. First and foremost, I would like to express my sense of gratitude and indebtedness to my supervisors **Prof. Mini Sreejeth and Prof. Madhusudan Singh,** Department of Electrical Engineering, Delhi Technological University for their inspiring guidance, valuable suggestions, encouragement and help in providing necessary facilities and resources during the entire period of my research work. They always made themselves available for me despite of their busy schedules. It was a great opportunity to carry out my research work under their guidance and to learn from their research expertise.

I am grateful to **Prof. Rachana Garg**, Head and DRC Chairperson of the Department of Electrical Engineering, for her immense support and valuable guidance during my entire Ph.D. tenure. I extend my gratitude and thanks to all **SRC and DRC members** for providing me valuable insights for the research work. I would like to express my gratitude to Delhi Technological University faculties and authorities for providing me necessary facilities for the completion of my research work.

I would also like to extend my gratitude to **Mr. Radhakrishna Upadhyay and Mr. Ashok Poddar** for sharing their invaluable experiences. I also wish to thank my colleagues, including **Dr. Surya Kant, Dr. Saket Gupta, Dr. Akash Seth, Dr. Avdhesh Kumar, Ms. Shilpa Ranjan, Mr. Brijendra Sangar, Mrs. Poonam Dhaka, Mr. Divyansh Shailly, Ms. Parul Kansal, Mr. Ganesh Jaiswal, Ms. Bhavya Bansal, Ms. Nimmi, Mr. Neeraj Kant, and Mr. Mukesh Gupta** from the Project and Research Lab, for their unwavering support and assistance.

I express my deepest admiration to my mother, **Smt. Ravi Goswami,** and my brothers, **Vikram Goswami and Dr. Devant Goswami**, for their unwavering support and constant encouragement throughout this research work.

Above all, I am profoundly grateful to my dearest Banke Bihari Ji for being my enduring strength and support throughout my life.

ARVIND GOSWAMI
(2K19/PhDEE/01)
Department of Electrical Engineering
Delhi Technological University, Delhi

ABSTRACT

The renewed global interest and international efforts to reduce dependency on exhaustible fossil fuels have provided the necessary impetus to the electric vehicle (EV) related research areas including battery systems, motors, drive controllers and different driving mechanisms for automotive applications. The major technological challenges faced by the earlier EV systems were heavy electric batteries, inadequate performance of electric motors, lack of electronic control systems and cost issues. Over the years all these areas of concern have been adequately addressed by the existing research works and technological advancements for wider acceptance of EVs.

Permanent magnet motors (PMMs) are among the most prominent type of electric motors used in EV applications. Brushless DC (BLDC) motors and permanent magnet synchronous motors (PMSM) are the widely used PMMs in EV applications. Their inherent advantages such as fast response, compact size, light weight, high efficiency, brushless configuration, and good dynamic performance have given the major impetus to the wider application scope in EVs and automation industry applications. The development of BLDC motor drives with high performance characteristics coincided with the availability of dedicated motor controllers, high performance microcontrollers and inverters with power switching devices like power metal-oxide-semiconductor field-effect transistors (MOSFETs) due to advancements in VLSI techniques. This has led to their increased deployment in EV applications.

BLDC motors equipped with hall effect sensors (HESs) for feedback are a preferred solution where continuous tracking of rotor position is not required and discrete known positions at fixed angular interval are sufficient for the application. It is a commonly used arrangement in several types of EVs, home appliances, and automation applications. BLDC motor drives offer inherent advantages of increased power density, low maintenance requirements and precise control system mechanisms. The motor operation requires deployment of electronic commutation methods and control mechanisms that are implemented through a dedicated controller. Essential drive parameters such as phase currents, phase voltages, duty cycle of inverter switching signals, their synchronization and commutation sequence are all controlled and monitored by this controller. The control of motor torque and speed according to the application requirements is maintained by deploying appropriate software in the controller for implementing state machine logic and computational algorithms. Besides control of motor operation, provision for fault tolerant control (FTC) methods and diagnostic software routines are also essential in the motor controller design. Thus, controller

design is one of the most important aspects of a BLDC motor drive system.

This research work focuses on the design and development of the motor controller for sensored BLDC motor drives with three HESs. The simulation model of the 3-phase BLDC motor drive with trapezoidal BEMF profile is developed in MATLAB software platform for simulation and analysis. The hardware test bench set up for the research work includes 32bit ARM microcontroller based controller circuit with inverter and driver sections. The software development is carried out using the IAR IDE platform for ARM controllers.

The overall operation of drive control mechanism and associated application in BLDC motor drives with HESs is dependent on the integrity of the signals obtained from three HESs and, their synchronization with the motor back electromotive force (BEMF) profile. These HESs are mounted inside the BLDC motor in majority of the applications. Any error in HES signals directly affects the operation of the drive. The issues of mistiming in HES signals and delayed signal at the controller input terminals are reported in mass scale produced motors for applications like electric rickshaw and three wheeler EVs. HES signal issues arise mainly due to incorrect sensor positioning owing to mechanical, mounting, or production problems. Other factors like ageing, degradation, and filter circuit component failure in the controller circuit also contribute to the HES signal mistiming. The inaccurately timed HES signals result in mistimed switching of the inverter switches in the controller. This causes deviations in the commutation instants. This can further cause increased current and torque ripples, noise and jerks along with inaccurate position control in the drive. Besides, there are other issues of unwanted glitches in the HES signals that need to be addressed by the controller without allowing disturbance in the control scheme. These types of errors have a more pronounced effect on drives employing small sized BLDC motors with higher numbers of poles. Furthermore, the FTC schemes need to be developed in such a way that one type of fault control operation does not hinder the implementation of other FTC schemes in controller. The integrity of the original state machine model, startup routines and control system stability must remain intact by implementation of the FTCs and correction schemes in the controller.

The presented research work includes analysis and mitigation of the faults related to HES signal timings. The mapping of unbalanced HES signals with corresponding HESs is investigated for mitigating the effects of this type of fault in a better and efficient way. Furthermore, the investigation and estimation of commutation delay angles by establishing a direct approximation relation with DC link current profile is presented. This is especially advantageous for applications relying only on DC link current measurement without phase current or BEMF estimation schemes. The possibility of actual implementation of the FTC schemes in motor controller is an important aspect from a practical application viewpoint. The

FTC schemes corresponding to HES signal timing issues, commutation delay and glitches in HES signals are proposed in the research work. These FTC schemes can be incorporated in the controller without requiring any modifications to the circuit, control algorithm, state machine model, or application guidelines. Other FTC techniques can be applied in accordance with the control algorithm.

The design and development of the motor controller is carried out by implimenting HES based BLDC drive control mechanism that is used in several EV applications. The controller is developed around a 32-bit STM32 ARM microcontroller for integration with 1 kW BLDC motor commonly used in electric autorickshaws. The hardware test bench setup is developed for motor controller integration and, for experimental verification of the proposed algorithms. In EV applications such as electric rickshaws, manual harness connectors are used to connect HESs and phase wiring connections of the motor and controller. Automatic phase sequence detection is required in these applications. Hence, the auto phase sequence detection method is also implemented and validated in the controller. This is required in EV applications particularly like electric rickshaws wherein the phase and HES terminals of motor and controller set are joined manually by harness connectors. Experimental validation of all proposed schemes is carried out in the developed motor controller hardware test bench setup for demonstrating controller operation and efficacy of the proposed solutions. Further study and analysis of the effect of the HES signal faults and improvements due to FTC scheme implementation on the motor performance such as phase voltage, phase current, DC link current profile and speed are carried out in the research work.

TABLE OF CONTENTS

LIST OF FIGURES

LIST OF TABLES

LIST OF ABBREVIATIONS

1.	EV	Electric Vehicle
2.	BLDC MOTOR	Brushless DC Motor
3.	PMSM	Permanent Magnet Synchronous Motor
4.	PMM	Permanent Magnet Motor
5.	HES	Hall Effect Sensor
6.	FTC	Fault Tolerant Control
7.	BEMF	Back Electromotive Force
8.	EM	Electric Motor
9.	DC	Direct Current
10.	IM	Induction Motor
11.	SRM	Switched Reluctance Motor
12.	SynRM	Synchronous Reluctance Motor
13.	PM	Permanent Magnet
14.	PMAC	Permanent Magnet AC
15.	PMDC	Permanent Magnet DC
16.	PWM	Pulse Width Modulation
17.	DSP	Digital Signal Processor
18.	BMS	Battery Management System
19.	e-rickshaw	Electric Rickshaw
20.	LSM	Least Squares Means
21.	PID	Proportional Integral Derivative
22.	FOC	Field Oriented Control
23.	DTC	Direct Torque Control
24.	EMI	Electromagnetic Interference

25.	VSI	Voltage Source Inverter
26.	ZCD	Zero Crossing Detection
27.	ASIC	Application Specific Integrated Circuit
28.	SPWM	Sinusoidal Pulse Width Modulation
29.	SVPWM	Space Vector Pulse Width Modulation
30.	DFT	Discrete Fourier Transform
31.	MTPA	Maximum Torque Per Ampere
32.	IGBT	Insulated Gate Bipolar Transistor
33.	RMS	Root Mean Square
34.	EMC	Electromagnetic Compatibility
35.	FFT	Fast Fourier Transformation
36.	SOT	Second Order Taylor
37.	PI	Proportional Integral
38.	MOSFET	Metal Oxide Semiconductor Field Effect Transistor
39.	IC	Integrated Circuit
40.	ADC	Analogue to Digital Converter
41.	DMA	Direct Memory Access
42.	NTC	Negative Temperature Coefficient
43.	RTD	Resistance Temperature Detector
44.	PCB	Printed Circuit Board
45.	HAL	Hot Air Levelling
46.	RPM	Revolution Per Minute
47.	DSO	Digital Storage Oscilloscope
48.	FOT	First Order Taylor
49.	LPF	Low Pass Filter
50.	SOC	State of Charge

LIST OF SYMBOLS

The list of symbols used in this dissertation are given below. Some other symbols which are not mentioned here are described locally.

1.	N	Number of Winding Turns Per Phase
2.	l	Length of the Rotor
3.	r	Internal Radius of the Rotor
4.	B_ϕ	Rotor Magnet Flux Density
5.	ω	Angular Velocity
6.	i	Instantaneous Phase Current
7.	L	Equivalent Phase Inductance
8.	R	Equivalent Phase Resistance
9.	M	Mutual Inductance
10.	θ	Rotor Position
11.	P	Number of Pole Pairs
12.	T_e	Electromagnetic Torque
13.	T_l	Load Torque
14.	J	Moment of Inertia of Rotor
15.	B	Viscous Friction Coefficient
16.	E	Back EMF Voltage
17.	V_{dc}	Voltage of DC Link Supply
18.	I_{dc}	DC Link Current
19.	v_a, v_b, v_c	Phase Terminal Voltages
20.	i_a, i_b, i_c	Individual Stator Phase Currents
21.	e_a, e_b, e_c	BEMFs of Three Phases
22.	$R_a,\ R_b, R_c$	Individual Stator Phase Resistances

23.	L_a, L_b, L_c	Individual Stator Phase Inductances
24.	N	Neutral Point in Star Connected Stator Winding
25.	v_n	Neutral Point Voltage
26.	H_A, H_B, H_C	Hall Effect Sensors
27.	Φ_a, Φ_b, Φ_c	Angular Deviations of Hall Sensors
28.	S_i (i=1 to 6)	Time Span of 60º Electrical Sector
29.	S_e	One Electrical Cycle Time Span
30.	$\Delta\Phi_i$ (i=1 to 6)	Deviation in 60º Electrical Sector Span
31.	Φ_0	Net Average Estimated Value of the Observed HES Angular Shift
32.	η	System Efficiency
33.	^{0}E	Degree Electrical
34.	E_P	Peak Values of Phase BEMF
35.	I_P	Peak Values of Phase Current
36.	P_e	Power Supplied at the DC Source End

CHAPTER 1

INTRODUCTION

1.1 OVERVIEW

The resurgence of global interest and concerted international endeavours aimed at diminishing reliance on finite fossil fuels have catalysed advancements in research pertaining to electric vehicles (EVs), particularly focusing on battery systems, motors, drive controllers, and various propulsion mechanisms for automotive applications [1]-[2]. Brushless DC (BLDC) motors and permanent magnet synchronous motors (PMSM) stand out as the predominant types of permanent magnet motors (PMMs) utilized in EVs [3]. BLDC motors, fitted with hall effect sensors (HESs) for feedback in sensored mode of operation, emerge as a favoured solution in scenarios where continuous tracking of rotor position isn't imperative, and discrete positions determined at fixed angular intervals are sufficient for the application requirements [4].

BLDC motor based drive operation necessitates the implementation of electronic commutation methods and control mechanisms that are facilitated by a dedicated controller [5]. The controller governs and supervises crucial drive parameters such as phase currents, phase voltages, duty cycle of inverter switching signals, their synchronization, and commutation sequence [6]. Moreover, it ensures the regulation of motor torque and speed in accordance with the application's demands by employing tailored software and integrating state machine logic with computational algorithms [7]. In addition to managing motor operation, incorporating fault tolerant control (FTC) techniques and diagnostic software routines is imperative in the design of motor controllers. Consequently, the design of the controller emerges as a pivotal aspect in the architecture of a BLDC motor drive system [8].

The effective operation of the drive control mechanism and its application in BLDC motor drives equipped with three HESs relies on the reliability of the signals obtained from these sensors and their synchronization with the motor's back electromotive force (BEMF) profile. Any discrepancies in the HES signals directly impact the drive's performance [9]. Issues with HES signals typically stem from inaccuracies in sensor positioning due to mounting or production related issues [10]-[11]. When HES signals are mistimed, it results in improper switching of the inverter switches within the controller, leading to deviations in commutation timings. This, in turn, can cause heightened current and torque fluctuations, increased noise and jerking, as well as inaccurate position control within the drive. The

unexpected glitches in the HES signals are another real time application issue that needs to be addressed by the controller [12]-[14].

The FTC schemes for BLDC motor drives must be designed to ensure that one type of fault control operation does not disrupt the implementation of the other FTC schemes within the controller. It is imperative that the implementation of FTC and correction schemes in the motor controller does not compromise the integrity of the original state machine model, startup routines, and overall stability of the control system [15]-[16]. Study and analysis of the effect of the HES signal faults and possible FTC scheme implementation in the controller for improved performance parameters of phase voltage, current profiles, DC link current, torque and speed parameters are important aspects of the overall drive BLDC motor system design for EV applications.

1.2 PERMANENT MAGNET MACHINES

Various types of electric motors (EMs) used in electric vehicles (EVs) are categorized into Direct Current (DC) motors, Induction motors (IM), Switched Reluctance Motors (SRM), Brushless DC (BLDC) motors, Permanent Magnet Synchronous Motors (PMSMs), and Synchronous Reluctance Motors (SynRM) [17]. Among these, BLDC motors and PMSMs are classified as Permanent Magnet (PM) Machines and are widely adopted in EVs due to their advantages such as high operating speeds, power output, cost-effectiveness in manufacturing and maintenance, durability, and efficiency. DC motors are burdened with high maintenance costs and operational faults during commutation. IMs exhibit high losses due to winding presence in both stator and rotor. SynRMs are noted for their complex control requirements. In recent years, BLDC motors, PMSMs, and SynRMs have gained prominence due to their competitive capabilities in EV applications [18]-[19].

In traditional doubly excited electric machines, excitation is achieved through electric windings in both the armature and field, which are powered by external sources of electric energy. In contrast, in PM machines, the necessary magnetic field is generated by magnets, eliminating the need for field windings and an external electrical source for excitation. As a result, PM machines do not suffer from copper losses associated with field windings, thereby enhancing their overall performance. Moreover, since PMs provide the magnetic field, these machines are lighter and more compact. The use of permanent magnets is particularly advantageous for EV applications. However, PM machines generate a continuous magnetic field flux, which lacks the adjustability of the field current in traditional doubly excited electric machines [20].

PM machines can be classified into two main types based on their excitation methods: PMAC (Permanent Magnet AC) and PMDC (Permanent Magnet DC) machines. PMDC machines resemble DC commutator machines but incorporate permanent magnets instead of field windings. On the other hand, PMAC machines are synchronous machines where permanent magnets are installed in the rotor to generate the magnetic field, eliminating the need for rotor windings. These machines are characterized by their straightforward structure, benefiting from the absence of a commutator and brushes [21]-[22].

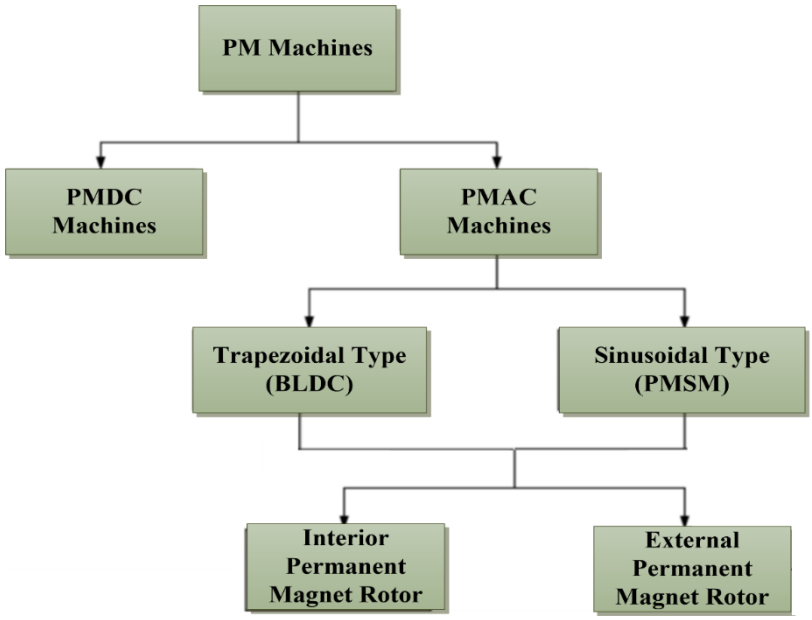

Fig. 1.1 Types of permanent magnet machines.

PMAC machines are further categorized based on commutation methods into trapezoidal and sinusoidal type. BLDC motors have trapezoidal shaped BEMF profile and stator windings are fed with square wave currents with pulse width modulation (PWM) control to create the required torque profile. PMSMs have sinusoidal shaped BEMF with distributed stator windings and require balanced three phase sinusoidal currents for operation [23]-[25].

The BLDC motor has similar working principle as that of a typical DC motor that is based on Lorentz force law. The stator of BLDC motor consists of current carrying conductor while the rotor has PMs. BLDC motor does not need any commutator or brush. Instead, it requires control circuitry and hall sensors or encoders for rotor position sensing. It is a kind of synchronous motor in which the stator and rotor magnetic fields rotates at the same frequency [26]-[27]. The BLDC motor features high efficiency and good controllability due to their linear speed/torque characteristics, giving predictable speed regulation. The major differences between BLDC and PMSM motors are summarized in Table 1.1 [28].

Table 1.1 Comparison of BLDC and PMSM Motors.

BLDC Motors	PMSM Motors
Synchronous machine	Synchronous machine
Fed with PWM controlled square wave currents	Fed with sinusoidal currents
Trapezoidal BEMF profile	Sinusoidal BEMF profile
Discontinuous stator flux variation	Continuous stator flux variation with position
Phase switching off at 60° rotor position change	No abrupt phase switching
Two phases ON at the same time	Ideally three phases ON at the same time
High torque ripple at commutation instances	Little torque ripple at commutation instances
Audible range low order current harmonics	Less harmonics due to sinusoidal excitation
Higher core losses due to harmonic content	Lower core losses
Less switching losses	Higher switching losses.
Relatively simple control algorithms	Computationally complex control algorithms

BLDC motor drives are increasingly popular across a wide array of consumer and industrial applications due to their versatility in handling various speed ranges, from constant to varying loads. In applications where the load remains relatively constant, such as electric fans, open loop control schemes are typically employed. These control schemes are favored for their simplicity and cost effectiveness, making them suitable for mass scale deployment.

Specific applications of BLDC motor drives span diverse fields like in:

- **Household Appliances:** Washers, dryers, and compressors.
- **Aerospace:** Robotic arms and centrifugal pumps.
- **Automotive:** Electric vehicle drive systems, steering control, and fuel pumps.
- **Automation Industry:** Process and machinery control, conveyor belt operation, and computerized machine control.

These applications benefit from the reliability, efficiency, and precise control offered by BLDC motor drives, as evidenced in various studies [29]-[31].

1.3 BLDC MOTOR DRIVES IN AUTOMOTIVE APPLICATIONS

BLDC motors utilize a permanent magnet rotor and a wound stator, coupled to a power electronic switching circuit. The availability of high-energy-density PM materials at competitive prices, along with the commercial accessibility of low-cost microcontrollers and the decreasing costs of powerful digital signal processors (DSPs) and microcontrollers, supported by advancements in semiconductor power switches, has significantly expanded the

application scope of the BLDC motor drives. This technology is now competitive in meeting the stringent requirements of EV applications [32].

The construction of BLDC motors ensures thermal resilience and cooler operation within vehicles [33]-[34]. Their brushless nature eliminates the risk of dangerous brush sparking. Prior to EV applications, BLDC motors were widely employed in automobiles for CD players, power windows, wipers, and other systems. In EVs, BLDC motors with external magnetic rotor arrangements can serve as hub motors. Such BLDC hub motors are particularly common in two-wheelers, where they are integrated directly into the wheel hub of the vehicle [35]-[37].

The two types of voltage application techniques that can be applied on PMAC machines based on the configuration of the supply to motor windings are:

- **Sinusoidal:** Sinusoidal voltage is applied to the 3-phase winding in this technique. The sinusoidal voltage provides a smooth motor rotation and fewer ripples. It is employed in PMSM drives with several control algorithm variations.
- **Trapezoidal:** The voltage is applied to two phases at a time and the third phase is left idle in this technique. Trapezoidal voltage is simpler to implement and less complex. It is employed in BLDC motor drives.

The major sections of the BLDC motor based drive for EV applications include [2], [6]:

- Battery with DC supply management system
- Microcontroller based control unit
- Three phase inverter circuit
- Inverter driver circuit
- BLDC Motor
- Shaft load mechanism
- User input and control system

BLDC Motor being the primary propulsion source, it’s efficient operation and accurate control is the primary function of the microcontroller based control unit. It governs the motor operation and manages the commutation sequence implementation based on the feedback on the rotor's position provided by the HES signals to the controller in sensored mode of operation [38]-[39]. In sensorless control, the phase current profiles are used instead of HES signals for rotor position estimation and commutation sequence implementation [40].

In the trapezoidal commutation scheme the 3-phase inverter driven by a microcontroller

applies the power from DC battery source onto three motor phases according to the 120^0 commutation sequence. The battery management system (BMS) monitors and manages the energy storage unit's health and performance of battery cell units. The BLDC motor drive system with three HESs and current sensing is shown in Fig.1.2. All these components work synergistically for smooth and responsive control of the BLDC motor in the drive according to the control scheme implemented [5], [31].

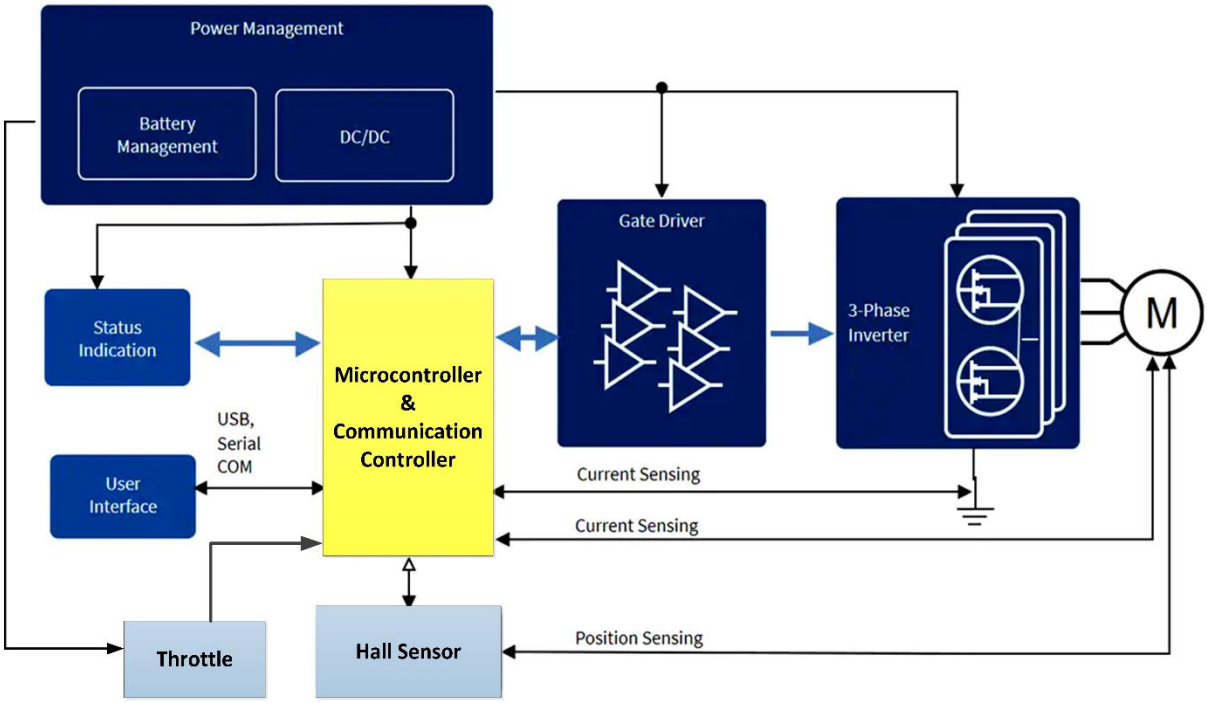

Fig. 1.2 Block diagram of the BLDC motor drive system.

1.4 BLDC MOTOR CONTROL SCHEMES

The BLDC motor operates as an AC synchronous motor where permanent magnets on the rotor generate the rotor flux, while windings on the stator produce electromagnet poles. When the stator windings are energized in a specific sequence, a rotating magnetic field is induced on the stator, which causes the rotor (acting like a bar magnet) to align with and chase after these magnetic poles. This principle forms the basis of operation for synchronous permanent magnet motors. Effective torque production requires precise control of the lead between the rotor and the rotating field, necessitating accurate knowledge of the rotor position. In most cases, three-phase configurations are used on the stator side due to their balance between control precision and the number of power electronic devices required to manage stator currents. Increasing the number of poles on the rotor typically increases torque output for the same current level. However, there's a point where adding more magnets becomes less

effective due to the space required between them, limiting further torque gains. Moreover, higher pole counts generally escalate manufacturing costs. Hence, the number of poles in a BLDC motor is a compromise between cost, torque performance, and physical size [28], [41].

The key to effective torque and speed control of a BLDC motor is based on relatively simple torque and BEMF equations, which are like those of the DC motor. The BEMF magnitude and the torque terms can be written as [10], [41]:

$$E = 2NIrB_{\phi}\omega \tag{1.1}$$

$$T = \left(\frac{1}{2}i^2\frac{dL}{d\theta}\right) - \left(\frac{1}{2}{B_{\phi}}^2\frac{dR}{d\theta}\right) + \left(\frac{4N}{\pi}B_{\phi}rl\pi i\right) \tag{1.2}$$

The torque equation includes terms related to the number of winding turns per phase *N*, the length of the rotor *l*, the internal radius of the rotor *r*, the rotor magnet flux density B_{ϕ}, the motor's angular velocity ω, the phase current *i*, the phase inductance *L*, the rotor position θ, and the phase resistance *R*. The torque expression incorporates parasitic reluctance torque components in its first two terms. The third term contributes to mutual torque, which is the primary mechanism for torque generation in BLDC motors. Additionally, the BEMF is directly proportional to the motor speed, while torque production is nearly proportional to the phase current. Control of commutation in BLDC motors relies on dedicated circuitry. To ensure proper commutation, feedback of the rotor's position is essential for the supporting circuitry. Depending on the method used to detect rotor position, BLDC motor control is broadly categorized into two schemes: sensored and sensorless control.

1.4.1 SENSORED CONTROL SCHEME

Sensored control scheme with three HESs is the most widely adopted technique for BLDC motor drives. In this scheme three HESs are placed inside the motor. Their combined signal pattern varies at interval of electrical 60^0 degrees rotor rotation. Each sensor provides either a high or low output based on the polarity of magnetic pole close to it. Rotor position is determined by analysing the binary output pattern of all three sensors. Based on this output pattern, the voltages to the motor's three phases are switched [42]-[43].

The HES based commutation scheme offers several advantages in BLDC motor control. Firstly, its control algorithm is straightforward and easy to implement, making it cost-effective for various applications. It excels in starting the motor efficiently at very low speeds, ensuring reliable operation from standstill conditions.

However, this approach also has drawbacks. Implementing HES-based commutation requires integrating separate HESs within the motor housing and additional hardware for

processing sensor signals and protecting against interference. This increases both complexity and cost compared to sensorless alternatives.

Applications demanding high torque at low speeds, such as electric rickshaws (e-rickshaws) or electric bicycles, benefit significantly from the HES based sensored control scheme. Figure 1.3 illustrates the sensored BLDC motor speed control scheme utilizing three HESs [44]-[45].

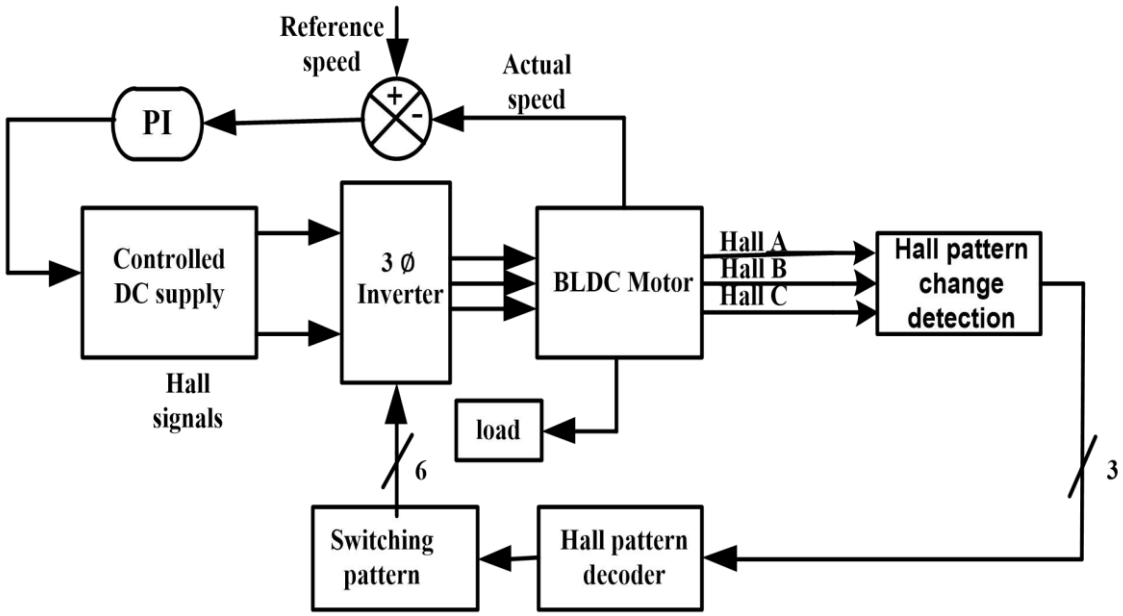

Fig. 1.3 Sensored control of BLDC motor with three HESs.

1.4.2 SENSORLESS CONTROL SCHEME

In sensorless commutation for BLDC motors, the control technique relies on the BEMF induced in the unpowered phase to determine the timing of commutation. Specifically, the commutation is deemed complete when the induced BEMF in the idle phase reaches half of the DC bus voltage.

The block diagram illustrating the sensorless BLDC motor speed control scheme is depicted in Fig. 1.4. One significant advantage of sensorless commutation is the elimination of sensors and associated interface circuitry, which reduces complexity and cost. However, this approach requires a sophisticated control algorithm to accurately detect and utilize the BEMF signals for commutation timing.

Despite its benefits, sensorless commutation has limitations. It may struggle with accurately detecting low levels of induced BEMF at low motor speeds. Additionally, the design must incorporate phase BEMF estimation or current measurement circuitry to ensure reliable operation [46]-[48].

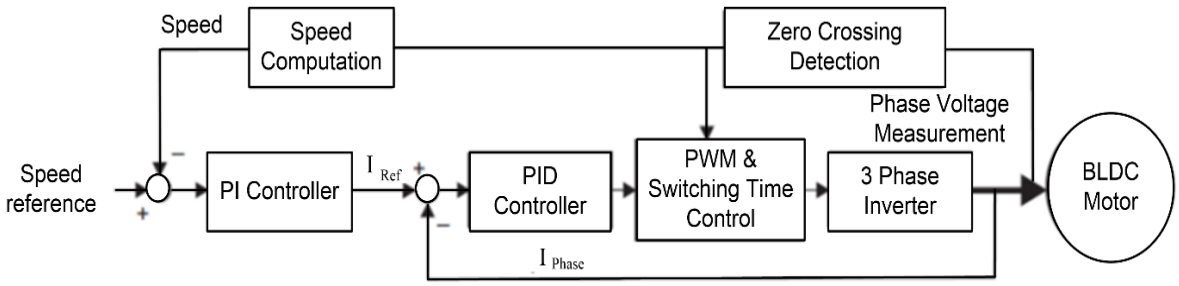

Fig. 1.4 Sensorless control of BLDC motor.

1.5 MOTIVATION AND RESEARCH OBJECTIVES

The wide range of features and advantages of BLDC motors make these extremely useful in present day applications particularly in EVs. It is one of the most promising technological advancements in modern era. The extensive use of BLDC motor in automobile industry and other electrical appliances has pushed the need to develop the best and optimized drive systems [4], [20], [30], [49]. This has led to increased research efforts in this field in the recent years including motor controller design and development. These factors coupled with the advancements in battery systems present novel research opportunities in the field of control and operation of BLDC motor dives. The possibility of industrial and automotive usage of the research work is a great motivation factor for working on operation and control of BLDC Motor.

The primary objective of the presented research work is design and development of sensored BLDC motor drive controller for electric vehicle applications and, analysis and mitigation of HES signal based faults. The simulation work includes fault simulation and analysis of the proposed mitigation schemes. The hardware test bench setup including motor controller is realized using an e-rickshaw BLDC motor set. The development of FTC schemes related to misalignment of HES signals and commutation timings are the major objectives of the research work. The proposed schemes are implemented and tested on the developed hardware test bench.

The research objectives of the presented work for design and implementation of BLDC motor drive controller for electric vehicle application are:

1. Design, mathematical modeling, simulation and analysis of brushless dc motor drive
2. Controller design and laboratory prototype development for experimental validation
3. Implementation of the trapezoidal commutation scheme based control of brushless dc motor drive for electric vehicle application

4. Investigation and mitigation of effect of unbalanced hall sensor signals on BLDC motor drive performance for electric vehicle application.
5. DC Link current based commutation delay compensation in BLDC motor drive for electric vehicle application.

1.6 SCOPE OF THE WORK

This research work is mainly focused on the design and development of the controller for sensored BLDC motor drives. The scope of its operation includes sensored drive with three HESs used in low to medium power EV applications like e-rickshaws. The motor controller design itself is the most important part of the BLDC motor applications. The controller is also required to handle several other issues in real time applications besides the normal drive control functionalities. These issues include interchanged phase connections with motor phase terminals, errors or deviations in HES signals and commutation timing issues. These issues cause distortion in switching pattern, loss of synchronization, deviation in feedback and miscalculation of the drive parameters. This adversely affects the drive performance and may lead to malfunctioning or stalling of the system. Therefore, the study and analysis of these HES signal related issues and associated errors in the drive operation are essential for the development of the relevant FTC schemes. Ideally, these FTC schemes should be such that their implementation does not require changes in core commutation method, switching scheme, interrupt logic and hardware circuit in the controller besides, adhering to the necessary inverter protection conditions.

The design of the motor controller and laboratory test bench for validation and performance evaluation in practical implementations are the major objectives of the work. The scope of the present research work includes analysis and mitigation of HES signal timing related faults. The mapping of unbalanced 60° electrical duration sectors to the corresponding HESs with mistimed signals is an important step in mitigating the effects of this fault.

Furthermore, the investigation and estimation of commutation delay angles by establishing a direct approximation relation with DC link current profile is especially advantageous for applications relying only on DC link current measurement. These applications work without phase current measurement or BEMF estimation schemes for control and inverter switching time synchronization. The possibility of actual implementation of the FTC schemes in motor controller is an important aspect from a practical application viewpoint. Therefore, development of FTC schemes that are easier to implement without hindering the use of other FTC schemes is an important area of research in controller

development field. Study and analysis of the effect of the faults and improvement due to FTC scheme implementation on performance parameters of phase voltage, current profiles, DC link current, torque and speed parameters are important aspects of the overall system design.

1.7 ORGANIZATION OF THE THESIS

The thesis for the research work is organized into the following chapters:

Chapter-1: This chapter presents an introduction and background of PM Machines, overview of BLDC motor drives in automotive applications, BLDC motor control schemes, motivation and research objectives and, scope of the research work.

Chapter-2: Includes a literature review on modeling and simulation of the BLDC motor drive, commutation schemes, sensored and sensorless control schemes, review of existing studies on HES faults in BLDC motor drives and, identified research areas according to the research gaps.

Chapter-3: Discusses the mathematical modeling of the BLDC motor, HES based BLDC motor drive control system, implementation of the trapezoidal commutation and simulation of mistimings in HES signals.

Chapter-4: Presents the design and development of BLDC motor controller and the experimental test bench set up details. The design description of the controller including power supply circuit, protection arrangement, inverter and driver circuit, HES based feedback scheme, controller circuit layout design and fabrication and software development and deployment are explained sequentially. The testing of various sections of the controller is presented and its implementation in the test bench setup for validation with 1kW BLDC motor is discussed in the chapter. Further study of unwanted glitches in the HES signals and their effects on the inverter driving signals is carried out by experimental implementation of the proposed method. Finally, the method for detection and correct identification of phase sequence of BLDC motor by the controller is presented in the chapter.

Chapter-5: Discusses the unbalanced HES signal faults in BLDC motor drives. The proposed method to detect, classify and map mistimed HES signals to corresponding HESs is presented. The categorization scheme for such faults is proposed with signal analysis and information extraction procedure. The FTC scheme implementation in controller is explained in detail. Finally the experimental validation of the proposed scheme in the controller is presented. The unbalanced HES signals and their effects on sensored BLDC motor drive operation are investigated. The results of proposed FTC scheme are compared with another scheme that is based on the least squares means (LSM) based dynamic speed estimation

method. The steady state and dynamic performance improvements over faulty condition are discussed. The improvements in motor phase current, phase voltage and DC link current profiles are discussed alongwith ripple content in stator phase and DC link currents at different loads. Finally the comparison of additional memory loading requirements is presented and applicability of the proposed scheme is discussed in the chapter.

Chapter-6: Discusses the commutation delay issues in sensored BLDC motor drives and, the proposed estimation and correction scheme is presented in this chapter. Commutation delay in sensored BLDC motor drives due to unbalanced HES signals and their effects are discussed. A method to estimate commutation delay angle in electrical degrees by using approximation relation with DC link supply current is proposed. The implementation of the scheme without changing hardware circuit or state machine model in controller is discused. Finally the experimental validation of the proposed scheme carried out in the controller at different load conditions and performance improvements are discussed.

Chapter-7: Summarizes the design, dvelopment and implementation of the controller for EVs. The proposed estimation and mitigation schemes, benefits and controller implementation are concluded. The future scope of the proposed work in this field is outlined at the end of this chapter.

1.8 CONCLUDING REMARKS

This chapter presents an overview of the research work presented in this dissertation. The motivation and scope of the work are outlined along with the major objectives of the research. The introduction and background of BLDC motor drives and control schemes are introduced alongwith discussion on relevancy of the presented research work in automotive applications. Finally the chapterwise organisation of this dissertation is presented.

CHAPTER 2

LITERATURE REVIEW

2.1 INTRODUCTION

The state-of-the-art technologies, methodologies, and approaches in BLDC motor controller design have been reported in the existing literature. Their understanding is crucial for the design and development of BLDC motor drives and controllers. The common challenges and issues faced in BLDC motor control, existing strategies for efficiency improvements, noise reduction, different control algorithms and HES integration are some of the major factors in the research and design efforts. There are various control techniques used in BLDC motor controllers, such as proportional integral derivative (PID) control, sensorless control, field oriented control (FOC), direct torque control (DTC), etc. Literature survey helps in comparing these techniques, understanding their advantages and limitations, and selecting the most suitable approach for your specific application. The case studies and practical applications of BLDC motor controllers in various fields such as automotive, aerospace, robotics, and industrial automation are extensively reported in research papers and application notes. Studying these cases provides insights into real-world implementation challenges and solutions.

In this chapter, literature review is presented on mathematical modeling and simulation of the BLDC motor drive, its operation and control schemes based on sensored and sensorless control techniques and different commutation methods for drive operation. The existing literature on faults in BLDC motor drives, issue of torque ripples and wholistic view of BLDC motor drive in automotive applications are reviewed. Based on the literature review carried out, a detailed state of art discussion is presented. Finally, the research gaps have been identified, and the research areas have been discussed for the presented research work

2.2 DESIGN, MODELING AND SIMULATION OF BLDC MOTOR DRIVE

The fundamental details of BLDC motor design, construction and principal of operation have been extensively explored in the existing literature [4], [18].

Krishnan, R. [23] presented a comprehensive mathematical modeling and analysis of the PMSMs and further development of trapezoidal BEMF based BLDC motor system. The analysis of relationship between parameters of flux linkages, stator phase currents and torque are presented in detail. Performance of the BLDC motor was investigated by using hysteresis

and PWM current controllers and comparison with PMSM drive is explained.

In their review, M. Jain et al. [50] provided an overview of PM motors, distinguishing between two primary types based on their BEMF profile: PMSM, which feature a sinusoidal wave BEMF, and PM BLDC Motors, characterized by a BEMF of trapezoidal waveshape. It is noted that BLDC motors with trapezoidal BEMF typically exhibit higher torque output compared to PMSMs with sinusoidal BEMF.

The motor structure and selection of magnet materials based on the required magnetic field density within the rotor of BLDC motors are discussed in [20]-[22], [51]. Ferrite magnets are commonly used due to their availability but suffer from lower flux density. In contrast, alloys such as Neodymium (Nd), Samarium Cobalt (SmCo), and Neodymium Iron Boron (NdFeB) offer higher magnetic densities. Consequently, these alloy magnets generate greater torque per unit volume compared to ferrite magnets, enhancing the power-to-size ratio of BLDC motors, which is particularly advantageous for in-wheel motor applications.

Padmaraja Yedamale et al. [25] provided a technical application note emphasizing that BLDC motors represent a modern variant of traditional DC motors, employing electronic commutation rather than brushes. This characteristic contributes to reduced maintenance requirements, lower susceptibility to noise, and decreased power dissipation in the air gap compared to brushed DC motors, attributable to the absence of brushes.

S.L. Tade et al. [52] highlighted that while BLDC motors offer advantages such as reduced maintenance and improved efficiency, they are typically more expensive than traditional DC motors. This higher cost is primarily attributed to the need for a motor drive controller for electronic commutation and often a rotor position sensor. However, recent trends in BLDC motor drive design have been addressing these cost concerns effectively.

By modeling the electrical, mechanical, and electromagnetic interactions within the motor, the analysis of the effect of different parameters such as voltage, current, and load torque on the motor's performance is carried out in [35].

Pillay, P. et.al [53] presented a comprehensive detailed analysis of PM motor drive modeling. Simulation models are used to study and analyze the behavior of the BLDC motor. The simulation model development is explained in a step-by-step manner. The torque, speed and current characteristics are elaborately explained with explanations.

G. Adam et al. [26] created a Matlab Simulink model for a BLDC control system. The system operates with a single-phase 220V/50Hz power supply and features a three-phase BLDC motor. The motor is characterized by a sinusoidal BEMF waveform and a rotor design with salient poles. This model serves to simulate and analyze the performance of the BLDC

motor under specified operating conditions.

Mehmet Cihat Ozgenel [54] developed a mathematical model for a star-connected stator winding BLDC motor, utilizing the equivalent electrical circuit. The model incorporates three phase winding self-inductances in henry (H) with the phase winding resistance in ohms (Ω). This model serves to analyze and predict the operational characteristics of the BLDC motor under various operating conditions.

Kommula, B. N. et.al [55] provided a detailed mathematical model of BLDC motors, which is crucial for understanding their behavior and performance characteristics in different operational scenarios. The authors implement fuzzy logic control techniques to regulate the operation of BLDC motors. Fuzzy logic offers advantages in handling nonlinearities and uncertainties inherent in motor dynamics, thereby enhancing control accuracy and robustness. The study explores the practical application of the developed model and control strategy in both automotive and industrial environments. This includes optimizing motor performance for efficiency, reliability, and responsiveness to varying load conditions.

Development of simulation models to study and analyze the dynamic behavior of BLDC drive systems is explained in [49], [56]. Mathematical modeling of BLDC motor drive systems is crucial for their analysis and control. These presented models provide a theoretical framework to understand and predict the behaviour of the motor under various operating conditions, facilitating the design and optimization of control algorithms. Overall, this analysis helps in designing the control strategies and fault condition simulations for FTC development before implementing the conditions in real time hardware systems [57].

In their study, J. S. Park et al. [58] introduce a mathematical model to characterize HES signals affected by misalignment. Assuming constant-speed operation, they derive equations describing the interval of compensated HES signals. Following this compensation process, the authors propose an advanced angle adjustment method to optimize motor performance based on the compensated signals found in existing literature.

2.3 BLDC MOTOR OPERATION AND CONTROL

The BLDC control systems can be classified into two categories based on rotor position detection method:

- Sensored control and,
- Sensorless control

The detailed description and analysis on both, HES based operation as well as senesorless

operation of BLDC motor drive is presented in [25], [59]-[64]. The characteristic curves and method to implement these schemes in the actual controller are discussed along with the operational principles of a 3-phase BLDC motor.

2.3.1 SENSORED CONTROL

The sensored control scheme of a BLDC motor drive utilizes HESs or encoder arrangements for precise position detection and speed calculation. HESs are usually mounted on the non-rotating end inside the BLDC motor in a fixed position such that their output signals have 120-degree phase difference between them. This arrangement is used to accurately detect the rotor angle [60]-[61]. Figures 2.1 shows the internal view of BLDC motor. The stator windings and HES placement can be observed. The equivalent angular arrangement is illustrated in Fig. 2.2.

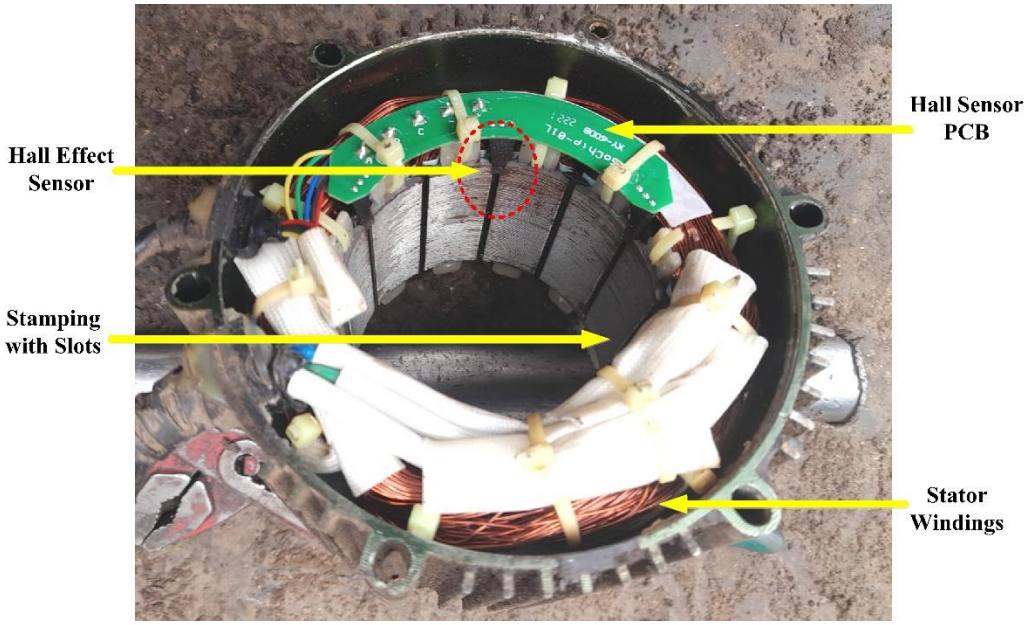

Fig.2.1. Internal structure of BLDC motor with HES placement.

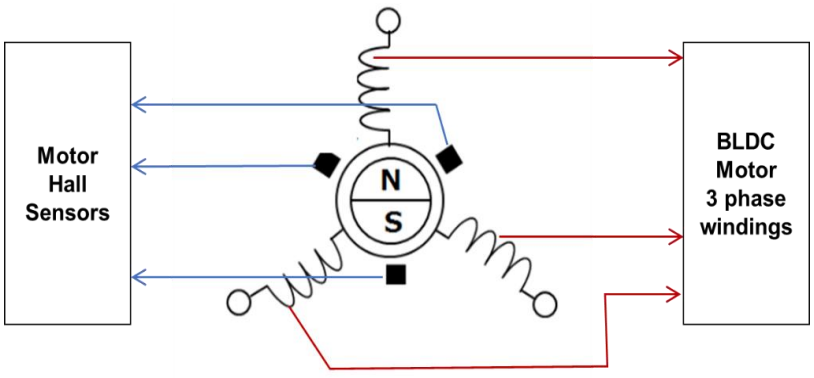

Fig. 2.2. Equivalent HES positions with respect to the stator windings in BLDC motor.

This setup ensures reliable and accurate sensing of the rotor position, essential for effective control and operation of the BLDC motors across a range of industrial and automotive applications.

While commutation of BLDC motors using HESs simplifies the process, it comes with several critical drawbacks. The drawbacks of BLDC motor drive with hall sensors are discussed in [9], [14], [16], [62]. These include:

- **Regular Maintenance Needs:** BLDC motors with HES require periodic maintenance due to wear and tear of the sensors and potential mechanical issues associated with their mounting and placement positions in the stator.
- **High Electromagnetic Interference (EMI) Radiation:** HES can emit electromagnetic interference, which may interfere with nearby electronic devices and sensitive equipment.
- **Temperature Sensitivity:** The performance of HES can be affected by changes in temperature, potentially leading to inaccuracies in position detection and motor control.

These drawbacks highlight the trade-offs involved in selecting sensor types for BLDC motor commutation, where alternatives like encoder based systems may offer improved reliability and performance in applications requiring high precision and robustness. Typically, HESs are employed for low resolution applications, while optical encoders are preferred for high resolution applications.

Square wave control of BLDC motors commonly employs a six-step commutation method, where the commutation pattern is managed by a 3-phase inverter consisting of six switching devices. This method involves sequentially activating one high side device in one phase, one low side device in another phase, and leaving both devices in off state in the remaining phase [25], [63]-[64]. This approach allows for straightforward control of the motor's speed and direction by selectively switching the phases of the inverter, ensuring efficient and reliable operation in various industrial and automotive applications.

Wael A. Salah, et.al. [34] introduced a novel switching technique aimed at minimizing torque ripples caused by current commutation in BLDC motor drives. Their proposed PWM control strategy, implemented using a low-cost 8-bit PIC microcontroller, successfully mitigated torque ripples. The results of their study showed a reduction of torque ripples compared to conventional PWM control methods. Additionally, the proposed technique facilitated smoother phase current profiles and effectively reduced current spikes,

contributing to improved motor performance and operational stability. Overall, Salah et al.'s research demonstrates significant advancements in enhancing the efficiency and reliability of BLDC motor drives through innovative PWM control strategies.

X. Zhang et al. [65] discussed the application of HES feedback systems in BLDC motors, emphasizing their effectiveness across different speed ranges. They note that HESs provide signals indicating rotor position, making them suitable for applications requiring lower resolution. In contrast, optical encoders are preferred for high-resolution applications where precise positional accuracy is critical. This distinction underscores the versatility and application-specific considerations in choosing sensor types for optimal BLDC motor control and performance.

D. S. Nair, et.al. [66] provided a detailed explanation of motor speed calculations in BLDC motor drives using HESs. They established that motor speed correlates directly with the frequency of the squared wave signal generated by the HESs. By measuring these frequencies, the paper demonstrates how to accurately determine and control the motor speed. Moreover, the study presented an analysis focusing on explicit torque control for PM motors with trapezoidal BEMF. Specifically, it explored strategies to reduce switching frequency while maintaining a constant hysteresis band. This approach is crucial for optimizing motor performance and efficiency in various operational conditions. This research contributes valuable insights into the practical implementation of speed measurement and torque control techniques for BLDC motors, highlighting their significance in enhancing motor control precision and overall system efficiency.

C. K. Lad, et.al. [67] discussed the effectiveness of conventional control approaches in managing commutation torque ripple across different speed ranges in BLDC motors. They highlighted that methods such as overlap angle control technique perform well in low and intermediate speed ranges. However, at high speeds, particularly under rated power conditions, PWM methods face limitations in effectively reducing commutation torque ripple. This limitation is primarily due to the finite DC link voltage of the Voltage Source Inverter (VSI), which constrains the performance of PWM based control strategies at higher speeds.

S. S. Bharatkar et al. [68] introduced a novel 180-degree switching mode aimed at reducing torque ripple magnitude and commutation time at higher speeds in BLDC motors. Their analysis revealed that compared to the conventional 120-degree conduction mode of the inverter, the 180-degree switching mode effectively decreases torque ripple and shortens commutation times. The study proposes a dual mode switching technique to optimize commutation torque ripple in BLDC motors, supported by computer simulations and

experimental validations to substantiate the effectiveness of the proposed approach.

Y. Cao et al. [69] introduced an optimized combination of PWM modulation patterns aimed at achieving smooth torque control across the full speed range of BLDC motors. The paper investigates eight unipolar modulation patterns and proposes a strategy for smooth braking torque control. It derives and compares the speed ranges for each pattern where braking torque is controllable and commutation torque ripple can be minimized.

Pratikanta Mishra et al. [70] proposed an optimized modified PWM method that ensures effective torque control throughout the entire operational spectrum of the motor. It is based on the torque control performance observed across different speed ranges for each modulation pattern. This approach aims to enhance motor performance, reduce torque ripple, and optimize energy efficiency in various application scenarios.

These research works provide valuable insights into sensored control techniques for BLDC motors, highlighting their role in achieving precise and efficient motor control across diverse operating conditions.

2.3.2 SENSORLESS CONTROL

Sensorless BLDC motor control uses BEMF for determining the position of the motor's rotor with respect to the stator. The block diagram of the controller based sensor less control configuration is illustrated in Fig. 2.3.

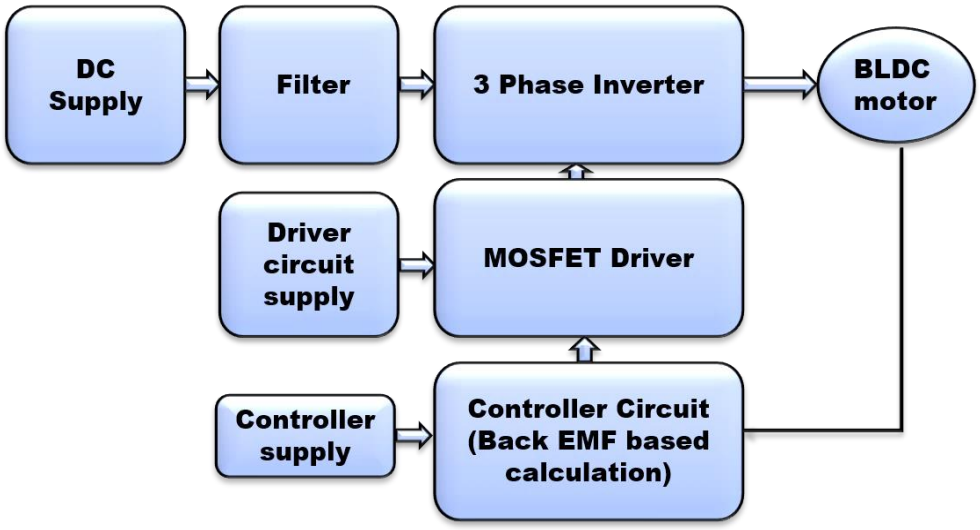

Fig. 2.3. Block Diagram of sensorless BLDC motor control system.

P. Damodharan, et.al. [40] introduced a novel technique for detecting BEMF zero crossings in BLDC motors using line voltages. Their method amplifies the BEMF signal, leveraging measurements from only three motor terminal voltages, thus eliminating the need

for motor neutral voltage. The paper proposes operating the motor in sensorless mode by employing this innovative zero-crossing detection algorithm.

Kan [46] states that during startup, the motor initiates triggering devices at the detected zero crossings using the proposed algorithm. Once running, correct commutation timing is maintained by implementing a 30° delay from these zero crossing points. The study demonstrates that the motor starts smoothly and operates in sensorless mode even under varying loads and load transients. Simulation and experimental results validate the effectiveness and suitability of the proposed method in practical applications.

In this control scheme, a current sensing shunt mechanism is employed across all three phases to detect the zero crossing of each phase current, forming the basis of the entire control algorithm [46]-[47]. However, a significant drawback arises when the rotor of the motor is stationary. In such situations, no BEMF is generated. The absence of BEMF means that the drive circuitry lacks crucial information necessary for accurate motor control. Overcoming this challenge adds complexity to the sensorless control method [48], [64].

J. Gamazo-Real, et.al. [71] presents a comprehensive review focusing on sensorless methods for controlling BLDC motor drives, encompassing an examination of historical sensor based approaches, their limitations, and advancements. The study underscores how sensorless technology has enhanced the performance and reliability of BLDC motor drivers by refining conventional control and sensing techniques. The review encompasses an overview of BEMF sensing methodologies, including Terminal Voltage Sensing, Third Harmonic Voltage Integration, Terminal Current Sensing, BEMF Integration, and PWM strategies. Additionally, it provides a succinct analysis of key estimation and modeling techniques such as the Sliding-mode Observer, Extended Kalman Filter, Model Reference Adaptive System, Adaptive observers (Full-order and Pseudoreduced-order), and Artificial Neural Networks.

Jianwen Shao, et.al. [72] introduce a novel method for detecting BEMF) in sensorless BLDC motor drives, specifically designed to operate without requiring information about the motor's neutral point voltage. The approach enables direct extraction of the accurate phase back EMF signal from the motor terminal voltage by strategically selecting PWM techniques and sensing strategies. Consequently, this method exhibits insensitivity to switching noise, eliminates the need for filtering, and ensures excellent motor performance across a broad range of speeds. The study includes a thorough analysis of the circuit model and experimental validation, confirming the theoretical analysis and highlighting the benefits of this innovative technique.

T.-H. Kim et al. [73] introduce a sensorless position detection technique for BLDC motors centered on a speed independent position function. This method utilizes a function of flux linkage that remains consistent across different speeds, coupled with the differential equations governing the stator phase windings. By leveraging these principles, the technique estimates commutation instants from near 1.5% of rated speed to high speeds with accuracy. This approach ensures precise commutation pulses during both steady-state and transient conditions without the need for BEMF measurement or sensing terminal voltages. This simplifies the sensorless operation of BLDC motors, offering reliability and performance across a wide range of operational speeds and conditions as demonstrated through simulations and experimental validations. In the application note and study of [63] and [74], an in-depth analysis of the BEMF based sensorless 120° square wave commutation control method for BLDC motors is presented. Fundamentally, BEMF is explained as the voltage induced in a coil that opposes the change in magnetic flux inducing it. However, detecting BEMF induced in motor windings during rotation poses challenges because motor terminals are occupied with the drive voltages.

In the 120° commutation scheme, only two of the three motor phases conduct current at any given time, while the third remains inactive. BEMF manifests at the terminals of the non-conducting phase, where it is utilized for rotor position detection. Specifically, the method detects zero crossing points of BEMF at each phase terminal to ascertain the rotor's position accurately. This approach enables sensorless operation by leveraging the natural signals generated within the motor during commutation cycles.

K. D. Carey et al. [75] present the derivation of a motor model and the development of a hybrid controller that combines FOC and DTC techniques. This novel controller integrates the strengths of both FOC and DTC to optimize motor performance. Simulation results of the controller demonstrate robustness against uncertainties in parameters, such as inductance and resistance, and is resilient to noise in voltage and current measurements. The study highlights the advancement in motor control techniques by leveraging the complementary advantages of FOC and DTC, offering enhanced performance, robustness, and stability in various operating conditions.

The reduction of motor maintenance, less cost, and less complexity of stator laminations are some of the main advantages of the sensorless control of the BLDC motors. However, the sensorless control algorithms are more complex in computation and implementation aspects than the conventional switching techniques [40], [73], [76].

Sensorless BLDC motor drives face several challenges that include the requirement for

neutral potential and issues related to offset errors from integration. Additionally, difficulties in starting and low-speed commutation, along with the inherent complexity of control algorithms, constitute the primary drawbacks of sensorless BLDC motor drives. These drives necessitate specialized starting algorithms to accelerate the BLDC motor to a speed where BEMF can be reliably sensed [55], [77]. These challenges underscore the ongoing research and development efforts aimed at overcoming these limitations to enhance the performance and reliability of sensorless BLDC motor drives.

2.4 BLDC MOTOR COMMUTATION SCHEMES

The two fundamental commutation methods are Trapezoidal and Sinusoidal commutation. There are different PWM techniques that are used in BLDC motor control systems in conjunction with these methods. The following literature reviews the diverse strategies employed in controlling BLDC motors for various application requirements.

2.4.1 TRAPEZOIDAL COMMUTATION

The 120° square-wave commutation method for brushless DC motors is extensively discussed in [24], [63] emphasizing aspects such as commutation waveforms, rotor position detection using HESs, and sensorless methods based on BEMF zero crossing points.

Typically, Hall Effect sensors are positioned with a fixed 120 electrical degree phase difference on the non-rotating end inside the BLDC motor. This setup allows the sensors to detect the rotor angle consistently. HESs play a crucial role in accurately determining the rotor position during operation, facilitating precise commutation of motor phases.

Additionally, the research papers explore sensorless techniques that rely on detecting zero crossing points of the BEMF generated in the motor windings. These methods enable rotor position detection without the need for physical sensors, enhancing the simplicity and reliability of BLDC motor control systems.

The application notes referenced in [25] and [63] elaborate on the 120° square wave commutation method for BLDC motors, focusing on several key aspects including commutation waveforms, rotor position detection utilizing HESs, and sensorless techniques based on BEMF zero crossing points.

Azarudeen A, et.al. [78] explore the comparison between conventional PWM and digital PWM control schemes. Their study reveals that digital PWM control yields advantages such as reduced speed ripple and improved current waveform, leading to enhanced average torque and overall performance compared to conventional methods. Moreover, digital PWM's

straightforward implementation makes it suitable for integration into low-cost Application Specific Integrated Circuits (ASICs). This characteristic makes it particularly well-suited for applications where minimizing torque or speed ripple is not critical. The research underscores the practical benefits and potential cost-effectiveness of digital PWM control in various motor drive applications.

Mehmet Cihat Ozgenel et al. [79] conducted experimental and simulation studies comparing the performance of BLDC motors under 120º conduction mode and 150º conduction mode control strategies. Their study revealed that the BLDC motor controlled by the 150º conduction mode inverter achieved superior results in terms of power output, torque production, and operational speed compared to the motor controlled by the 120º conduction mode inverter. These findings underscore the advantages of employing a wider conduction angle for optimizing BLDC motor performance in various practical applications.

In the context of 120° commutation for BLDC motors, the commutation sequence is managed using a three-phase bridge inverter comprising six switching devices. This configuration operates as follows: one phase features the activation of the high-side device, another phase activates the low-side device, and the third phase has both the high-side and low-side devices in off position [80]. This control scheme ensures precise and efficient operation of BLDC motors across varying load conditions, enhancing performance and reliability in diverse applications.

Yong Keun Lee [81] analyzed the persistent issue of torque ripple in BLDC motor drives, attributing its cause to two main factors: non symmetric commutation of phase currents and phase current shift errors. These factors contribute significantly to torque fluctuations and are challenging to mitigate completely, even with advancements in sensor and sensorless BLDC motor control technologies.

In BLDC motor systems, the commutation of armature currents leads to ripple due to stator winding inductance and variations in BEMF, resulting in pulsating torque [82]-[83]. Minimizing torque ripple is crucial for achieving precise speed and position control.

In an ideal scenario, a BLDC motor with trapezoidal BEMF driven by a constant source voltage would have instantaneous current rise to steady state, producing torque without ripple. However, real world conditions introduce time constants in current response, causing current ripple due to inductance, which directly affects torque ripple [84].

Conventional control methods [85] often exacerbate torque ripple, primarily due to phase current commutation [86]-[87]. To mitigate this issue, various control algorithms have been proposed, as documented in the literature [88]-[96]. Hysteresis current control offers superior

current control capability but faces challenges related to switching frequency adjustments according to hysteresis band width and BEMF magnitude. In contrast, PWM current control provides a constant switching frequency but at the expense of lower current control capability. PWM methods include unipolar PWM with 120º conduction, which minimizes switching losses and current ripple but sacrifices dynamic current response. On the other hand, bipolar PWM enhances dynamic current response but increases switching losses and current ripple compared to unipolar PWM methods. Hysteresis current control and PWM current control are commonly utilized to reduce torque ripples in BLDC motors [52], [97].

2.4.2 SINUSOIDAL COMMUTATION

Sine wave control employs PWM techniques to generate three-phase sine-wave voltages, resulting in sinusoidal currents.

G. Adam, et.al. [26] introduce an innovative control approach for BLDC motors, aiming to overcome limitations associated with traditional methods while ensuring that source current waveforms closely approximate sinusoidal shapes, aligning with established standards.

The critical analysis with advantages is presented in [45], [49]. Unlike square wave control, which relies on discrete commutation events, sine wave control does not involve the concept of commutation. This method offers several advantages: it reduces torque ripple and minimizes current harmonics compared to square wave control, thus enabling more precise control of BLDC motors.

Jorge, et.al. [98] describes sine wave control, which approximates sinusoidal waveforms using PWM methods to output three-phase sinusoidal voltages, resulting in corresponding sinusoidal currents. Unlike square-wave control, sine wave control does not involve switching off phases for durations. However, sine wave control requires higher-performance controllers compared to square-wave control, and maximum motor efficiency may not be achieved under this method.

Meghana N Gujjar, et al. [99] conducted a comparative performance analysis of FOC applied to BLDC motors using Sinusoidal Pulse Width Modulation (SPWM) and Space Vector Pulse Width Modulation (SVPWM) techniques. Simulation results indicate that the SVPWM technique enhances system performance by reducing motor current draw, achieving smoother speed response, and mitigating torque ripple compared to SPWM.

B. Pavan Kumar, et.al. [100] conducted a comparative study of three different control schemes for BLDC motors: Sinusoidal FOC, and Hysteresis Control, focusing primarily on

output torque ripple. The study found that FOC significantly reduces torque ripple, but it is associated with substantial transient dynamics. In contrast, sinusoidal FOC schemes were proposed as a solution to mitigate these transient dynamics while maintaining effective torque ripple reduction.

Wei-Feng Zhang, et al. [101] conducted a comparative analysis of three SVPWM schemes: 7-segment SVM, 5-segment SVM, and 3-segment SVM. The study focused on evaluating their performance based on simulation results, particularly in terms of reducing switching actions through the use of discontinuous modulating functions. The analysis indicated that all three SVM schemes exhibited similar utilization of the DC bus voltage. Additionally, the harmonic characteristics were found to be influenced by the modulation index, while both the DC bus voltage utilization and harmonic content were affected by another modulation index.

C. Lin, et.al. [102] focussed on the design of a driver for BLDC Motors using a quasi-sinusoidal voltage source inverter with SVPWM technology. Their study details an innovative method to generate quasi-sinusoidal voltages using only digital HESs. The designed system specifically targets a 600 W BLDCM intended for electric vehicles. Results indicate that the proposed system effectively reduces torque ripple compared to traditional six-step driving systems.

The application notes in [103] outline a control strategy utilizing instantaneous BEMF position for generating sinusoidal PWM pulses to control motors. The study underscores that the rotor's ability to remain synchronized with the stator flux hinges on the magnetic field strength and the magnitude of load torque disturbances. Once the rotor deviates from alignment with the stator flux during operation, it loses its ability to rotate further. Should the stator continue to be energized with sinusoidal currents, the rotor will experience periodic torque fluctuations in both directions corresponding to the frequency of the stator currents.

2.5 HES FAULTS IN BLDC MOTOR DRIVES

The study and mathematical model focusing on HES signals affected by misalignment are presented in [15], [38]-[39], [44], [65]. Assuming constant speed operation the formulation of equations describing the compensated intervals of these signals is presented in the literature. Subsequently, advanced angle adjustment methods from the literature to optimize these compensated HESs are derived.

A. Tashakori, et al. [9] provided a detailed analysis of the internal view of a BLDC motor equipped with HESs across various configurations. The study proposed a system for

detecting and identifying breakdowns in HESs based on sensor signals and Discrete Fourier Transform (DFT) analysis of measured motor line voltages. A simulation model was developed and presented, demonstrating that the FTC system requires minimal computational resources and can be seamlessly integrated as a subroutine within the main control program of the BLDC motor. Simulation results are discussed to validate the performance of the proposed system.

Krzysztof Kolano [16] introduced a motor control approach utilizing HES data for measuring rotational speed and motor rotor position. This method synchronizes the algorithm managing transistor operation cycles, ensuring optimal commutation timing irrespective of sensor placement accuracy. A notable feature is its capability to adjust commutation timing dynamically via software variables, eliminating the need for mechanically adjustable sensor orientation systems. The technique involves analyzing speed calculations within individual sectors to determine the BLDC motor shaft position accurately, making it suitable for applications requiring precise motor shaft positioning without additional absolute encoders. Furthermore, this control method effectively reduces inverter current amplitudes, motor noise emissions, and electromagnetic interference, enhancing environmental compatibility.

Salah W.A., et al. [34] elaborated on the electrical equations governing BLDC motors, formulated in terms of d- and q-axes stator currents and voltages. The paper explores the relationships among electromagnetic torque, rotor inertia, viscous friction coefficient, load characteristics, and mechanical rotor speed through mathematical expressions.

J. S. Park, et al. [57] introduced an online advanced angle adjustment method tailored for a sinusoidal BLDC motor, particularly addressing misaligned HESs. The method centers on estimating balanced rotor positions by compensating HES signals to equalize commutation sector intervals. Utilizing this position compensation technique, an advanced angle control method based on input voltage and current is applied seamlessly. This approach eliminates the need for additional configuration. The proposed method optimizes BLDC motor operation by aligning phase current with BEMF, thereby achieving efficient performance. Experimental results demonstrated effective tracking and maximum efficiency using the proposed method.

K. C. L. J. Kim, et al. [77] introduced a method to estimate high-resolution rotor position using low-resolution HESs in permanent magnet drives. They employed a vector-tracking position observer that utilizes discrete output signals from HESs. This observer includes a position error detector, which relies on the vector cross product of unit BEMF vectors derived from a stator electrical model. Additionally, a Proportional Integral (PI) controller is integrated to expedite the convergence of position errors to zero. This framework effectively

mitigates misalignment issues associated with HESs and enhances their transient operational capabilities.

Krzysztof Kolano [104] introduced a motor control method that utilizes HES data for measuring rotational speed and rotor position. Based on this information, the control system synchronizes the transistor switching algorithm, calculating optimal switching times to ensure optimal commutation points regardless of sensor placement accuracy.

ChatGPT

Park, Do-Hyeon et al. [105] propose a novel method to compensate for the misalignment effects of HESs in BLDC motor drives. They apply DFT to determine the magnitude of the fundamental frequency component, which correlates with the interval between adjacent HES signals, thereby identifying relative misalignment errors. Additionally, they utilize BEMF signals to compensate for absolute misalignment errors.

2.6 BLDC MOTOR DRIVES IN AUTOMOTIVE APPLICATIONS

The studies in [17], [32], [41], [106]-[108] have discussed the applications of BLDC motor drives in automotive domain. These BLDC motor drives with HESs are widely used in automobile applications. HES signal issues, Synchronization with BEMF profile, zero crossing detection, phase advancing, and harmonic analysis are examples of the research topics on HES based BLDC motor drives in automotive applications.

Vishnu Sidharthan P, et.al. [43] elucidated the motor modeling using mathematical equations for EV applications. They conducted MATLAB simulations to implement closed loop speed control of a BLDC motor. The hardware implementation utilized a microcontroller for motor control in EV applications. The controller generated the necessary PWM pulses to activate the respective stator windings, which were subsequently verified for their functionality.

Qingchao Zhang [101] introduced a maximum torque per ampere (MTPA) control strategy based on pseudo-dq transformation, specifically applied to the direct stator flux linkage in closed-loop control of BLDC motors. This approach is designed to accommodate various BLDC motors with non-ideal trapezoidal waveform BEMFs.

The study demonstrates that by employing this DTC scheme, simultaneous control of torque and flux linkage in BLDC motors is achievable. One significant advantage of this method is its ability to mitigate torque ripple caused by BEMF non idealities and commutation torque ripple typically observed in traditional DTC methods based on two phase conduction voltage vectors. The proposed control scheme enhances BLDC motor

performance by improving torque control accuracy and reducing copper losses, thereby making it suitable for EV applications.

Hanif F. Prasetyo, et.al. [109] proposed a method to develop a control module for BLDC motors comprising two sub modules: the test motor control submodule and the load motor control submodule for EV applications. The test motor control submodule regulates the speed of the test motor of the EV to replicate a predefined EV driving cycle. Concurrently, the load motor control submodule manages the torque or current applied to the load motor to simulate various loading conditions affecting the test motor.

A. Tashakori, et.al. [110] and Pellegrino, et.al. [37] presented a comparative study among DC, induction, BLDC, and SR motors, focusing on their suitability for EVs. The study simulated and compared speed, torque, and power characteristics, emphasizing key performance metrics such as high torque at low speeds, torque-to-size ratio, instant power capability, power density, efficiency, and energy savings over extended periods. BLDC motors were found to exhibit superior torque-speed characteristics, higher efficiency leading to significant long-term energy savings, a favorable power-to-size ratio, enhanced dynamic response, and noiseless operation compared to brushed DC, induction, and SR motors.

In contrast, SRMs were noted for their fault tolerance due to their design, offering advantages in situations involving electrical faults, vibrations, and mechanical shocks. However, BLDC motors, with their permanent magnet rotor, demonstrated higher dynamic response capabilities compared to SR motors. The study recommended fault detection, diagnosis, and prevention techniques based on dynamic model parameter estimation to mitigate noise susceptibility.

Z. Q. Zhu, et.al. [111] proposed a method to analyze the torsional vibration transfer function of drive systems using cogging torque as a constant excitation source. They introduced improved DTC schemes for BLDC motors, which account for non-sinusoidal BEMF, cogging torque, and commutation torque ripples in the case of BLDC motors. The study systematically investigates the stator torsional vibration of under different DTC schemes and alternative torque ripple compensation strategies.

Experimental findings in [112], [108] highlight that under BLDC DTC operation, cogging torque and distorted phase currents during commutation intervals play significant roles in stator torsional vibration. The torsional vibration spectra observed in both operating modes exhibit harmonics at frequencies multiples of six times the fundamental electrical frequency. The amplitudes of these harmonics are influenced by the magnitude of exciting torque harmonics and the torsional vibration transfer function of the stator assembly.

F. Yang, et.al. [113] proposed a series-resonant MOSFET full-bridge converter for efficient power transfer, achieving zero voltage switching and boosting the DC bus to higher voltages. They coupled this with an insulated-gate bipolar transistor (IGBT) inverter to drive a 1-kW/6000-r/min BLDC, ensuring high efficiency, low cost, and compact size. The design includes a variable output voltage feature in the DC/DC converter, enabling a method to reduce commutation torque ripple and minimize mechanical vibration.

R. Sreejith, et.al. [114] explored the requirements of BLDC motor drives by simulating their application in a three wheeler EV. The study focused on calculating torque, power demands, and battery capacity based on various parameters. They developed a methodology to determine motor and battery specifications tailored to typical three wheeler EVs, considering both direct drive and geared drive configurations. Simulations were conducted to evaluate performance under continuous and short-time loadings, aligning with root mean square (RMS) and peak ratings of the EV drive motor.

Jiadan Wei, et.al. [115] introduced a control strategy aimed at mitigating commutation and conduction torque ripples in BLDC drives used in household appliances. They outlined the primary causes of torque ripples in BLDC motors as follows:

- The torque ripple during commutation arises from the different rates at which current changes in the phases involved in switching. This results in deviations in current flow in the non-commutating phase, leading to commutation torque ripple.
- Imperfections in motor design and manufacturing contribute to non ideal BEMF waveforms, which may deviate from trapezoidal or sinusoidal forms. Traditional chopping control schemes that generate quasi-square wave currents during normal conduction intervals contribute to conduction torque ripple.

EMI is another factor that is required to be factored in the controller and motor design for EV applications. The studies in [113], [107]-[108] address the critical aspect in the operation of BLDC motors, particularly in the context of their electromagnetic compatibility (EMC) characteristics. The effect of parasitic elements in the load circuitry on EMI is emphasized. These parasitics can include stray capacitances, inductances, and resistances inherent in the motor drive system and its associated components. The insights into the interplay between stator structures, EMI, and vibration characteristics of BLDC motors are discussed for understanding of motor design for improved EMC and mechanical stability.

2.7 STATE OF ART DISCUSSION

Significant literature has been reported on permanent magnet machines, BLDC motor drives, their applications particularly in automotive applications. The efficient control and operation of three phase BLDC motors is necessary for EV and other battery powered applications. The mathematical model, simulation and analysis of the BLDC motor drive control and operation using MATLAB software platform have been reported in the research works [23], [35], [52], [78], [102]. The hardware design of the controller development with 32bit ARM microcontroller based inverter and driver circuitry, software development and deployment on test bench with implementation of control schemes is reported in the application notes with summary guidelines for industrial grade application design aspects [98], [103], [116]-[119]. Various types of missing hall sensor signal faults have been extensively reported in the existing literature. However, there is scope of further study and analysis on mistiming of HES signals, their effect on switching angle deviations and consequent drive performance degradation are next steps for further analysis.

Various FTC schemes of phase angle advancement and signal reconstruction, based on the concept of instantaneous speed averaging, extrapolation, or other complex methods like Fast Fourier Transformation (FFT) are there in literature for faults related to HESs [60]-[61], [105]. The existing studies and methods which can be utilized in the FTC schemes to overcome the effect of the HES faults have been broadly classified into two categories as speed dependent methods and detecting unexpected timings of HES transitions in [11], [120].

The direct redundancy approach for HES fault and correcting mistimed switching signals by increasing number of HESs has been presented. The DC link and phase current based commutation angle corrections are presented in [86], [121]-[123]. This approach results in hardware modification and increase in cost if implemented in EV controller design.

Speed based fault detection schemes function on the time interval between two or more consecutive transitions and calculating rotor speed based on this data set. Thus, any incorrect transition will provide either higher or lower estimates than correct and expected speed value. The resultant acceleration or deceleration in short span can be too large and can be detected subsequently. The rotor position or speed estimation based algorithms have limitations during acceleration and deceleration periods. The instantaneous change in the electrical angle when the misleading angle due to non varying speed is corrected at HES signal transition instant itself, causes abrupt change in current and torque profiles. Therefore, methods have been proposed to distribute the error in more than one electrical cycle comparable to moving average data processing. This approach results in low-frequency distortions because of

continuous modification of the electrical speed [67], [124]-[125]. Most of these methods have been developed around sensorless approach of PMM operation.

The moving average based method is used to obtain rotor position by employing LSM on linear interpolated values of previous sector. The values calculated are used as initial electrical angles for the next sector and for speed estimation. During each HES transition signal, a compensation algorithm is employed to correct the deviation in electrical angle. This method is reported with higher execution time and memory requirement along with possibility of jerks because of discontinuity introduced at each HES transition signal. Speed estimation using six sample moving average with second order Taylor (SOT) approximation method to obtain electrical angle is explained in [126]-[127]. However, the method doesn't consider the case when extreme values of electrical angle are reached due to HES misalignment issue and, the inherent fixed angle fault value along with other variables obtained in this method. The method is vulnerable to effects by noise, which is inherent in the BLDC motor operation in EV applications.

The methods discussed can be modified for actual hardware and software implementation in EV controller. However, if the complete process up to signal reconstruction involving error estimation itself, is repeated after each hall transition, then it may cause longer execution time of interrupt subroutine and, can interfere in the inverter switching timings. Ideally, there should not be a delay between switching off and switching on. However, in actual systems there is dead time insertion between change of conduction switches of the inverter leg for accounting switching off and on time [7], [46]. Additional delay caused by not giving proper switching command after HES transition signals will cause distortion in the applied motor phase signals and deviation from the intended signal pattern [58], [128].

The EV controller systems use starting software routines for initialization of machine state and observing the startup parameters like voltage, hall signal etc. for further operation [7], [96]. The acceptable solutions for these types of faults should essentially confirm to the guidelines for incorporation in EV controller applications. The cases where other HES faults occur which cannot be instantly diagnosed and require time for detection and compensation, the functionality of the FTC method under fast speed change or sudden load change may become non feasible [129]-[130], [57]. Furthermore, the overall angular correction may not be calculated correctly because of combined effect of both static component of angular error due to HES misalignment and, the effect of fault occurred during run time operation. Hence, if the static part of the angular correction required is already separated and known independently, the possibility of identification and mitigation of effects due to other faults

increases significantly. This forms the basis of the proposed schemes in this research work that can be incorporated in the controller along with the starting routines for faster fault diagnosis and required corrections.

2.8 IDENTIFIED RESEARCH AREAS

Based on the extensive literature review and study of the literature on BLDC motor drives and motor controllers, along with their use in EV applications, the following major areas of research have been identified:

- The motor controller is an integral part of BLDC motor drives. Implementation of the electronic commutation methods and control mechanisms necessitate a dedicated controller. It supervises crucial drive parameters such as phase currents, phase voltages, duty cycle of inverter switching signals, their synchronization, and commutation sequence to control the drive operation. The controller design itself is the most important and challenging aspect of a BLDC motor application.
- The mathematical modeling and simulation of the BLDC motor drive is required to check the synchronized commutation timings with HES signals and, to check the HES signal faults in the drive before implementation on physical hardware set up. In the hardware test setup, testing and verification of the controller circuit operation by integrating with BLDC motor is necessary before deploying for full capacity operation. Detection of phase sequence, HES connection verification and detection of any glitch in the HES signals are required to be tested during motor controller integration.
- The HES based faults, including sensor damage and motor running on less than three HESs, have been studied and reported in the existing literature. However, the study and analysis of HES signals with non-ideal timings is still an area of research for fault effect mitigation.
- The possible mapping of errors related to the timing issues of the HES signals in the drive are essential for the development of the relevant FTC schemes. These issues cause distortion in the switching pattern, loss of synchronization, deviation in feedback, and miscalculation of the parameters.
- Investigation of delayed commutation and the possibility of its estimation by the DC link current profile is another research area. This has potential scope for application in drives that rely only on DC link current measurement.
- Different types of FTC schemes based on different types of parameters and control

schemes have been reported in the literature. However, more research work is needed for applications that work without phase current measurement or BEMF estimation schemes for control and inverter switching time synchronization. The study and analysis of the effect of the faults and FTC development for this segment of application is an important area of research with the potential scope of real time implementations.

- The possibility of actual implementation of the FTC schemes in motor controllers is an important aspect of the present day research requirements. The inclusion of FTC schemes for these faults has implications in terms of additional memory requirements, interrupt scheduling interference, and calculations involving complex algorithms in real time. Thus, the development of easy-to-implement FTC schemes is a research prospect in the area of BLDC motor drives.

2.9 CONCLUDING REMARKS

In this chapter, a detailed review of the modeling and simulation of BLDC motor drives, sensored and sensorless control schemes, and commutation methods has been carried out. The issues of inherent torque, speed ripples, and HES based faults have been investigated in the existing literature. Various kinds of HES faults, including sensor breakdown and methods for estimation of speed, have been particularly investigated in the existing literature. However, the need to investigate the timing deviations of the HES signals and further mapping with HESs is required for the development of computationally and memory efficient FTC schemes. On the controller side, all the FTC schemes, along with the required commutation and control schemes that can be implemented in real time, must adhere to the basic requirements of the 3-phase inverter switching and interrupt sequencing mechanisms. The need to develop FTC schemes such that their implementation requires fewer additional resources, and less execution time is well established from the existing literature. There are several techniques that have been reviewed to minimize the HES fault effects, including those based on DC link current only. Based on the reported experimental and research works in the literature, a comprehensive discussion on the current state of the art is provided, outlining the rationale and prerequisites for the presented research. Finally, the major areas of research and existing gaps have been identified for finalizing the proposed research objectives.

CHAPTER 3

MODELING AND SIMULATION OF BLDC MOTOR DRIVE

3.1 INTRODUCTION

This chapter discusses the mathematical modeling of the BLDC motor followed by the implementation of HES based drive control system. Implementation of the trapezoidal commutation scheme is carried out in the drive. Since this research work includes integration of HES signal timing issues that are encountered in BLDC motor drives in EV applications, the simulation of mistiming in HES signals is also carried out for use in further implementation in the FTC schemes presented in Chapters 5 and 6.

The motor drive modeling and simulation are carried out in MATLAB/Simulink simulation environment. The equivalent circuit of the drive along with the fundamental voltage equations of BLDC motor is used as a base for system development. The HES signal based trapezoidal commutation method is simulated and verified for correct drive operation. Further provision for implementing timing deviations of the HES signals in the simulation model is also added. This is tested and verified by implementing deviations for one HES, two HES and three HESs separately in the simulation model. Simulation results and the verification by the timing calculations confirm the successful implementation of the HES signal deviations in the model.

3.2 MATHEMATICAL MODELING OF THE BLDC MOTOR DRIVE

The methodology for modeling a BLDC motor is akin to that of a three-phase synchronous machine. A three-phase voltage source is applied to the BLDC motor, with a notable distinction being that the source voltage doesn't have to be sinusoidal [10], [23], [56]. However, it's crucial to ensure that the peak voltage remains within the motor's maximum voltage limit [131].

Figure 3.1 illustrates the BLDC motor drive circuit with inverter and power supply. The equivalent circuit of the stator windings has three star connected phases with resistive and inductive elements. The BEMF for each phase is also included in the circuit. The phase currents and voltages are marked and used in the equations derived by accounting for the phase terminal voltages and current circulations in the circuit. The three phases are assumed to represent ideal case scenario by having equal parameters with symmetrical BEMF and current profiles.

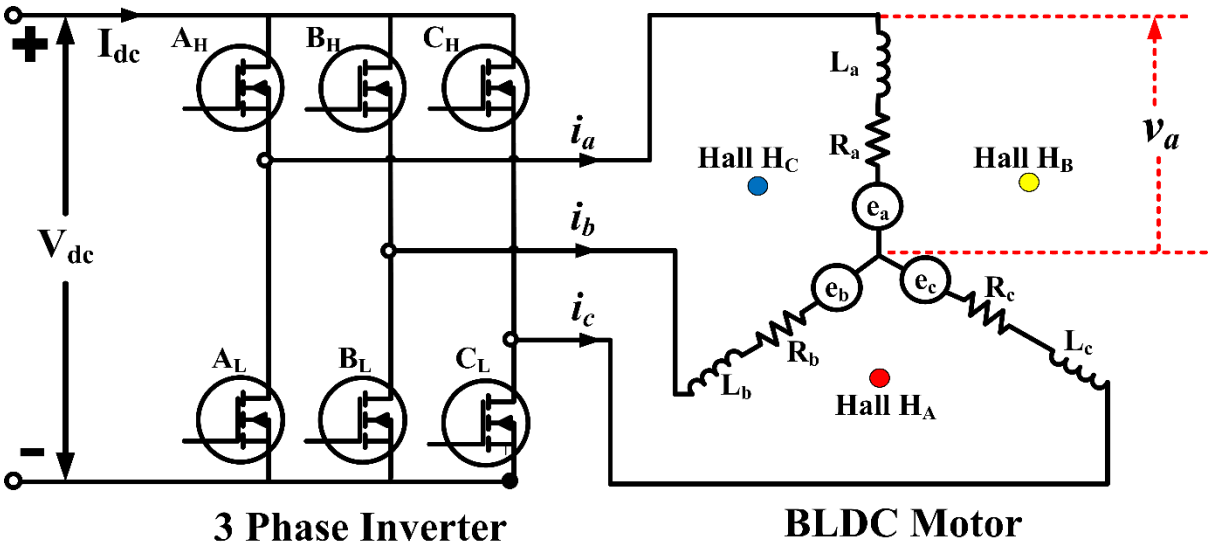

Fig. 3.1 Equivalent circuit of sensored BLDC motor drive with three phase inverter.

Since $R_a = R_b = R_c = R$ for symmetrical winding parameters, the voltage equations of the BLDC motor are derived as follows [10]:

$$v_a = Ri_a + L\frac{di_a}{dt} + e_a \tag{3.1}$$

$$v_b = Ri_b + L\frac{di_b}{dt} + e_b \tag{3.2}$$

$$v_c = Ri_c + L\frac{di_c}{dt} + e_c \tag{3.3}$$

where v_a, v_b, v_c are terminal phase voltages, i_a, i_b, i_c are input currents of the motor. L represents armature self-inductance, R armature resistance of stator phase winding, and e_a; e_b; e_c are trapezoidal BEMF of the three phases. The phase wise voltage equations in the matrix form can be represented as

$$\begin{bmatrix} v_a \\ v_b \\ v_c \end{bmatrix} = \begin{bmatrix} R & 0 & 0 \\ 0 & R & 0 \\ 0 & 0 & R \end{bmatrix} \begin{bmatrix} i_a \\ i_b \\ i_c \end{bmatrix} + \frac{d}{dt} \begin{bmatrix} L_a & L_{ab} & L_{ac} \\ L_{ba} & L_b & L_{bc} \\ L_{ca} & L_{cb} & L_c \end{bmatrix} \begin{bmatrix} i_a \\ i_b \\ i_c \end{bmatrix} + \begin{bmatrix} e_a \\ e_b \\ e_c \end{bmatrix} \tag{3.4}$$

The effects of saturation and iron losses are assumed to be negligible in this representation. Because of symmetrical stator windings the three phase self inductances and resistances are equal. The mutual inductances between all phase pairs are also identical [64]. Thus, following relations can be used in the further analysis

$L_a = L_b = L_c = L$

and

$$L_{ab} = L_{ac} = L_{ba} = L_{bc} = L_{ca} = L_{cb} = M \tag{3.5}$$

Hence, the Eqn. (3.4) can be rewritten as

$$\begin{bmatrix} v_a \\ v_b \\ v_c \end{bmatrix} = \mathrm{R}\begin{bmatrix} 1 & 0 & 0 \\ 0 & 1 & 0 \\ 0 & 0 & 1 \end{bmatrix}\begin{bmatrix} i_a \\ i_b \\ i_c \end{bmatrix} + \begin{bmatrix} \mathrm{L} & \mathrm{M} & \mathrm{M} \\ \mathrm{M} & \mathrm{L} & \mathrm{M} \\ \mathrm{M} & \mathrm{M} & \mathrm{L} \end{bmatrix}\frac{\mathrm{d}}{\mathrm{dt}}\begin{bmatrix} i_a \\ i_b \\ i_c \end{bmatrix} + \begin{bmatrix} e_a \\ e_b \\ e_c \end{bmatrix} \tag{3.6}$$

The BEMF profile in the BLDC motor is dependent on the rotor position and its peak value is proportional to the speed. Thus, BEMF for each phase be as represented as follows:

$$e_a = \mathrm{K_b f_{as}}\ (\theta)\omega \tag{3.7}$$

$$e_b = \mathrm{K_b f_{bs}}\left(\theta + \frac{2\pi}{3}\right)\omega \tag{3.8}$$

$$e_c = \mathrm{K_b f_{cs}}\left(\theta - \frac{2\pi}{3}\right)\omega \tag{3.9}$$

where $\mathrm{K_b}$ represent the BEMF constant [V/ rad/second], θ represent the electrical rotor angle [ºE] and ω speed of the rotor [rad/sec] respectively. The trapezoidal BEMF profile is represented by three functions.$\mathrm{f_{as}}$; $\mathrm{f_{bs}}$; $\mathrm{f_{cs}}$ for the respective phases wherein the one phase trapezoidal function $\mathrm{f_{as}}(\theta)$ is described as [10], [21]:

$$\mathrm{f_{as}}(\theta) = \begin{cases} \frac{6}{\pi}\theta & 0 < \theta \le \frac{\pi}{6} \\ 1 & \frac{\pi}{6} < \theta \le \frac{5\pi}{6} \\ 1 - \frac{\left(\theta - \frac{5\pi}{6}\right)}{\frac{\pi}{6}} & \frac{5\pi}{6} < \theta \le \frac{7\pi}{6} \\ -1 & \frac{7\pi}{6} < \theta \le \frac{11\pi}{6} \\ -1 + \frac{\left[\theta - \left(\frac{11\pi}{6}\right)\right]}{\frac{\pi}{6}} & \frac{11\pi}{6} < \theta \le 2\pi \end{cases} \tag{3.10}$$

The other two phase functions $\mathrm{f_{bs}}$ and $\mathrm{f_{cs}}$ are 120º apart from $\mathrm{f_{as}}(\theta)$ in balanced 3 phase configuration and can be expressed as

$$\mathrm{f_{bs}} = \mathrm{f_{as}}\left(\theta + \frac{2\pi}{3}\right) \tag{3.11}$$

and

$$\mathrm{f_{cs}} = \mathrm{f_{as}}\left(\theta - \frac{2\pi}{3}\right) \tag{3.12}$$

The rotor angle in electrical degrees is related to the mechanical rotor angle as follows

$$\theta = \frac{\mathrm{P}}{2}\theta_{\mathrm{m}} \tag{3.13}$$

where P represents the number of pole pairs and θ_{m} the rotor angle in mechanical degrees.

The total power developed can be obtained by combining the three phase powers as $\mathrm{e_a I_a} + \mathrm{e_b I_b} + \mathrm{e_c I_c}$ which is equal to the power denoted by the product of electromagnetic torque and speed. Thus, following relation is obtained for electromagnetic torque.

$$\mathrm{T_e}\ \omega = e_a I_a + e_b I_b + e_c I_c \tag{3.14}$$

The motor mechanical motion equations in terms of torque and loading are:

$$T_e - T_l = J\frac{d\omega}{dt} + B\omega \quad (3.15)$$

T_l stands for the load torque, J is the moment of inertia of the rotor, and B is the viscous friction coefficient.

3.3 DRIVE SIMULATION WITH TRAPEZOIDAL COMMUTATION

The BLDC motor's structure closely resembles that of a PMSM. Windings are situated on the stator, while permanent magnets are mounted on the rotor [132]. Thus, simulation model is developed using the basic PMSM structure in MATLAB Simulink environment. The BEMF waveshape is configured trapezoidal as required for BLDC motor. In a standard drive configuration with three HESs, there are six valid combinations of the binary output signals in an electrical cycle. Thus, one electrical cycle is divided into six sectors of 60°E interval. This signal pattern is used to track rotor position and direction of rotor rotation [44]. The sequence for inverter switching is determined by the sector number and is synchronized with the transitions detected on the HES signals. The 120° trapezoidal commutation switching sequence referenced to circuit of Fig. 3.1 is presented in Table 3.1 [9], [105].

The simulation model for BLDC motor is shown in Fig. 3.2. The working principle of control of BLDC motor according to the 120º trapezoidal commutation scheme is used in this model. The rotor speed is compared with the reference speed and the difference error is used to control the 3-phase inverter switching for adjusting the applied terminal voltage at motor phases. The difference between reference and actual speed is used with a PI controller that is used as a speed controller. An ideal torque source provides the load. The BLDC motor parameters are presented in Table 3.2.

Table 3.1 Switching sequence for trapezoidal commutation scheme with HES signal pattern.

S. No.	**Rotor Angle (^{0}E)**	**Hall Sensor Signal**			**Switching Pattern**						**Phase Voltage**		
i	Φ	H_A	H_B	H_C	A_H	B_H	C_H	A_L	B_L	C_L	Phase C	Phase B	Phase A
1	0^0-60^0	0	0	1	1	0	0	0	1	0	0	$-V_{dc}$	$+V_{dc}$
2	60^0-120^0	1	0	1	1	0	0	0	0	1	$-V_{dc}$	0	$+V_{dc}$
3	120^0-180^0	1	0	0	0	1	0	0	0	1	$-V_{dc}$	$+V_{dc}$	0
4	180^0-240^0	1	1	0	0	1	0	1	0	0	0	$+V_{dc}$	$-V_{dc}$
5	240^0-300^0	0	1	0	0	0	1	1	0	0	$+V_{dc}$	0	$-V_{dc}$
6	300^0-360^0	0	1	1	0	0	1	0	1	0	$+V_{dc}$	$-V_{dc}$	0

Table 3.2 Simulation model parameters.

Machine Parameters		
Number of pole pairs P	4	
Stator resistance per phase R_s	2.8750	Ω
Stator self-inductance per phase L_s	8.5	mH
Stator mutual inductance M_s	0.00001	H
Flux linkage established by magnets	0.076394	V.s
Rotor inertia J_m	0.0004	$Kg.m^2$
Rated Power	1	kW
Rated Speed	3000	RPM
Rated Voltage	48	V
Viscous Damping	0.001	Ns/m

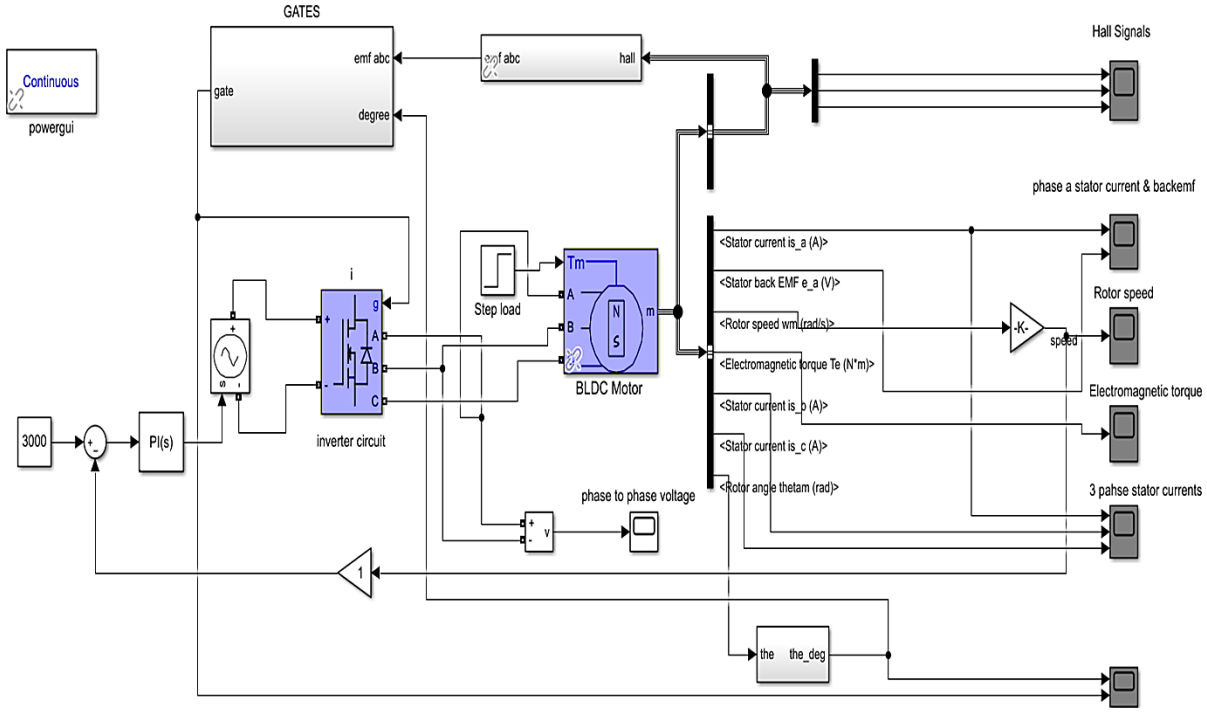

Fig. 3.2 Matlab simulation model of the BLDC motor drive system with HESs.

The HES signal based commutation scheme is implemented by utilizing the rotor angle information of the motor. The rotor angle is first converted in the range of -180º to +180º. This angle is further processed using logical gate operations as shown in Fig. 3.3. The HES signal pattern is obtained according to the rotor angle with one HES transition obtained after every 60ºE rotor rotation. For an individual HES, the logical value transition occurs after 180ºE rotor rotation. Thus, for a correctly working drive with 3 HESs system working correctly, every 3rd transition signal is from the same HES.

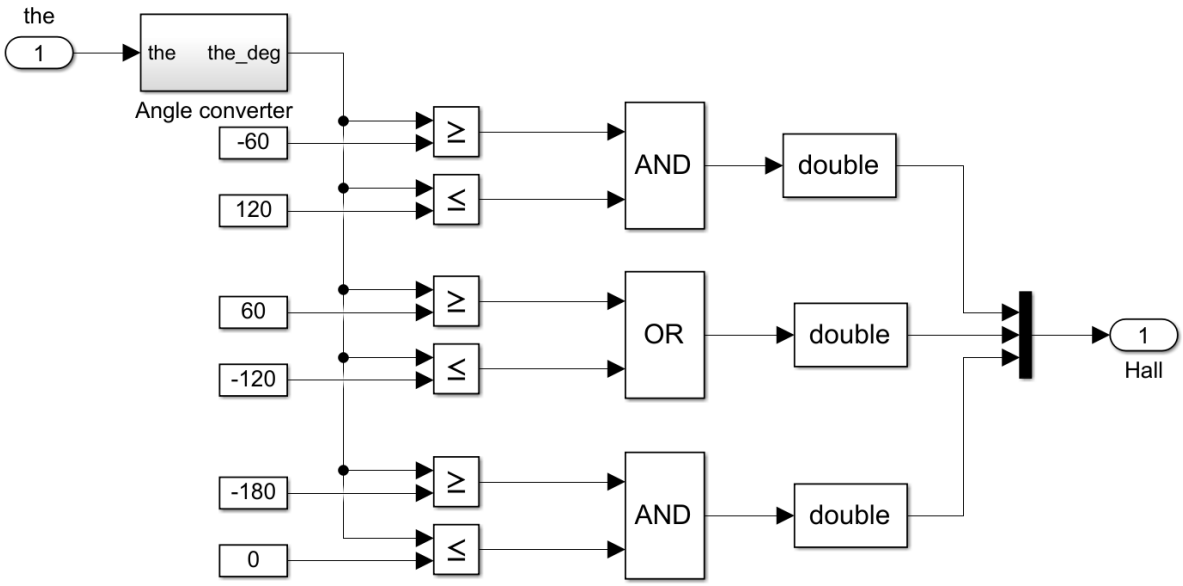

Fig. 3.3 HES signal implementation in simulation model.

Simulation results of the drive confirm trapezoidal commutation scheme implementation with three HESs. Simulation is carried out for 3.5 seconds. Figure 3.4 shows the synchronized speed and torque profile of the motor. For better observability the profiles up to 0.2 second are presented. Figure 3.5 shows the HES signals obtained near the end of simulation at steady speed. To validate the derived HES signal pattern in the drive, the three HES signals are XORed to obtain the transition signals that correspond to 60ºE sector boundaries. It is observed that each HES signal transition occurs after 180ºE interval; at no point all three HESs are of same logic level; HES signals are 120º apart from each other and, the spans of all three HES signals at any logic level are equal which confirms the equal durations of 60ºE sectors.

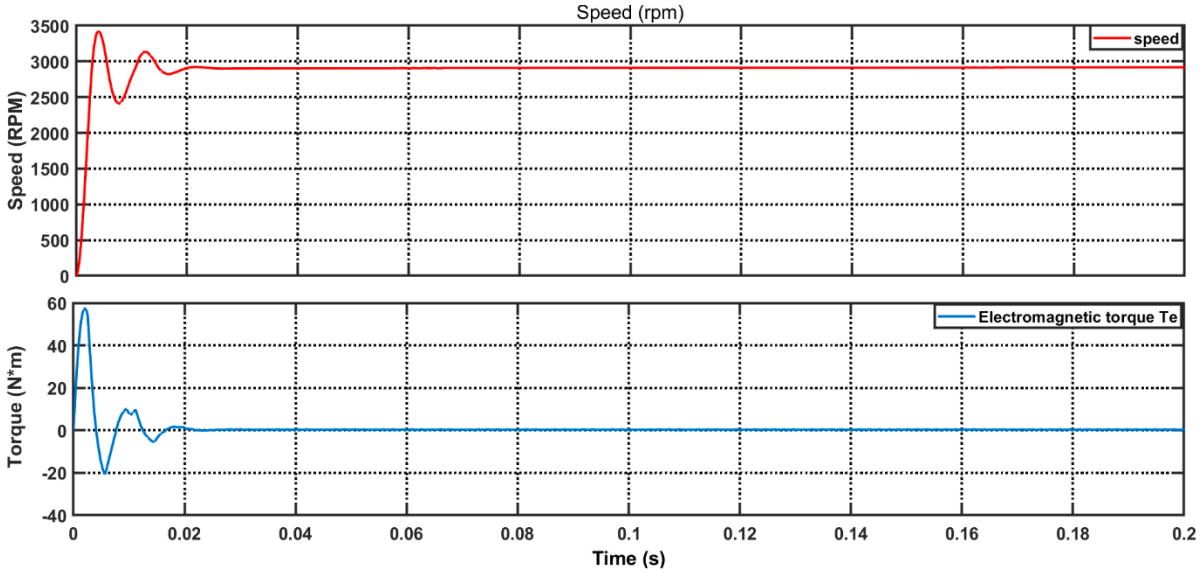

Fig. 3.4 Rotor speed and torque waveforms from starting.

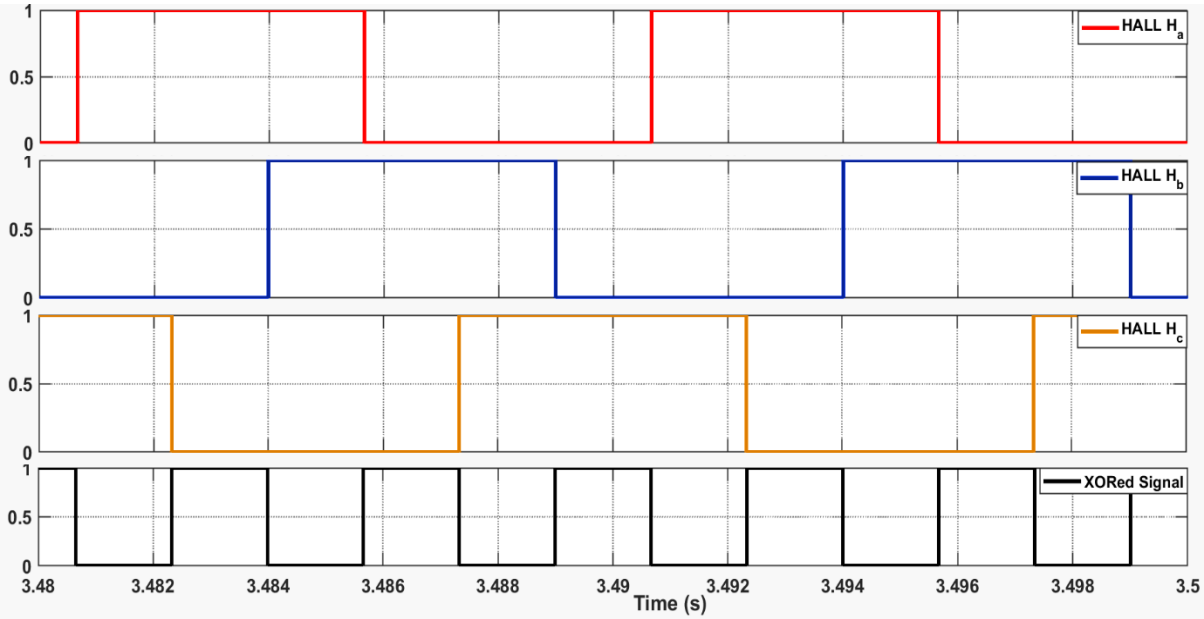

Fig. 3.5 Synchronized HES signals and equivalent 60ºE sectors.

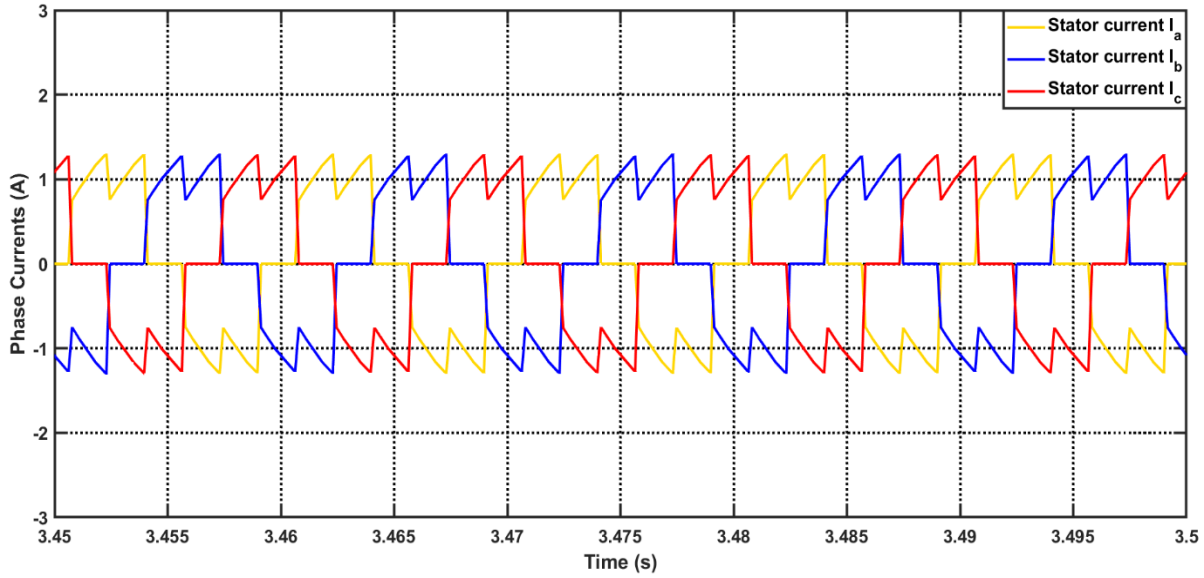

Fig. 3.6 Balanced three phase stator current profiles.

The balancing of all three stator phase currents is required at steady state operation of the drive and at no load, these currents should be centred around zero with same magnitude of peak values in positive and negative direction for ideal case drive operation. The current profiles of the simulation shown in Fig. 3.6 confirm this requirement with balanced three phase currents that are 120ºE apart in the trapezoidal commutation scheme.

Further validation is carried out by checking the synchronized pattern between stator phase current and BEMF profile. Figure 3.7 shows the phase current and BEMF profiles for one phase. The synchronization at zero crossing points and BEMF peaks attained in both

directions match with the direction of the current through the phase. The BEMF attains the desired peak values in both directions and is centered at zero value. Figure 3.8 shows the speed and torque profiles near steady state. The inherent ripples are observable in the graphs centered around a nearly stable value.

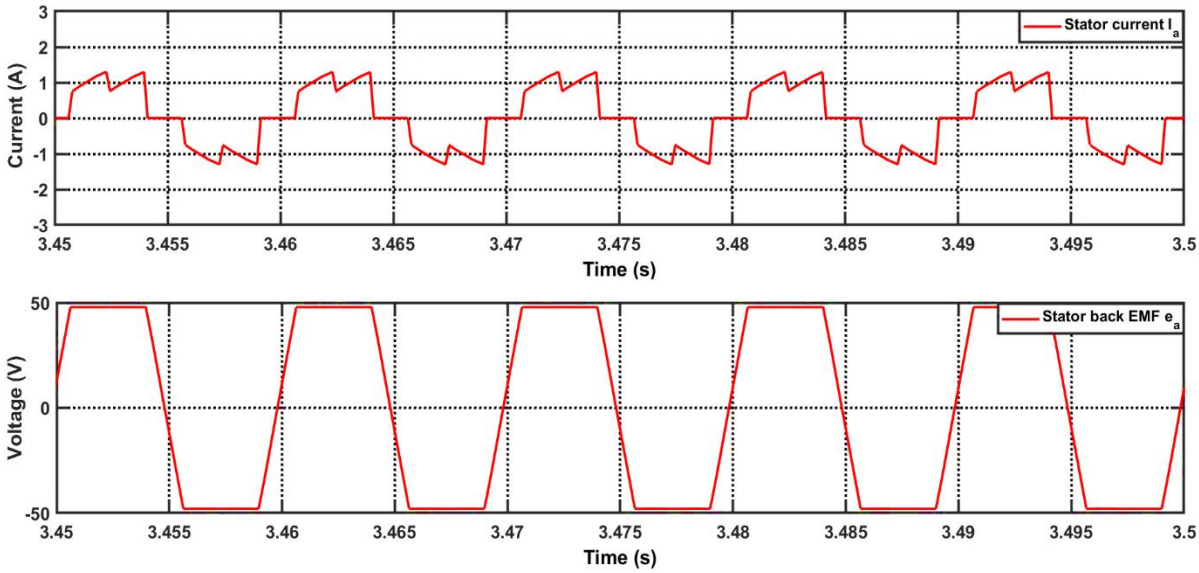

Fig. 3.7 Synchronized stator phase current and BEMF profiles.

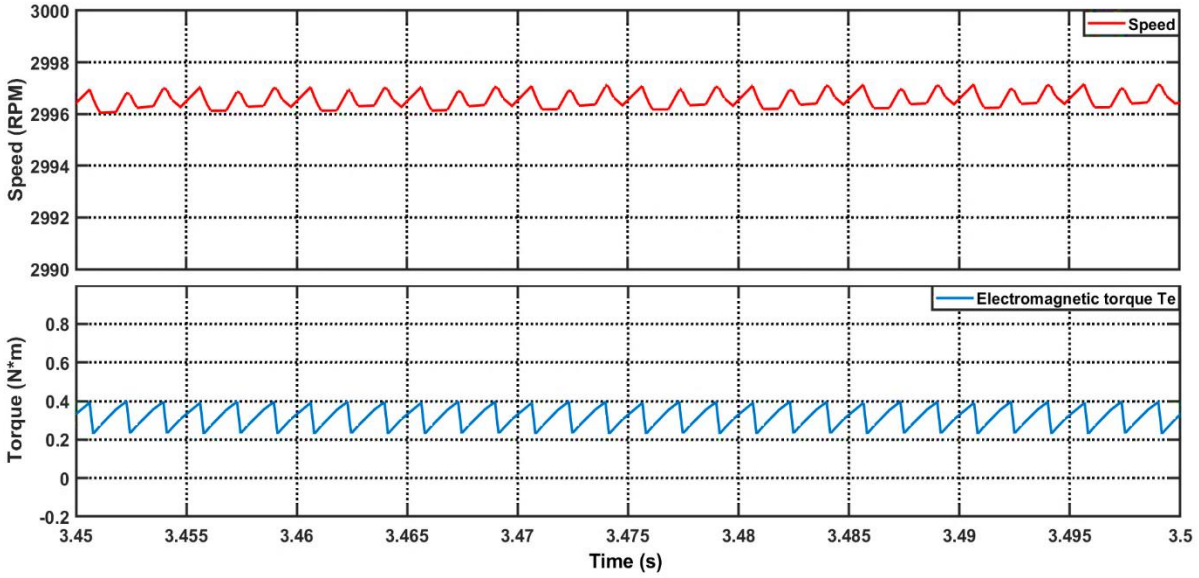

Fig. 3.8 Balanced speed and torque profiles with ripples.

3.4 IMPLEMENTATION OF THE HES SIGNAL IMBALANCE IN SIMULATION MODEL

The functioning of overall motor and control system depends on the integrity of HES signals. These signals are used to accurately detect rotor position at fixed angular intervals. The timing of the transition of HES signals indicates the control system that rotor has rotated

by electrical 60ºE sector. The commutation timings and pattern of the inverter switching system for the motor control operation are synchronized with these signals [127], [129]. The estimated speed calculation is also calculated according to the time taken by the rotor to traverse one sector. The time duration between two HES signals indicates the time rotor has spent in that sector. When the HESs are not placed accurately in the motor or, due to any other factor, the signals provided by HESs do not correspond to exact 60ºE rotor movement, the switching signals of the inverter circuit are also not timed exactly at 60ºE rotor movement. Thus, misalignments of the HES signals cause errors in the motor control and its operation [12]. Therefore, implementation of deviations in HES signal timings in the simulation model and verification of the effect on 60ºE sector spans is necessary before development of FTCs for physical hardware implementation. The arrangement of Fig. 3.3 allows the change in HES angle boundary values and subsequent implementation of the angular deviation in the HES signal timings. This permits the simulation of delay or advancement of HES signal. This method is used for implementing deviations in one, two or three HES signals separately in the simulation model.

Simulation with One Misaligned HES Signal: Figure 3.9 shows the implementation of 10º deviation in one HES signal by changing the boundary angle to -170º from -180º. This arrangement represents a particular case when only one HES signal is misaligned but the rest two are correctly timed. The angular span between two HESs is altered in this case with one span extended, and the next span reduced by the same angle. The same method is applied for introducing two HES and three HES signal unbalancing in the simulation model.

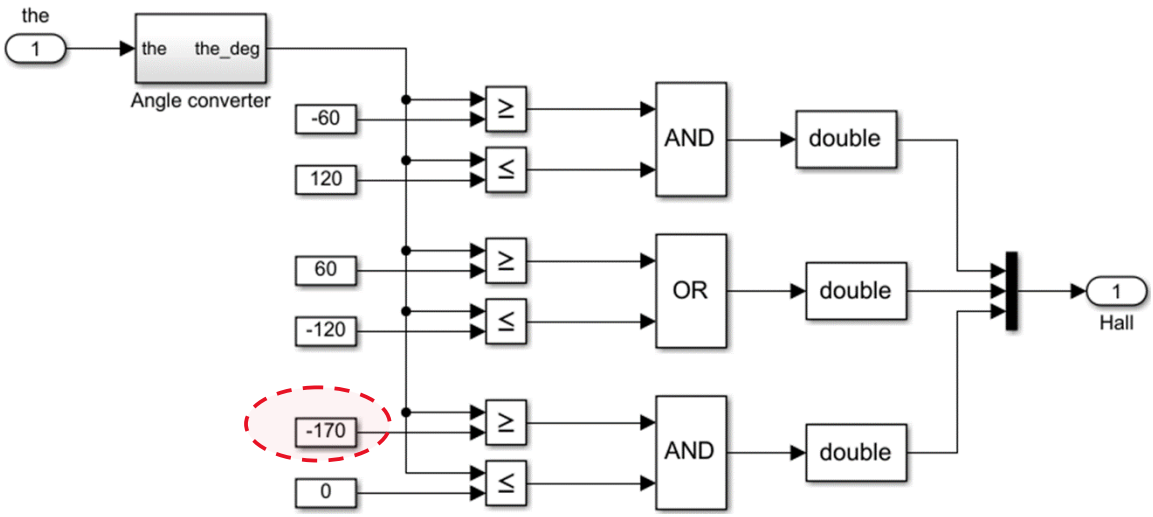

Fig. 3.9 HES signal deviation implementation in simulation model.

Figure 3.10 shows the derivation of the commutation switching signals from the three signals that are based on the HES signals with deviations. Using these derived BEMF signals, six switching signals are obtained that include effect of the HES signal mistiming. These signals numbered from u1 to u6 are further processed in the function block for angular span correction by comparing with the rotor angle information which is termed as “degree” input in the block. The final output signals of the block named g1 to g6 are commutation signals with correction of the HES signal deviations. The arrangement permits correction in the timing of the commutation signals for testing, verification and analysis for FTCs presented in chapters 5 and 6.

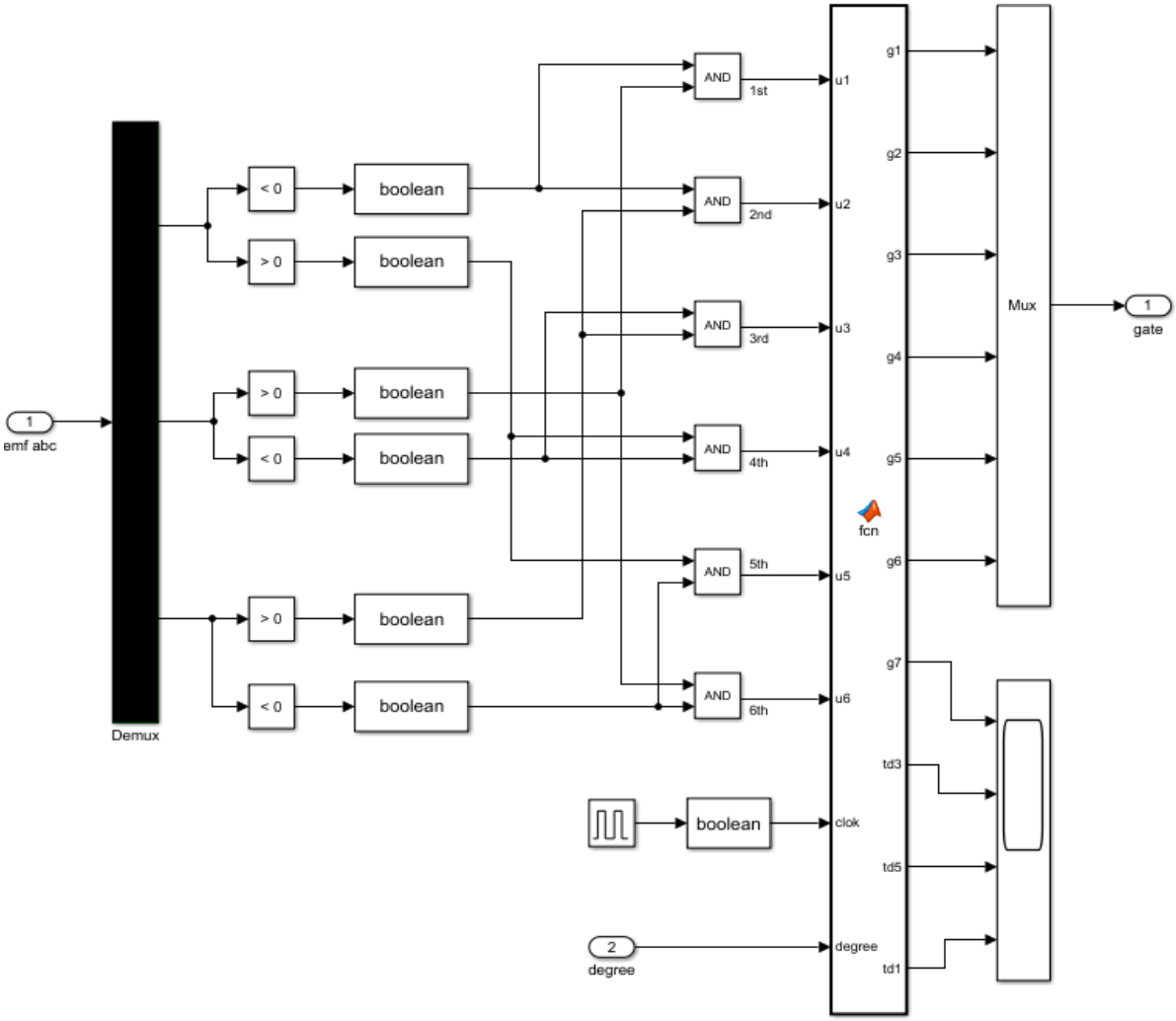

Fig. 3.10 Derivation of the commutation switching signals with misaligned HES signals.

For a single pole pair motor, electrical degree span of altered sectors can be expressed as equation (3.16) where $\Delta\phi$ stands for deviation in the sector duration

Extended sector span = $(60° + \Delta\emptyset)$

Reduced sector span=$(60° - \Delta\emptyset)$ (3.16)

For P no. of pole pairs the electrical degree span of two affected sectors and angle deviation are expressed using equations (3.17) and (3.18) respectively where Δt refers to time deviation in the sector duration.

Extended sector span = $60° + \frac{\Delta\emptyset}{P}$

Reduced sector span= $60° - \frac{\Delta\emptyset}{P}$ (3.17)

$\Delta\phi = \Delta t \times \frac{(p \times \omega)}{60} \times 360$ (3.18)

Besides the angular span change of sector, the starting and end timings of the sector are also offset by a certain angle. This has significant consequences in case of multiple HES signal misalignments.

The calculations and resultant observations from the simulation are summarized in Table 3.3 for validating the implementation of HES misalignment in the simulation model. The approximate deviation found out in hall sensor placement is near to the exact value of 10º. The deviation less than 0.1º is neglected as calculation and observation error. The two consecutive sectors at serial number 4 and 5 are affected by the misaligned HES signals with equal compression and elongation of the respective sector durations. The rest four durations are of normal span indicating four normal commutation switching timings.

Table 3.3 Verification table for one HES signal unbalancing in simulation model.

S. No.	Sector Duration (ms)	Deviation From Ideal Sector Duration Δt (ms)	Deviation From Ideal Sector Duration (ºE)	Deviation Neglecting Calculation Error Δϕ (ºE)	Angular Deviation Δθ in mechanical degrees
1	0.842	-0.000452911	-0.000806805	0	0
2	0.843	0.000954709	0.017006964	0	0
3	0.841	-0.001045291	-0.018620574	0	0
4	0.699	-0.143045291	-2.548175721	-2.548175721	-10.19270288
5	0.99	0.147954709	2.635630954	2.635630954	10.54252381
6	0.84	-0.002045291	-0.036434342	0	0

The simulation results confirm trapezoidal commutation scheme implementation with one HES signal misalignment. Figure 3.11 shows the HES signal pattern obtained near the end of simulation at steady speed. The two consecutive sectors that are elongated and shortened respectively are highlighted. The early low to high transition of HES signal H_b is also highlighted in the presented HES signal patterns.

Figure 3.12 shows the synchronized speed and torque profile of the motor. The unbalancing in the three phase currents is shown in the Fig. 3.13. The I_b phase current shown in the blue coloured profile shows marked increase in the peak current in the positive conduction current values. The corresponding return current also shows increase as shown in the yellow coloured current profile I_a. These observations confirm the imbalanced commutation switching that is caused by the deviation introduced in the HES signal in the simulation model.

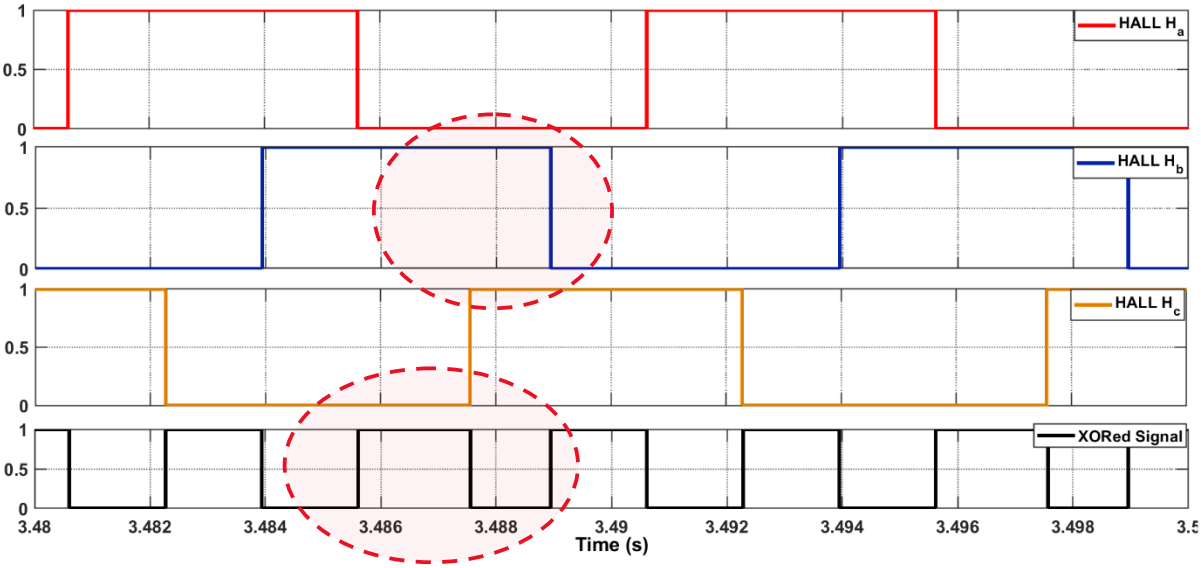

Fig. 3.11 HES signal pattern with early low to high transition of H_b and resultant deviation in two sector spans.

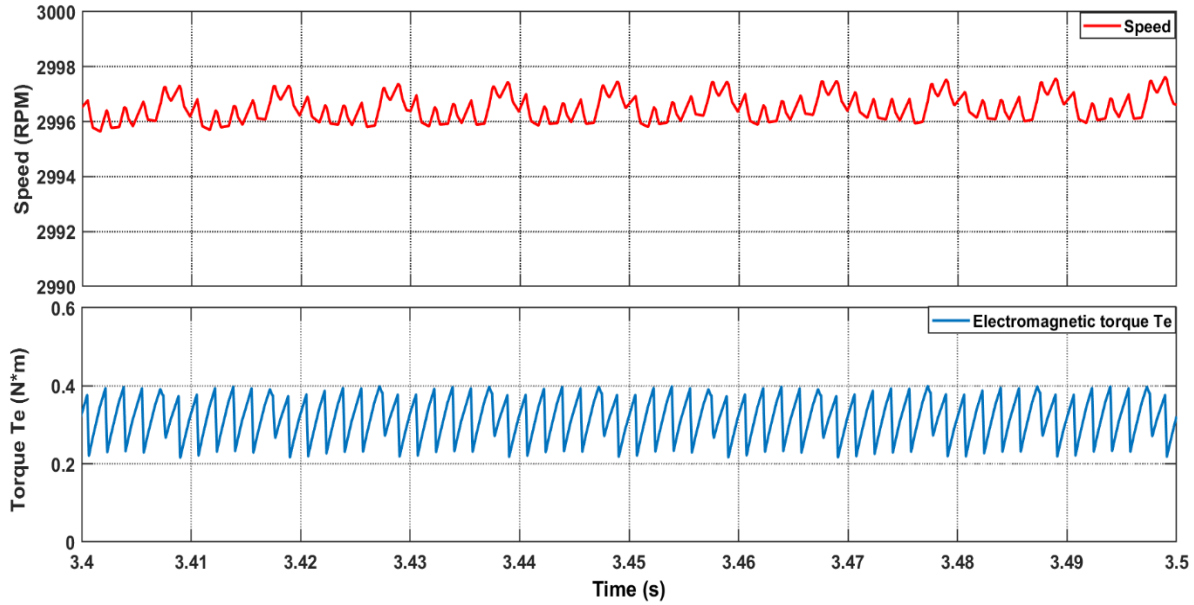

Fig 3.12 Speed and torque profiles with one misaligned HES signal.

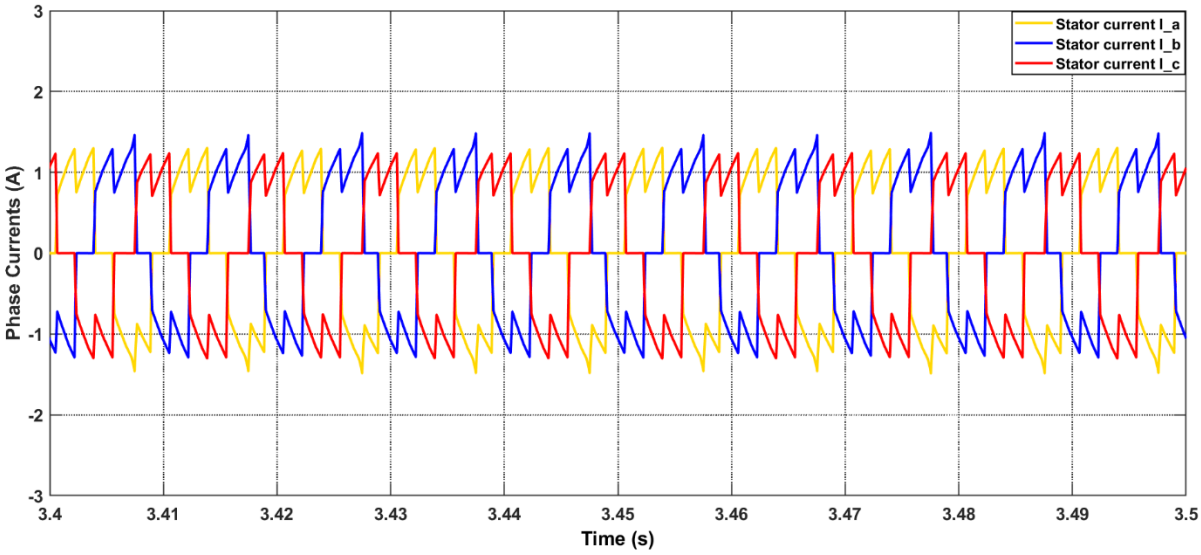

Fig. 3.13 Unbalanced three phase currents due to one misaligned HES signal.

Simulation with Two Misaligned HES Signals: Simulation of the drive with misalignments in two HES signals is carried out by introducing 10º and 4º deviations in the model. The calculations from the simulation and resultant observations are summarized in Table 3.4 for validating the implementation with deviations in two HES signals. The approximate deviation obtained from output signal timings are near to the exact values of 10º and 4º and observed in four affected sector durations. These four sectors are consecutive with alternate increment and decrement in the sector durations. The other two sectors with normal span are also consecutive in the sequence of six sectors of one electrical cycle.

Table 3.4 Verification table for unbalancing of two HES signals in simulation model.

S. No.	Sector Duration (ms)	Deviation From Ideal Sector Duration Δt (ms)	Deviation From Ideal Sector Duration (ºE)	Deviation Neglecting Calculation Error Δϕ (ºE)	Angular Deviation Δθ in mechanical degrees
1	0.842	0.000318059	0.005664	0	0
2	0.842	-0.000318059	-0.005664	0	0
3	0.786	-0.056318059	-1.002912	-1.002912	-4.011648
4	0.898	0.055681941	0.991584	0.991584	3.966336
5	0.701	-0.141318059	-2.516592	-2.516592	-10.066368
6	0.983	0.140681941	2.505264	2.505264	10.021056

Figure 3.14 shows the HES signals with two highlighted misaligned transitions having timing deviations. The sector span pattern obtained confirms the presence of four affected sectors that are also highlighted. Figure 3.15 shows the synchronized speed and torque profile

of the motor. The higher variation in both the profiles are clearly visible as compared to the normal speed and torque profile of the drive presented in Fig. 3.8.

The unbalancing in the three phase currents is presented in the Fig. 3.16. The I_b and I_a phase currents shown in the blue and yellow coloured profiles show marked deviations from the balanced current profiles. These observations confirm the implementation of the imbalanced commutation switching that is caused by the deviation introduced in two HES signals in the simulation model.

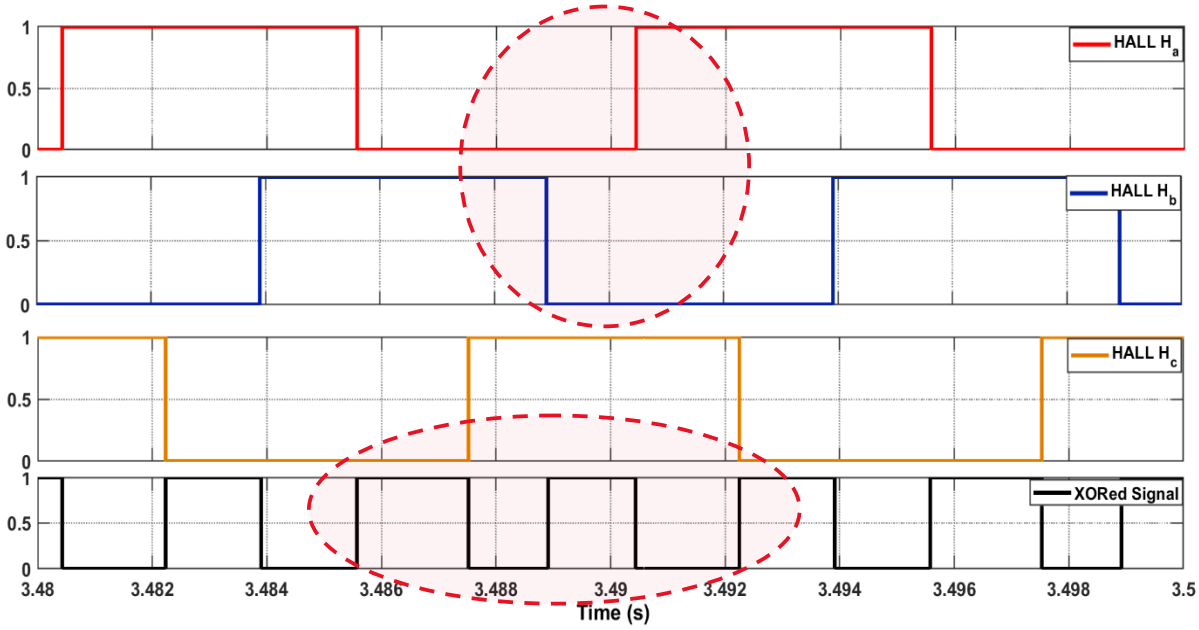

Fig. 3.14 HES signal pattern due to mistimed transitions of H_a and H_b with resultant deviations in sector spans.

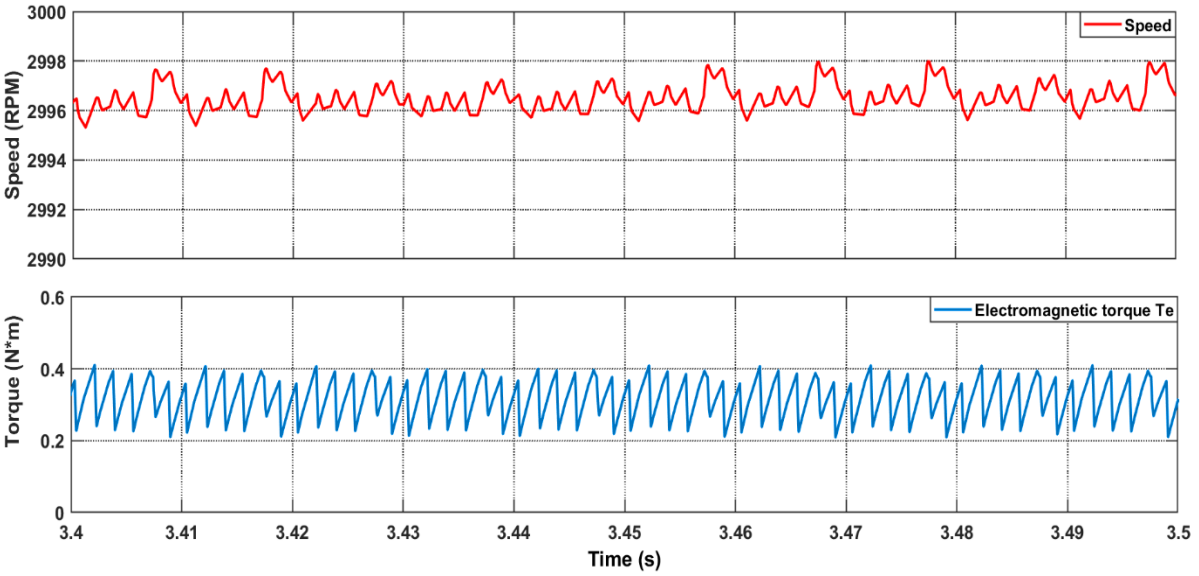

Fig. 3.15 Speed and torque profiles with two misaligned HES signals.

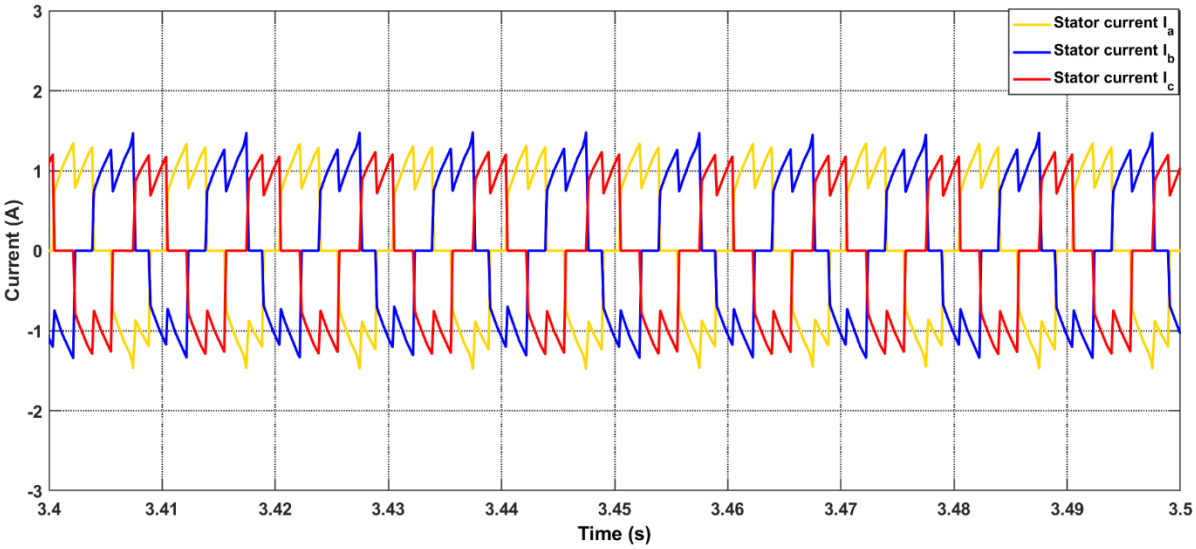

Fig. 3.16 Unbalanced three phase currents with two misaligned HES signals.

Simulation with Two Misaligned HES Signals: Simulation of the drive with misalignments in three HES signals is carried out by introducing 10º, 6º and 4º deviations in the model. The calculations from the simulation and resultant observations are summarized in Table 3.5 for validating the implementation. The approximate deviations obtained from output signal timings are near to the implemented values. All six sectors in one electrical cycle are observed to be affected in the durations. Figure 3.17 shows the HES signal timing deviations. The observed sector span pattern also confirms the presence of all six affected sectors. Fig. 3.18 shows the synchronized speed and torque profile of the motor. The higher variations in both the profiles as compared to Fig. 3.8 are clearly visible. The unbalancing in the three phase currents is shown in Fig. 3.19. The three phase currents show deviations from the balanced current profiles of Fig. 3.6. These observations confirm the imbalanced commutation switching caused by the deviation introduced in all HES signals in the simulation model.

Table 3.5 Verification table for unbalancing of three HES signals in simulation model.

S. No.	Sector Duration (ms)	Deviation From Ideal Sector Duration Δt (ms)	Deviation From Ideal Sector Duration (ºE)	Deviation Neglecting Calculation Error $\Delta\phi$ (ºE)	Angular Deviation $\Delta\theta$ in mechanical degrees
1	0.758	-0.085182244	-1.515370689	-1.515370689	-6.061482754
2	0.814	-0.029182244	-0.519144776	-0.519144776	-2.076579105
3	0.87	0.026817756	0.477081136	0.477081136	1.908324543
4	0.701	-0.142182244	-2.52938635	-2.52938635	-10.1175454
5	0.982	0.138817756	2.46953296	2.46953296	9.878131841
6	0.928	0.084817756	1.508886545	1.508886545	6.03554618

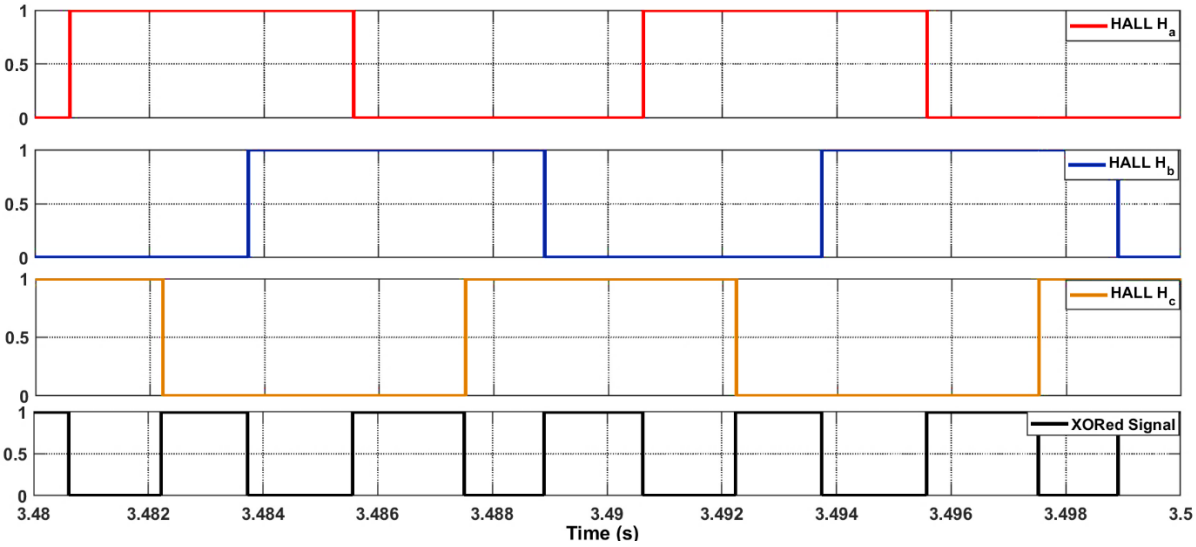

Fig. 3.17 Unequal sector spans with all three HES signals unbalanced.

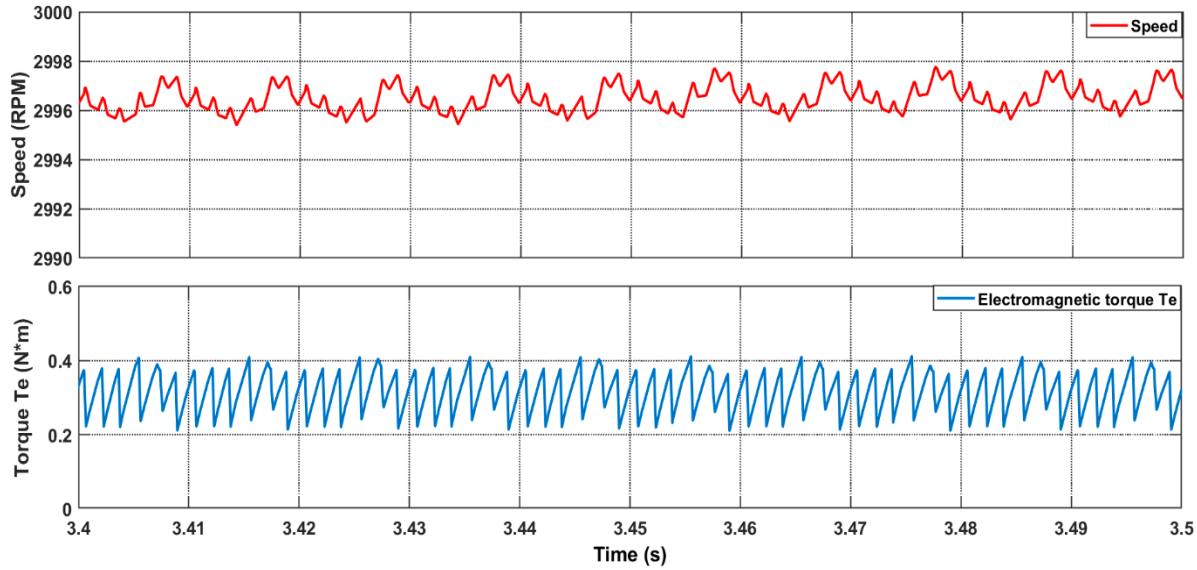

Fig. 3.18 Speed and torque profiles with three misaligned HES signals.

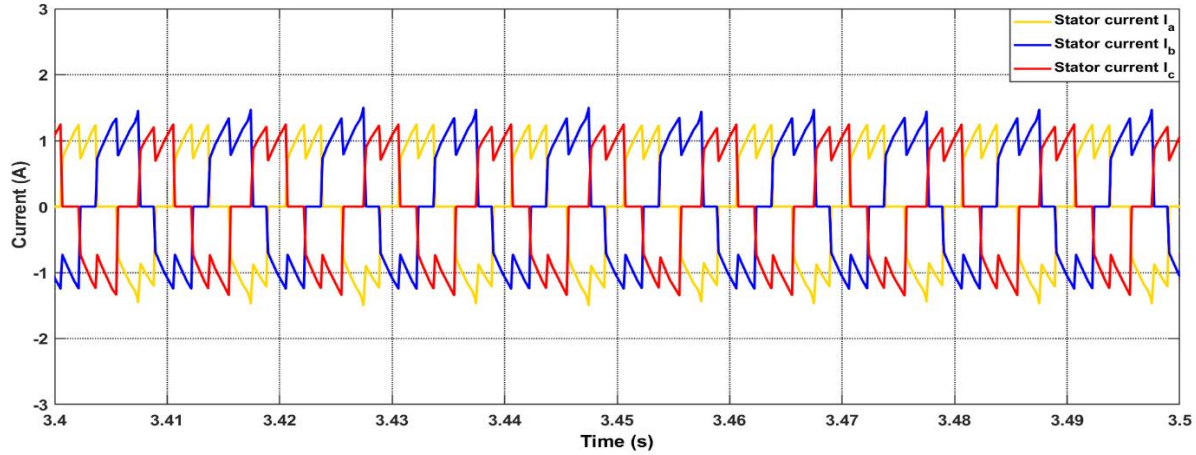

Fig. 3.19 Unbalanced three phase currents with three misaligned HES signals.

3.5 CONCLUDING REMARKS

This chapter presented a discussion on the operation of the BLDC motor drive along with the basic equations showing mathematical relation between motor parameters of phase currents, voltages and BEMF. To implement the trapezoidal commutation scheme with HESs, the BLDC motor drive simulation model is developed. In this model the provision for implementation of timing deviations in HES signals is incorporated. The simulation model is verified for normal operation and further implementation of HES signal deviations in one, two and three HESs is verified sequentially. The calculations from the simulation and resultant observations are summarized to validate these implementations in the model.

The performance of the drive with HES signal misalignment faults is verified using this Matlab simulation model with consistent observations in relation to the inter linked drive parameters, that confirm to the mathematical model presented in this chapter. The effects of HES misalignments on commutation circuit switching timings are directly observable. The profiles of rotor speed, electromagnetic torque, switching cycle duration and phase currents are also presented and increased perturbations are observed in the torque and speed of the motor with HES signal misalignment. The phase current profile is also found to be more distorted in the faulty case. Considering overall importance of HES position fault and signal misalignments in applications like e-rickshaw where cost effective solutions are needed without modification in drive system and circuits, the simulation model and study presented in this chapter confirm the effects of HES misalignment fault in drive operation. This forms the basis for further analysis and development of FTCs for fault effect mitigation.

CHAPTER 4

DESIGN AND DEVELOPMENT OF BLDC MOTOR CONTROLLER WITH EXPERIMENTAL TEST BENCH IMPLEMENTATION

4.1 INTRODUCTION

In EV drive systems, the controller design is one of the most important aspects. Its functionalities include overall application control and operation of BLDC motor. The controller provides dedicated signal processing and controls various operational units of the overall application. It monitors important drive parameters such as phase currents, phase voltages, rotor speed besides synchronizing various control events in the drive. The controller is responsible for implementing the trapezoidal commutation scheme by generating the inverter switching signals with precise timing intervals. It also controls the PWM duty cycle in the inverter [7], [96], [103], [133].

This chapter elaborates on the design of a BLDC motor controller for low to medium power EV applications like e-rickshaws. The controller design is based on the STM32F103C8T6 series microcontroller with specific features such as dedicated PWM channels, timers, and flexible input/output (I/O) ports for commercial motor control applications [134]. The controller is used for controlling BLDC motor operation, detection of throttle signal, HES signals, speed estimation, and to control the parameters in open loop and closed loop operation.

The proposed controller design integrates a scheme for detecting HES connections during starting of the drive to improve its operational reliability [117]. The method by default detects and assigns the correct HES sequence in the controller. Furthermore, modifications are incorporated in the heat sink design to address the issue of controller overheating in applications such as e-rickshaws. Hardware based over current protection method is also incorporated into the design [135], [154]. Additional functionality of automatic phase sequence detection of the BLDC motor is also incorporated in the design and tested in the hardware test bench.

The hardware test bench is developed for testing and experimental validation of the laboratory prototype using a 48 V,1 kW BLDC motor of an electric e-rickshaw application, powered by 48 V, 72 Ah battery pack. The software development is carried out using STM32CubeMX utility software with IAR IDE Embedded Workbench for ARM microcontrollers.

4.2 DESIGN DESCRIPTION OF THE CONTROLLER

The basic function of the controller is to control the operation of the 3-phase inverter circuit that is used to drive the three phase BLDC motor. It is the core fundamental operation around which the complete state machine logic, commutation logic, interrupt sequencing and other functions are implemented [118].

BLDC motor drive consists of a power supply section, an inverter circuit with solid state switches, inverter driver circuit and a microcontroller based control and communication system. Six step commutation method is used in voltage control mode to develop the control logic for the motor. The rotor position detection and feedback system are implemented using three HESs [5], [8]. The STM32 microcontroller generates PWM signals for high voltage side switching of the motor drive circuitry while the low voltage side switches are either in on state or off state without PWM. Switching frequency of 16 KHz is used in the design. Duty cycle is varied to control current, voltage, speed and acceleration parameters in both open loop and closed loop control [119].

The three HESs provide 120ºE apart binary output signals. The microcontroller decodes the HES signal pattern and accordingly determines the next switching sequence for commutation from the preassigned sequence list. Rotor position and speed estimation are based on the timings of these HES signals. To meet the power requirements of the EV controller, the metal oxide semiconductor field effect transistor (MOSFET) switches with the advantages of high operating frequency and small conduction losses are used in the design [5]. The illustrative block diagram of the controller system is shown in Fig. 4.1 and the specifications are summarized in the Table 4.1 [28], [118].

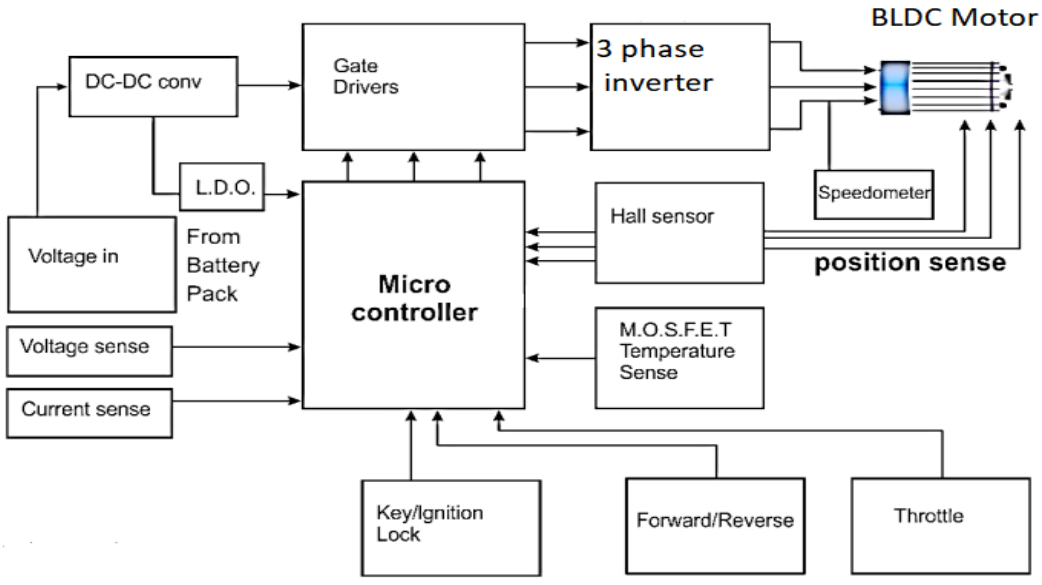

Fig. 4.1 Block diagram of the BLDC motor controller for EV application.

Table 4.1 Controller specifications.

Controller Type	Trapezoidal
Input Voltage Range	42 – 56 V DC
Nominal Voltage	48 V DC
Nominal Power	1 kW
Peak Power	2.8 kW
Nominal Continuous Current	20 A
Peak Current	60 A
Rotor position detection method	3 HESs
Hall Sensor Signals	120ºE apart

The dedicated timers in the microcontroller are used for generating the reference timing signals in the controller. These reference time signals are required for event synchronisation and speed calculations. The controller design includes analog processing circuits for current, voltage and throttle signal sampling. The accelerator throttle acts like a potentiometer arrangement to supply voltage signal that is proportional to the applied rotation of the throttle handle. It uses an analog HES based approach for detection of the speed command.

The controller operation requires handling of changing speed and load with constant adjustments in the switching of inverter circuitry. This results in generation of heat in the controller circuit itself. Thus, the heating and temperature management are also an integral part of the controller design. These factors must be kept in predefined limits for an EV drive to operate at desired optimum performance level. A heat sink is connected with the inverter switches for discharging the heat. It is further connected with the outer casing of the controller with fins for proper heat dissipation through automatic air contact. The heat sink design and its placement are an essential part of the controller design [1], [135].

The overall hardware design of the controller essentially includes a microcontroller with attached external circuitry for reading and processing the drive parameters including supply voltage, dc link current, throttle values, HES signals and temperature. The analog signals are filtered and scaled to the 3.3 V low voltage level for interfacing with the microcontroller circuit. Based on the information extracted from these signals, the microcontroller implements the motor control logic. The PWM output signals are used to control the voltage applied at each motor phase. The section wise description of the controller design is further elaborated in the next subsections.

4.2.1 POWER SUPPLY CIRCUIT AND PROTECTION

The controller system is fed from a 48 V, 72 Ah battery system that is used in several EV applications with inbuilt BMS [136]. Capacitor filters are used at input terminals. Battery input voltage is further scaled down to the 12 V, 5 V and 3.3 V regulated supplies. Each supply is filtered individually at output terminals. Reverse protection is provided by a full bridge circuit. A TVS diode provides the required surge protection. The electronic subsystem of an EV deploys reverse battery protection. This is required by international standards for maintaining supply quality of EVs and by original equipment manufacturer also [2]-[3], [146]. Fig. 4.2 shows the power supply circuit with protection and LC filtering circuit.

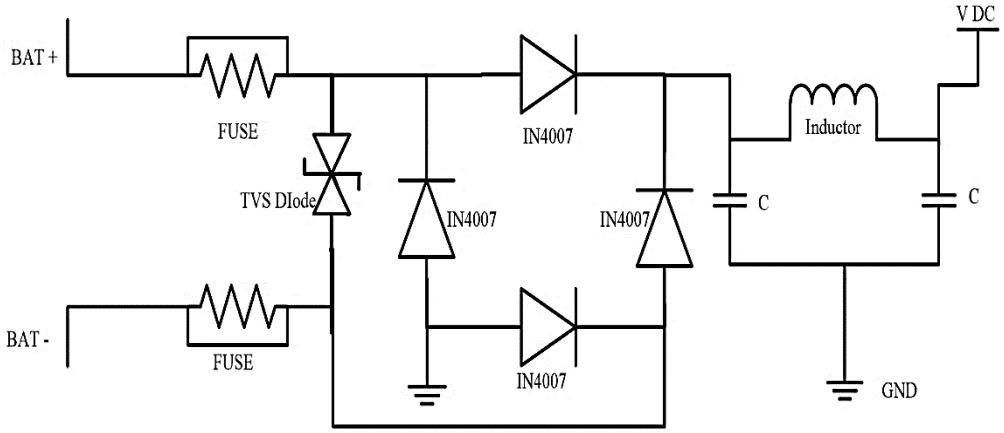

Fig. 4.2 Input power supply circuit with protection and filtering.

Transients are also an important factor which must be considered in the controller design. During transients some systems can be put in the disabled condition in EVs but, applications running for essential activities are required to be operational in this case also. Hence TVS diode is used to avoid the shutdown and instead, it shunts the transients using 12 V overvoltage shutdown scheme in the design. This ensures the clamping of the transients only beyond harmful voltage levels but not at the normal system input voltage level. Clamping levels of positive going transients is above the battery jump start level and up to the maximum limit of the devices connected downstream. Reverse clamping clamps voltages beyond battery supply to protect device shorting during reverse battery connections [119], [137].

The motor phases are fed through a 3- phase inverter at battery supply voltage levels. The driver circuit for the inverter operates at 12 V level. Figure 4.3 shows the DC-DC converter circuit using MP9486A regulator integrated circuit (IC) for obtaining 12 V supply. It is a step down switching regulator used in the high voltage circuitry. Continuous current up to 1A can

be delivered using this IC. Further, 12 V is stepped down to 5 V and is used for throttle and HES supplies. It is further downed to 3.3 V and used for the microcontroller circuit.

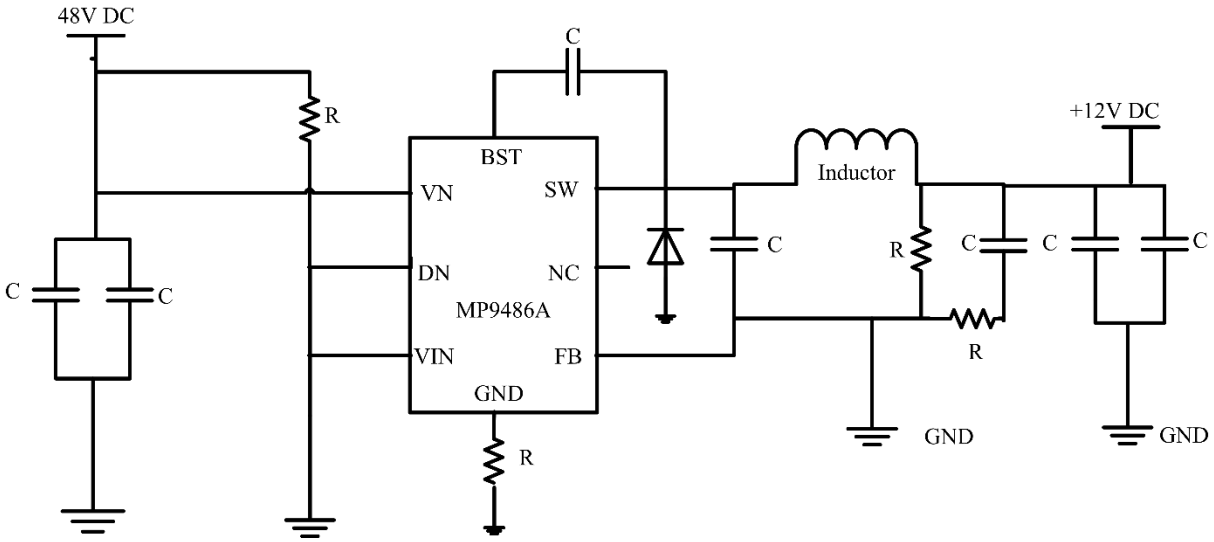

Fig. 4.3 DC-DC converter circuit for 12 V supply.

Table 4.2 summarizes the consistency check in the performance of power section over 20 V to 60 V input range. The output of all three sections of 12 V, 5 V and 3.3 V are consistently same over this range. This validation is essential for the voltage sensitive microcontroller and other low voltage parts to function accurately in the full operational range [138].

Table 4.2 Power supply output voltage level up to undervoltage and overvoltage limits.

Power Supply	**Section wise output voltage**		
Input Voltage	**12 volt**	**5 volt**	**3.3 volt**
20 volt	11.86	5.00	3.30
30 volt	11.86	5.00	3.30
40 volt	11.86	5.00	3.30
50 volt	11.86	5.00	3.30
60 volt	11.86	5.00	3.30

4.2.2 INVERTER AND DRIVER CIRCUIT

The STM32 microcontroller provides six switching signals through the dedicated port pins that are internally linked to a timer. These 3.3 V switching signals are used by BD2320, an IC based driver powered by 12 V to provide switching signals to the inverter MOSFET switches. This circuit implements the 3-phase inverter scheme by utilizing the six switch

circuitry configuration. A total number of twenty four N channel Power MOSFETs K100E10N1 with 100 A and 100 V capacity are used in the design [139]. Four MOSFETs are connected in parallel to form a single switch. This is done to achieve a higher current carrying capacity in the combined switch formed by these MOSFETs.

The driver circuit for this switching arrangement in one phase is shown in Fig. 4.4. It is identical for other phases. Each MOSFET of the four parallel MOSFET combination is connected to the driver IC through a resistance R1. Further R1 is connected in parallel with a Schottky diode and 22 ohm resistance to create a fast discharging path during switching cycles. Bootstrap capacitor of 0.2 uF, 100 V is used with each driver IC and, for fast discharging schottky diode BAT46, 100 V is used. Bootstrapping is done for each phase switching circuit at the start of the motor run operation [140].

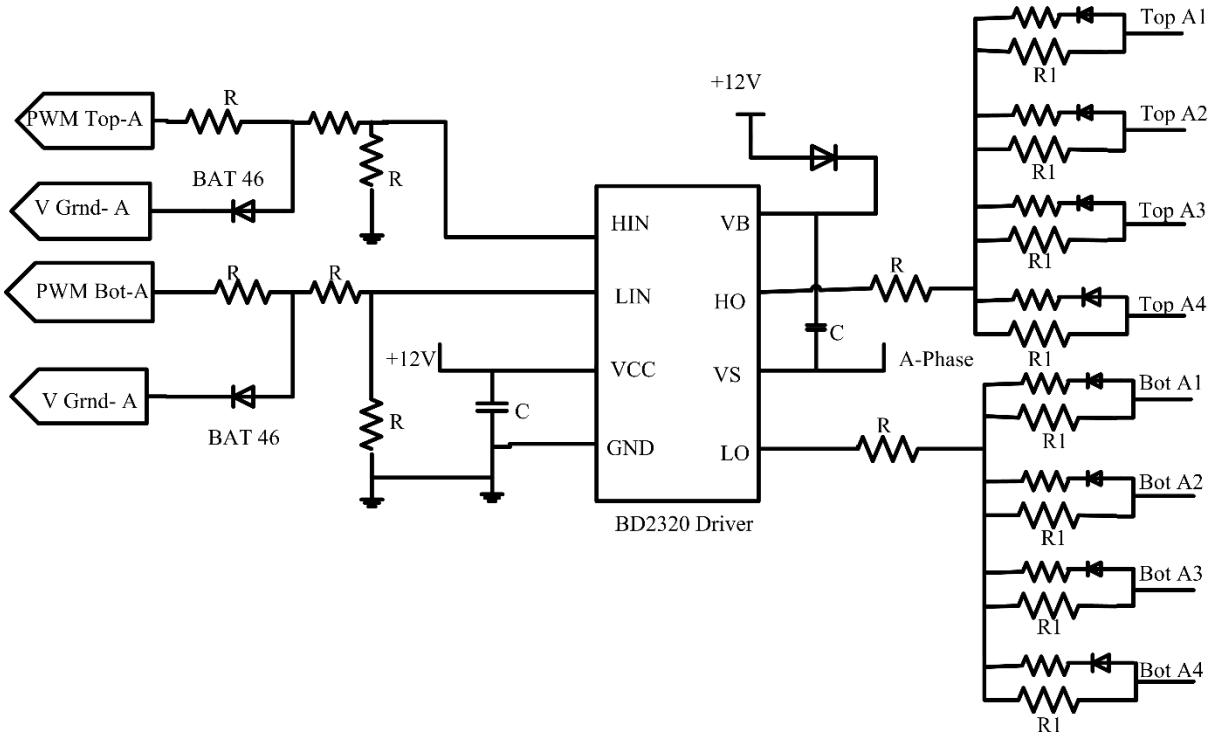

Fig. 4.4 Inverter switch driver circuit for one phase.

4.2.3 OVER CURRENT PROTECTION SCHEME

A comparator circuit is used in the design to compare current values with preset limits to directly provide hardware stop signal without any delay to prevent short circuit operation. Additionally, BMS also detects short circuit and abnormal high current values to shut the supply for drive protection.

The current supplied by the battery source is continuously sampled by the microcontroller for drive control. The interfacing circuit shown in Fig. 4.5 is used to transform the current

signal to the required voltage signal. It is further filtered, amplified and offset balanced for analogue to digital converter (ADC) input. It is used by microcontroller in control algorithm implementation. The ADC is operated in direct memory access (DMA) mode with buffering. This mode allows independent and parallel operation of ADC as a peripheral along with the core program execution.

The process of current sampling, filtering, conversion of readings in software and subsequent comparison with upper and lower limits can effectively cause latency in the detection of current values crossing the threshold limits. The final intended corrective action execution in the controller hardware is further delayed due to switching actions also. This can have severe damaging effect on the controller circuitry and motor in case of over current reaching peak limit values. To avoid this situation, a hardware oriented approach to implement auto cut off in over current case is used. This corrective action is independent of the software implementation and without any risk of possible latency in software.

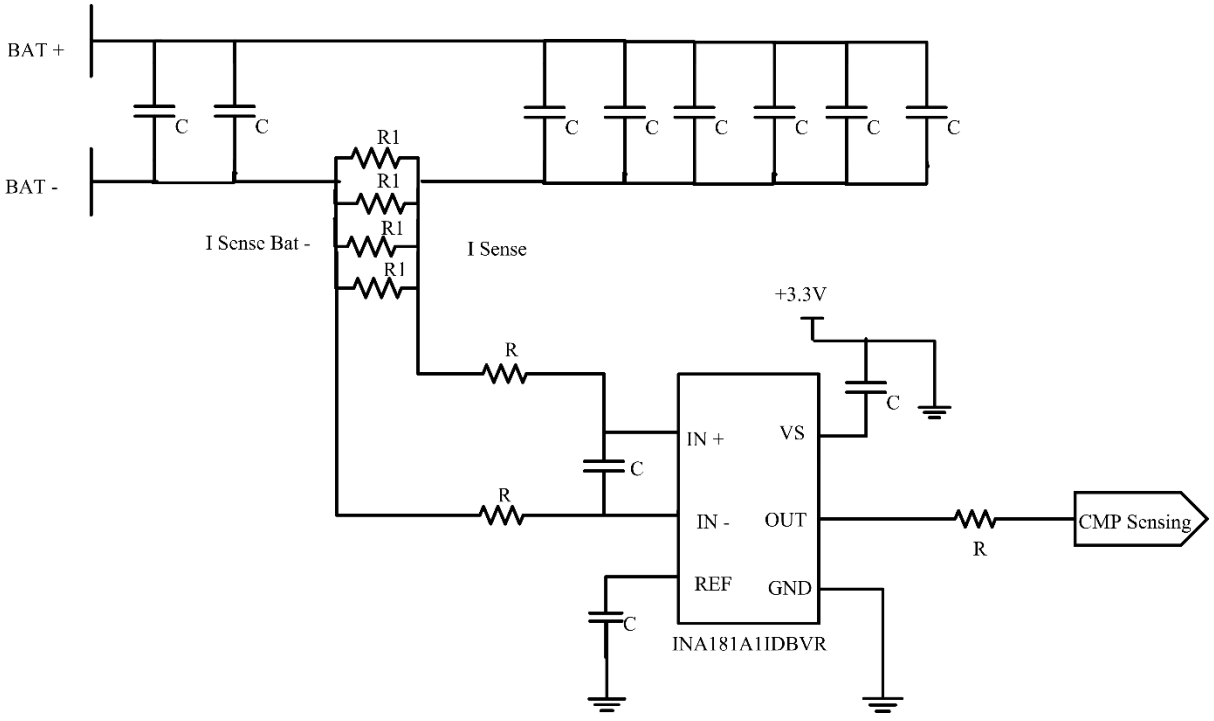

Fig. 4.5 Current sensing through shunt resistance.

The current sensing circuit is shown in Fig. 4.5. The proposed scheme is implemented using INA181A1IDBVR amplifier [141]. It is a cost-optimized, bidirectional, current-sense amplifiers which senses voltage drops across current sensing resistors. It allows common-mode voltages to range from –0.2 V to +26 V. The INA181A integrates a matched resistor gain network with four fixed-gain options: 20 V/V, 50 V/V, 100 V/V, or 200 V/V. This

matched gain resistor network minimizes gain error and reduces the temperature drift.

The next circuit shown in Fig. 4.6 is used to compare the sensed current to the preset values. This is accomplished by using LM393D comparator circuit [142]. It is powered by a single supply of 2.7 V to 5.5 V and can draw up to 260 μA current. The device operates in a temperature range of –40°C to +125°C. It is available in standard SOT-23, 8-pin package. The voltage level corresponding to the prefixed current value is set at the -ve input channel through a resistance. This value is set by resistances at the IN+ and IN- input terminals as shown in the circuit. The current sensed is applied to the +ve input channel of comparator. When the value of the current crosses the peak set limit, the comparator output signal is generated which triggers the switch, MOSFET Q1 in the circuit. The active low signal EN is generated which triggers the switch Q2 shown in circuit. This provides a low resistance path to the microcontroller drive signals and effectively breaks the signal connection between microcontroller and MOSFET switch driver IC. Thus, the driving circuit of MOSFET switches stops working. Consequently, motor driving is stopped immediately. This method provides automatic protection to the motor drive section in the situation of overcurrent.

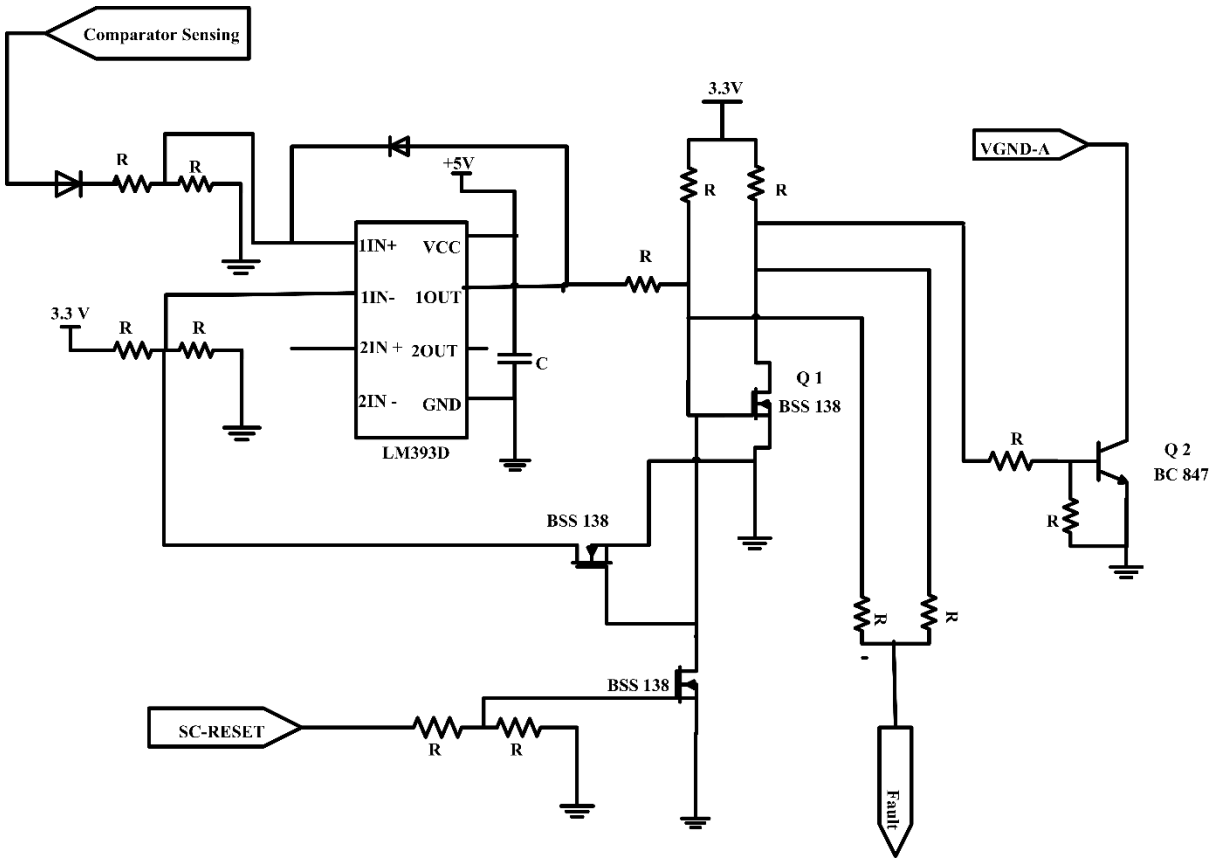

Fig. 4.6 Current comparison circuit for over current protection.

4.2.4 HEAT SENSING WITH NTC THERMISTOR

The negative temperature coefficient (NTC) thermistor is used for temperature sensing of the controller. The main advantage of NTC is it's coefficient of temperature sensitivity which is normally five times more than that of silicon based temperature sensors and, around ten times more than resistance temperature detectors (RTDs). However, there is inherent non-linearity between temperature and resistance values obtained by NTC resistors. Precise values are obtained by adjusting approximated values with errors in the software. Figure 4.7 shows the temperature sensing circuit using NTC S3K103 [143]. Table 4.3 shows the temperature values obtained using the circuit against the measured values.

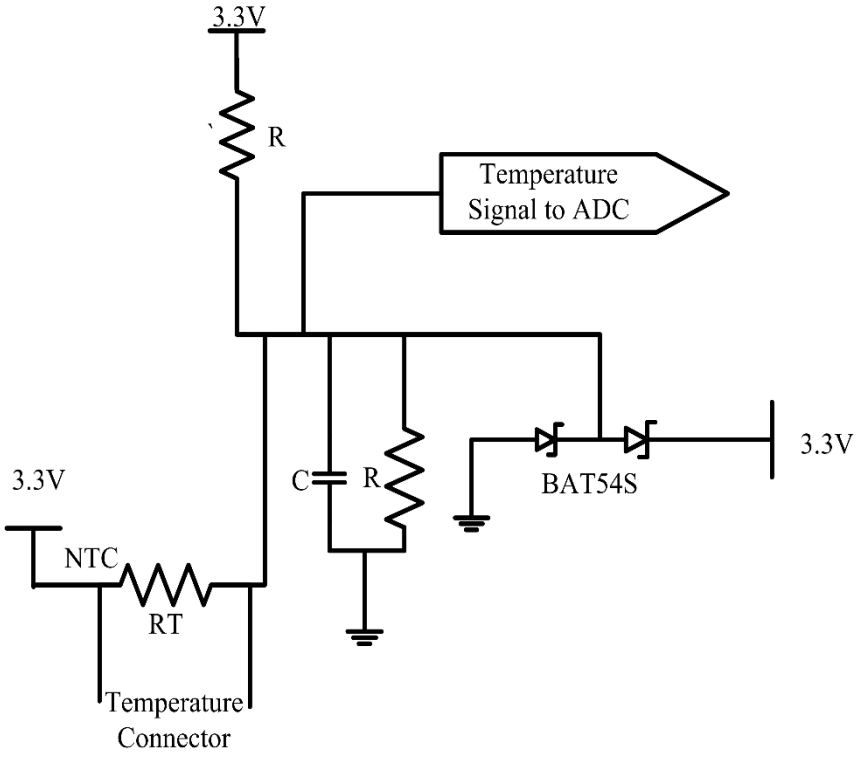

Fig. 4.7 Temperature sensing circuit using NTC S3K103.

Table 4.3 Experimental versus measured temperature values.

Measured Temperature (°C)	ADC Count	Temperature Estimated (°C)	Difference (Actual-Estimated) (°C)
21.9	1799	19.63	2.27
36	2438	33.9	2.1
43.1	2705	40.69	2.41
50	2920	46.88	3.12
53.6	3052	51.15	2.45
63	3257	58.84	4.16

NTC S3K103 can be used in the temperature range of −55°C to 200°C. The final readings are obtained by software calculation on the ADC count obtained. The estimated error can be fixed by a calibration table. The final readings are used with offset adjustment. This whole arrangement is cheaper in cost and very easy to implement, making it suitable for low cost EV controller designs.

4.2.5 HES SIGNAL PROCESSING

HES signals from motor are connected to the microcontroller input pins through a 3.3 V pull up arrangement. Capacitors are used at each input signal to filter out any spike. Figure 4.8 shows the HES signal processing circuit. HES damage or failure is often reported in EV applications. These sensors can become nonfunctional due to damage or disconnection. In such cases the value read from the faulty sensor remains fixed for rest of the operation.

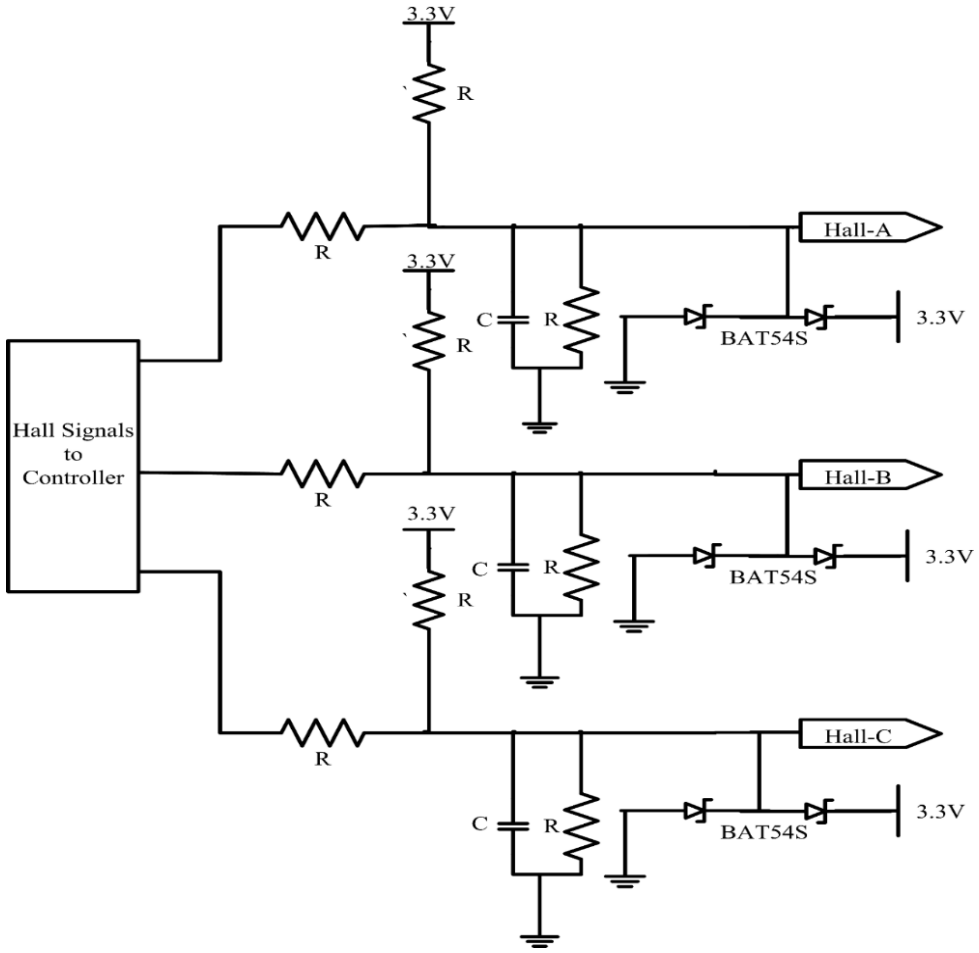

Fig. 4.8 HES signal processing circuit.

Application of HESs in the design is based on the interrupt generation mechanism in microcontroller. HES failure detection and corresponding interruption of the main application

are handled in software. Figure 4.9 shows the flow chart of the correct HES sequence verification process in the controller.

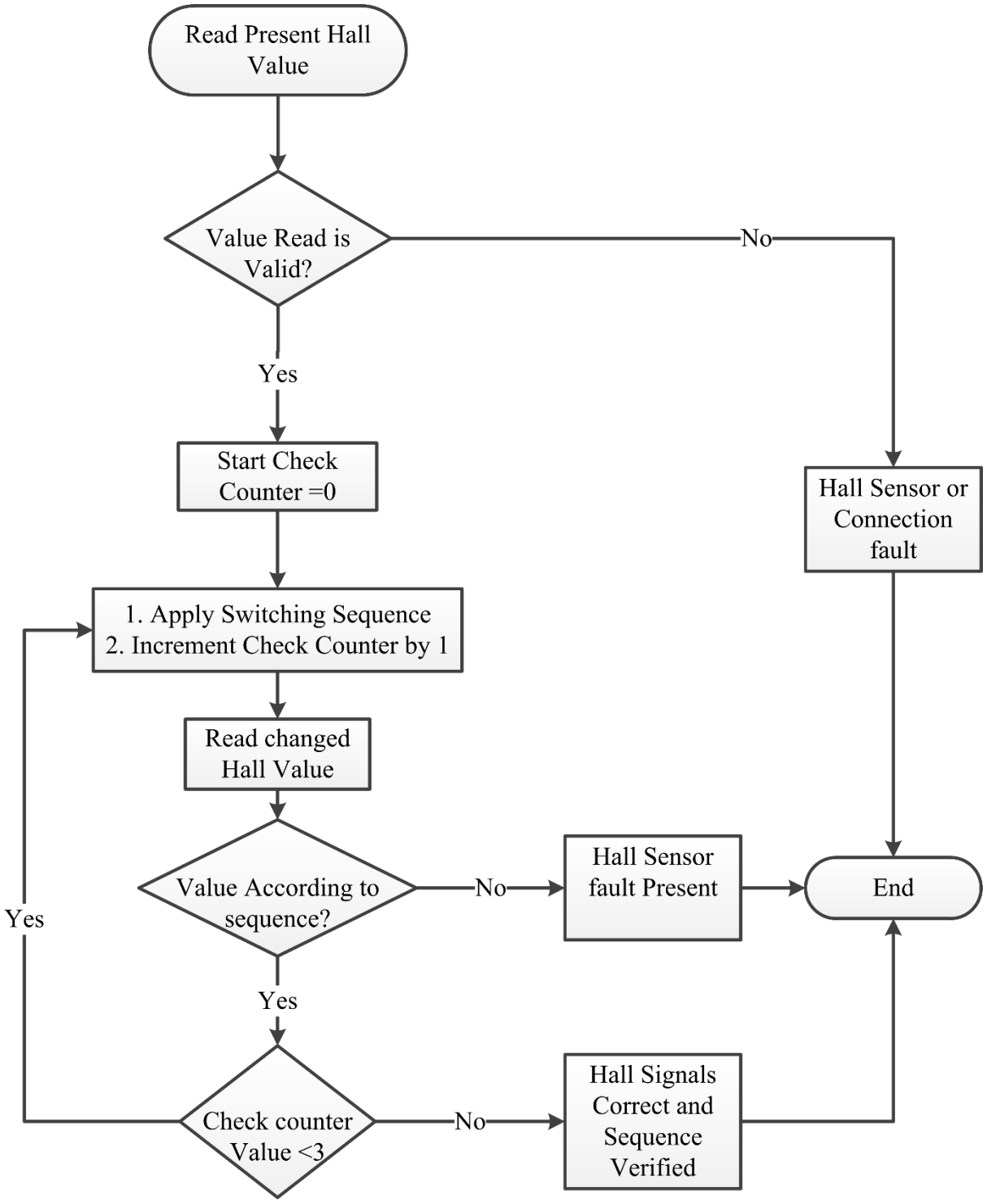

Fig. 4.9 Flow chart for correct HES sequence verification process in the controller.

During malfunction of HES signals, corrective action takes place within sub millisecond duration. During the initial start of motor operation, three consecutive switching signals are

applied in either forward or reverse direction because in normal operating condition, three consecutive HES signals must contain exactly one transition from each HES. Failure of transition on any of the HES indicates fault. The three hall values obtained are checked against the predefined sequence. If the values are correct according to the sequence, the motor hall connections and sequence are verified.

4.2.6 CONTROLLER CIRCUIT LAYOUT AND FABRICATION

The controller circuit is fabricated on double sided printed circuit board (PCB). Base copper thickness of 70µ and finish copper thickness of 90µ, laminate TG 130 of surface finish with Sn-Pb of hot air levelling (HAL) is used. The controller sections are strategically placed in the design for separation of high and low voltage sections. The fabricated prototype circuit is shown in the Fig. 4.10.

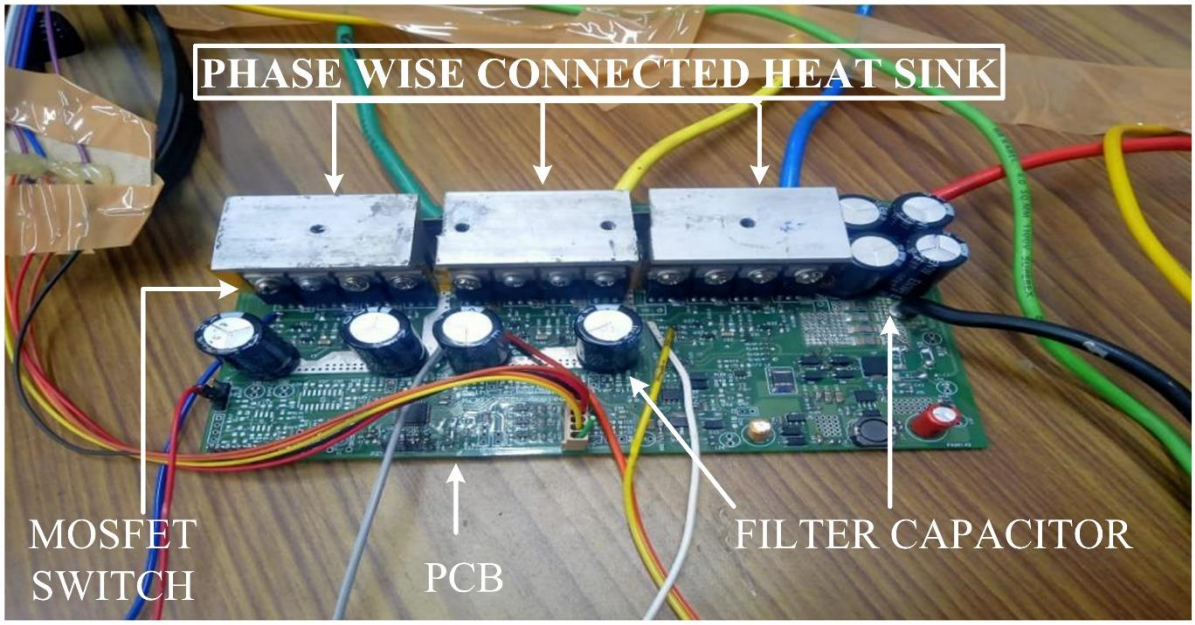

Fig. 4.10 Fabricated controller prototype circuit.

4.2.7 CUSTOMIZED HEAT SINK DESIGN

Overheating of the controller and MOSFET switch burning are reported in many cases in EV applications. The heat sink arrangement becomes more crucial aspect for the overall life span of the controller. Application specific heat sink arrangement is proposed and implemented in the design. Phase wise attachment of the heat sink with MOSFET switches is shown in Fig. 4.10. Considering the size and cost constraints in the design of the controller, the following changes are proposed in the existing heat sink design:

- The single piece heat sink is divided into three parts. Each part pertaining to one single phase of the BLDC motor.

- The per phase 8 number of MOSFETs are connected to one single heat sink piece rather than all 24 MOSFETs connected to a single long heat sink as in conventional design. This arrangement permits phase wise separation of heating. By detecting excessive heating in one heat sink piece, the phase with possible fault conditions can be isolated and treated accordingly.
- Cutting of heat sink into three pieces provides provision of more space for heat dissipation as it permits a gap of around 2 mm between the heat sink pieces.
- Phase wise separation of the heat sink reduces the effect of vibrations on MOSFET switches. A as a single long path for wave travelling is not available for vibration to travel due to cutting of heat sink into 3 parts.
- The effective area of heat sink for heat dissipation gets increased in the present design.
- The mounting of MOSFETs is more robust in the present design.

4.3 MOTOR CONTROLLER INTEGRATION

The motherboard level testing of the controller hardware and software drivers during the motor controller integration is necessary before final test bench setup. The integration is tested for commutation sequence and driver validation. This hardware set up for controller motor integration and validation is shown in Fig. 4.11.

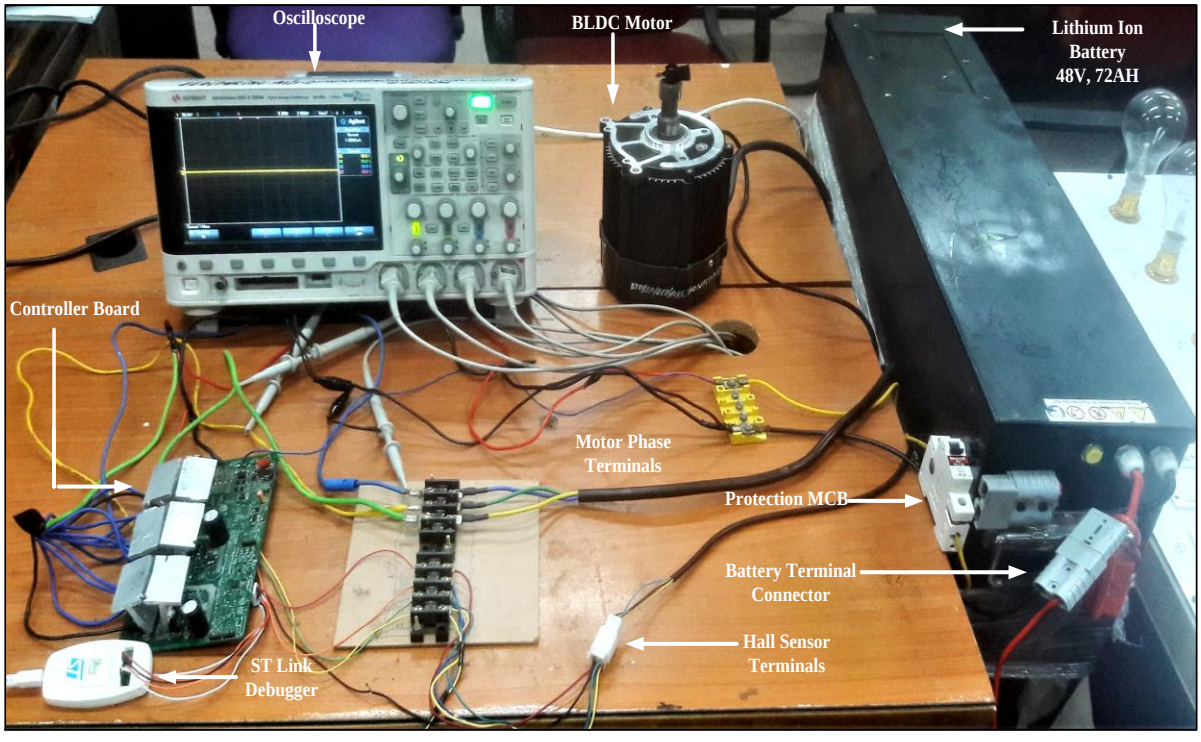

Fig. 4.11 Motor controller integration testing setup.

The section wise test results of power supply and ADC sections are already presented in the previous section. The controller is further tested with an 8 pole BLDC motor rated at 48 V and 1 kW power. It is powered by 48V, 72Ah lithium ion battery pack for testing purposes. The controller board is tested initially in open loop to validate the hardware and motor driver software functioning.

Figure 4.12 shows the phase voltage waveforms at a test speed of 815 revolution per minute (RPM). The voltage is measured against battery supply negative terminal voltage as reference. This represents the applied voltage at motor phase terminals with BEMF. The three phase voltage waveforms confirm to 120º trapezoidal commutation method.

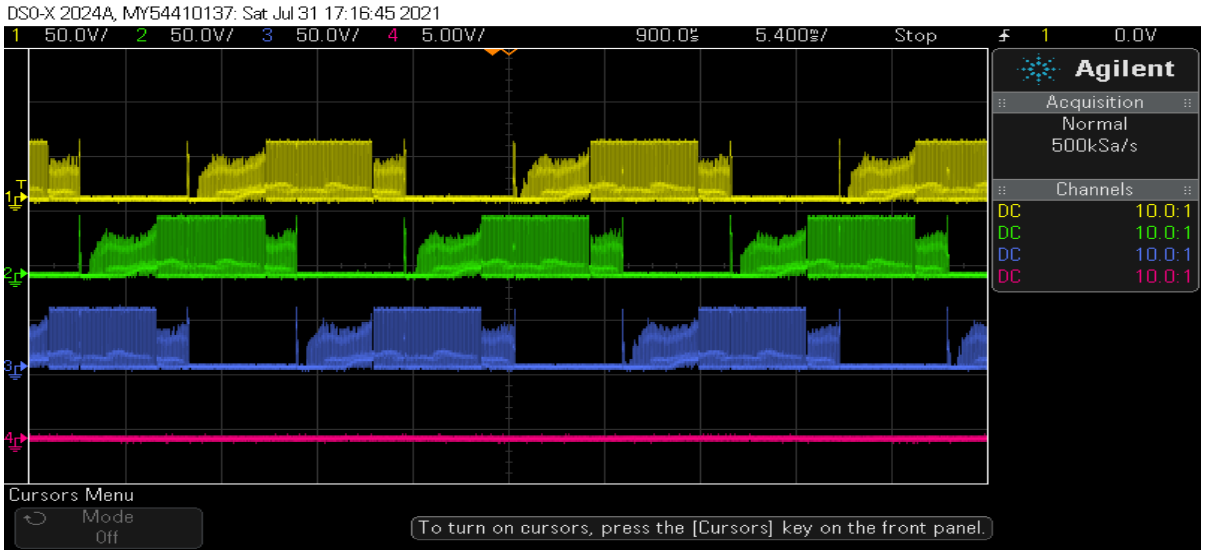

Fig. 4.12 Phase terminal voltages measured against battery supply reference.

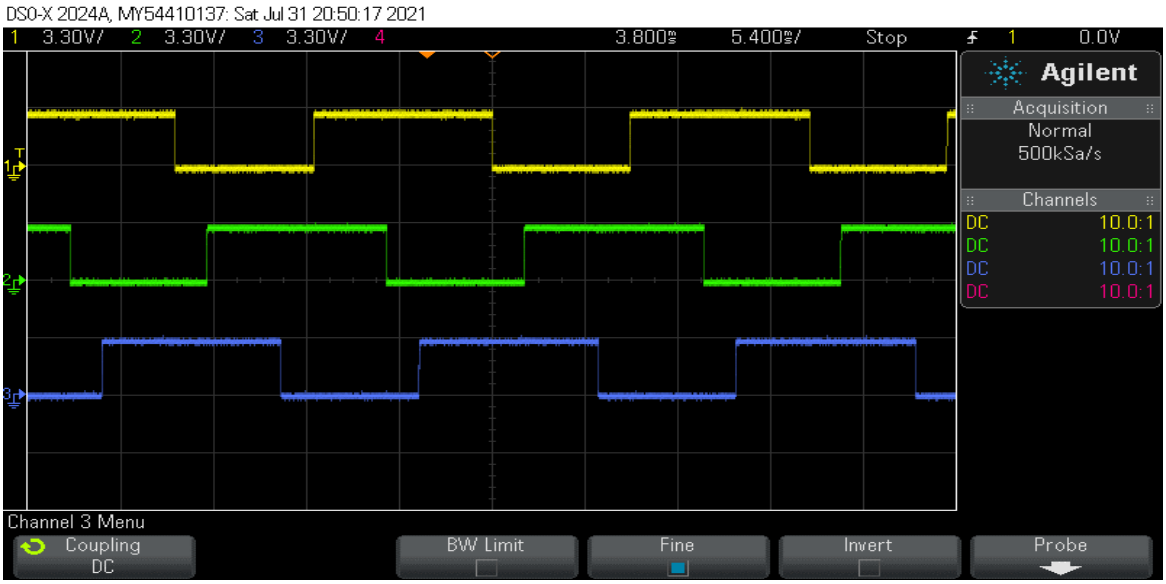

Fig. 4.13 HES output signal check.

The output signals observed at the HES terminals of the motor are shown in Fig. 4.13. Six transitions representing six segments each of 60º electrical rotation are visible in any one period of each HES. The voltage level of each signal is stable at 3.3V as per the intended level in the design. Additional features of automatic phase sequence detection and HES signal integrity check are also verified during motor controller integration process. These are further described in the following sub sections.

4.3.1 MITIGATION OF HALL SENSOR GLITCH EFFECTS

The functioning and signal integrity of HESs is affected by the error in their placement besides ageing and mechanical fatigue. One of the major effects of these errors is the presence of small duration pulses or glitches at either rising or falling end of the HES signal transitions. Thus, one of the issues that controller design is required to handle is of glitches or unwanted pulses along with the normal HES signals. Since the complete controller software design and operation of the drive is dependent on the HES output signals, any unwanted or noise signal leads to a logic level detection in the controller, that is not according to the rotation sequence. This can lead to incorrect switching pattern application to the inverter if the anomaly is not corrected by the appropriate methods [9], [144].

Normal HES output signals are shown in Fig. 4.13 and signals with glitch effect are presented in Fig. 4.14 for comparison. When the HES signals and corresponding signal pattern is not accurate, switching signals for inverter section are also not exact according to the switching sequence presented in Table 3.1. This can cause serious errors in motor control operation [120].

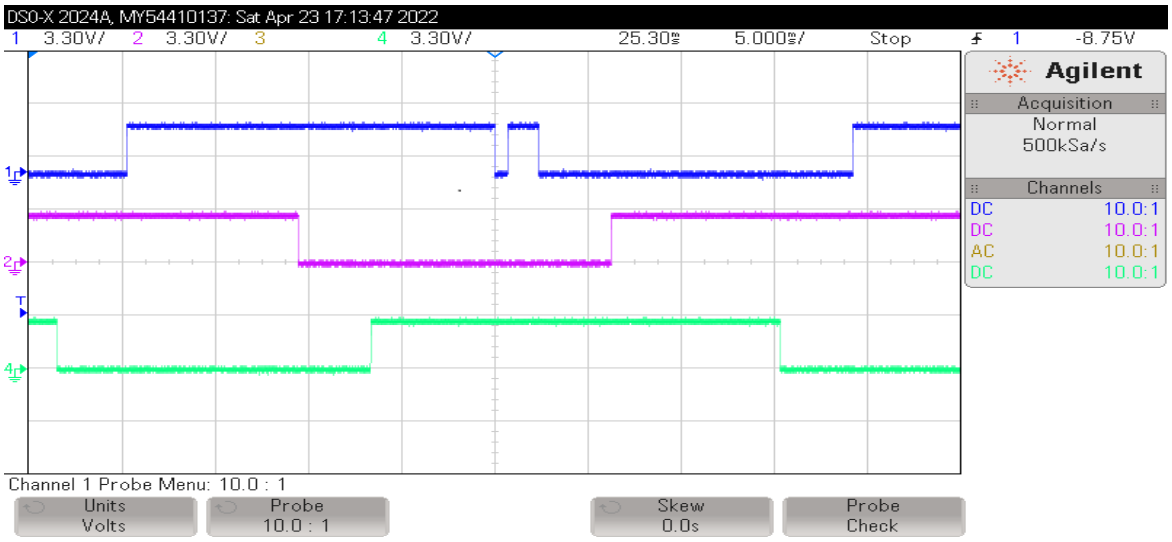

Fig. 4.14 HES output signals with glitch in one HES signal.

The glitch effect results in increase in torque ripples, noise and current ripples during motor operation. Further, the drive controller design also becomes more complex when the existing design is changed to address these issues. Occurrence of such type of issues is mainly reported in BLDC motors with higher number of poles, smaller in size and repaired motor controller sets [44], [45].

The glitch effect on phase voltage profiles is shown in Figures 4.15 to 4.16. The three HES output signals and corresponding voltage profile of one motor phase, when HES signal transitions are normal without any glitch are shown in Fig. 4.15. The three HES signals with glitch and corresponding voltage profile of one motor phase are shown in Fig 4.16.

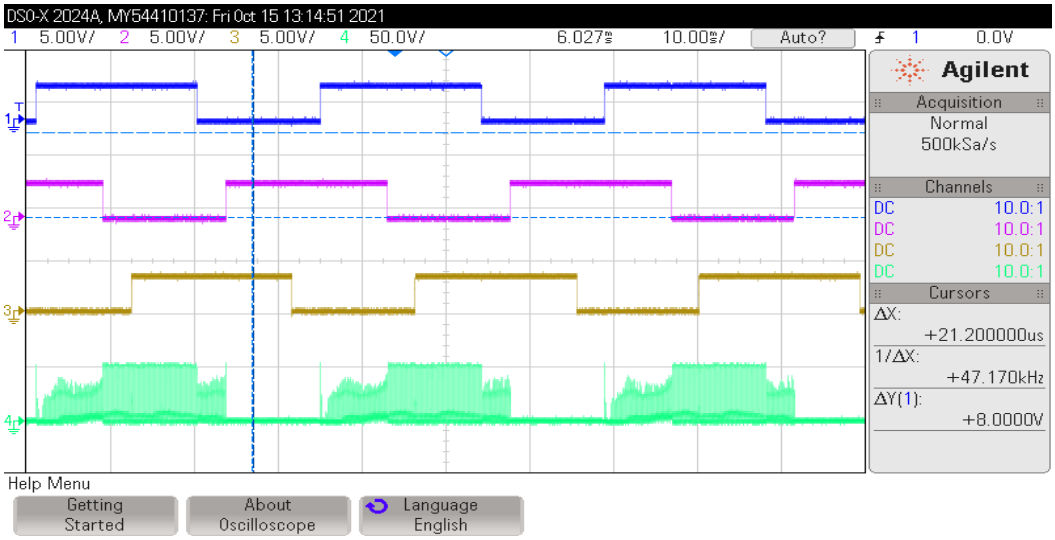

Fig. 4.15 Normal HES transition signals with one motor phase voltage waveform.

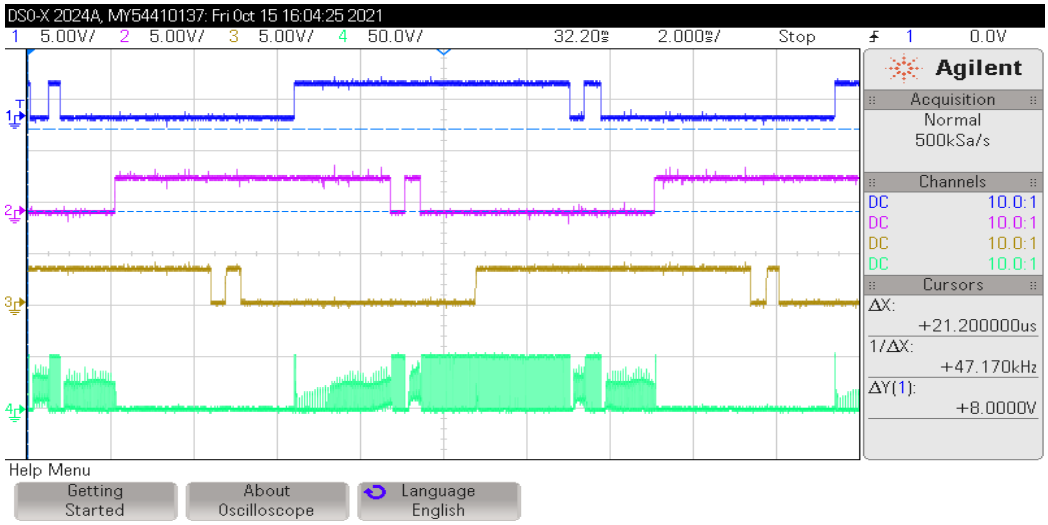

Fig. 4.16 HES transition signals and phase voltage waveform with glitch effect.

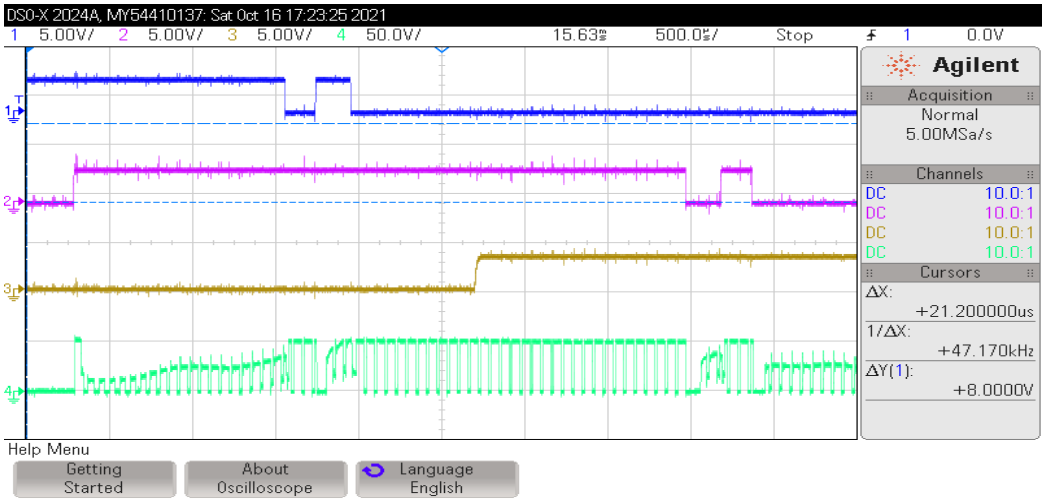

Fig. 4.17 HES transition signals with glitch and phase voltage waveform showing floating phase effect due to wrong switching pattern.

The enlarged motor phase voltage profile in Fig. 4.17 shows the floating phase condition when the first HES signal, depicted in yellow coloured waveform and second hall signal, depicted in green coloured waveform have glitch effects in their waveforms. This is because glitch causes the detection of new HES signal pattern which is not according to the required sequence. When the HES signals have glitches as shown, the HES signal pattern read by controller will be different than the normal pattern.

In Fig. 4.15 the normal HES signal binary sequence after 101 is 001. In the Fig. 4.16, the HES signal pattern change is from 101 to 001 as expected, but due to the glitch effect, next pattern read is again 101. This leads to various possible actions that can be implemented in the controller. If switching sequence is executed according to the HES values read without any check, it will not be according to the intended sequence. Alternately, if switching off operation of one inverter switch is carried out but, switching on of the next phase is avoided because of automatic check in the software to avoid short circuit of the inverter switches, the motor phase will become floating till new correct switching pattern is executed [12]. The floating phase or unwanted switching transitions cause more current ripples, higher current flow and overheating of controller as well as of motor winding. Even if a time delay check is implemented for detection of the glitch, it will have to be executed with a software delay which can be interrupted by other functional interrupts in the controller design. Hence it is also not feasible in commercial applications designs of EV controllers.

In this research work. the glitch effect is mitigated by the method of comparing the present HES signal pattern with the previous one and going for corrective check only in the condition of this pattern not matching with the expected value. During rest of the operation

time, no controller time is spent on corrective check because HES signal paatern is on the expected line. During corrective check, no switching operation is performed even for one leg of inverter phase. Thus, previous state is maintained and last switching pattern, which is correct, is extended during the glitch duration also. Thus, floating phase condition is avoided as shown in Figures 4.18 and 4.19. The corrected voltage profile of one motor phase is shown against the HES signal with glitch effect in these figures.

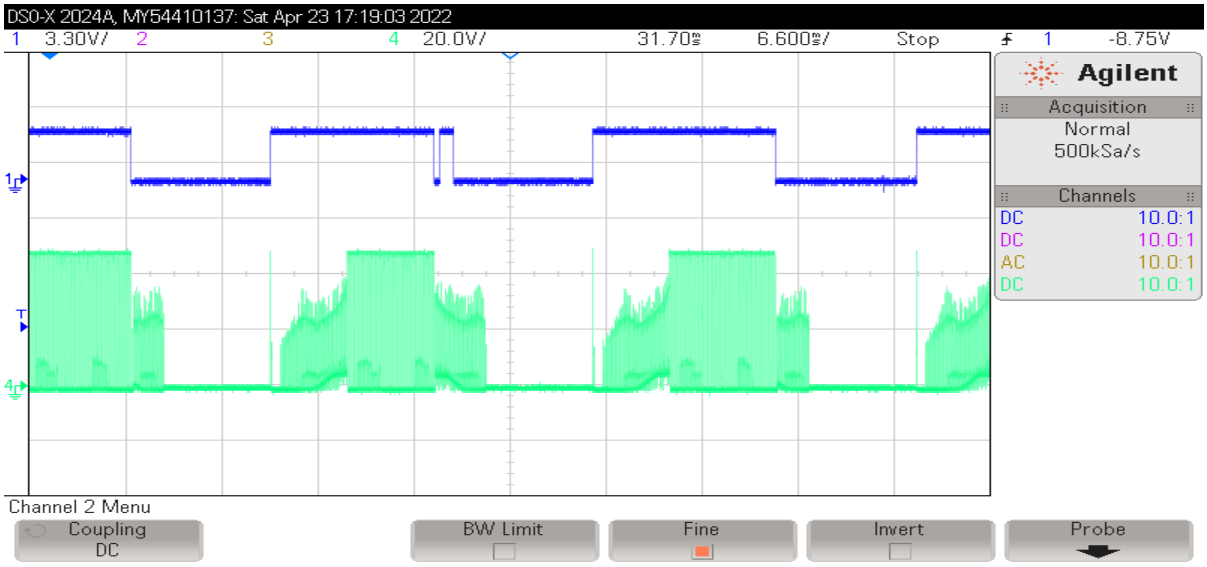

Fig. 4.18 Motor phase voltage waveform when HES glitch effect is mitigated.

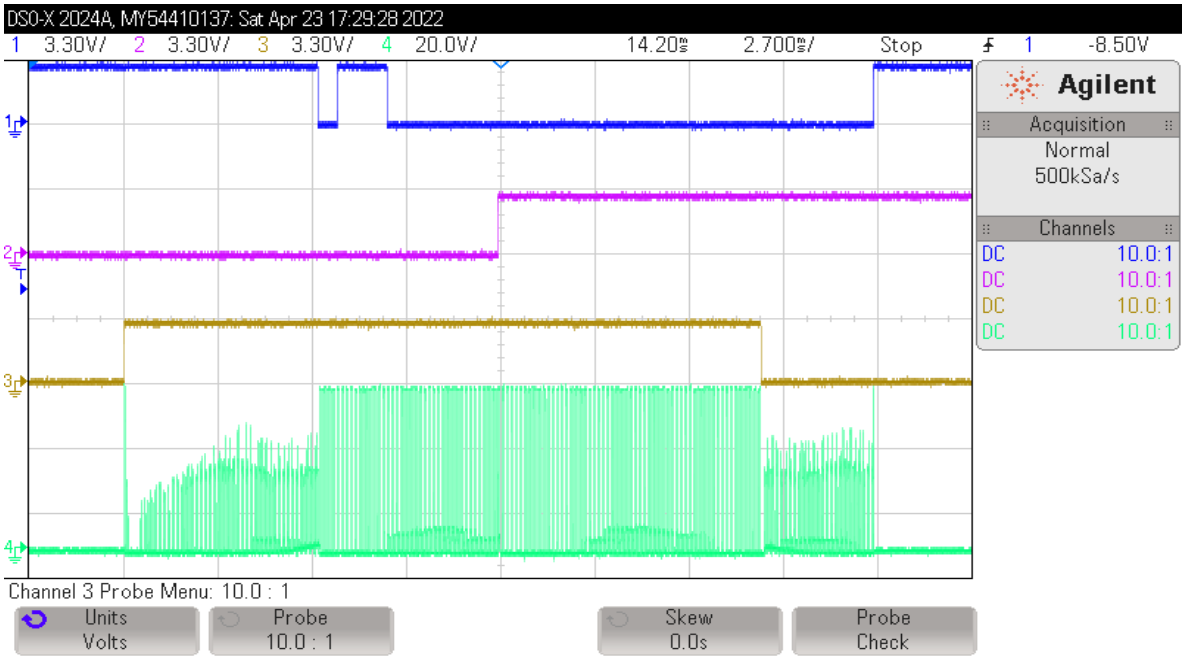

Fig. 4.19 Phase voltage waveform without floating phase effect when glitch effect is mitigated by the corrective mechanism.

The effect of glitches in the HES signals is successfully avoided by the controller without causing any additional delay in commutation switching. The executed commutation sequence corresponds to the required values of Table 3.1. The floating phase condition is entirely avoided. The BLDC motor is checked for speed ramping up to the rated value and is able to run at full speed without getting affected by the glitches present in the HES signals.

4.3.2 AUTOMATIC PHASE SEQUENCE DETECTION

During integration process of motor and controller set, the three phase motor wiring terminals are required to be connected with the corresponding controller terminals that are fixed and appropriately defined with respect to the HES placements in the motor. This sequential arrangement and HES number mapping is essential for the execution of correct commutation sequence.

The structure of BLDC motors is based around the stator windings and a rotor with permanent magnets. The correct sequence of energizing the stator windings is necessary to produce rotational motion. In the case of changed motor phase sequence, the phase that gets energized is different than the desired one when switching scheme is implemented according to the commutation table. In this scenario, rotor may move with jerk or may not move at all, depending on its position with respect to the 3 HESs. In some cases, rotor experiences jerky movement in reverse direction also. All these possibilities render the drive effectively inoperative for any application. Therefore, automatic phase sequence detection is crucial for the BLDC motor control systems.

In applications particularly like e-rickshaws, the phase and HES terminals of motor and controller set are joined by harness connectors. If the terminals are wrongly connected and not properly identified in the controller, then it leads to wrong phase sequence identification by the controller [12], [20].

The phase sequence mapping with respect to HES signals can be obtained as there are fixed three phases. However, complicating the matter is their respective position with respect to the three HESs. When the controller implements the switching sequence according to the detected HES signal values, only the particular phase gets energized according to the switching sequence [60]-[61]. Rotor motion or jerk depends on the phase that gets energized at that particular commutation instant.

All the possibilities discussed so far, are encountered at least once in one complete electrical cycle when actual phase sequence is different from the one intended. This can

damage the drive, motor shaft or the inverter circuitry if the rotor gets stalled and phase energization is persisted [44], [145]. Different cases pertaining to the changed phase sequence are presented in Fig. 4.20 and 4.21.

Figure 4.20(a) represents the correct reference phase sequence and the corresponding HESs with respect to the phase windings are also shown. The HES placement is left unaltered in rest of the figures as HES mounting is not changed in any way. Only the motor phase connections are altered which are represented by the red coloured phase names. Figure 4.20 (b) represents the case when all three phases are rotated in clockwise direction and, Fig. 4.20(c) represents the case when all three phases are rotated in anticlockwise direction. Further rotation or interchange results in the repetition of the previous cases.

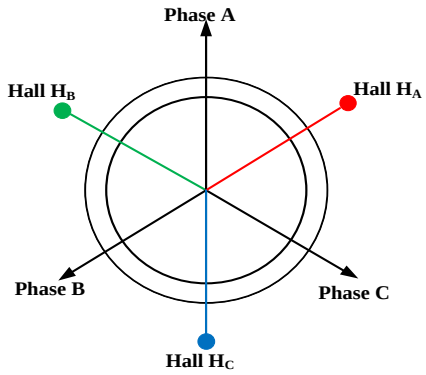

(a) Normal phase sequence referred to fixed HESs.

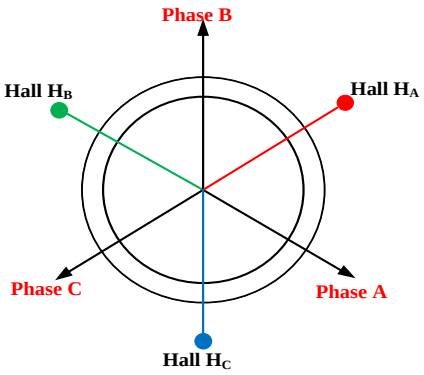

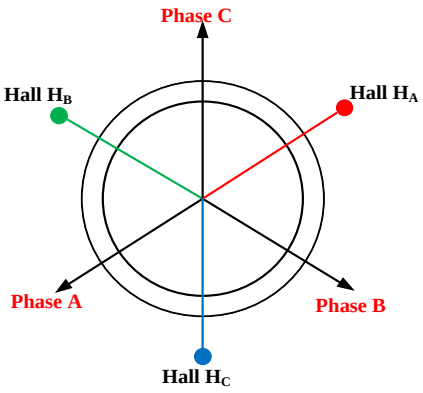

(b) 3 phases shifted in clockwise direction. (c) 3 phases shifted in counterclockwise direction.

Fig. 4.20 Phase sequence possibilities in normal condition and, when all 3 phases are rotated in one direction.

Figure 4.21 represents the cases when any two phases are interchanged. The interchanged

phases are shown in red colour while the remaining phase is represented in black. All three possibilities of interchanged phase pairs are represented in Fig. 4.21.

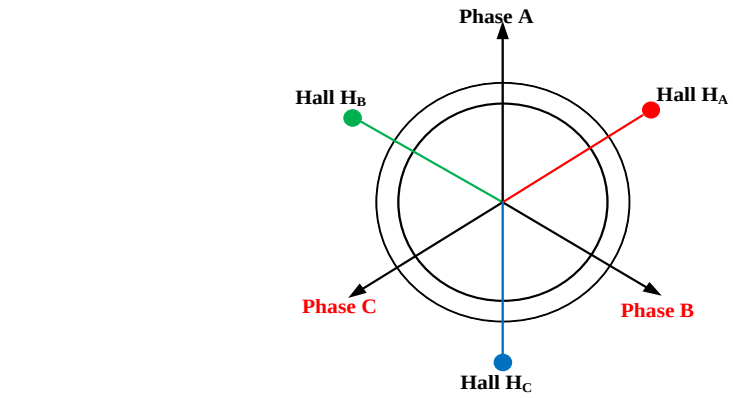

(a) Phase B and C interchanged.

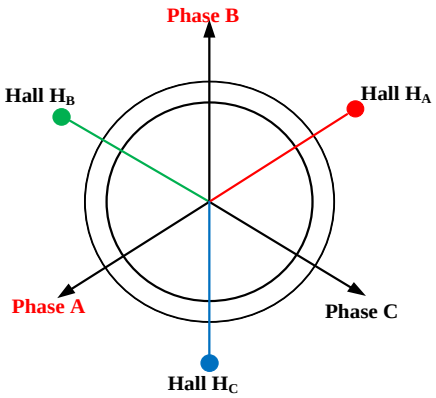

(b) Phase A and B interchanged.

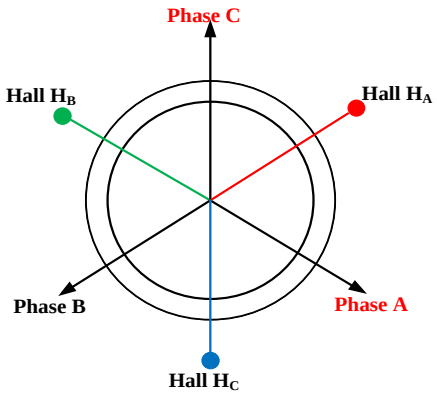

(c) Phase A and C interchanged.

Fig. 4.21 Phase sequences when two phases are interchanged.

Different combinations presented in Figures 4.20 and 4.21 are used to detect different phase sequences in the controller. Whenever HES value change is detected on a particular switching sequence, next forward firing sequence is checked and compared with the previous one. One direction of movement is taken as reference forward direction. If the changed HES values correspond to forward movement in any of the cases presented, then new phase sequence is assigned in the controller.

The phase sequence numbering that is assigned to the microcontroller pins corresponding to each phase is changed according to the detected sequence. The flowchart in Fig. 4.22 shows the auto phase detection scheme and its integration in the motor controller.

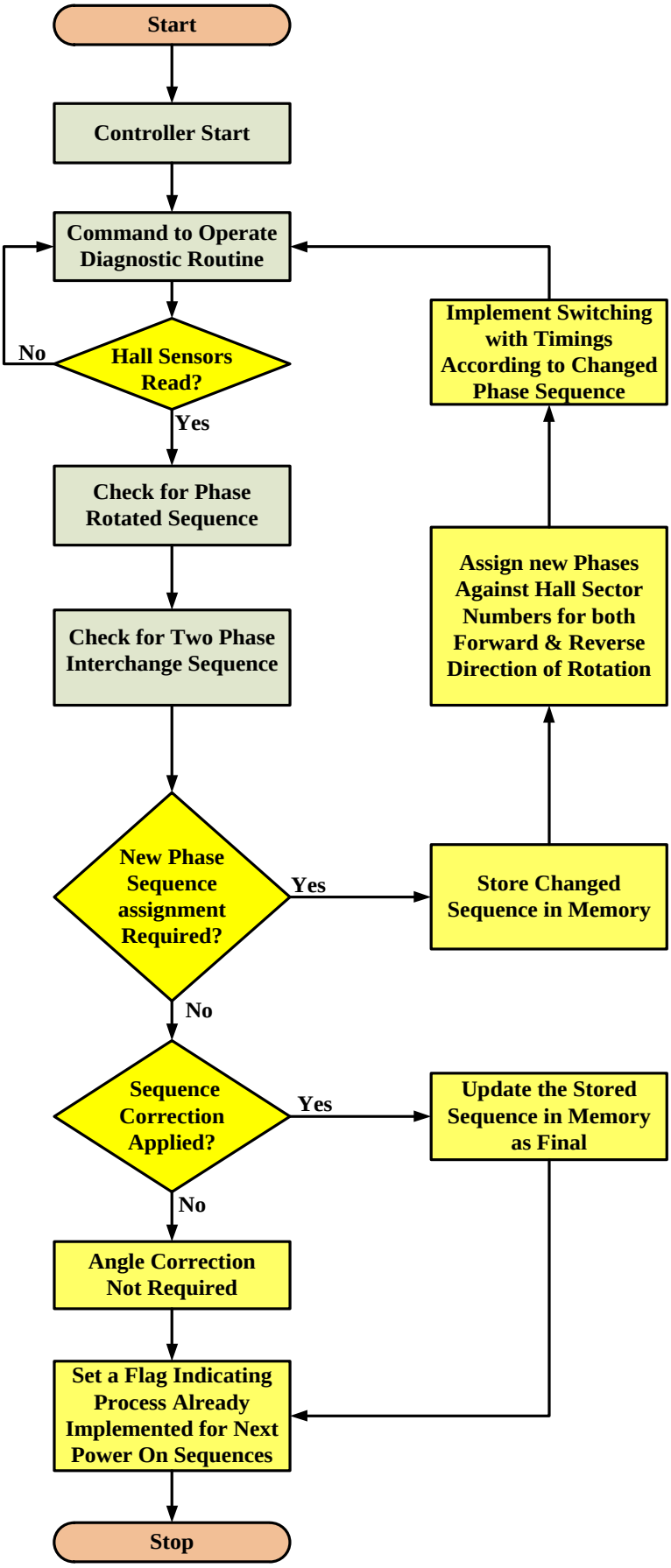

Fig. 4.22 Flowchart of the auto phase detection scheme implementation in controller.

The presented scheme makes it possible to implement the original switching scheme without changing phase sequence in switching table in controller software. Instead, the phase sequence assigned to the controller input pins is changed by the diagnostic routine. Accordingly, a flag is also set in the controller software for using the new assigned phases in the future operations.

Manual intervention is not required to change the phase connections. The phase B is assigned as phase A, phase A is assigned as phase C and phase C is assigned as phase B in the reconfigured phase assignments in controller for the case of Fig. 4.20(b). The phase A is assigned as phase B, phase C is assigned as phase A and phase B is assigned as phase C for case of Fig. 4.20 (c). In the case of Fig. 4.21(a) phase B and C are interchanged on pins assigned. Similarly for the cases of Fig. 4.21(b) and 4.21(c), phases A, B and phases B, C are interchanged. After these reassignments, the original switching scheme according to the commutation scheme is implemented in the subsequent operations.

When the phase sequence detection is carried out in the controller, the worst-case time taken for detection is less than 80 milliseconds as shown in Fig. 4.23. The two spikes in DC link current mark this time span. This time is achieved with a duty cycle of 8%.

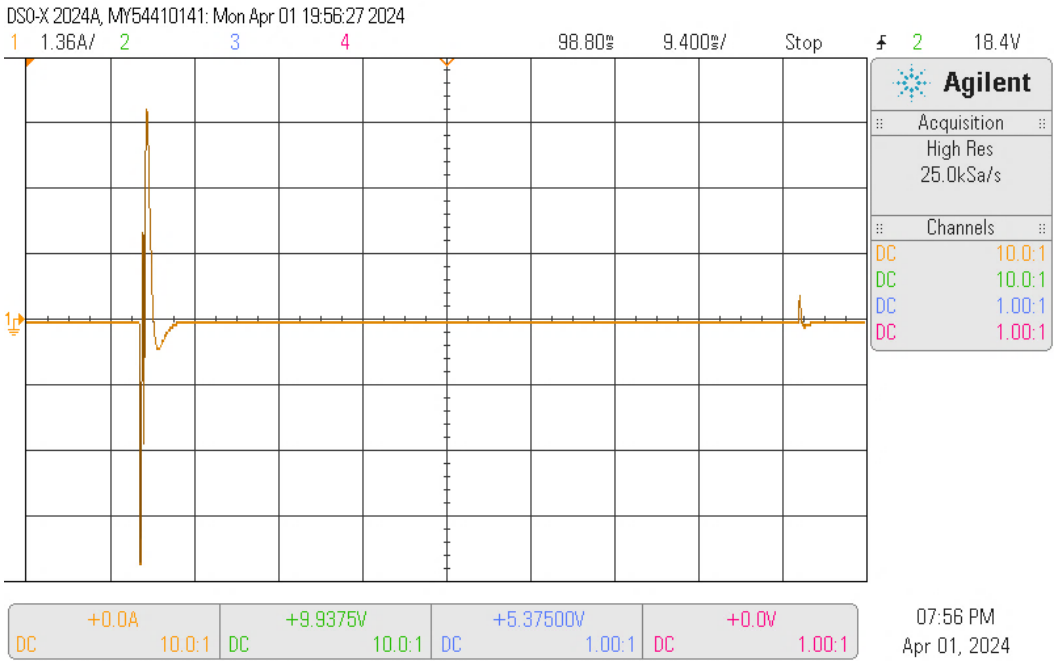

Fig. 4.23 Automatic phase sequence detection process timing check.

The proposed method is developed and implemented in EV controller design, and it confirms to the following features:

- The phase sequence detection is carried out without requiring any additional hardware

component.

- Its implementation is without using any phase current measurement.
- It can be implemented in the software in any controller design as a part of starting procedure or diagnostic routines.
- It does not interfere in microcontroller interrupt subroutine scheduling and switching scheme remains unchanged according to the commutation table.

4.4 EXPERIMENTAL HARDWARE TEST BENCH DEVELOPMENT

The final hardware test bench developed for testing and experimental validation of laboratory prototype is shown in Fig. 4.24. The main motor remains the 48 V, 1 kW BLDC motor of an e-rickshaw application. The set up is powered by 48 V, 72 Ah battery pack. Two other motors of 900 Watt and 1000 Watt are also used for testing purposes. Two motors are mechanically coupled to realize a motor-generator set up of BLDC motors.

The controller is tested to validate the hardware and motor driver software functioning. Nominal switching frequency of 16 kHz is used in the design with 120° trapezoidal commutation scheme. The proposed system incorporates HES signal fault detection and, method to detect correct motor phase sequence. Other features in the design are proposed considering the issue of overheating of controllers in e-rickshaw type of applications. Over current protection is also incorporated in the design.

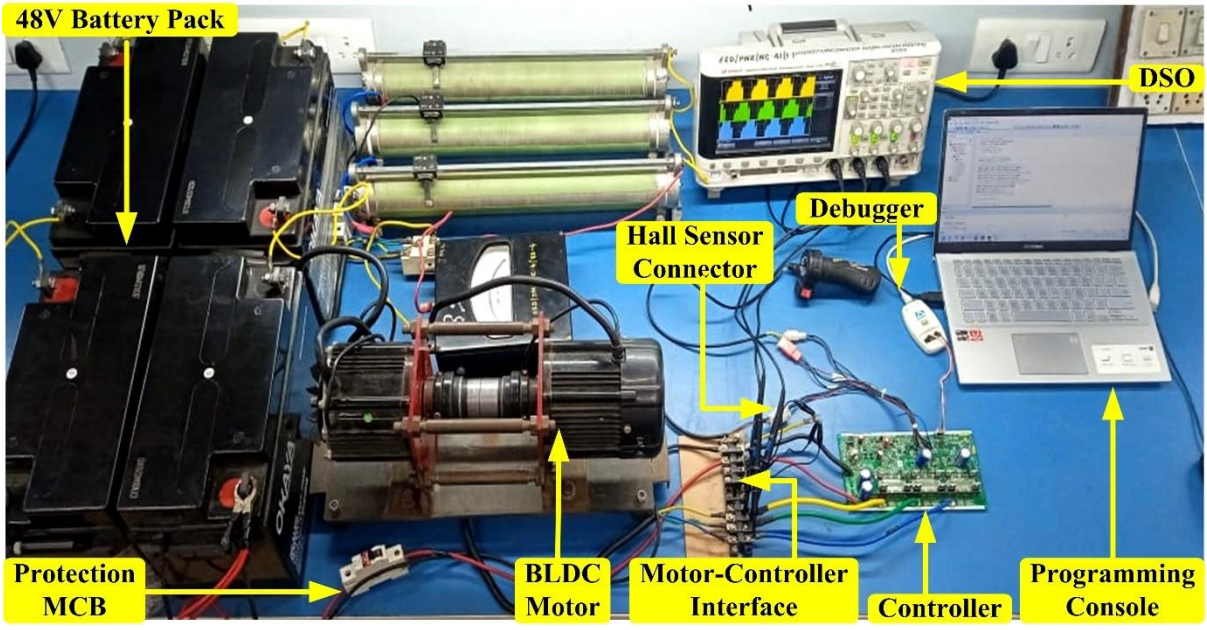

Fig. 4.24 Final experimental hardware test bench set up for controller prototype.

The final hardware test bench set up includes digital storage oscilloscope (DSO), DC supply, multi-meter, Anderson connectors, wire harness connectors, connecting cables, and programming console. The dynamic performance of the system is examined using the four channel KEYSIGHT INFINII VISION DSO-X 2024A DSO. The 600 V capacity differential voltage probe is interfaced with DSO to check phase to phase voltage profiles at motor terminals. Fluke 325 True RMS Clamp Meters are used to check DC link current and phase currents. Three other TEKTRONIX current probes are interfaced with DSO to obtain phase and DC link current profiles.

4.5 CONCLUDING REMARKS

The design and testing of the proposed 3-Phase BLDC motor controller are elaborated in this chapter. The controller can be deployed in low to medium power EV applications like e-rickshaws and Tuk-Tuk. It is based on 32 bit STM103 series microcontroller that is already used in several industry standard application designs. The controller is designed for 1kW BLDC motor with peak current capacity up to 60 A, and input voltage in the range of 42-56 V. It incorporates solutions for correct HES sequence detection, HES glitch effect correction and auto phase sequence detection. All these diagnostic methods are implemented without requiring any modification in the control algorithm. The state machine model, controller circuit, and application methods regarding other FTC schemes in the controller remain unaffected.

Further, an improved heat sink design is implemented for handling overheating of the controller. The over current situation is handled by a separate hardware based approach in addition to the microcontroller software based scheme. These low cost feature enhancements improve the functionality of the controller and render it more useful in different types of applications. The motherboard level testing of controller hardware and software drivers is carried out to validate the design of the controller. Finally, motor controller integration is successfully tested with trial runs of the BLDC motor.

CHAPTER 5

FAULT DETECTION AND MITIGATION SCHEME FOR UNBALANCED HES SIGNALS IN BLDC MOTOR DRIVES

5.1 INTRODUCTION

BLDC motors can be operated in sensored mode with HESs or encoders. EV applications, such as two-wheelers, e-rickshaws, and tuk-tuk, leverage the cost-effective drive mechanism by employing BLDC motors with three HESs. The controllers in these applications use HES signals to manage the switching timing and commutation sequence [9], [120]. The control mechanism of the drive relies on the integrity of HES signals and their synchronization with the BEMF profile of the motor phases [59]. However, discrepancies in HES signal timings are observed due to factors like aging, the mounting process of HESs, winding, and the placement of sensors. This issue is frequently reported in mass scale produced motors, especially for low voltage EV applications. This is documented in experimental studies also [60]-[61]. Compounding this challenge, there are limitations and difficulties in precisely assembling stator lamination sheets with HESs in various slot numbering per pole fixtures. Consequently, the accurate positioning of sensors is often compromised. The problem gets more pronounced in machines with a higher number of poles, resulting in error of significant electrical degrees even for minor discrepancies [15], [105].

In this chapter, an investigation into HES unbalancing faults in sensored BLDC motor drives is presented. To minimize the effects of these faults, an FTC scheme is introduced for implementation in the motor controller without necessitating any modification to the system architecture or core commutation method. The proposed scheme involves the detection, classification, and estimation of fault extent during the starting phase of the controller. This allows for subsequent corrections without the need for repetitive error estimations or, requiring identification of a valid reference signal separately to rectify inverter switching mistiming, as is typically required in classical methods [38].

The categorization component of the scheme allows mapping of faults with their corresponding HESs. Its verification is checked in the MATLAB/Simulink model. Experimental validation is carried out in the hardware test bench set up consisting of the controller, and a 1 kW BLDC motor from an e-rickshaw for validation. The proposed method demonstrates superior steady state and dynamic performance over faulty conditions when compared to another scheme that is based on the LSM of speed estimation.

Results indicate a reduction in peak-to-peak values and ripple content in both phase currents and the DC link current when employing the presented scheme. This reduction contributes to an observed increase in efficiency and nominal torque per ampere. The transient response with sudden load changes is also checked. It demonstrates a superior response with implementation of the proposed scheme in controller. A comparison of the increased memory loading of the controller with both schemes, as well as normal operation without any correction scheme, is presented. The proposed scheme has least share of repetitive calculations of the controller during runtime operation which is an important factor for controller implementation.

5.2 HES SIGNAL UNBALANCING IN BLDC MOTOR DRIVES

The voltage output signals from the HESs are influenced by the strength of the applied magnetic field, which varies according to the rotation of the rotor's magnetic poles [146]. In a standard drive configuration with three HESs, there are six valid combinations of the binary output signals in an electrical cycle. Thus, one electrical cycle is divided into six sectors each spanning 60°E interval. This signal pattern is used to track rotor position and direction of the rotor rotation [4]. The sequence for inverter switching is determined by the sector number and is synchronized with the transitions detected on the HES signals [118].

The equivalent circuit of sensored BLDC motor drive with three phase inverter has already been discussed in chapter 3 with Fig. 3.1 and commutation Table 3.1. However, for easier referencing and, with changed HES numbering against the phase windings, the inverter and switching scheme referenced in this chapter are presented in Fig. 5.1 and Table 5.1. The corresponding phase voltage and phase current patterns against HES signals are illustrated in Fig. 5.2 along with the BEMF pattern for 120° trapezoidal commutation.

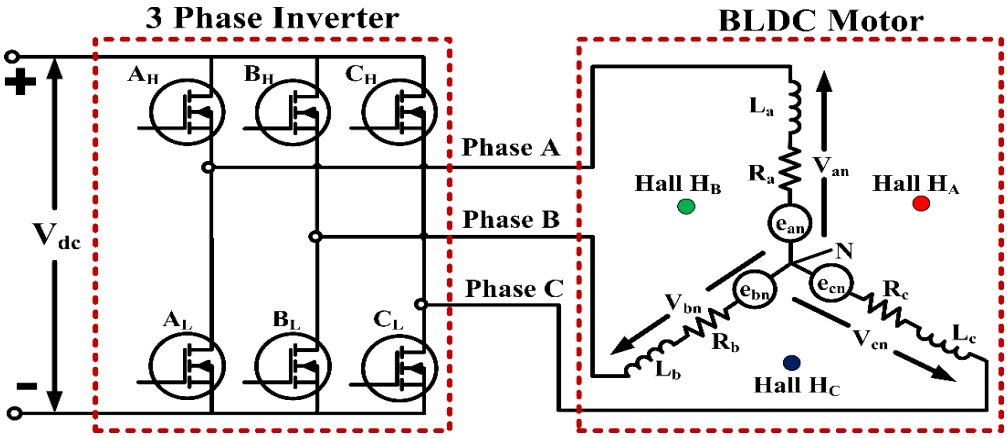

Fig. 5.1 BLDC motor and inverter circuit with HESs.

Table 5.1 Switching sequence with HES signal pattern.

Sector No.	**Rotor Angle (^{0}E)**	**Hall Sensor Signal**			**Switching Pattern**						**Phase Voltage**		
i	Φ	H_C	H_B	H_A	A_H	B_H	C_H	A_L	B_L	C_L	Phase C	Phase B	Phase A
1	0^0-60^0	0	1	0	1	0	0	0	1	0	0	$-V_{dc}$	$+V_{dc}$
2	60^0-120^0	1	1	0	1	0	0	0	0	1	$-V_{dc}$	0	$+V_{dc}$
3	120^0-180^0	1	0	0	0	1	0	0	0	1	$-V_{dc}$	$+V_{dc}$	0
4	180^0-240^0	1	0	1	0	1	0	1	0	0	0	$+V_{dc}$	$-V_{dc}$
5	240^0-300^0	0	0	1	0	0	1	1	0	0	$+V_{dc}$	0	$-V_{dc}$
6	300^0-360^0	0	1	1	0	0	1	0	1	0	$+V_{dc}$	$-V_{dc}$	0

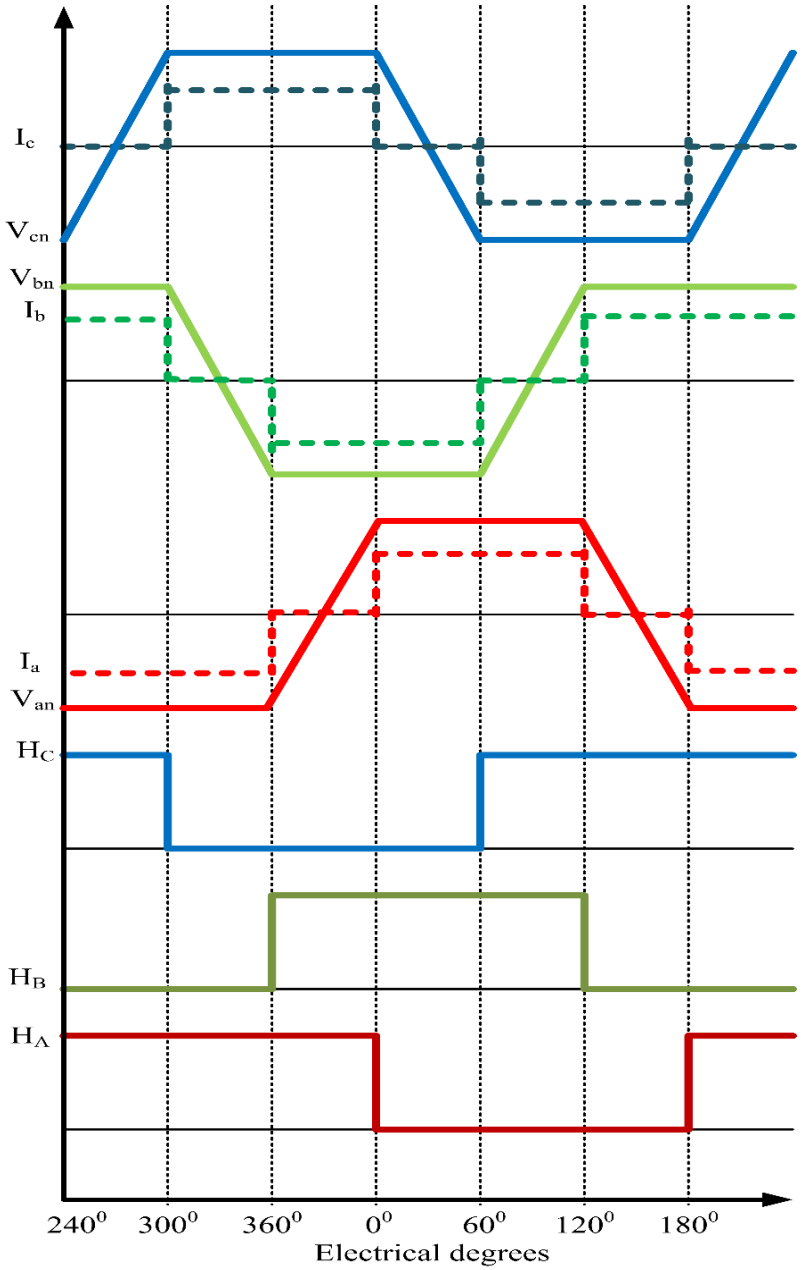

Fig. 5.2 Phase voltage, stator current and BEMF profiles with HES signals in ideal case.

In the sensored BLDC motor drives, unbalanced HES signals can significantly affect several major functions of the drive such as [16], [146]:

1. Calculation of Rotor Speed and PWM Duty Cycle: The HES signals are crucial for accurately determining the rotor position, which is essential for calculating the speed of the motor. Imbalanced HES signals can lead to inaccurate estimations of speed and PWM duty cycle for the applied motor phase voltages.

2. Inverter Switching Pattern Determination: The commutation sequence in a BLDC motor is determined based on the rotor position sensed by the HES signals. Unbalanced HES signals can lead to incorrect commutation sequence and improper inverter switching patterns.

3. Detection of Forward and Reverse Rotor Rotation: Imbalance in the HES signals can lead to incorrect determination of rotor rotation direction, potentially causing irreversible issues during motor drive operation.

4. Motor Starting Sequence: During motor startup, the controller relies on the HES signals to initiate the correct starting sequence. Imbalanced HES signals can disrupt this sequence, leading to issues such as motor stalling or failure to start.

Overall, obtaining accurately timed balanced HES signals is crucial for the proper operation and performance of a sensored BLDC drive. Any imbalance can lead to inaccuracies in speed control, commutation sequence determination, direction detection, and motor starting, impacting the overall efficiency and reliability of the system.

Various FTC schemes have been proposed for the sensored control of BLDC motors to address HES signal timing issues. These schemes often involve phase angle advancement and signal reconstruction techniques that rely on concepts such as instantaneous speed averaging, extrapolation, or other complex methods [12]-[13], [38], [57].

While these methods show promise and can be adapted and modified for implementation in sensored BLDC motor applications, it is important to note that the process of signal reconstruction, especially for 60°E sectors, introduces challenges such as increased execution time and complexity in the software subroutine functions. This complexity arises from the inherent need for repeated error estimations during signal reconstruction for each 60°E sector. If this correction process affects interrupt subroutines during drive operation in any way, the interrupt and task scheduling can be disrupted in the controller, potentially leading to distortions in the applied phase voltages with damage to the drive itself [16], [117], [119].

These factors highlight the need for careful consideration and optimization when implementing FTC schemes to address the HES faults without adversely impacting software execution and system performance.

5.3 PROPOSED CATEGORIZATION SCHEME FOR UNBALANCED HES SIGNAL FAULTS

The proposed scheme includes both detection and correction methods tailored to handle errors stemming from one, two, or three HES faults. Each fault type is detected and mapped to corresponding HESs. This mapping enables swift and precise rectification of mistimed switching signals resulting from unbalanced HES signals, enhancing system reliability and performance.

An essential feature of the proposed scheme is its seamless integration into the motor controller without necessitating any changes to the circuit, control algorithm, or state machine model. Moreover, the proposed method does not impose any restrictions on the application of other FTC schemes within the controller. This ensures that the detection and mitigation of other runtime faults remain unaffected. Thus, the proposed method allows continued utilization of state machine model as required by the control algorithm.

In the ideal scenario, HES signals are evenly spaced, representing exact 60°E sectors. The cases wherein HES signals are unbalanced are depicted in Fig. 5.3 to Fig. 5.6 for different scenarios. The unbalanced HES signals are shown by shifting each HES by an angular error equivalent to a certain degree from the ideal placement. The impact on the 60°E sectors is illustrated in these figures. The ideal HES placements (H_A, H_B, H_C) are depicted with solid lines, while dotted lines represent HESs with errors. Angular deviations are denoted as Φ_a, Φ_b, and Φ_c, respectively for each HES and "n" represents sector span with normal duration. HES mistiming faults are further categorized into the following cases to facilitate easier detection and rectification.

1. **Case 1: Single hall signal unbalancing**

In this case, only one HES signal is mistimed while the other two signals are correctly timed. This condition is illustrated in Fig. 5.3, wherein H_a represents the HES with the delayed signal. As a result of this condition, one electrical sector extends to $60° + \Phi_a$, while the adjacent sector shrinks to $60° - \Phi_a$. Consequently, there are two sector spans with deviations of same degree but opposite sign from ideal sector duration of 60°E. Rest four sector spans are of normal duration.

The observed cyclic sector span deviation pattern for both directions of rotation in Case 1 can be represented as:

$+\Phi_a$, $-\Phi_a$, n, n, n, n or

$-\Phi_a$, $+\Phi_a$, n, n, n, n

where “+” and “-” signs represent sector span elongation and compression respectively.

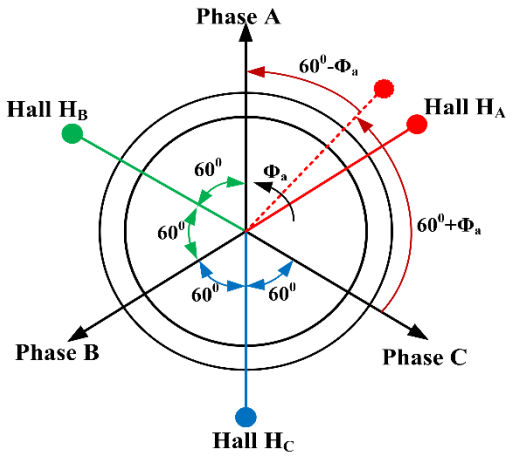

Fig. 5.3 Representation of equivalent unbalancing due to one mistimed HES signal.

2. Case 2(A): Two HES signals unbalanced in the same direction

In the scenario where one HES signal is correctly timed and two are mistimed, it results in an alteration in four consecutive sector spans, while the remaining two consecutive sectors retain their normal span. This leads to two conditions, as depicted in Fig. 5.4, where Φ_a represents the first deviation when transitioning from normal span sectors to altered span sectors, and Φ_b represents the second deviation. Figure 5.4(a) illustrates the condition when $\Phi_a > \Phi_b$, while Fig. 5.4(b) shows the scenario when $\Phi_a < \Phi_b$.

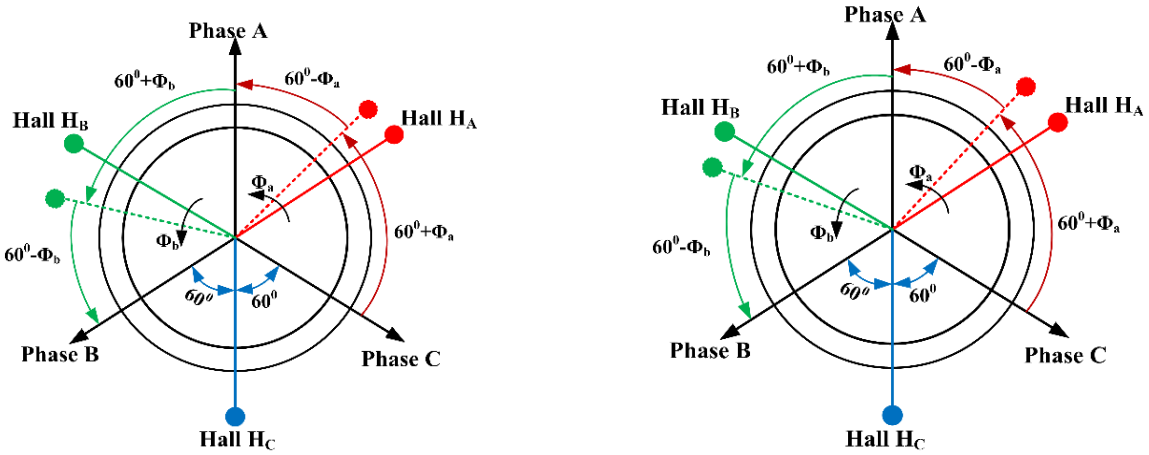

(a) $\Phi_a > \Phi_b$ (b) $\Phi_a < \Phi_b$

Fig. 5.4 Equivalent misalignments due to two unbalanced HES signals in the same direction.

In the both cases depicted in Fig. 5.4, the sector span deviations follow the pattern 60^0 + Φ_a, 60^0 - Φ_a, 60^0 + Φ_b, 60^0 - Φ_b. Therefore, the sector span deviation pattern in Case 2(A)

with unbalanced HESs H_A and H_B can be represented as:

$+\Phi_a$, $-\Phi_a$, $+\Phi_b$, $-\Phi_b$, n, n

In case of reverse direction of rotation, sector span deviation pattern is:

$-\Phi_b$, $+\Phi_b$, $-\Phi_a$, $+\Phi_a$, n, n

3. Case 2(B): Two HES signals unbalanced in the opposite direction

Figure 5.5 illustrates two possible conditions when misalignments of both the HESs are in opposite directions. This results in a sector span pattern of $60^0 - \Phi_a$, $60^0 + \Phi_a$, and $60^0 + \Phi_b$, $60^0 - \Phi_b$, considering a counterclockwise direction of rotation. Therefore, the sectoral span deviation pattern for both possible conditions of Case 2(B) with unbalanced HESs H_A and H_B can be represented as:

$-\Phi_a$, $+\Phi_a$, $+\Phi_b$, $-\Phi_b$, n, n or

$+\Phi_a$, $-\Phi_a$, $-\Phi_b$, $+\Phi_b$, n, n

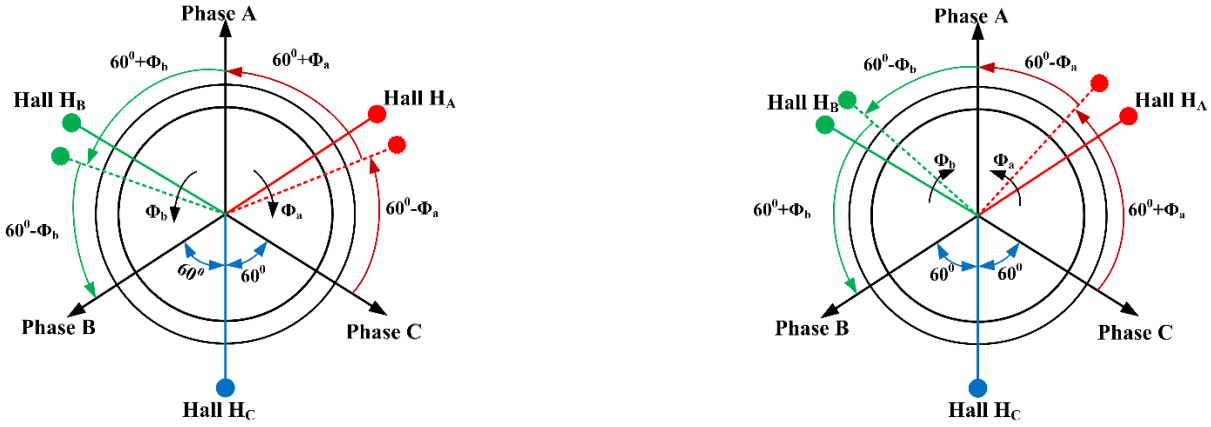

(a) Divergent case. (b) Convergent case.

Fig. 5.5 Equivalent HES unbalancing in opposite directions due to two HESs.

4. Case 3: Three HES signal unbalancing

When all three HES signals show unbalanced timings, the resultant sector duration pattern consists of six sectors arranged in three pairs with deviations, as depicted in Fig. 5.6. In each pair, one sector is expanded, while the next sector is compressed by the same degree. The sector spans in pairs are as follows:

- $60^0 + \Phi_a$, $60^0 - \Phi_a$
- $60^0 + \Phi_b$, $60^0 - \Phi_b$
- $60^0 + \Phi_c$, $60^0 - \Phi_c$

Therefore, the resultant sector span deviation pattern for Case 3 can be represented as:

$+\Phi_a$, $-\Phi_a$; $+\Phi_b$, $-\Phi_b$; $+\Phi_c$, $-\Phi_c$

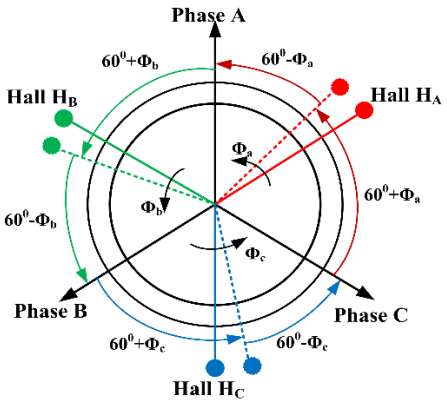

Fig. 5.6 Sector span pattern with three unbalanced HESs.

5. Case 4: Three HES signal unbalancing with common error

The particular case when all three HES signals show mistiming, but the observed degree of deviation is same for all the three signals, can be detected and corrected separately. This situation may occur due to deviation in HES mounting in one direction, where each HES is moved by same degree from its ideal placement, or due to runtime effect common to all three HESs. Even an error introduced at a sub degree level during stator stamping cutting for HES adjustment can result in a significant deviation in the 60^0E sector span in this case.

The resultant deviation for Case 4, can be referred to Fig. 5.6 with common deviation value for all HESs. Taking Φ_0 as the equivalent HES signal deviation Case 4 can be represented as:

$\Phi_a=\Phi_b=\Phi_c=\Phi_0$

The corresponding sector span deviation pattern is:

$+\Phi_0$, $-\Phi_0$; $+\Phi_0$, $-\Phi_0$; $+\Phi_0$, $-\Phi_0$

In case of reverse direction of rotation, sector span deviation pattern is:

$-\Phi_0$, $+\Phi_0$; $-\Phi_0$, $+\Phi_0$; $-\Phi_0$, $+\Phi_0$.

5.4 IMPLEMENTATION OF THE PROPOSED DETECTION AND CORRECTION SCHEME IN CONTROLLER

The correction method based on the proposed detection and categorization scheme is developed for implementation in the controller during the initial integration of the motor controller. Subsequent operations can implement the estimated corrections without computational overheads or disturbing the state machine model in the microcontroller. The

block diagram of the controller with inclusion of the proposed scheme is shown in Fig. 5.7. The proposed scheme conforms to the following features for integration in a sensored BLDC motor controller:

1. It does not introduce new complex variables with lengthy calculations. This is crucial because even a small latency in switching signal execution at higher speeds can result in significant changes in switching angles directly affecting the drive operation.
2. The execution time of interrupt subroutines corresponding to the switching sequence implementation remains unaffected.
3. It does not interfere with other periodically executed critical functions in the microcontroller such as PWM generation, duty cycle estimation, ADC and DMA buffering operations.
4. The state machine logic and sequence of operations in the target application remain unchanged without addition of any new physical or pseudo component to the controller.

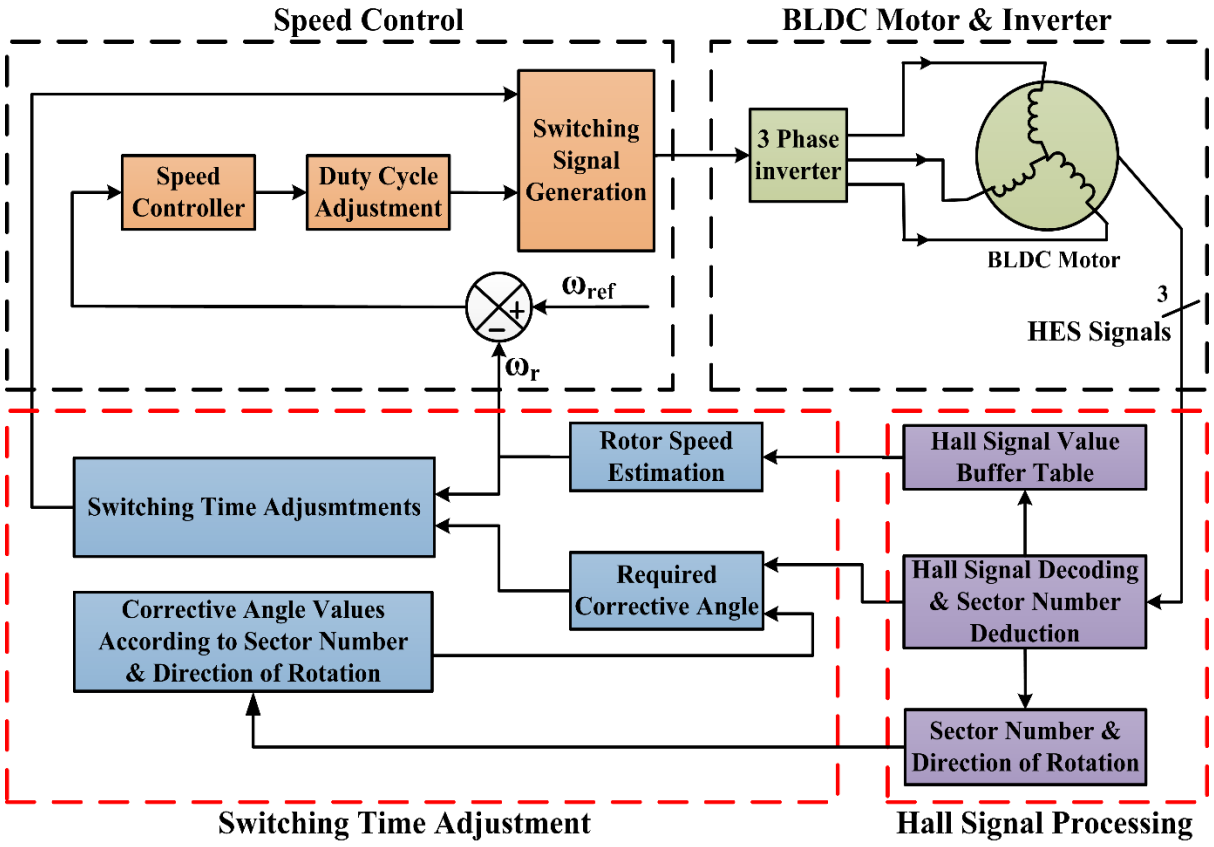

Fig. 5.7 Block diagram of the controller with HES signal mistiming correction.

Application of the proposed scheme in the controller is presented in the main flow chart of Fig. 5.8. The highlighted subprocess corresponds to sequential detection of the cases of unbalanced HES signal timing errors. This detection process is further elaborated in detail

and presented in the flow chart in Fig. 5.9 with final decision on whether error is due to HES shifting or not.

The FTC data values are stored in the microcontroller's non-volatile memory during the motor controller integration process, along with a flag indicating the application of the presented FTC for further operations. This prevents the repetition of error detection and estimation. Once ascertained, the required corrections related to the present and upcoming HES signal pattern are stored separately for both forward and reverse directions of rotation. The proposed FTC scheme executes the following sequential steps in the motor controller:

- Sectoral spans S_i (i=1 to 6) are calculated as:

  $$S_i=t_{i+1}-t_i \quad (5.1)$$

- One electrical cycle time span S_e is calculated as:

  $$S_e=\sum S_i=S_1+ S_2+ S_3+ S_4+ S_5+S_6 \quad (5.2)$$

- Rotor electrical speed ω_e and mechanical speed ω_r are calculated using Eqn. (5.3) where P is number of pole pairs.

  $$\omega_e = (1/S_e) *60$$

  $$\omega_r = (1/P)*(1/S_e) *60 \quad (5.3)$$

- Ideal 60° E sector duration (S_0) is obtained as:

  $$S_0 = S_e/6 \quad (5.4)$$

- Deviation of each electrical 60° sector from ideal sector duration are calculated as:

  $$\Delta S_i = S_0-S_i \quad (5.5)$$

- Angular sectoral spans Φ_i are calculated using Eqn. (5.6).

  Ideal sector span = Φ_0 =60°

  Angular sector span= $\Phi_i = 60*(S_i/S_0)$

  $$\Phi_i = 360*(S_i/S_e) \quad (5.6)$$

- The sectoral spans are checked for adhering to the mutual relation of Eqn. (5.7):

  $$\Phi_1+\Phi_2+\Phi_3+\Phi_4+\Phi_5+\Phi_6=6\Phi_0=360° \quad (5.7)$$

- Deviation of each sector from ideal span is calculated using Eqn. (5.8):

  $$\Delta\Phi_i = \Phi_0-\Phi_i \quad (5.8)$$

- Cumulative sum of all six sectoral angular spans equals to one electrical cycle which equals to $6\Phi_0$. Using Eqn. (5.7), the cumulative sum of six consecutive sectoral deviations is equal to zero as in Eqn. (5.9).

  $$\sum\Delta\Phi_i = \Delta\Phi_1+\Delta\Phi_2+\Delta\Phi_3+\Delta\Phi_4+\Delta\Phi_5+\Delta\Phi_6$$

  $$\sum\Delta\Phi_i = 6\Phi_0-(\Phi_1+\Phi_2+\Phi_3+\Phi_4+\Phi_5+\Phi_6)$$

$$\sum \Delta\Phi_i = 0 \quad (5.9)$$

- The subsequent cases represented in Equations (5.10-5.17) are subject to validation of relation in Eqn. (5.9) for each observation set for individual case.
- Fault detection and classification are based on the case scenarios represented in Figures from 5.3 to Fig. 5.6. Equations (5.11 and 5.12) represent the conditions for the Case 1 fault as shown in Fig. 5.3.

$$\Delta\Phi_i = -\Delta\Phi_{i+1}; \quad (5.10)$$

$$\Delta\Phi_1 = \Delta\Phi_3 = \Delta\Phi_5 = \Delta\Phi_6 = 0; \quad (5.11)$$

$$\Delta\Phi_2 = -\Delta\Phi_3 \quad (5.12)$$

- In Case 2(A), two starting sectors with deviations must be of opposite signs and same magnitude. The next two sector deviations separately must be of opposite sign with same magnitudes. This condition is represented in Eqn. (5.13).

$$\Delta\Phi_i = -\Delta\Phi_{i+1};$$

$$\Delta\Phi_{i+2} = -\Delta\Phi_{i+3};$$

$$\Delta\Phi_{i+4} = \Delta\Phi_{i+5} = 0 \quad (5.13)$$

The observed deviation pattern for the case shown in corresponding Fig. 5.5 is:

$$\Delta\Phi_2 = -\Delta\Phi_3;$$

$$\Delta\Phi_2 = -\Delta\Phi_3;$$

$$\Delta\Phi_5 = \Delta\Phi_6 = 0 \quad (5.14)$$

- The Case 2(B) condition for two convergent HES signal deviation patterns can be represented through Eqn. (5.15).

$$\Delta\Phi_i = -\Delta\Phi_{i+1};$$

$$\Delta\Phi_{i+2} = -\Delta\Phi_{i+3};$$

$$\Delta\Phi_{i+1} * \Delta\Phi_{i+2} > 0;$$

$$\Delta\Phi_{i+4} = \Delta\Phi_{i+5} = 0 \quad (5.15)$$

- In Case 3 the deviations in consecutive sectors in a pair must be of opposite sign and same degree. This can be expressed through Eqn. (5.16).

$$\Delta\Phi_i = -\Delta\Phi_{i+1};$$

$$\Delta\Phi_{i+2} = -\Delta\Phi_{i+3};$$

$$\Delta\Phi_{i+4} = -\Delta\Phi_{i+5} \quad (5.16)$$

- The particular condition for Case 4 wherein all three HES signals exhibit equal unbalancing can be expressed in Eqn. (5.17) as:

$$\Delta\Phi_i = -\Delta\Phi_{i+1} = \Delta\Phi_{i+2} = -\Delta\Phi_{i+3} = \Delta\Phi_{i+4} = -\Delta\Phi_{i+5} \quad (5.17)$$

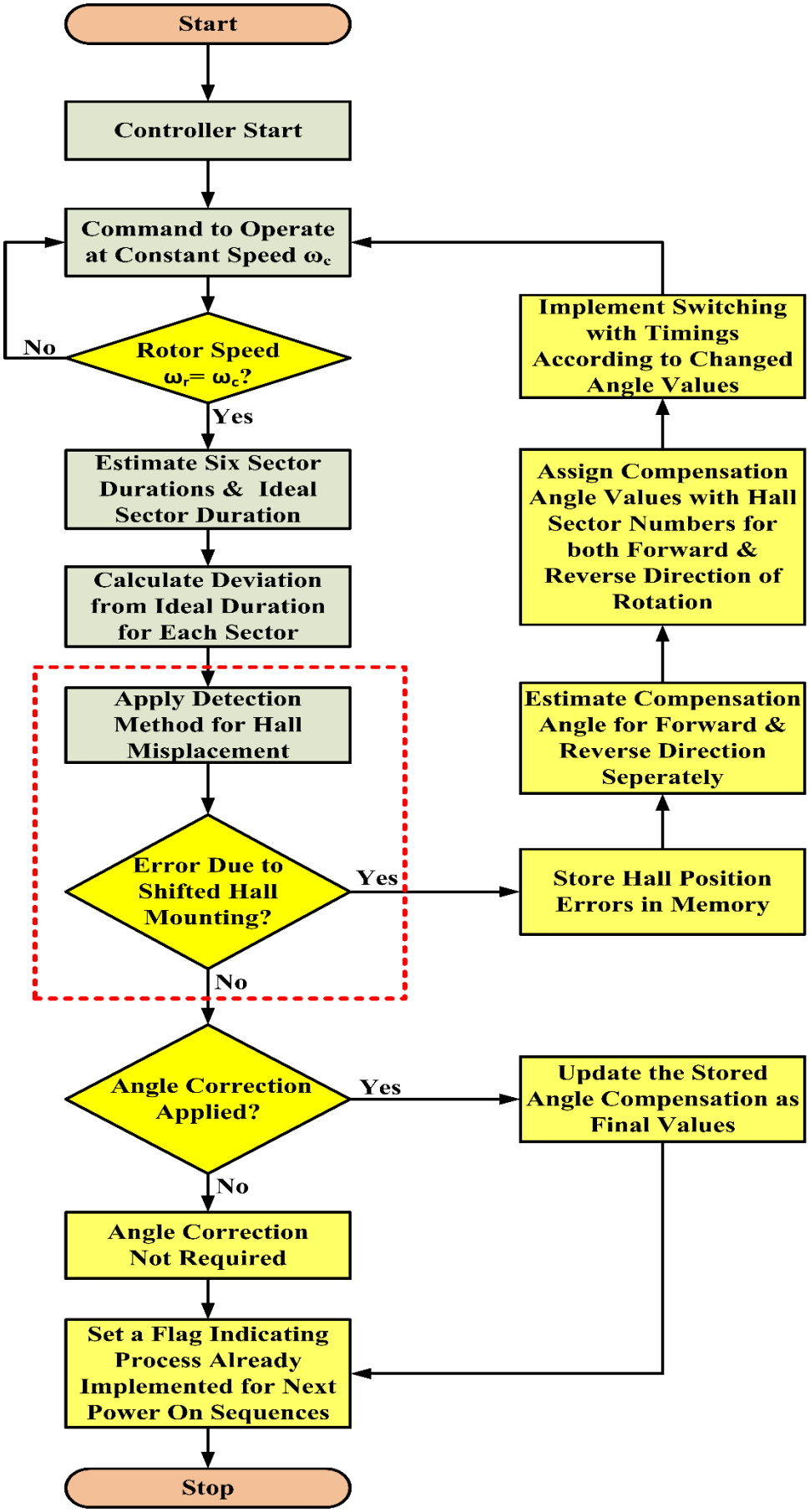

Fig. 5.8 Flowchart of FTC scheme integration in the motor controller.

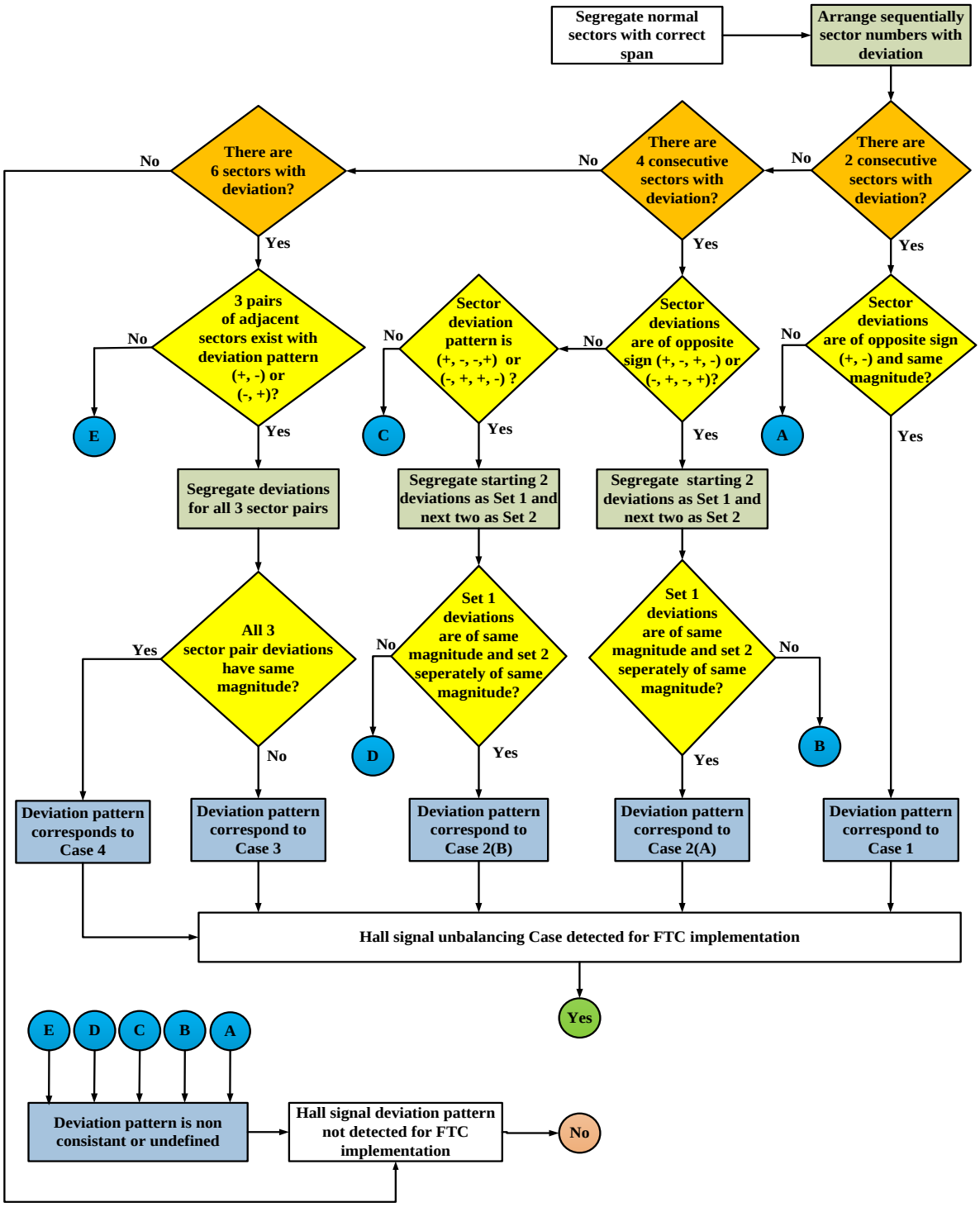

Fig. 5.9 Detection and categorization sub-process flowchart.

5.5 SIMULATION RESULTS AND ANALYSIS

The proposed scheme is modeled and simulated in MATLAB software using a 1 kW, 3-phase, 4-pole pair BLDC motor with a speed of 3000 RPM. The cases described in Section 3 are implemented in the model. The cases are correctly identified, and error correction is applied accordingly. A summary of the equivalent error detection and category checks

obtained for the different types of cases using HES signals is presented in Table 5.2. The resultant HES signal pattern for Case 1 is presented in Fig. 5.10 and it confirms to the unbalancing characteristics described in section 5.3.

Table 5.2 Detection and categorization pattern check.

Implemented				**Detected**			
Case	**Error (^{0}E)**			**Case**	**Error (^{0}E)**		
1	0	0	10	1	0	0	10.37
2(A)	0	4	10	2(A)	0	4.02	10.04
2(B)	0	-6	10	2(B)	0.01	-5.98	10.01
3	-6	10	6	3	-6.06	9.98	6.03
4	20	20	20	4	20.02	19.96	20.01

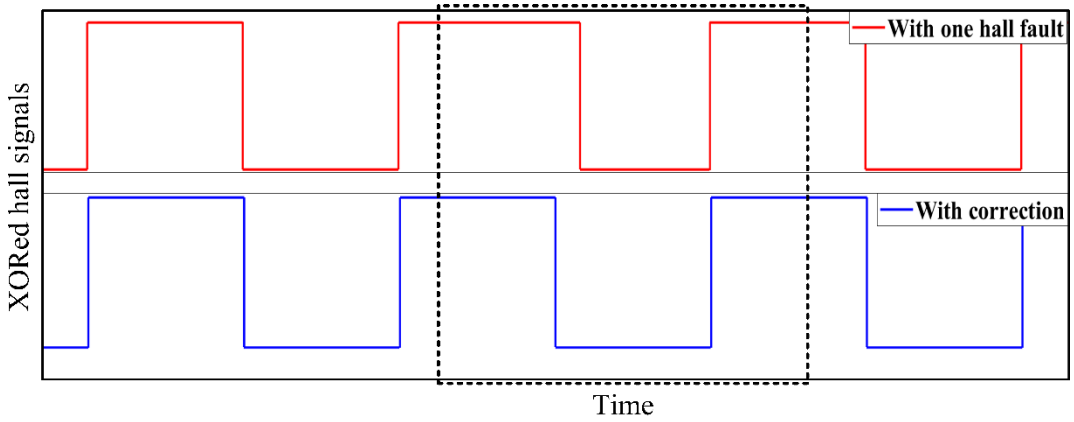

Fig. 5.10 Case 1 sector extension and compression pattern.

The corresponding correction is implemented at unit step load and the observed differences are shown through Figures 5.11, 5.12 and 5.13. Figure 5.11 illustrates the correction in the speed profile, while Fig. 5.12(b) shows the reduction in torque ripples as compared to Fig. 5.12(a). Corresponding phase currents are depicted in Fig. 5.13, and the reduction in peak-to-peak current variations is shown in Fig. 5.14 with application of the proposed FTC scheme.

The comparative waveforms for the faulty case and one with correction applied are presented in Figures 5.11 through 5.14. These results demonstrate the successful detection, estimation and correct mapping for the category of Case 1 according to the categorization scheme. The rotor speed, torque, phase current waveforms are presented for analysis. The application of the switching correction according to the detected case and estimated values validates the efficacy of the proposed scheme.

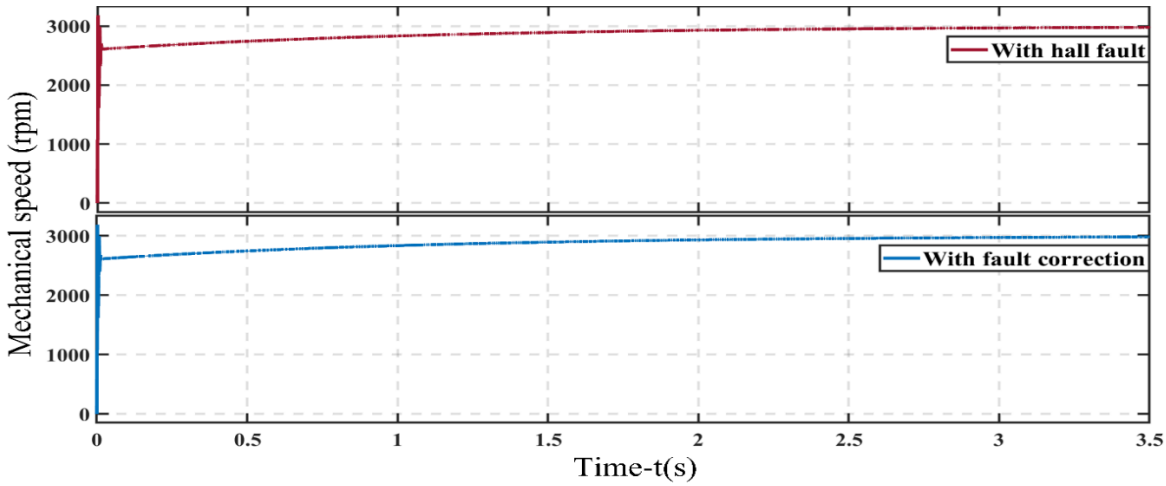

(a) Full range profile.

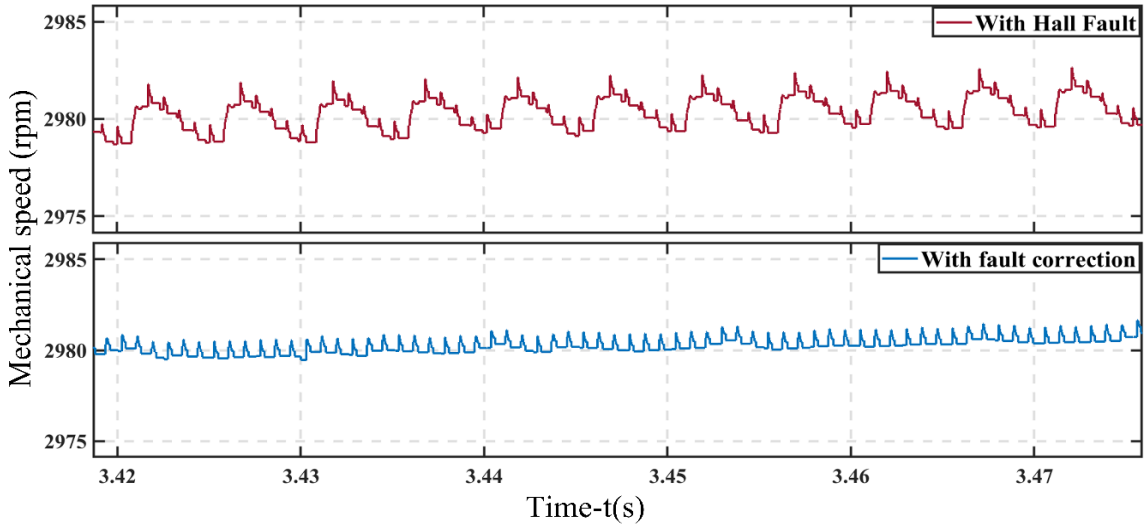

(b) Enlarged speed variations.

Fig. 5.11 Rotor speed profile at step load.

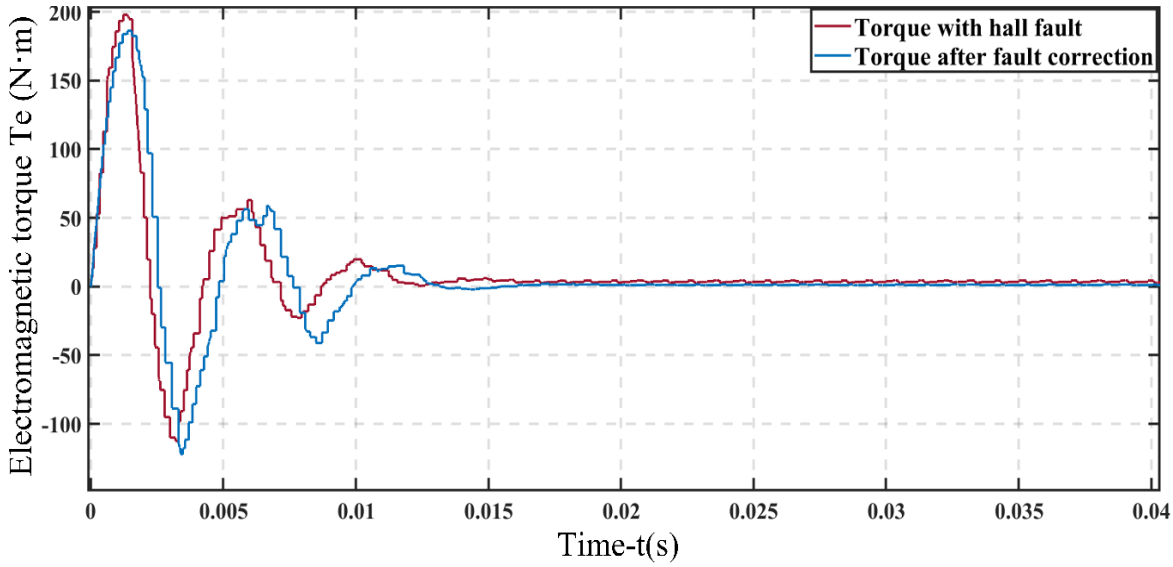

(a) Full range profile.

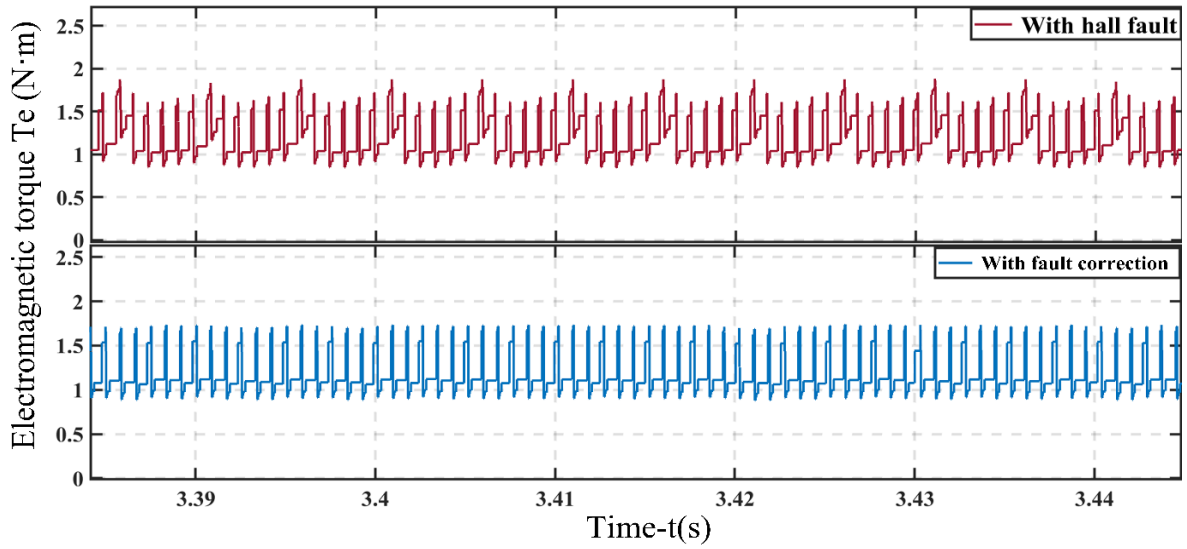

(b) Enlarged torque ripples.

Fig. 5.12 Electromagnetic torque at step load.

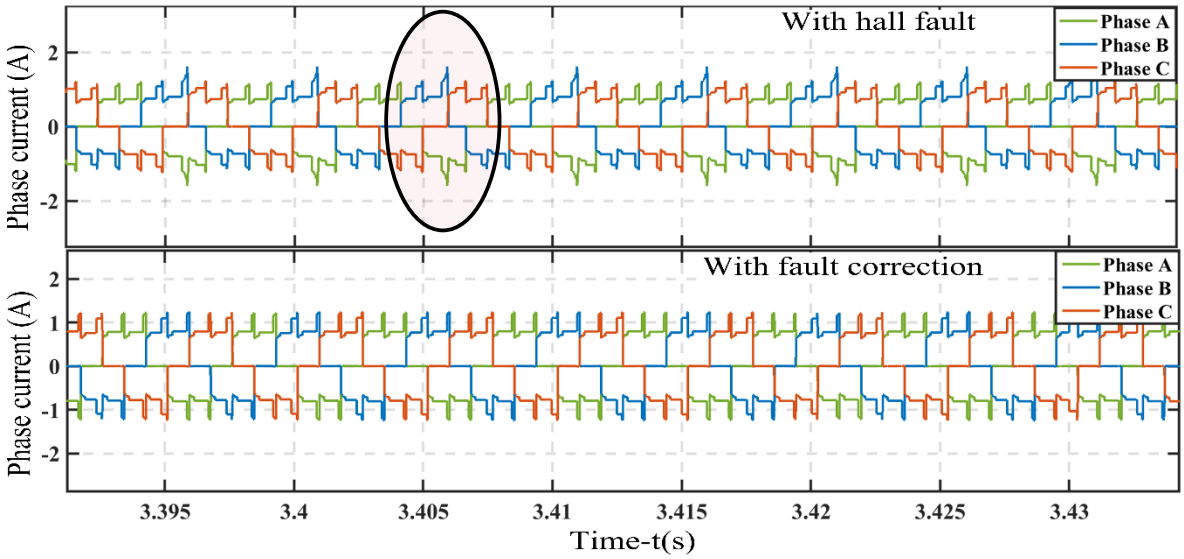

Fig. 5.13 Three phase stator current profile at step load.

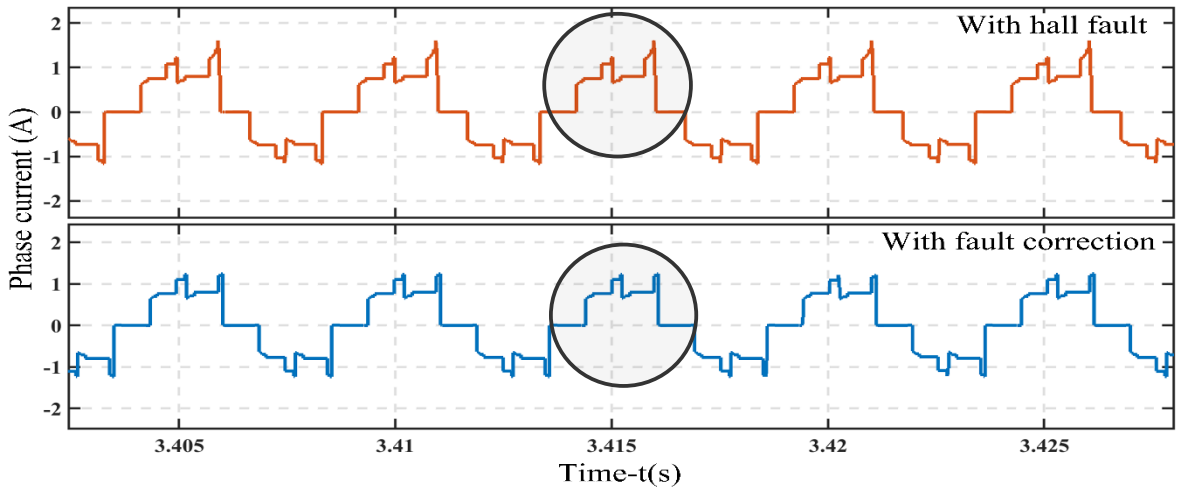

Fig. 5.14. Single phase stator current distortions at step load.

5.6 EXPERIMENTAL VALIDATION

The proposed scheme is tested using a 1 kW BLDC motor commonly used in electric autorickshaws. The motor controller is developed around a 32-bit STM32 ARM microcontroller, and the inverter switching scheme is based on 120^0 Trapezoidal commutation. The experimental test bench setup is already shown in Fig. 4.25 in chapter 4. For reference, its configuration is outlined in Table 5.3. The HES signal error is investigated for detection and identification. The motor controller response is compared in both conditions, with and without FTC implementation.

Table 5.3 Experimental setup details.

Rated Motor Parameters		**Test Bench Setup**	
Power	1 kW	DC Supply	48 V,72 Ah
Voltage	48 V	Controller	STM32301
Speed (RPM)	3000	Switching Method	120^0 Trapezoidal
Pole Pairs	4	Hall Sensors	3
Winding	3 Phase Star	PWM Frequency	16 kHz

The BLDC motor in the setup has a detected fault pattern of Case 4. The angular shifts detected for each sector in electrical degrees are presented and summarized in Table 5.4. The net average estimated value of the observed angular shift Φ_0, is 21.37°E.

The effect of these unbalanced HES signals on sectors and switching timing pattern are presented in Fig. 5.15. Sector boundaries are denoted as t_i (i=1 to 6). The high voltage side switching signals observed at the microcontroller PWM output port are shown for each phase.

The switching pattern of Fig. 5.15 leads to non-ideal voltage profiles at motor phase terminals when measured against the DC link -ve terminal as reference. Elongation of one sector and compression of the next one are observed. BEMF is abruptly cut before reaching the zero-crossing point and appears as a sudden voltage in the other phase, creating a non-ideal situation for phase current, phase voltage, and electromagnetic torque.

Table 5.4 Check table for observed angular deviation pattern.

Sector (S_i)	**S_1**	**S_2**	**S_3**	**S_4**	**S_5**	**S_6**
$\Delta\Phi_{i,}$ (^{0}E)	-21	+21.34	-21	+21.3	-22.28	+21.3
$\Delta\Phi_{i,}$ i=1,3,5	-ve		-ve		-ve	
$\Delta\Phi_{i,}$ i=2,4,6		+ve		+ve		+ve

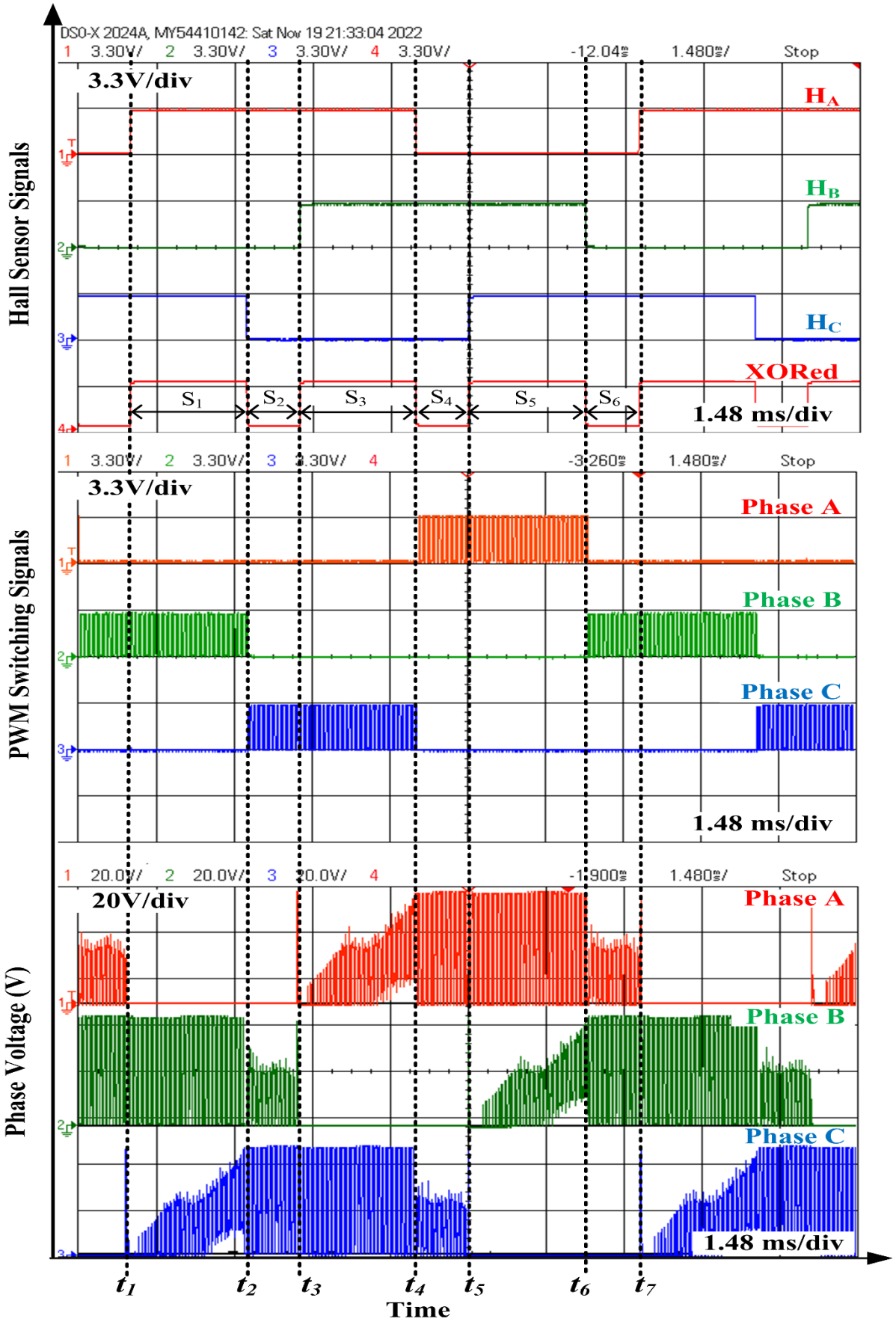

Fig. 5.15. Motor phase voltage profiles and PWM switching signals with unbalanced HES signals.

The seven instants marked as t_1 to t_7 represent the commutation instants that are according to the mistimed HES signals that are not exactly synchronized with sectoral boundaries corresponding to 60^0E span. As a result, the net sector durations are unequal as observed in Fig. 5.15. The time duration from t_1 to t_2 is not equal to the duration from t_2 to t_3. The starting sector in the first half region of each 120^0 conduction region for each phase is shortened while the next sector in the second region gets elongated automatically.

The motor phase voltage profiles with unbalanced HES signals, without any correction, are depicted in Fig. 5.16(a). In contrast, Fig. 5.16(b) illustrates the phase voltage profiles after applying the correction according to the proposed scheme. An enlarged view of the phase voltage waveforms for one complete positive conduction cycle, including the rising and falling of BEMFs up to the zero crossing points, is also provided for comparison purposes. The DC RMS and AC RMS components are measured using inbuilt DSO measurement functions, where the relations $RMS\ value^2 = [DC\ RMS^2 + AC\ RMS^2]$ and $Average\ value = (RMS\ value/1.11)$ hold true for the calculations.

In Fig. 5.16(a), the average phase voltage measures 20.29 V, whereas in Fig. 5.16(b), after implementing the proposed scheme, it rises to 21.23 V, indicating a net increase of approximately 4.6%. Furthermore, with the application of the proposed FTC scheme, the DC RMS value increases by approximately 3%, from 28.45 V to 29.3 V.

Abrupt switching of the phase voltages leads to distortions in phase currents, as depicted in Fig. 5.17(a). However, upon applying the proposed FTC method, the current profile improves significantly, as illustrated in Fig. 5.17(b). Specifically, there is an observed reduction of nearly 30% in peak-to-peak values of phase currents. Moreover, the FTC method achieves an estimated reduction of approximately 46% in the AC RMS component and a reduction of around 50% in ripple content. Peak values of phase currents are higher compared to the net current drawn from the DC battery source because peak values correspond to the sudden short duration current rise and fall over the nominal current profile envelope. Since the same hardware setup and inverter are used for all cases, these current profiles are used for performance comparison.

The DC link current profiles depicted in Fig. 5.18(a) and Fig. 5.18(b) illustrate significant improvements when employing the FTC method. Specifically, a reduction of approximately 47% in peak-to-peak current and a 13% decrease in average current are observed. Furthermore, the AC RMS is lowered by 38%, while the ripple content experiences a nearly 29% decrease. These improvements highlight the effectiveness of the FTC method in mitigating current distortions and enhancing overall performance.

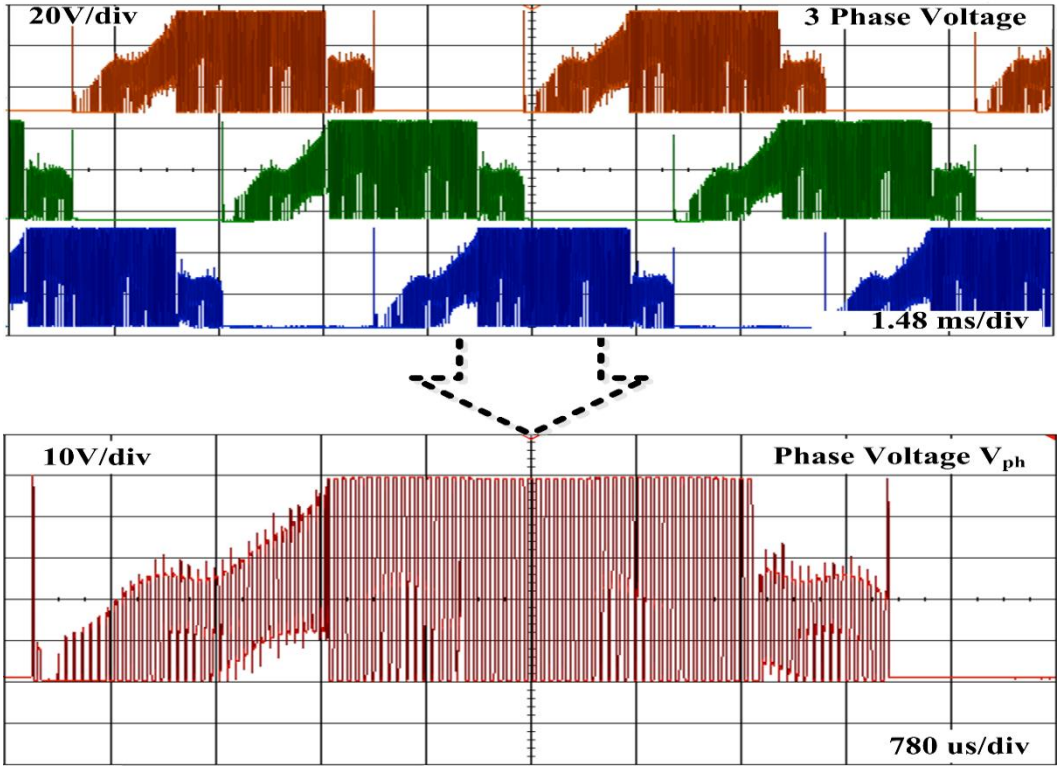

(a) Without any correction

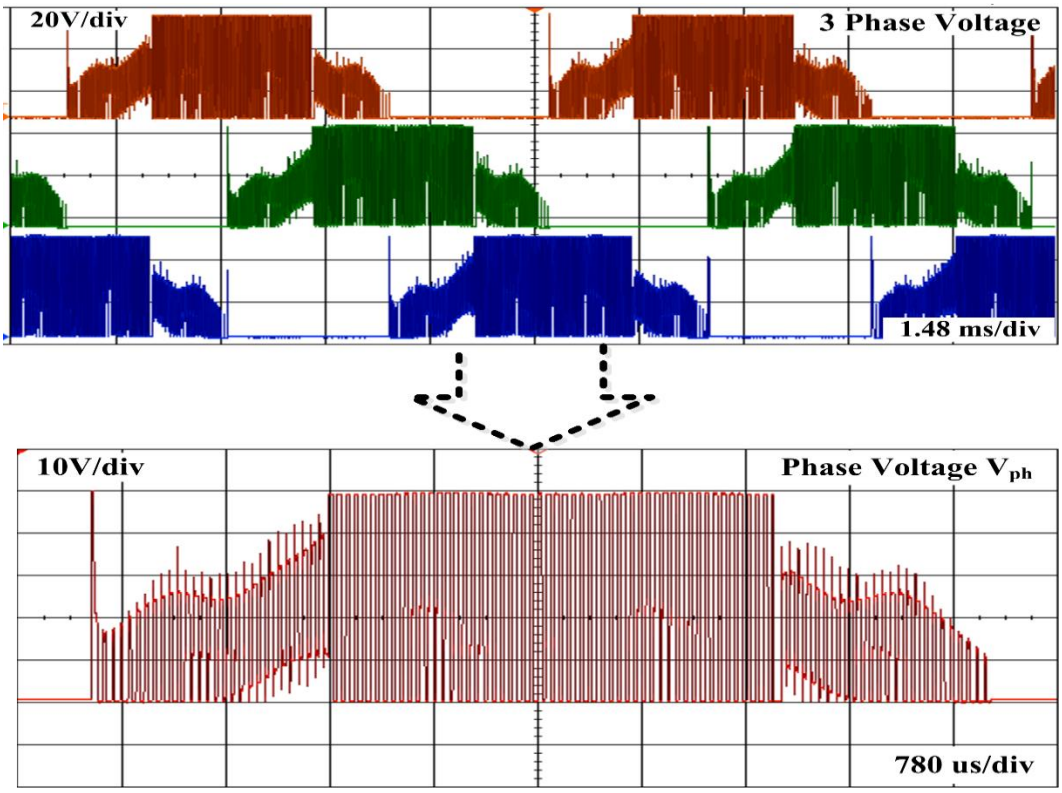

(b) With correction by proposed method

Fig. 5.16 Measured voltage profile of BLDC motor with unbalanced HES signals.

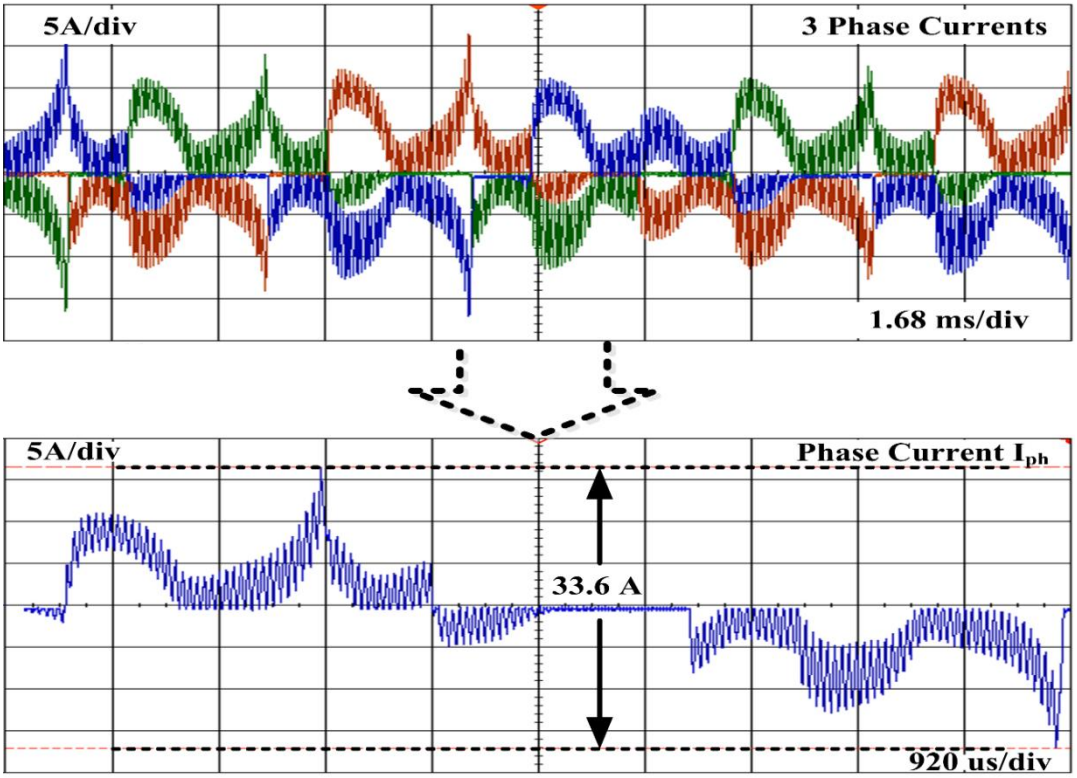

(a) Without any correction.

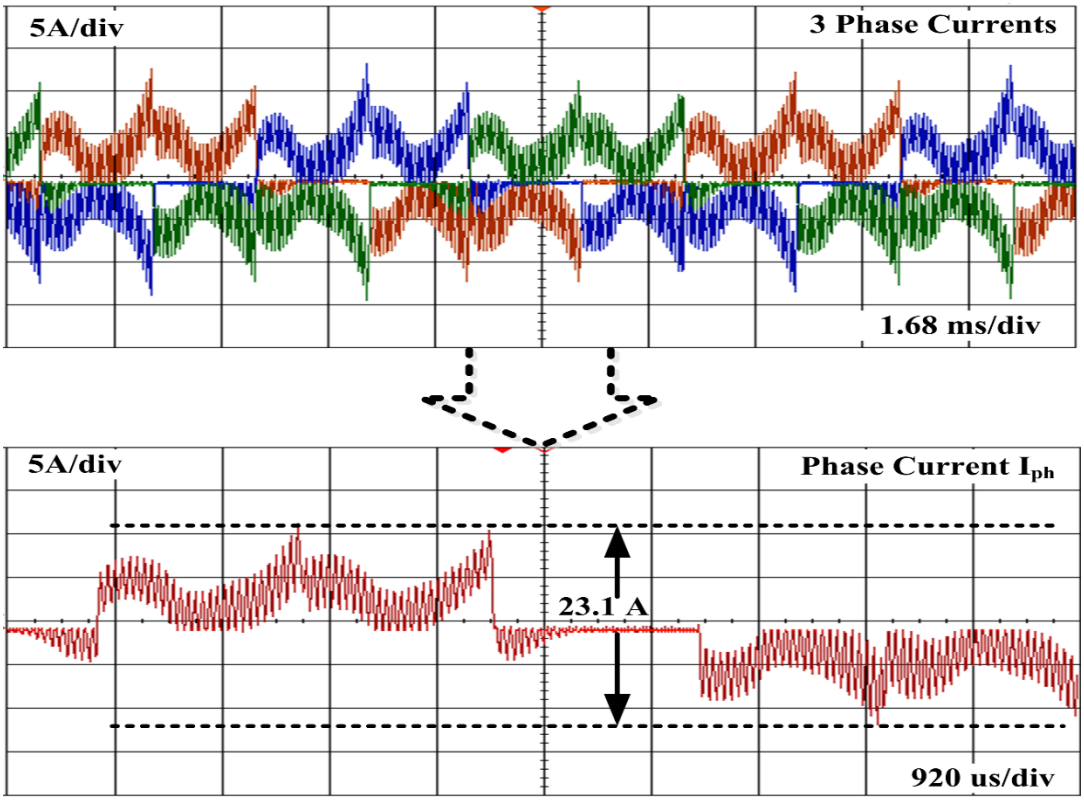

(b) With correction by proposed method

Fig. 5.17 Measured three phase and single phase current profile of BLDC motor with unbalanced HES signals.

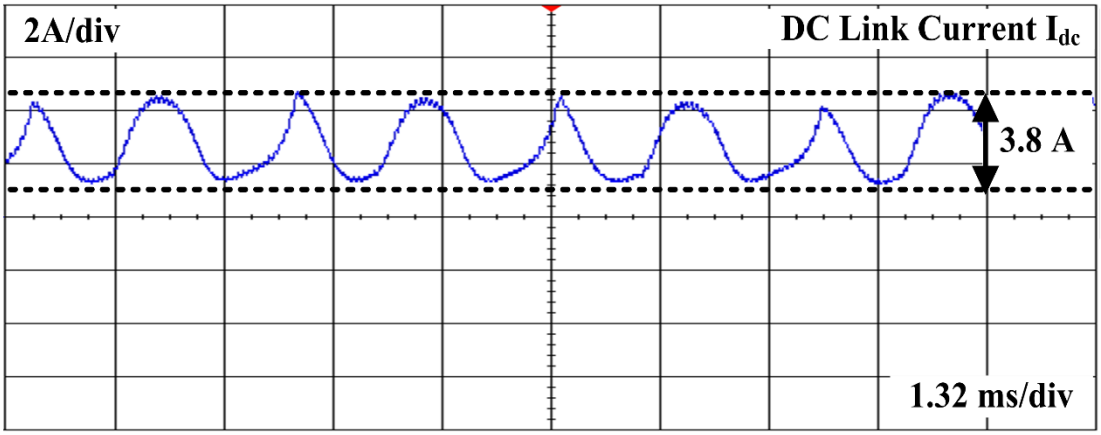

(a) Without any correction

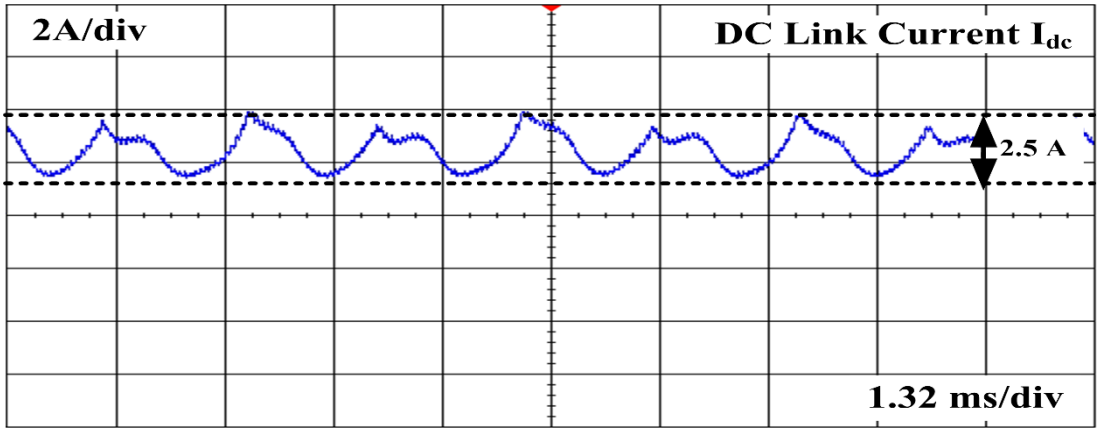

(b) With correction by proposed method

Fig. 5.18 Measured DC link current with peak-to-peak variation.

5.7 PERFORMANCE EVALUATION AND COMPARISON

The validity of the proposed scheme is further checked, and performance compared with another existing method that is applicable in the fault case. In further analysis, Method 1 refers to the proposed scheme implementation, Method 2 operation without any correction, and Method 3 pertains to the existing scheme implementation for FTC. Method 3 uses the First-order Taylor (FOT) series to estimate the electrical angle and linear interpolation based on the LSM to estimate average speed with initial angle for the next electrical period [15], [38], [105], [135]. This leads to angular correction to be re-calculated for each electrical cycle with or without changes in speed. The performance comparison is summarized in Table 5.5 for the implementation of the proposed scheme and existing method. It is observed that the proposed method has the least ripple content in both current and voltage along with the least

DC link current. Peak-to-peak DC link and phase currents are also minimum with the proposed scheme. The average phase voltage observed for Method 1 is 21.23 V while it is 20.29 V and 15.61 V respectively for Method 2 and Method 3. The corresponding measured DC RMS voltage is 29.3 V, 28.5 V, and 23.44 V for Method 1, Method 2, and Method 3 respectively. This is due to adjustments in durations of 120° conduction periods in Method 1 as shown in Fig. 5.16. Further, abrupt ending of BEMF rising and falling sections is also reduced in Method 1, thus improving the average and DC component in the phase voltage.

Table 5.5 Controller implementation comparison.

	Phase Current (A)			**DC Link Current (A)**			**Phase Voltage (V)**		
	Method 1	Method 2	Method 3	Method 1	Method 2	Method 3	Method 1	Method 2	Method 3
Peak to Peak	23.1	32.8	42.27	2.5	3.8	4.10	49	49	49
Average	4.150	16.5	0.89	2.401	2.655	2.64	21.23	20.29	15.61
DC RMS	4.8	4.47	5.38	2.5	2.87	2.59	29.3	28.5	23.44
AC RMS	2.398	4.46	5.28	0.667	1.079	1.06	20.3	19.99	17.75
Ripples	49.95%	98.9%	98%	26.68%	37.59%	40.88%	69.28%	70.14%	75.70%

The memory loading in STM32 Microcontroller implementation is compared in Table 5.6. Memory usage and loading values are obtained from IAR software development platform for STM32 ARM controller. Additional memory required using proposed Method 1 is approximately 25% more as compared to Method 2. However, only 24% of it is used for continuously repetitive calculations in the controller, and most of the calculations are handled during the start of the controller, which leads to single execution controller load part to nearly 76%. Method 3 has a similar additional memory requirement of 26%, but it requires more repetitive computational effort as compared to the proposed method.

Table 5.6 Memory utilization comparison.

Method	**Memory (bytes)**	**Extra memory required**	**Repetitive execution part (%)**	**Single execution part (%)**
1	23,601	4,676	24	76
2	18,925	0	0	0
3	23,897	4,972	64.3	35.7

Further comparisons at 30% and 100% loading of the motor are summarized in Table 5.7 and Table 5.8 respectively. The DC link supply current ripple content is minimum in all conditions with the proposed method. It is reduced by 20% at 30% load, and by 12% at full load condition. This is on the expected lines for a BLDC motor at full load during stable operating conditions. DC RMS current is also minimal for the proposed method.

Table 5.7 Experimental result comparison at 30% load.

	Phase Current (A)			**DC Link Current (A)**			**Phase Voltage (V)**		
	Method 1	Method 2	Method 3	Method 1	Method 2	Method 3	Method 1	Method 2	Method 3
Peak to Peak	52	72	74	10.1	8.4	14.1	50	50	50
Average	0.14	0.19	0.37	19.71	20.21	19.82	25.98	23.4	23.28
DC RMS	16.8	16.6	16.8	19.6	20.3	20.0	32.4	30.5	30.6
AC RMS	16.8	16.6	16.8	1.75	1.89	2.41	19.34	19.54	19.84
Ripples	100%	100%	100%	8.93%	9.3 %	12.06%	59.69%	64.06%	64.84%

Table 5.8 Experimental result comparison at 100% load.

	Phase Current (A)			**DC Link Current (A)**			**Phase Voltage (V)**		
	Method 1	Method 2	Method 3	Method 1	Method 2	Method 3	Method 1	Method 2	Method 3
Peak to Peak	52	72	74	10.1	8.4	14.1	50	50	50
Average	0.14	0.19	0.37	19.71	20.21	19.82	25.98	23.4	23.28
DC RMS	16.8	16.6	16.8	19.6	20.3	20.0	32.4	30.5	30.6
AC RMS	16.8	16.6	16.8	1.75	1.89	2.41	19.34	19.54	19.84
Ripples	100%	100%	100%	8.93%	9.31%	12.06	59.69%	64.06%	64.8 %

Mechanical speed waveforms are estimated from the digital oscilloscope data and, are graphically filtered for the speed curve results presented in Fig. 5.19 and Fig. 5.20. Figure 5.19 shows the full range speed ramp curves and Fig. 5.20 shows speed curves with sudden load application for evaluating the transient response of all three methods. Figure 5.19(a) shows the speed ramp curve for 30% load condition and Fig. 5.19(b) for 100% load.

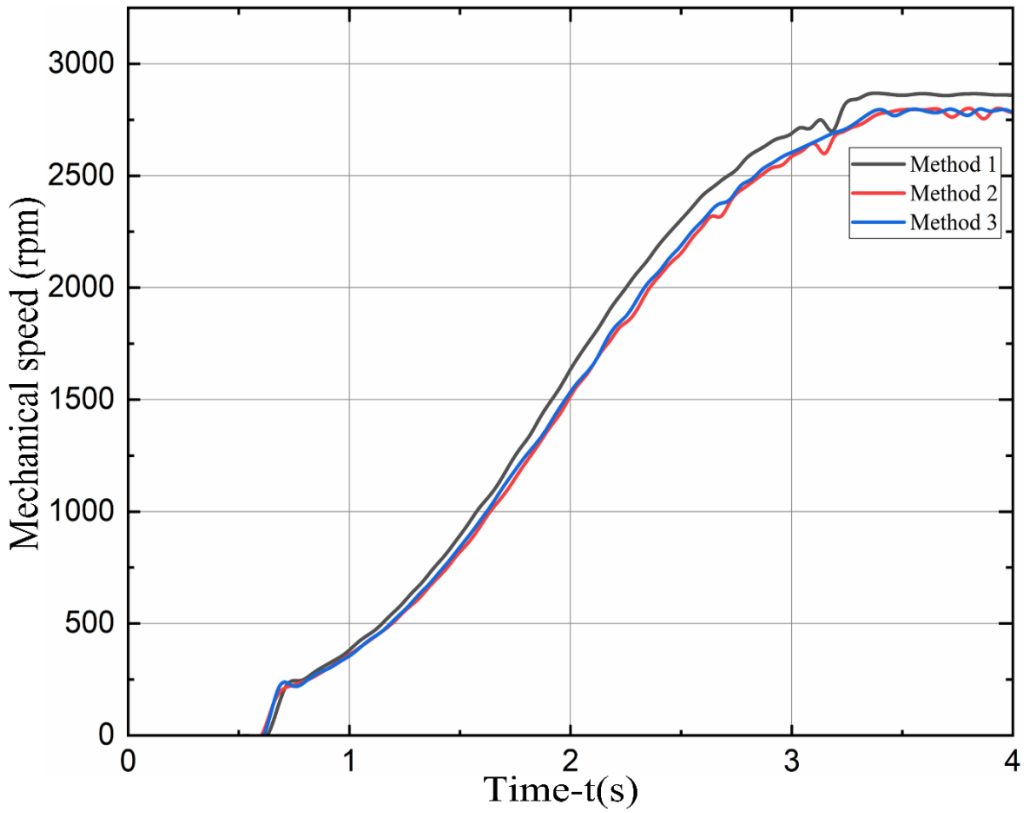

(a) 30% loading

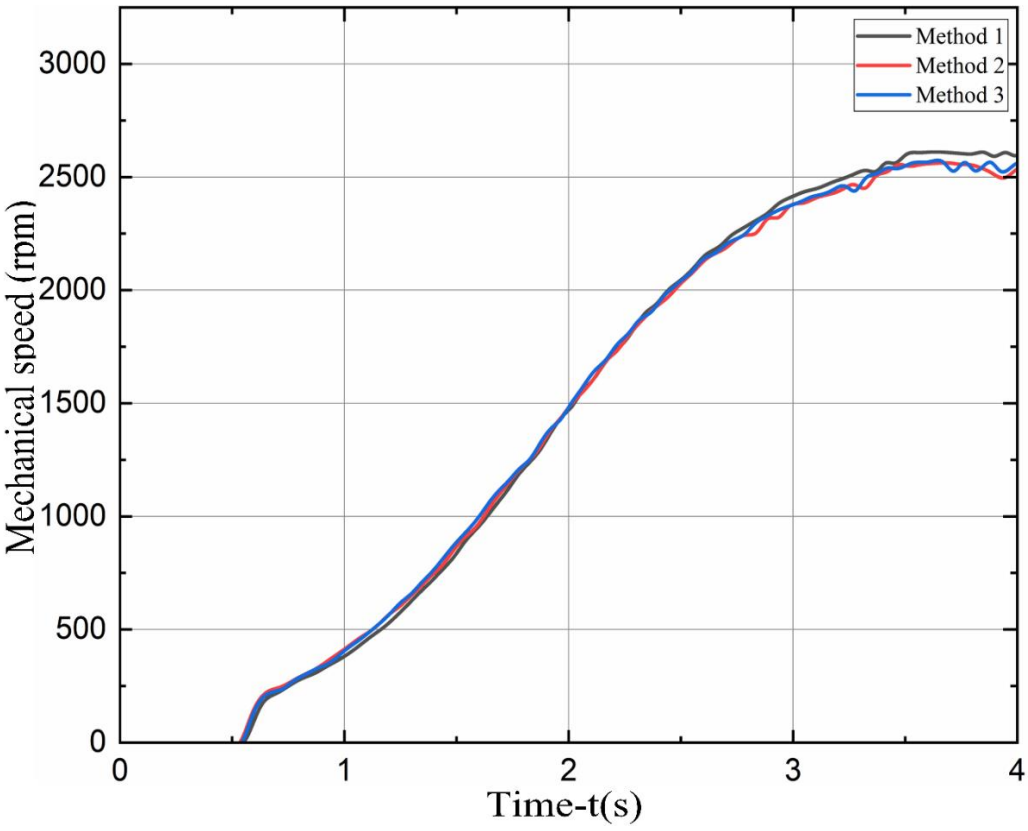

(b) 100% loading

Fig. 5.19. Estimated mechanical speed curves for all three methods.

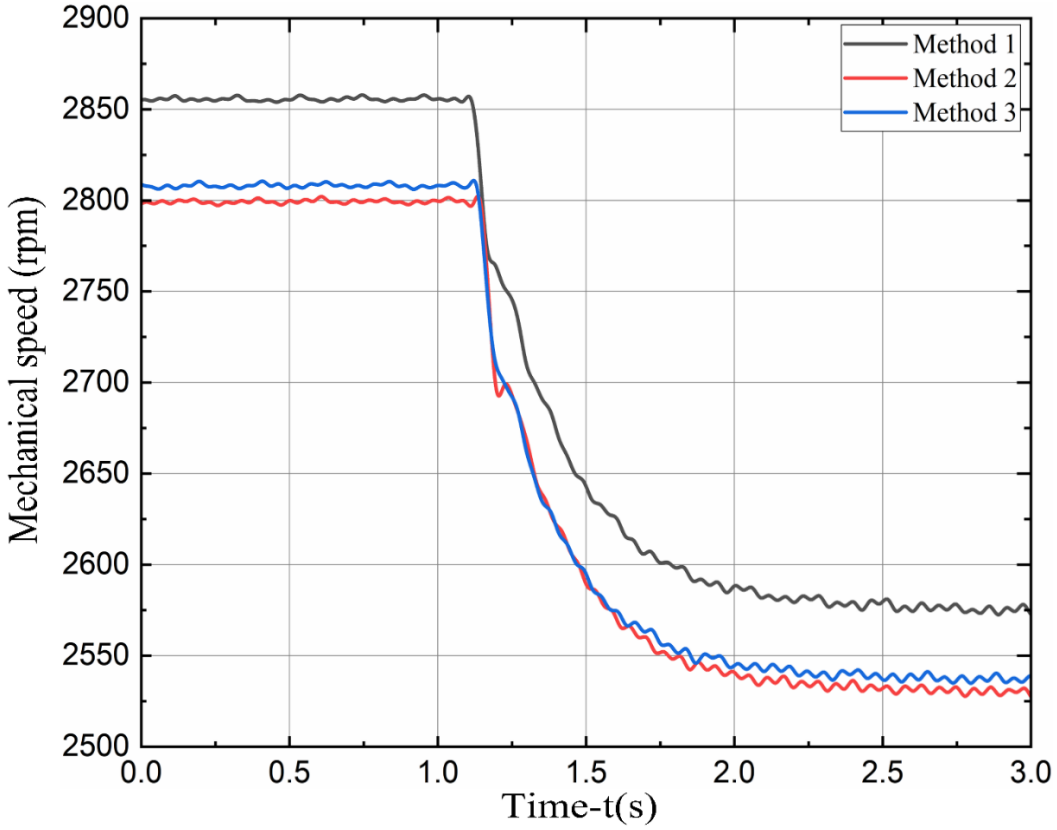

(a) Full speed change profile

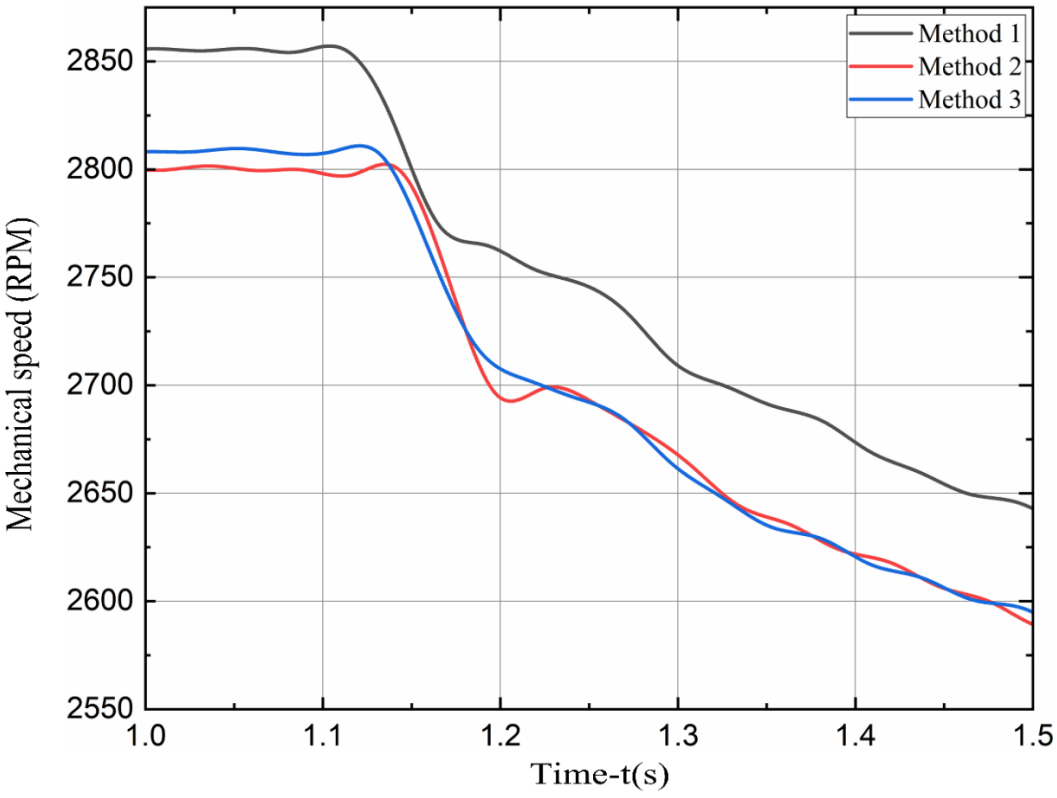

(b) Transient response.

Fig. 5.20. Estimated mechanical speed curves with sudden load application.

The motor speed ramping starts after initial boundary condition checks and bootstrapping in the controller, with initial push at t=0.6 second. It's evident that Method 1 achieves a more accurate steady-state speed compared to the other two methods. At a 30% load condition, the final speed difference between Method 1 and Method 2 is observed as 60 RPM, and at full load, it's observed as 50 RPM. The transient response of the system is assessed using all three methods by imposing a sudden full load on the drive operating at rated speed. The estimated speed curves are shown in Fig. 5.20(a) and Fig. 5.20(b). In Method 1, a nearly steady decline in speed begins around t = 1.25s. Method 2 exhibits a more pronounced speed dip around t = 1.2s. Notably, Method 1 demonstrates the quickest approach to achieving a steady slope of speed decrease, as depicted in Fig. 5.20(b).

5.8 CONCLUDING REMARKS

The scheme for controlling the effects of unbalanced HES signals in BLDC motor drives is presented in this chapter. The complete FTC scheme, its integration in the controller and, comparison results with another method applicable in the same type of faults are discussed in detail. Simulation studies and experimental tests conducted on a test bench with a 48 V, 1 kW BLDC motor verify the proposed detection and estimation method. Results indicate improvements in motor phase current, phase voltage, and DC link current profiles with reduced peak-to-peak values. The ripple content in stator phase and DC link currents at different loads are also found to be significantly reduced with application of the proposed scheme. Additionally, the proposed scheme imposes less additional memory loading compared to another scheme that is based on the method of LSM of error in speed estimation.

The efficiency and torque per ampere are compared among the three methods of operation. Method 2, without any FTC, is taken as the base and values are normalized to 1 unit. Other values are presented in comparison to the base values and presented in Table 5.9.

Table 5.9 Normalized efficiency and torque per amper.

	Efficiency Scaling			**Normalized Torque / Ampere**		
Method	**1**	**2**	**3**	**1**	**2**	**3**
100% Load	1.008	1	0.96	1.025	1	0.99
30% Load	1.015	1	0.93	1.014	1	0.95
No load- 50% PWM Duty	1.022	1	0.91	1.096	1	0.94

The proposed scheme of Method 1 exhibits the highest efficiency, with an increment ranging from 0.8% to 2.2%, and nominal torque/ampere increment varying from 2% to 9%. Further combined performance comparison among all three methods is summarized in the radar diagrams of Fig. 5.21.

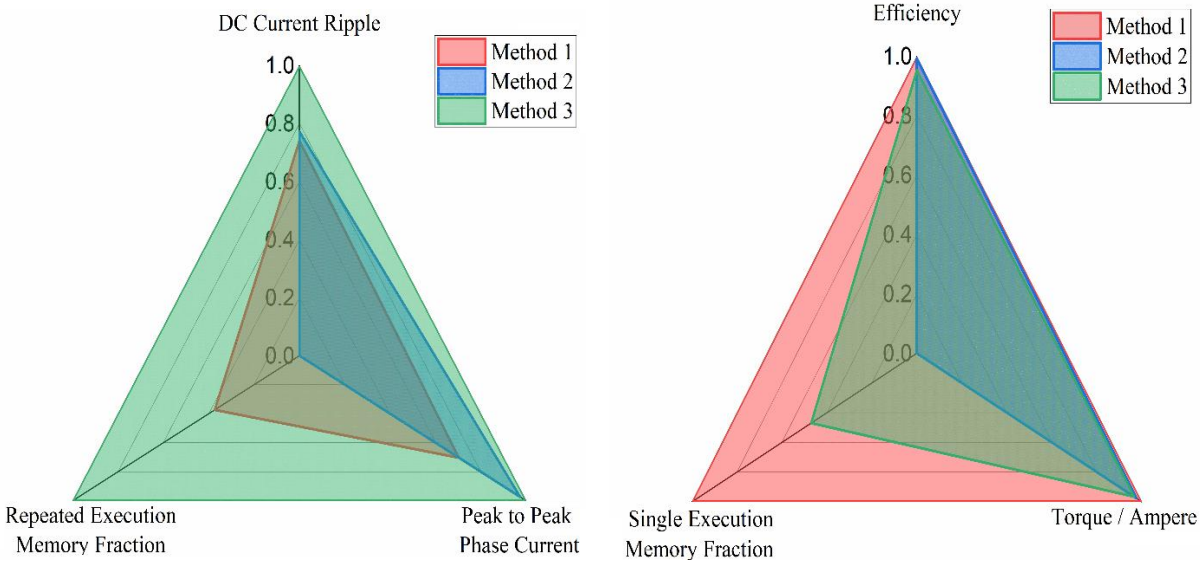

(a) Minimum value parameters (b) Maximum value parameters.

Fig. 5.21. Per-unit radar diagram for experimental result comparison at steady state.

Figure 5.21(a) presents the radar diagram for combined comparison based on the phase current, DC current ripple, and memory execution as parameters. The proposed method has the minimum area and represents the optimum strategy to achieve the best performance level. In Fig. 5.21(b), the radar diagram for combined comparison is based on the efficiency and torque per ampere parameters. Proposed Method 1, with the maximum area, again represents the optimum strategy based on the selected parameters.

An important outcome of this FTC mechanism is the reduced heating of the controller and fewer battery discharge/charge cycles due to the reduction in peak-to-peak and RMS values of phase and DC link currents. This contributes to better efficiency of the motor controller system and increases the possibility of battery life enhancement with better power utilization without the need for additional hardware costs.

The proposed scheme may find utility in automotive applications such as two-wheelers and e-rickshaws, which are cost sensitive, as well as in other applications where controller circuit modification for HES signal faults is not feasible.

CHAPTER 6

DC LINK CURRENT BASED COMMUTATION DELAY COMPENSATION METHOD IN BLDC MOTOR DRIVES

6.1 INTRODUCTION

The accurate rotor position detection using HES signals is an essential requirement for precise BLDC motor control in sensored mode of operation. The inverter switching timings and commutation instants of the BLDC motor drive essentially rely on these signals. The HES signals are synchronized with motor's BEMF profile which is indicative of varying rotor position and speed of rotation. Therefore, any delay between actual rotor position and corresponding HES signals results in disruption of synchronization between inverter switching timings and corresponding ideal switching instants [16], [120]. This loss of synchronization has detrimental effects on the drive performance and effectively renders the drive as non-optimal solution. The motor performance is adversely affected with increase in phase currents and reduction in efficiency. Traditional methods for addressing the issues of these delays include implementation of phase advancing schemes and hardware modifications in the drive circuits [38], [147].

This chapter delves into the commutation delays observed in sensored BLDC motor drives resulting from unbalanced HES signals. A novel method for estimating the commutation delays in electrical degrees using only the DC link current is proposed. It is based on a direct error approximation relation between switching signal delays and DC link supply current. Once estimated, these error values can be compensated in the further drive operations as fixed angular compensations to minimize the fault effect. The method provides a practical approach to address the switching delay issue with an easy to implement scheme in the existing controller without necessitating additional hardware changes.

The proposed method is validated through MATLAB Simulink models for two motors with different values of switching delay angles. It is further tested on an experimental test bench featuring a controller and a 1 kW BLDC motor of an e-rickshaw. The tests are carried under various load conditions. Simulation and hardware test results demonstrate that the mean estimated commutation delay falls within ±1° electrical degrees of the actual value across different error and load conditions. The incorporated corrections based on these estimated delay angles lead to reduction in peak-to-peak DC link current, increase in nominal torque generated per ampere, and decrease in DC current ripple content. Both simulation and

experimental results confirm the effectiveness of the proposed method in estimating and mitigating the effects of the commutation delay.

6.2 COMMUTATION DELAY IN BLDC MOTOR DRIVES

The commutation delay errors consist of both fixed and variable components, influenced by factors such as switching frequencies, sudden load changes, and control algorithm implementation. The fixed error component is the most prominent one in commutation delays and it can be caused by several factors, including [127], [148]:

1. HES Mounting Issues: Issues related to HES positioning or mounting slot alignment within the motor can lead to delayed HES signals. Even minor spatial deviations can result in significant errors in commutation instants in terms of electrical degrees. The effect gets more pronounced as the number of pole pairs in BLDC motor increase.

2. Aging: Over time, components within the HES system, such as sensors may degrade, leading to delayed signal detection by the controller. This factor can exacerbate the timing discrepancies and contribute to the fixed delay in commutation instants.

3. Failure or Degradation of HES Signal Filters: If the components responsible for filtering HES signals degrade or fail, it can lead to delays in signal detection at the controller inputs. This further results in delay in commutation switching instants.

Ensuring smooth system operation in drives with commutation delay requires fault mitigation methods that are easy to integrate with existing controller structures and control schemes. Addressing these factors is crucial for ensuring the accurate synchronization of commutation signals with the motor's BEMF profile, essential for optimizing system performance and efficiency Controllers in HES based applications employ various current measurement schemes for operation and keeping a check on drive parameters [117]-[118]. Continuous measurement of three phase currents is a common method, where ZCD points of the phase currents are utilized for operation, synchronization, and fault detection. Some schemes utilize the neutral point or create a virtual neutral point of the motor winding circuit to estimate the BEMF profile and ZCD of the BEMF for controlling commutation signal timings. Fault detection and switching synchronization rely on these ZCD points [125]. However, ZCD based methods may suffer from commutation interference pulses, which can degrade motor performance. To mitigate this issue, low pass filters (LPF) are often added in the drive circuitry. Implementing such schemes requires precise resistors and multistage filters, which can further introduce significant commutation delays. These delays can lead to performance degradation in the drive, resulting in increased levels of motor vibration and

audible noise [121]-[122]. Therefore, it's essential to carefully design and optimize the control schemes to minimize these types of drawbacks and ensure smooth operation of the BLDC motor drive system.

There are various difficulties and challenges in addressing these errors in mass scale produced motors for cost sensitive applications, where the scope of hardware modifications is quite limited. There are several such applications that rely on DC link current measurement and HES signals for complete control and drive operation. These types of applications can benefit from estimating commutation delay angles based on the DC link current profile. This method offers advantages, especially in scenarios where phase current measurement or BEMF estimation is not feasible or practical in the application. Therefore, it is advantageous to estimate commutation delay angles based on the DC link current profile to mitigate performance degradation in sensored BLDC motor applications [149]-[152].

6.3 COMMUTATION DELAY ANALYSIS AND ESTIMATION SCHEME

The equivalent circuit of sensored BLDC motor drive with three phase inverter has already been discussed in chapter 3 with Fig. 3.1 and commutation sequence in Table 3.1. However, for easier referencing and with neutral point inclusion in the further analysis, the circuit has been presented in Figure 6.1. The electrical cycle, spanning 360°E, is divided into six angular sectors with spans denoted as S_i (i= 1 to 6). Each sector can be mapped to a specific combination of binary output signals from the HESs, providing six valid signal combinations within the 360°E span. The inverter's switching sequence is synchronized with the six transition signals generated by the HESs.

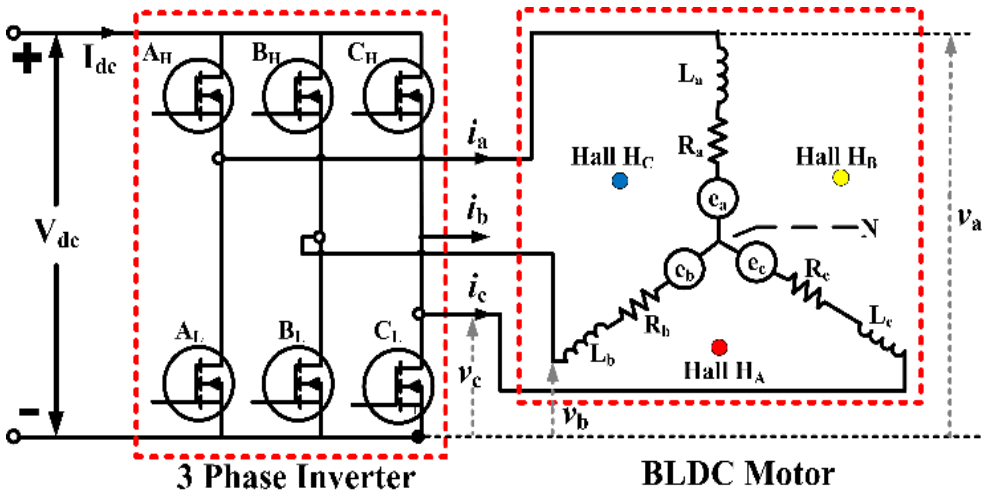

Fig. 6.1 Equivalent circuit of sensored BLDC motor drive with three phase inverter.

The circuit diagram in Fig. 6.1 depicts a three-phase star-connected stator winding BLDC motor without an external neutral point denoted by 'N'. The phase resistances and inductances are symbolized by R_a, R_b, R_c and L_a, L_b, L_c respectively. The HESs are denoted by H_A, H_B and H_C. Furthermore, e_a, e_b and e_c represent the back EMF of phases A, B, and C respectively. The neutral point voltage is represented by v_n. The high voltage side switches of the inverter are represented by A_H, B_H, and C_H, while A_L, B_L, and C_L denote the low voltage side switches. V_{dc} and I_{dc} denote the applied DC link voltage and current respectively. The symmetrical winding configuration phase parameters satisfy $R_a = R_b = R_c = R$ and $L_a = L_b = L_c = L$, where R and L are the equivalent phase resistance and inductance respectively, including the effect of mutual inductances. The three-phase voltages with respect to the DC link's negative terminal are denoted as v_a, v_b, and v_c, while the phase currents are denoted as i_a, i_b, and i_c respectively. T_e represents the electromagnetic torque, ω is the rotor angular velocity, T_l stands for the load torque, J is the moment of inertia of the rotor, and B is the viscous friction coefficient.

The voltage and current equation for the configuration in Fig. 6.1 can be mathematically expressed as [122], [125]:

$$v_a = Ri_a + L\frac{di_a}{dt} + e_a + v_n$$

$$v_b = Ri_b + L\frac{di_b}{dt} + e_b + v_n$$

$$v_c = Ri_c + L\frac{di_c}{dt} + e_c + v_n \quad (6.1)$$

The corresponding electromagnetic torque and phase current relation is:

$$T_e = \frac{e_a i_a + e_b i_b + e_c i_c}{\omega}$$

$$T_e\omega = e_a i_a + e_b i_b + e_c i_c \quad (6.2)$$

The motor mechanical motion equations in terms of torque and loading are:

$$T_e = T_l + J\frac{d\omega}{dt} + B\omega \quad (6.3)$$

$$T_e\omega = T_l\omega + J\omega\frac{d\omega}{dt} + B\omega^2 \quad (6.4)$$

Equation (6.4) represents the electromagnetic power developed, which is equivalent to the electromagnetic power expressed in terms of phase current and BEMF profile in equation (6.2). Assuming that the efficiency of the motor and controller set remains constant under constant speed and constant load operation, the relationship between torque and efficiency can be expressed as Eqn. (6.5), where η represents the combined system efficiency.

$$T_e\omega = \eta(V_{dc} * I_{dc}) \quad (6.5)$$

During non-ideal conditions where the commutation timing at the end of the 60^0E sector is delayed, the phase current in two conducting phases undergoes a sharp increase in peak value before actual commutation. Consequently, there is a sharp rise in the corresponding DC link current peak value, as illustrated in Fig. 6.2.

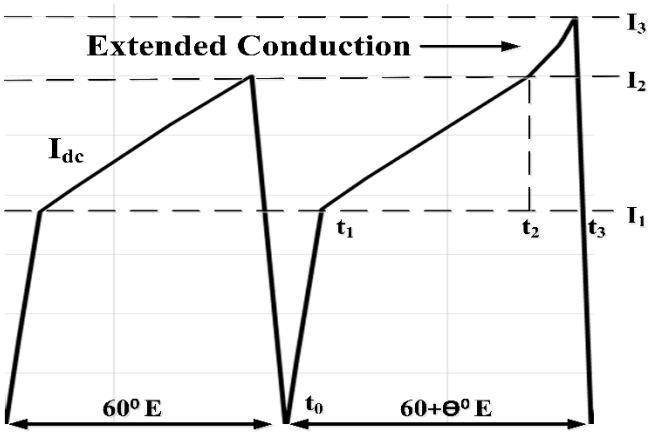

Fig. 6.2 DC link current during extended conduction.

The sharp increase in DC link current affects the commutation torque ripple reduction schemes due to the non-ideal relation between BEMF profile and switching signals. As a result, there is current warping before the actual turn off, leading to an increase in torque ripples [38]. During the time from t_0 to t_1 in Fig. 6.2, the DC link current rises to the commutation end value; from t_1 to t_2 it rises in synch with the conducting phase current; and from t_2 to t_3 extended conduction occurs due to the delayed commutation. Denoting the commutation switching delay as θ in electrical radians, and the peak values of the phase BEMF and phase current as E_P and I_P respectively, the electromagnetic torque can be expressed as a function of θ. Assuming the constant rotor velocity in Eqn. (6.3), the following relation can be obtained:

$$T_e'\omega = E_P I_P + \left(-E_P + \frac{E_p}{\pi/6} * \theta\right) \times (-I_P) + (-E_P * 0)$$

$$= E_P I_P + E_P I_P - \left(\frac{E_p}{\pi/6} * \theta\right)$$

$$T_e' = \frac{1}{\omega} * E_P I_P \left(2 - \frac{\theta}{\pi/6}\right) \quad [0 \leq \theta \leq \pi/6] \tag{6.6}$$

The error θ is assumed to be within the practical limits of the BEMF zero crossing points. Equation (6.6) is also valid for the angle advancement of θ, where $0 \leq -\theta \leq \pi/6$ holds true. During ideally timed commutation switching, $\theta = 0$ and using expression in (6.6) the torque

developed is given as:

$$T_e = \frac{1}{\omega} * 2E_P I_P \tag{6.7}$$

Hence, $T_e' < T_e$ since $\frac{1}{\omega} * 2E_P I_P > \frac{1}{\omega} * E_P I_P \left(2 - \frac{\theta}{\pi/6}\right)$.

The difference between T_e and T_e' increases when the value of θ increases. Thus, to maintain the torque value and speed, $I_P$increases with θ, which causes a sharp increase in the I_{dc} peak value. If phases A and B are conducting during the extended conduction period from t_2 to t_3, then $I_{dc} = i_a = - i_b = I$ and $i_c = 0$ in Fig. 1 circuit. Using KVL in the circuit:

$$V_{dc} = E\left(2 - \frac{\theta}{\pi/6}\right) + 2IR + 2L\frac{dI}{dt} \tag{6.8}$$

$$\frac{1}{L}\left(\frac{V_{dc}}{2} - E\right) + \left(\frac{E}{2L} * \frac{\theta}{\pi/6}\right) = I\left(\frac{R}{L}\right) + \frac{dI}{dt} \tag{6.9}$$

Differentiating Eqn. (6.9) yields:

$$\frac{E}{2L} * \frac{1}{\pi/6} * \frac{d\theta}{dt} = \frac{R}{L} * \frac{dI}{dt} + \frac{d^2I}{dt^2} \tag{6.10}$$

Using $\frac{dI}{dt}$ from Eqn. (6.9) results in:

$$\frac{E}{2L} * \frac{1}{\pi/6} * \frac{d\theta}{dt} = \frac{d^2I}{dt^2} - \frac{R^2}{L^2} I + \left(\frac{V_{dc}}{2} - E\right)\frac{R}{L^2} + \frac{R\,E}{2L^2} * \frac{\theta}{\pi/6} \tag{6.11}$$

$$\left(\frac{E}{2L} * \frac{1}{\pi/6}\right)\frac{d\theta}{dt} + \frac{R\,E}{2L^2} * \frac{\theta}{\pi/6} - \left(\frac{V_{dc}}{2} - E\right)\frac{R}{L^2} = \frac{d^2I}{dt^2} - \frac{R^2}{L^2} I \tag{6.12}$$

Equation (6.12) is a combined 2nd order differential equation in terms of I involving the 1st order differential terms of θ, which is computationally difficult to implement in the controllers and requires known initial values of both I and θ to obtain a solution. Furthermore, if the short-term speed variations in ω at the 60°E sector end are considered, the $\frac{d\theta}{dt}$ term itself is variable, making it difficult to even approximate the relation between I and θ. However, using Eqn. (6.4) and Eqn. (6.5), the total power P_e at the DC source supply end can be represented as:

$$P_e = \eta(V_{dc} * I_{dc}) \tag{6.13}$$

$$\frac{dP_e}{dt} = \eta * V_{dc} * \frac{dI_{dc}}{dt} \tag{6.14}$$

$$\frac{dP_e}{dt} = \frac{d}{dt}(T_l\omega + J\omega\frac{d\omega}{dt} + B\omega^2) \tag{6.15}$$

$$\frac{dP_e}{dt} = T_l\frac{d\omega}{dt} + J\left(\frac{d\omega}{dt}\right)^2 + J\omega\frac{d^2\omega}{dt^2} + 2B\omega\frac{d\omega}{dt} \tag{6.16}$$

Using the relations of Eqn. (6.14) and Eqn. (6.16):

$$\eta * V_{dc} * \frac{dI_{dc}}{dt} = T_l\frac{d\omega}{dt} + J\left(\frac{d\omega}{dt}\right)^2 + J\omega\frac{d^2\omega}{dt^2} + 2B\omega\frac{d\omega}{dt} \tag{6.17}$$

$$\frac{dI_{dc}}{dt} = \frac{1}{\eta * V_{dC}} \left[\left(2B \frac{d\omega}{dt} + J \frac{d^2\omega}{dt^2} \right) \omega + \left(T_l \frac{d\omega}{dt} + J \left(\frac{d\omega}{dt} \right)^2 \right) \right] \quad (6.18)$$

The average rotor speed variation $\frac{d\omega}{dt}$ during the time interval from t_2 to t_3, as shown in Fig. 6.3, can be treated as $\frac{\Delta\omega}{\Delta t}$ at a fixed load and taken as constant for estimation purposes. Thus, the average rate of variation of the DC link current during the extended conduction period can be related to the speed as:

$$\frac{\Delta I_{dc}}{\Delta t} = m * \omega_m + c \quad (6.19)$$

In HES based sensored BLDC drives, the automatic reference timing signals are obtained at 60°E intervals for speed calculation while in between values, if needed, are based on the interpolation or complex estimation methods. Therefore, measuring $\frac{d\omega}{dt}$ in the sub periods of t_2 to t_3 is practically difficult in microcontroller implementation. Hence relating it to DC link current is simple and easier for controller implementation since DC current is continuously measured and filtered for operation and boundary condition checks in controller.

6.4 IMPLEMENTATION OF THE ESTIMATION SCHEME IN CONTROLLER

The proposed scheme is designed to be implemented without requiring any changes to the hardware circuit or state machine model of the controller. This ensures compatibility and ease of integration with the existing systems. It aims to simplify commutation error correction and is designed for execution during the motor controller integration process. By estimating errors during this integration phase, the commutation timing corrections can be adjusted during the subsequent motor operations. This maintains the overall performance and reliability of the motor drive system. Equation (6.19) forms the basis of this method to estimate the commutation delay angle in practical applications, even if the motor parameters are unknown. The block diagram of controller design incorporating the proposed DC link current based commutation delay is shown in Fig. 6.3.

The parameters used in the approximation process can be estimated by running a check routine along with other diagnostic routines during the motor controller integration process. By running the motor at a constant load and a stable speed, the abrupt sharp increase in the DC link current can be observed until it reaches its peak value. This time duration can be estimated using the available timers in the microcontroller. The motor speed can be increased and made stable in steps to obtain multiple observation sets at the single load setting. Final estimation is obtained by linear approximation and averaging of the obtained values at different observation sets.

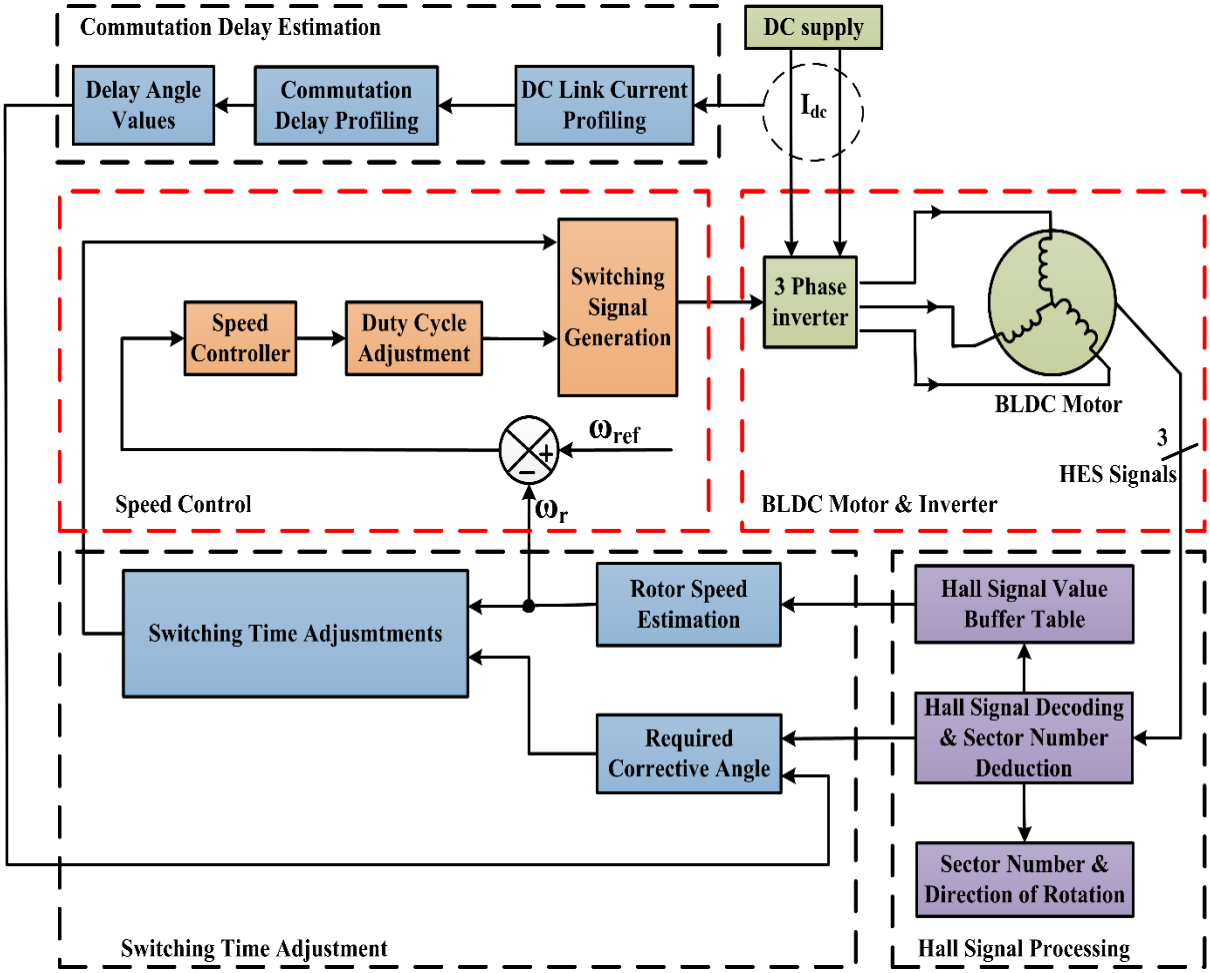

Fig. 6.3 BLDC motor controller with detection and correction of commutation delay using DC link supply current.

6.5 SIMULATION RESULTS AND ANALYSIS

Simulation analysis using a MATLAB Simulink model is carried out to validate the proposed method of relating DC link current with commutation delay using two different BLDC motors of 4 pole pairs, 3 HESs and speed of 2800 RPM. Motor M1 is rated 300 V, 0.9 kW and has phase resistance R of 2.8750 Ω. It has phase and mutual inductances of 8.5 mH and 0.01 mH respectively, flux linkage of 0.175Wb and rotor inertia J of $8x10^{-3}$ Kgm^2. Motor M2 is rated 48 V, 1 kW and has phase resistance R of 0.030 Ω. It has an equivalent phase inductance of 55 uH, flux linkage of 0.021 Wb, and rotor inertia J of $8x10^{-3}$ Kgm^2.

Three commutation delays equivalent to 10°E, 15°E and 22°E are implemented, and $\frac{\Delta I_{dc}}{\Delta t}$ is checked under rated load condition. Figure 6.4 shows I_{dc} for motor M1 with the highlighted part showing the extended conduction due to a delayed commutation that is equal to 15°E in one of the six switching signals shown by the red colored transitions. The actual and estimated delay angle values are presented in Table 6.1.

The resulting graph in Fig. 6.5(a) shows the relation between $\frac{\Delta I_{dc}}{\Delta t}$ and the mechanical speed ω_m is shown in Fig. 6.5(b) for both motors. It is observed to be nearly linear for both motors. Thus, a linear approximation according to Eqn. (6.19) can be used between $\frac{\Delta I_{dc}}{\Delta t}$ and the rotor speed ω_m.

When the linear relation is used to estimate Δt and the final delay angle θ, the graphical comparison of the resulting actual and estimated delay values is presented in Fig. 6.6(a) for motor M1 and for motor M2 in Fig. 6.6(b). It can be observed that the error between the actual and estimated θ lies between ±1°E for most parts of the curves in Fig. 6.6 at different speeds and error except for 1 observational point for each motor. Thus, providing a fairly accurate estimation of the delay angle.

Table 6.1 Actual and estimated delay angle values in simulation.

	Motor M1			**Motor M2**		
Actual Delay →	**10°**	**15°**	**22°**	**10°**	**15°**	**22°**
Speed (RPM)	**Estimated Delay (°E)**			**Estimated Delay (°E)**		
1000	10.71	15.33	21.31	9.01	14.69	21.26
1500	9.91	15.19	21.15	9.37	14.85	21.95
2000	9.85	14.96	21.75	9.83	14.95	22.11
2500	9.89	14.87	22.19	10.05	15.02	22.42
2800	9.97	15.01	23.03	10.13	14.81	22.50
3000	10.03	15.07	21.95	10.15	15.05	21.85

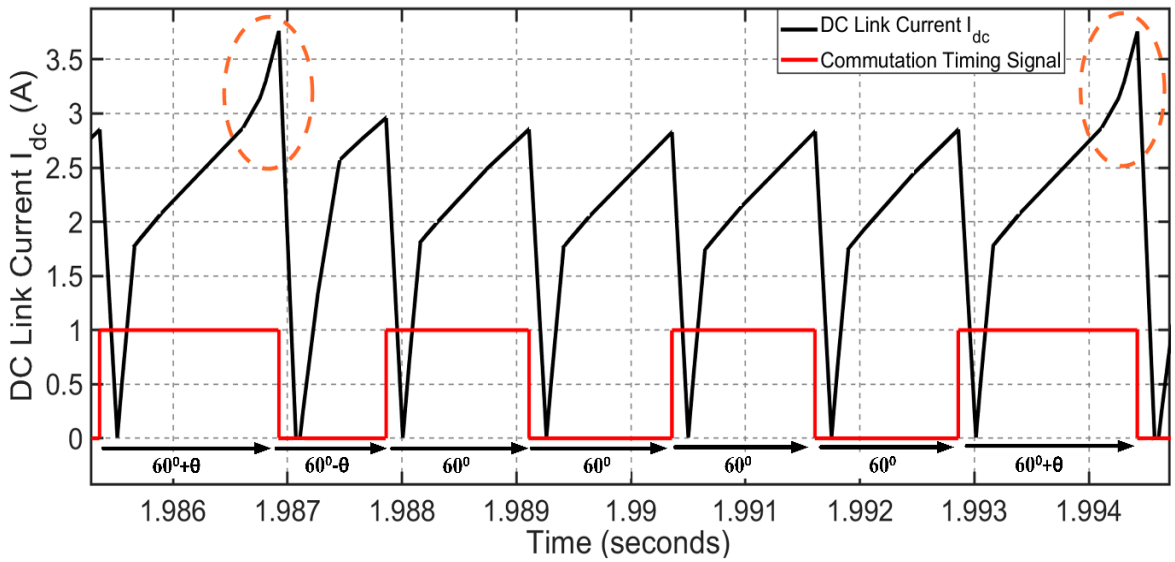

Fig. 6.4 DC link current I_{dc} with delayed commutation.

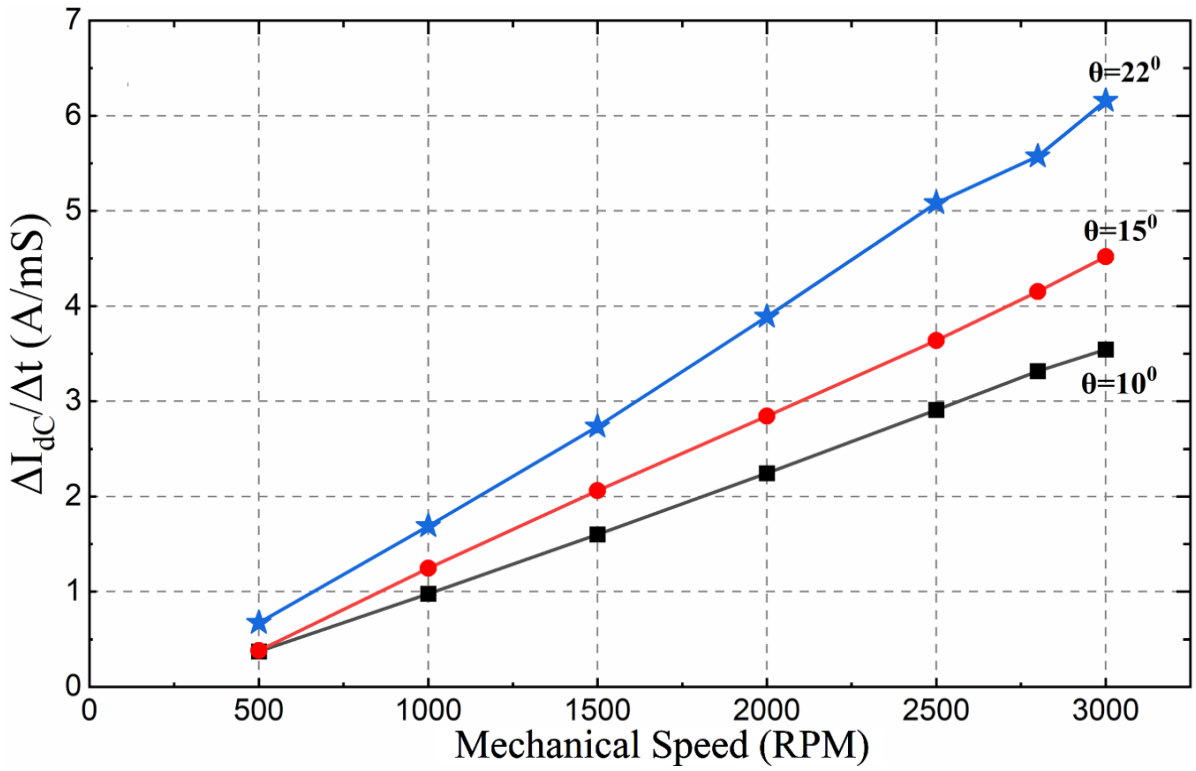

(a) Motor M1

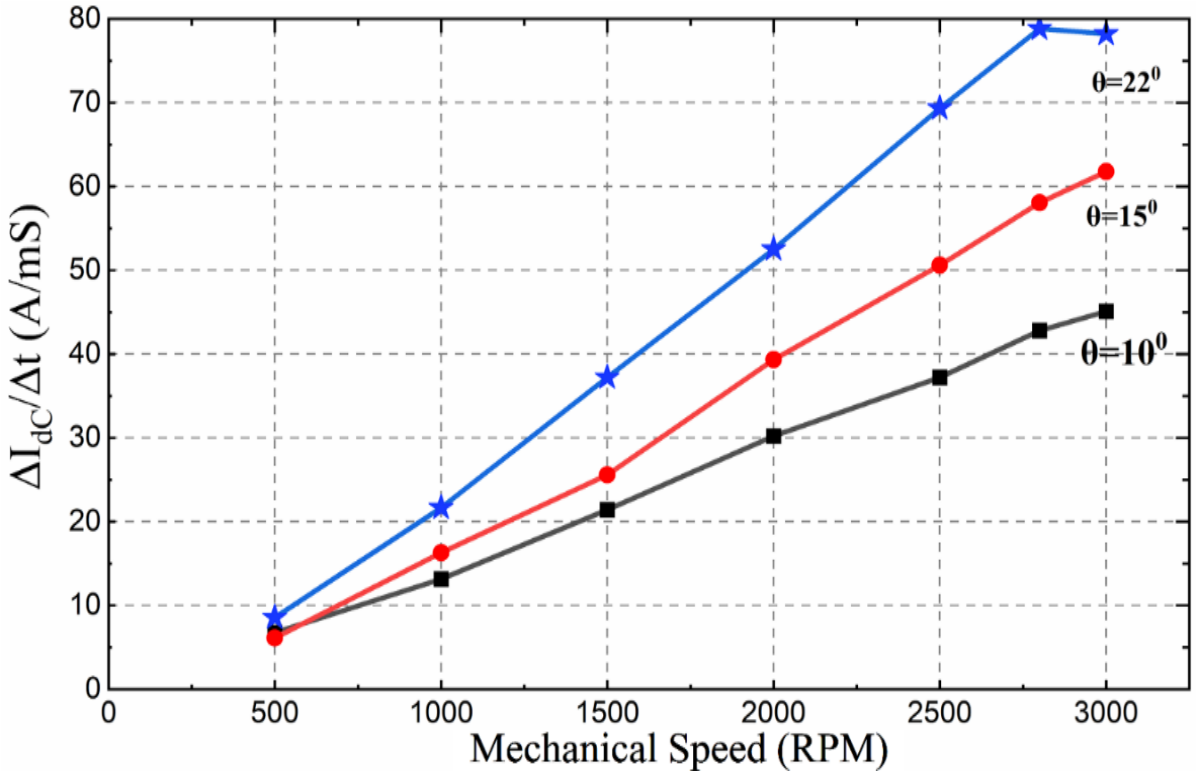

(b) Motor M2

Fig. 6.5 $\frac{\Delta I_{dc}}{\Delta t}$ versus mechanical speed with different values of delay angle θ.

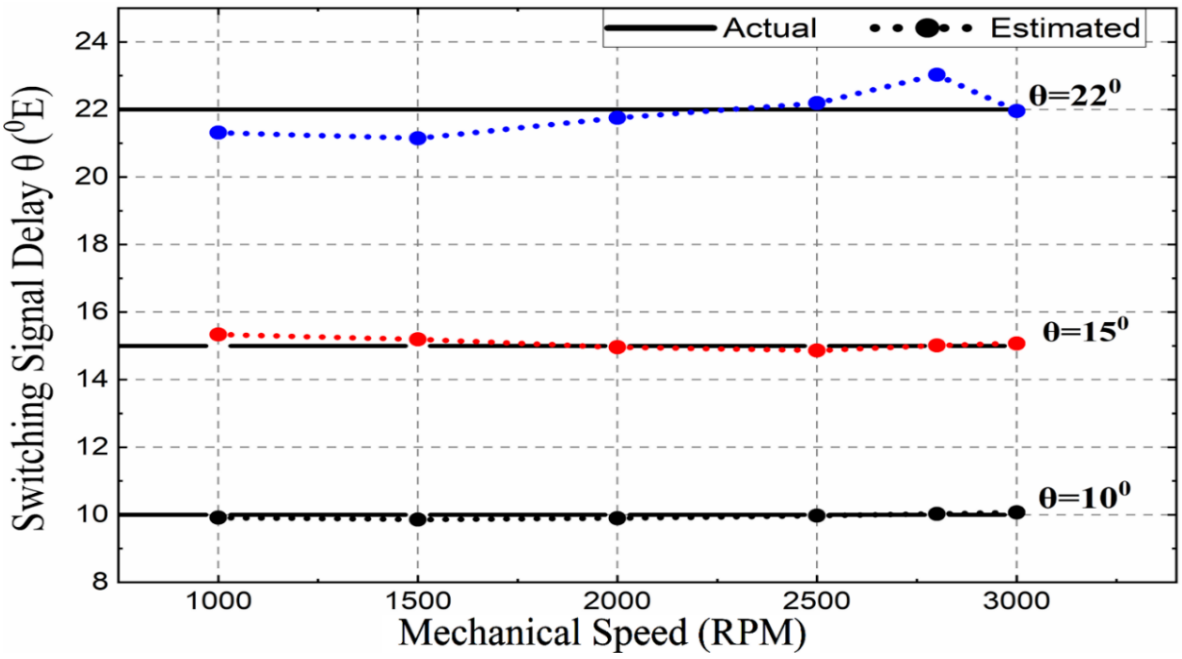

(a) Motor M1

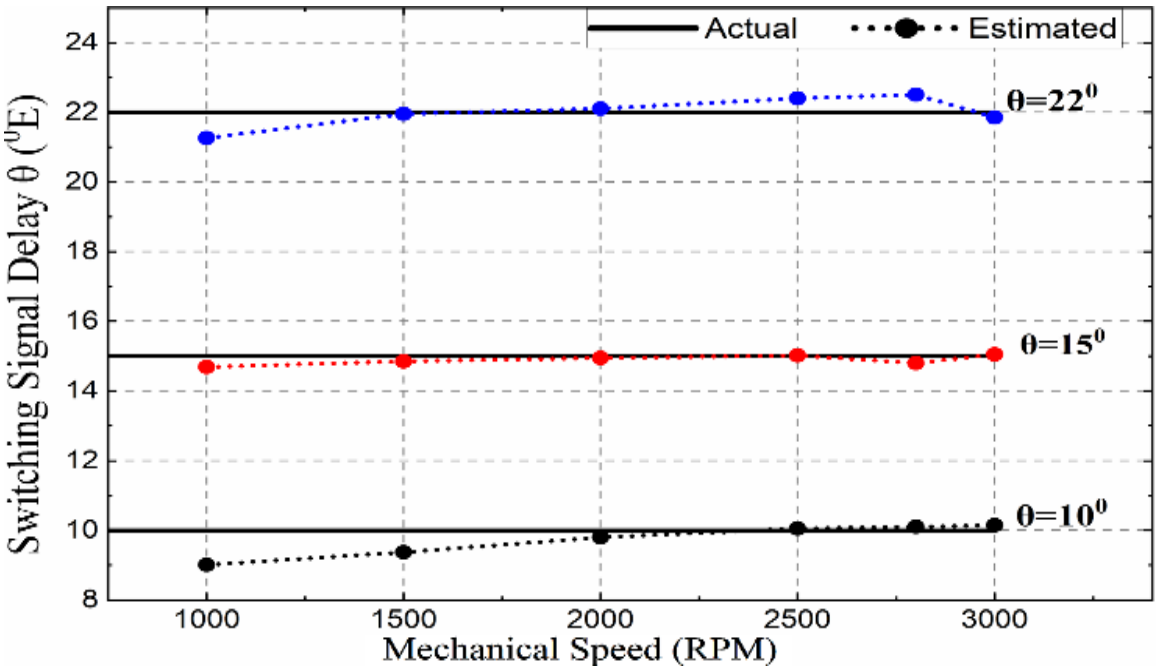

(b) Motor M2

Fig. 6.6 Actual and estimated delay angle θ with different values of rotor speed.

6.6 EXPERIMENTAL VALIDATION

The proposed scheme is tested using a 1 kW, 4 pole pair BLDC motor commonly found in e-rickshaws. This motor, rated at 48 V and 2800 RPM, features a star-connected winding and is equipped with 3 HESs. The controller, developed around a 32-bit STM32301 ARM

microcontroller, utilizes a 120° trapezoidal commutation scheme. During the motor test run, extended conduction due to delayed HES signals was observed, as shown in Fig. 6.7. The top two curves represent dc link current I_{dc} and phase voltage respectively, while the sector end commutation signal pulses are shown at the bottom.

In Fig. 6.8(a), the relation between the measured $\frac{\Delta I_{dc}}{\Delta t}$ and the speed ω_m is presented at different load values of 24%, 33%, and 70%, displaying a nearly linear correlation. Additionally, one experimental check was conducted with load varying according to speed, and the obtained results are depicted with a black colored curve. The pattern of the estimated delay angle obtained from the linear approximation relation with speed is depicted in Fig. 6.8(b). The dotted line represents the mean value of the reference angle for comparison. A motor test run was conducted for further experimental validation with the adjustment of the commutation delay angle according to the estimated value at 80% load. Figure 6.9 illustrates the improved phase voltage pattern and the DC link current with the corrected commutation signal pulses.

Table 6.2 provides the average estimated delay angle for each loading case and the final combined estimated average value. The deviation from this final value for each case falls within ±1°E. Thus, under constant load conditions, the delay angle can be approximated using the proposed method.

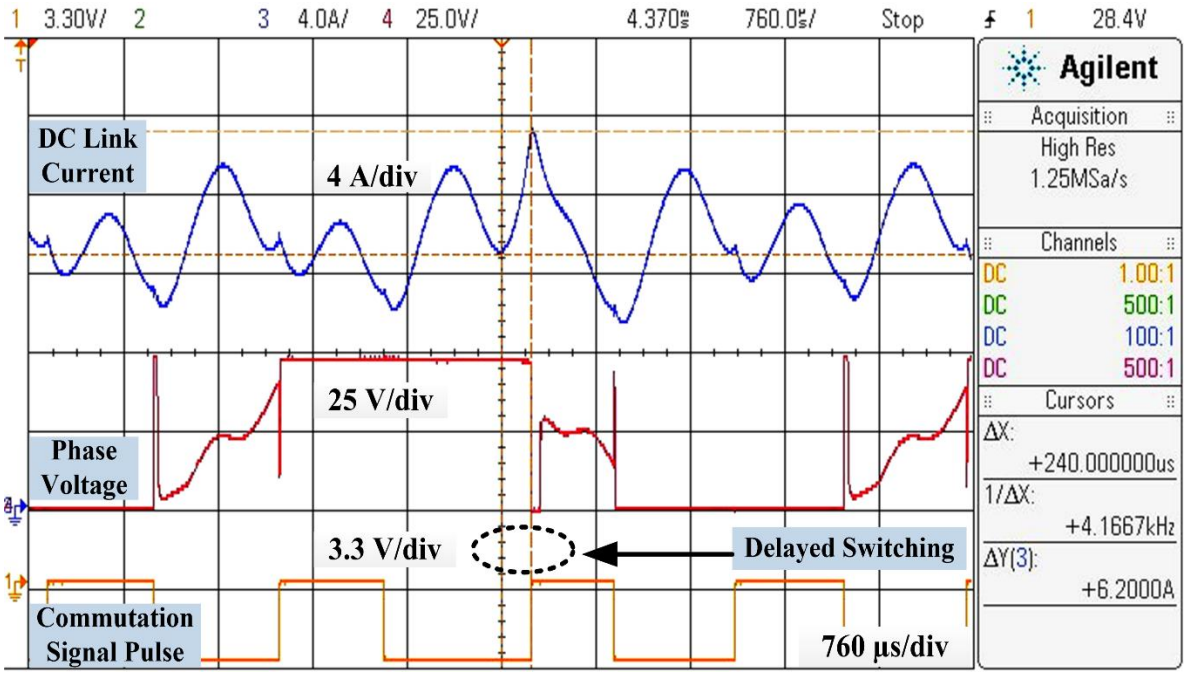

Fig. 6.7 DC link current I_{dc} and phase voltage with delayed commutation.

Table 6.2 Estimated delay angle values.

Loading	24%	33%	70%	Varying	Average
Estimated Delay (°E)	22.00	21.09	21.80	21.85	21.81

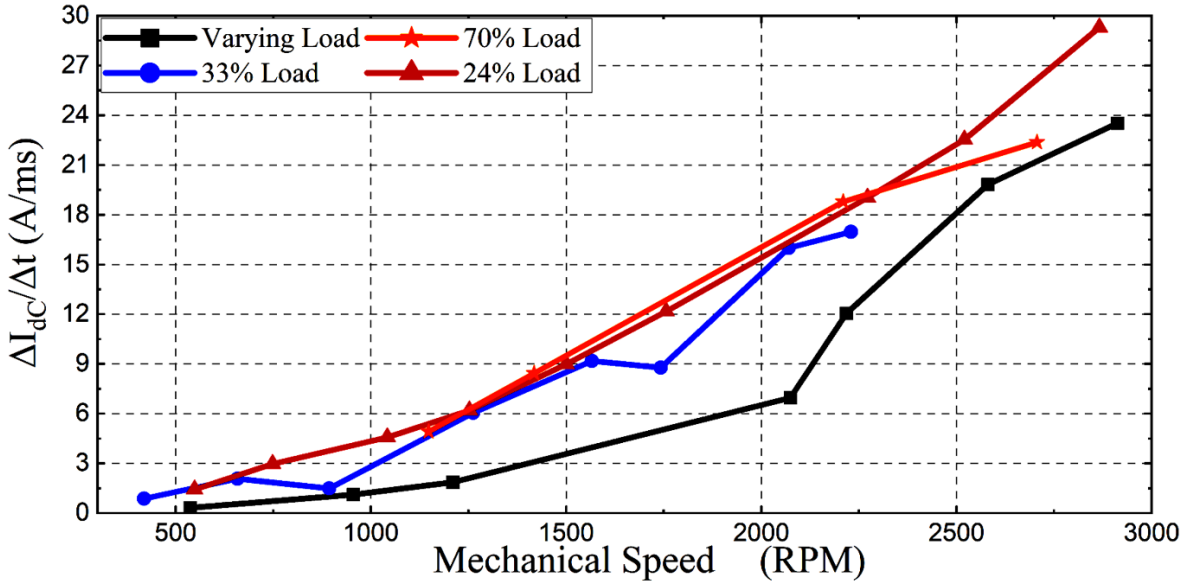

(a) $\frac{\Delta I_{dc}}{\Delta t}$ versus rotor speed

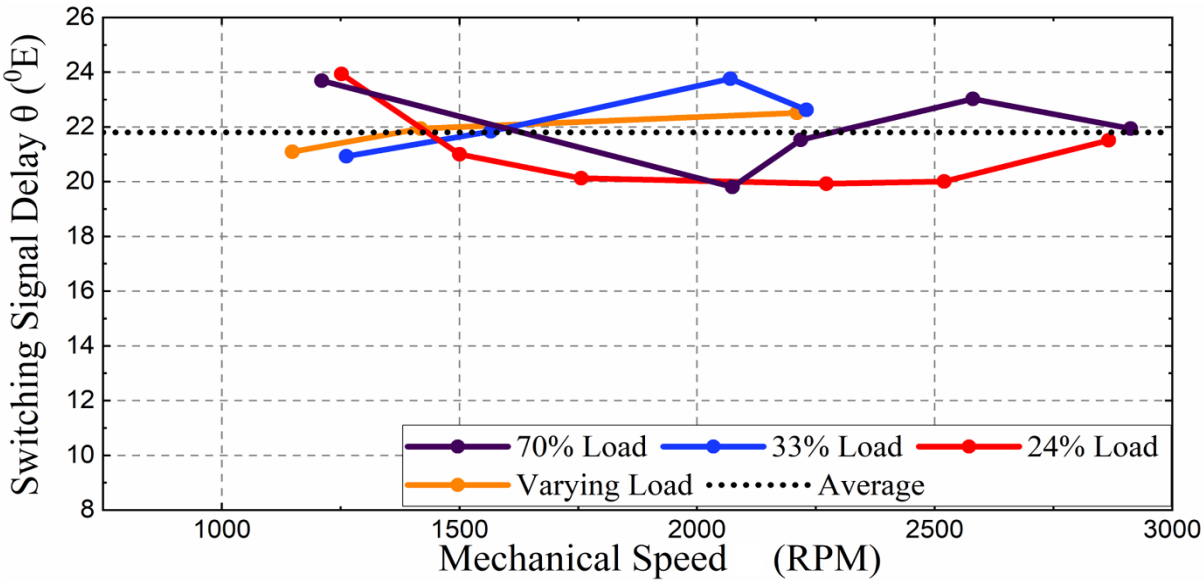

(b) Estimated delay angle θ versus rotor speed

Fig. 6.8. Estimation of the commutation delay using proposed relation at different load values.

The test runs shown in both Figures 6.7 and 6.9 are carried out with a 100% duty cycle to check the delay angle correction without the effects of constant PWM switching. The ripples

in the DC link current are reduced to 10% from their earlier value of 15%, the peak-to-peak variation of I_{dc} as a percentage of the DC RMS value is reduced to 39.5% from an earlier value of 72.4%. The observed reduction in the peak-to-peak I_{dc} is around 24% from the base value of 9.9 A. The variation in the current peak value is also reduced to the desired near zero from 5 A. The torque per ampere increases to approximately 1.028 times its earlier value, which is an improvement of around 2.8%.

The proposed method performs well when compared with another commutation optimization strategy that uses a moving average filter scheme. The reported experimental results for 60° sector duration with error under 1%, indicate a peak-to-peak current reduction of 4.14% from a base current of 14.5 A, and a current peak variation reduction of 75% from 2 A to 0.5 A. For commutation angle error that is greater than 5%, it has a reported current peak variation reduction of 25% [11, 129]. In another method that is based on the relationship between the phase voltage and speed, a current ripple reduction of 7% from initial 40% to 33% is reported [153].

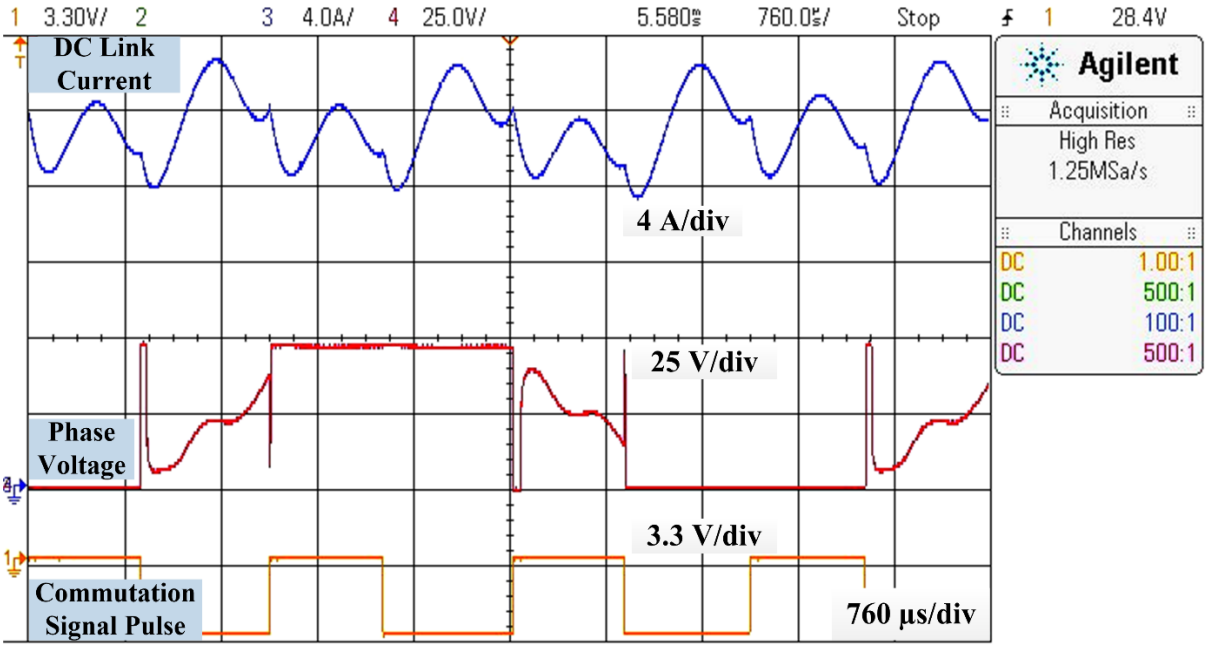

Fig. 6.9 Motor test run with correction applied according to the estimated delay angle.

When the motor is operated in the same operating conditions with the proposed FTC scheme and battery voltage is observed and compared with operation without any correction, the battery state of charge (SOC) can be estimated by the SOC curve specifications. The comparison of estimated battery discharge cycle durations is used to compare possible

increase in the battery life. Furthermore, by observation of the final settled value of the controller temperature in both cases, the relative reduction or increment of the heating due to proposed scheme implementation can be estimated.

The reduction in controller heating with the proposed method in the e-rickshaw motor controller set is approximately 2°C, and a single battery discharge cycle length increment is around 2%. Consequently, the estimated reduction in the discharge/charge cycles of the battery is around 1.96% with expected life increment of around 1.5%. Thus, the performance improvement of the drive by adjusting the commutation time validates the delay angle estimation by the proposed scheme for sensored BLDC motor drive applications.

6.7 CONCLUDING REMARKS

In this chapter a scheme for estimating the commutation delay and controlling its effects in the sensored BLDC motor drives is presented. The proposed scheme is developed by leveraging the DC link current, and it can be implemented in the controller without any additional signal sampling or filtering circuit requirements. Simulation analysis on two BLDC motors has demonstrated that the estimated delay angle error using the proposed linear approximation method remains within an acceptable range of ±1°E, even with an implemented error of 22°E. Experimental test results with a 48 V, 1 kW BLDC motor validate the estimation of delay angle under various load conditions. Adjustment of the commutation timing with the estimated delay angle has led to a reduction in DC current ripple of around 5% and an increase in nominal Torque/Ampere of around 2%. These performance improvements are comparable to other direct commutation optimization and HES misalignment compensation methods. Importantly, the proposed method reduces controller heating by around 2°C and decreases battery discharge/charge cycles, thereby extending the battery lifespan by approximately 1.5%. While the proposed method is valuable for cost and size restrictive automotive applications like three-wheelers and e-rickshaws, its application is limited to trapezoidal commutation methods with three HESs. Integration with phase current sensing based methods may pose challenges.

Future research could focus on analyzing the changes in electromagnetic torque harmonic content, motor vibration, audible noise, and the lifespan of inverter switches and driver components. Additionally, refinement of the method and its implementation considering EMI aspects for industry standard BLDC motor controller applications could be explored.

CHAPTER 7

CONCLUSION AND FUTURE SCOPE OF WORK

7.1 CONCLUSIONS

The main objective of this research work is the design and development of controller for sensored BLDC motor drives. The controller is designed for BLDC motors with three HESs. In EV applications it is mainly used in drives up to 1.5 kW range like in three-wheelers and e-rickshaws. The features of automatic motor phase sequence and handling of glitches in HES signals are included and tested in the design. The problem of HES signal errors due to placement and mounting issues is analysed with Matlab simulation models. The FTC scheme to detect, categorize and, estimate the HES signal errors is presented in the research work. Additionally, a novel method for commutation delay estimation based on DC link current is proposed. The design, implementation, and analysis of the proposed FTC schemes are carried out in the simulation and experimental hardware set up. These schemes work without requiring measurement of phase currents or BEMF profile estimation.

From the presented research work, following major points of considerations can be concluded for design and development of the controller in sensored BLDC motor drive development with HESs:

1. The motor controller design itself is an important aspect of the BLDC motor drive design. It controls and synchronises the crucial drive parameters such as phase currents, phase voltages, duty cycle of inverter switching signals, commutation sequence and timing.
2. The development and deployment of software for implementing state machine logic with computational algorithms is an important factor while designing the boundary conditions and operating parameters of the controller.
3. In addition to the normal drive control functionalities, the controller is also required to handle several other real time application issues. These issues include phase sequence detection, detection and validation of HES connections, errors handling for HES signals and, commutation timing issues, The starting and diagnostic software routines used for this purpose are important part of software development in the controller design.
4. The controllers use HES signals to manage the switching timing and commutation sequence. Overall drive control mechanism relies on the integrity of HES signals and their synchronization with the BEMF profile of the motor phases.
5. However, discrepancies in HES signal timings are observed due to factors like aging, the

mounting process of HESs, winding, and the placement of sensors. The limitations and difficulties in precisely assembling stator lamination sheets with HESs in various slot numbering per pole fixtures are also contributing factors. The issue is frequently reported in mass scale produced motors, especially for low voltage EV applications.

6. The above mentioned issues can cause distortions in switching patterns, loss of synchronization, deviation in feedback and miscalculation of the drive parameters. All these factors adversely affect the drive performance and may lead to total malfunctioning or stalling of the system. Therefore, study and analysis of these issues and associated error detection mechanisms in the controller is essential for the successful development of the corresponding FTC schemes.
7. The implementation of any FTC scheme in the controller must be carried out in a way such that it does not require changes in core commutation method, switching scheme, interrupt logic, event timings, or inverter protection schemes in the software. Therefore, the FTCs that adhere to these points have the potential for implementation in actual controller applications.
8. Commutation delays can be observed in sensored BLDC motor drives due to unbalanced HES signals or other run time factors. These delays are successfully linked to the DC link current profile without any need of phase current measurement or BEMF estimation for development of fault mitigation scheme. The investigation and estimation of commutation delay angles by establishing a direct approximation relation with DC link current profile is especially advantageous for applications relying only on DC link current measurement for drive operation.

The research work includes laboratory test bench development as a major objective for validation and performance evaluation of FTCs in controller. The possibility of actual implementation of the FTC schemes in motor controller is an important aspect from a practical application viewpoint. Therefore, development of FTC schemes that are easier to integrate without hindering the use of other FTC schemes is an important area of research in the controller development field. Study and analysis of the effect of the faults and improvement due to FTC scheme implementation on performance parameters of phase voltage, phase current profiles, DC link current, torque and speed parameters are important aspects of the overall system design.

Considering these points of observation, the presented research work and its major contributions are concluded as follows:

1. Design, mathematical modeling, simulation and analysis of BLDC motor drive in

MATLAB/Simulink environment. The sudy and analysis of effect of HES signals on commutation timing synchronization and drive operation is carried out in simulation.

2. Design and development of the motor controller is carried out using 32-bit STM32 ARM microcontroller for 48V,1 kW BLDC motor used in electric rickshaw type of applications. It is powered by 48V, 72 Ah battery pack.
3. Development of a laboratory hardware test bench is carried out and 120° trapezoidal commutation method is implementated for synchronization and control of the drive in sensored mode of operation.
4. The investigation and analysis of the glitch effects observed in HES signals in sensored BLDC motor drives are carried out. The correction method is implemented in the controller software and further verified on the hardware experimental setup.
5. Investigation on HES signal unbalancing faults in sensored BLDC motor drives is carried out and a fault effect minimization scheme for smooth implementation in motor controller without any modification in system architecture, or core commutation method is developed.
6. Design and implementation of a method for controlling the effect of commutation delay due to HESs, motor, and controller design factors in sensored BLDC motor drives is presented. The method is based on DC link current measurement and can be included in the controller without additional signal sampling and filtering requirements.
7. The implementation of the proposed schemes is verified using the hardware test bench. The FTC schemes' integration in controller and comparitive performance evaluation is carried out. Experimental tests are performed to validate the steady state and dynamic performance of the drive with proposed schemes.
8. An important outcome of the proposed FTC mechanisms is the reduced heating of the controller and fewer battery discharge/charge cycles. This contributes to better efficiency of the motor controller system and, increases the possibility of battery life enhancement with better power utilization without any need of additional hardware.
9. The proposed methods can be useful in the cost and size restrictive automotive applications of two wheelers, electric rickshaws, and other applications where controller circuit modifications are not feasible.

In conclusion, the design and development of BLDC motor drive controller is successfully carried out and implemented in the developed hardware test bench. In addition to the motor control and operation functions, the controller is also required to detect correct

motor phase sequence in several applications. Therefore, a method for detection and correct identification of phase sequence is implemented in the controller and verified on the experimental setup.

7.2 SCOPE OF FUTURE WORK

The presented research work including the controller design aspects and proposed FTC schemes can be further modified and improved for future applications as follows:

1. The proposed methods can be further tested and improved by the analyses of the changes in the vibration of the motor and audible noise during drive operation.
2. The effect of proposed schemes on the life span of the inverter switches and driver components can be analyzed for predictive maintenance in EV applications.
3. The effect on life span of DC link supply filter circuit and discrete components including capacitors, can be carried out seperately for further adoption of the proposed schemes in actual applications.
4. The effect on the EMI aspects of the controller can be used to refine the methods particularly the DC link current based commutation delay correction and its implementation, for adoption in industry standard controller applications.

REFERENCES

[1] Ehsani, Mehrdad, et al. "State of the art and trends in electric and hybrid electric vehicles." *Proceedings of the IEEE* 109.6 (2021): 967-984.

[2] Madichetty, Sreedhar, Sukumar Mishra, and Malabika Basu. "New trends in electric motors and selection for electric vehicle propulsion systems." *IET Electrical Systems in Transportation* 11.3 (2021): 186-199.

[3] Wang, Zhikun, et al. "Challenges faced by electric vehicle motors and their solutions." *IEEE Access* 9 (2020): 5228-5249.

[4] D. Mohanraj *et al*., "A Review of BLDC Motor: State of Art, Advanced Control Techniques, and Applications," in *IEEE Access*, vol. 10, pp. 54833-54869, 2022, doi: 10.1109/ACCESS.2022.3175011.

[5] J. Cheng, C. Lu, G. Zhang, C. Wu and Y. Huang, "Research and design of electric vehicle controller based on brushless DC motor," *2017 36th Chinese Control Conference (CCC)*, Dalian, China, 2017, pp. 10132-10136.

[6] Un-Noor, Fuad, et al. "A comprehensive study of key electric vehicle (EV) components, technologies, challenges, impacts, and future direction of development." *Energies* 10.8 (2017): 1217.

[7] Zilog. (2008). Electric Bike BLDC Hub Motor Control Using the Z8FMC1600 MCU, Application Note AN026002-0608. [Online]. Available: http://www.zilog.com/docs/z8encoremc/appnotes/AN0260.pdf.

[8] Hong-xing, Wu, Cheng Shu-Kang, and Cui Shu-mei. "A controller of brushless DC motor for electric vehicle." *2004 12th Symposium on Electromagnetic Launch Technology*. IEEE, 2004.

[9] A. Mousmi, A. Abbou and Y. El Houm, "Binary Diagnosis of Hall Effect Sensors in Brushless DC Motor Drives," in *IEEE Transactions on Power Electronics*, vol. 35, no. 4, pp. 3859-3868, April 2020.

[10] Sahana, K.M., Keerthi, T.G., Gouthami, Y. et al., "Design, Modelling and Parametric Analysis of a BLDC Motor in E-Bike to Predict Torque Range," Russ. Electr. Engin., vol. 94, pp. 129-137, 2023. [Online]. Available: https://doi.org/10.3103/S1068371223020098.

[11] D. A. Papathanasopoulos and E. D. Mitronikas, "Diagnosis of Defective Hall-effect Position Sensors in Brushless DC Motor Drives," *2019 IEEE Workshop on Electrical Machines Design, Control and Diagnosis (WEMDCD)*, 2019, pp. 137-142.

[12]M. Ebadpour, N. Amiri and J. Jatskevich, "Fast Fault-Tolerant Control for Improved Dynamic Performance of Hall-Sensor-Controlled Brushless DC Motor Drives," in *IEEE Transactions on Power Electronics*, vol. 36, no. 12, pp. 14051-14061, Dec. 2021.

[13]M. Aqil and J. Hur, “Multiple Sensor Fault Detection Algorithm for Fault Tolerant Control of BLDC Motor,” *Electronics*, vol. 10, no. 9, p. 1038, Apr. 2021.

[14]P. Alaeinovin, S. Chiniforoosh and J. Jatskevich, "Evaluating misalignment of hall sensors in brushless DC motors," *2008 IEEE Canada Electric Power Conference*, 2008, pp. 1-6.

[15]Zhang, Xi, Yiyun Zhao, Hui Lin, Saleem Riaz, and Hassan Elahi. 2021. "Real-Time Fault Diagnosis and Fault-Tolerant Control Strategy for Hall Sensors in Permanent Magnet Brushless DC Motor Drives" *Electronics* 10, no. 11: 1268. https://doi.org/10.3390/electronics10111268.

[16]Kolano, Krzysztof, Artur Jan Moradewicz, Bartosz Drzymała, and Jakub Gęca. 2022. "Influence of the Placement Accuracy of the Brushless DC Motor Hall Sensor on Inverter Transistor Losses" Energies 15, no. 5: 1822. https://doi.org/10.3390/en15051822.

[17]Yang, Zhi, et al. "Comparative study of interior permanent magnet, induction, and switched reluctance motor drives for EV and HEV applications." *IEEE Transactions on Transportation Electrification* 1.3 (2015): 245-254.

[18]Ward Brown and Microchip Technology Inc., “Brushless DC Motor Control Made Easy,” Application Note, Microchip Technology Inc., AN 857, DS00857A, 2002.

[19]Krishnan, V., et al. "Comparative analysis of electric motor prototypes in the electrical drive technology applications." *J. Inst. Eng.(India), Elect. Eng. Division* 4 (2020): 23-28.

[20]Kim, Hyung-Wook, et al. "Optimization methods of torque density for developing the neodymium free SPOKE-type BLDC motor." *IEEE Transactions on Magnetics* 49.5 (2013): 2173-2176.

[21]Haines, Gabriel, and Nesimi Ertugrul. "Wide speed range sensorless operation of brushless permanent-magnet motor using flux linkage increment." *IEEE Transactions on Industrial Electronics* 63.7 (2016): 4052-4060.

[22]Yazdan, Tanveer, et al. "A novel technique for two-phase BLDC motor to avoid demagnetization." *IEEE Transactions on Magnetics* 52.7 (2016): 1-4.

[23]R. Krishnan, “Electric Motor Drives: Modeling, Analysis, and Control,” Prentice-Hall, Upper Saddle River, 2001.

[24]B. K. Bose, Modern Power Electronics and AC Drives. Englewood Cliffs, NJ: Prentice Hall, 2001.

[25]P. Yedamale, “Brushless dc (bldc) motor fundamentals,” tech. rep., Microchip Technology Inc., 2003. 16, 18, 66.

[26]G. Adam, A. G. Stan, and G. Livint, “Improved brushless DC motor control algorithm for reducing source current harmonics simulation study,” in *ECMS*, pp. 171–174, 2012.

[27]Sakunthala, S., R. Kiranmayi, and P. Nagaraju Mandadi. "A study on industrial motor drives: Comparison and applications of PMSM and BLDC motor drives." *2017 International Conference on Energy, Communication, Data Analytics and Soft Computing (ICECDS)*. IEEE, 2017.

[28]Texas Instruments, "Hall Sensor-Based Trapezoidal Control of 230-V, 900-W Mains Powered BLDC Motor Drive Using DRV92250," TIDCAI3, 2015. [Online]. Available: https://www.ti.com/jp/lit/an/tidcai3/tidcai3.pdf?ts=1701203888989.

[29]E. C. Lee, “Application of brushless dc drives in blow molding," Published by Power Tech Industrial Motors, 1993.

[30]Kim, Hyun-Jung. "BLDC motors for robot vacuum cleaners." *The Transactions of the Korean Institute of Electrical Engineers P* 60.4 (2011): 172-174.

[31]Kumar, K. V. N. S., and Dr S. Prakash. "Modeling of a Commercial BLDC Motor and Control Using GA-controller for a BLDC Propulsion Application for Hybrid Electric Vehicle." *International Journal of Psychosocial Rehabilitation* 23.4 (2019).

[32]Shao, Jianwen. "An improved microcontroller-based sensorless brushless DC (BLDC) motor drive for automotive applications." *IEEE Transactions on industry applications* 42.5 (2006): 1216-1221.

[33]Iyer, K. Lakshmi Varaha, et al. "Investigation of interior permanent magnet motor with dampers for electric vehicle propulsion and mitigation of saliency effect during integrated charging operation." *IEEE Transactions on Vehicular Technology* 68.2 (2018): 1254-1265.

[34]Salah, W.A., Ishak, D., Zneid, B.A. et al.,” Implementation of PWM control strategy for torque ripples reduction in brushless DC motors,” in *Electr Eng* 97, 239–250 (2015). https://doi.org/10.1007/s00202-014-0329-7.

[35]R. A. Bhat P. S. Jadhav "Modeling and simulation of BLDC motor in electric power steering by using MATLAB" *2016 10th International Conference on Intelligent Systems and Control (ISCO)* pp. 1-6 2016.

[36]Kudelina, Karolina, et al. "Main faults and diagnostic possibilities of BLDC motors." *2020 27th international workshop on electric drives: MPEI department of electric drives 90th anniversary (IWED)*. IEEE, 2020.

[37]Pellegrino, Gianmario, et al. "Performance comparison between surface-mounted and interior PM motor drives for electric vehicle application." *IEEE Transactions on Industrial Electronics* 59.2 (2011): 803-811.

[38]C. Miguel-Espinar, D. Heredero-Peris, G. Igor-Gross, M. Llonch-Masachs and D. Montesinos-Miracle, "Accurate Angle Representation From Misplaced Hall-Effect Switch Sensors for Low-Cost Electric Vehicle Applications," in *IEEE Transactions on Industry Applications*, vol. 58, no. 4, pp. 5227-5237, July-Aug. 2022.a

[39]A. S. Al-Adsani, M. E. AlSharidah and O. Beik, "BLDC Motor Drives: A Single Hall Sensor Method and a 160° Commutation Strategy," in *IEEE Transactions on Energy Conversion*, vol. 36, no. 3, pp. 2025-2035, Sept. 2021.

[40]P. Damodharan and K. Vasudevan, "Sensorless brushless dc motor drive based on the zero-crossing detection of back electromotive force (emf) from the line voltage difference," *IEEE Transactions on Energy Conversion*,vol. 25, no. 3, pp. 66-668, 2010.

[41]Lee, Tae-Yong, et al. "Motor design and characteristics comparison of outer-rotor-type BLDC motor and BLAC motor based on numerical analysis." *IEEE Transactions on Applied Superconductivity* 26.4 (2016): 1-6.

[42]C. Lai and J. Huang, "Quasi-sinusoidal voltage source driver design for brushless DC motor with digital hall sensor feedback," *2016 International Automatic Control Conference (CACS)*, Taichung, 2016, pp. 212-217, doi: 10.1109/CACS.2016.7973911.

[43]P. Vishnu Sidharthan and Y. Kashyap, "Brushless DC Hub Motor Drive Control for Electric Vehicle Applications," *2020 First International Conference on Power, Control and Computing Technologies (ICPC2T)*, Raipur, India, 2020, pp. 448-453, doi: 10.1109/ICPC2T48082.2020.9071469.

[44]T. Nama, A. K. Gogoi and P. Tripathy, "Application of a smart hall effect sensor system for 3-phase BLDC drives," *2017 IEEE International Symposium on Robotics and Intelligent Sensors (IRIS)*, Ottawa, ON, Canada, 2017, pp. 208-212.

[45]D.-H. Lee, "Wide-range Speed Control Scheme of BLDC Motor Based on the Hall Sensor Signal," *Journal of Power Electronics*, vol. 18, no. 3, pp. 714–722, May 2018.

[46]Kan, Kai-Sheng, and Ying-Yu Tzou. "Adaptive soft starting method with current limit strategy for sensorless BLDC motors." *2012 IEEE International Symposium on Industrial Electronics*. IEEE, 2012.

[47]Ahfock, A., and D. Gambetta. "Sensorless commutation of printed circuit brushless direct current motors." *IET electric power applications* 4.6 (2010): 397-406.

[48]Liu, Gang, et al. "Sensorless control for high-speed brushless DC motor based on the line-to-line back EMF." *IEEE Transactions on Power Electronics* 31.7 (2014): 4669-

4683.

[49]D. Mohanraj, J. Gopalakrishnan, B. Chokkalingam and L. Mihet-Popa, "Critical Aspects of Electric Motor Drive Controllers and Mitigation of Torque Ripple—Review," in *IEEE Access*, vol. 10, pp. 73635-73674, 2022, doi: 10.1109/ACCESS.2022.3187515.

[50]M. Jain and S. S. Williamson, "Suitability analysis of in-wheel motor direct drives for electric and hybrid electric vehicles," *2009 IEEE Electrical Power & Energy Conference (EPEC)*, Montreal, QC, 2009, pp. 1-5, doi: 10.1109/EPEC.2009.5420886.

[51]Poudel, Bikrant, et al. "Toward less rare-earth permanent magnet in electric machines: A review." *IEEE Transactions on Magnetics* 57.9 (2021): 1-19.

[52]S.L. Tade, Ravindra Sor and S.V. KinkarA, "A Digital PWM Techniques and Commutation for Brushless DC Motor Control Applications: Review," *2016 IJAREEIE*, doi: 10.15662/IJAREEIE.2016.0504048.

[53]P. Pillay and R. Krishnan, "Modeling, simulation, and analysis of permanent-magnet motor drives. II. The brushless DC motor drive," in *IEEE Transactions on Industry Applications*, vol. 25, no. 2, pp. 274-279, March-April 1989, doi: 10.1109/28.25542.

[54]Mehmet Cihat Ozgenel, "Design, implementation, and application of 150-degree commutation VSI to improve speed range of sensored BLDC motor," *Review of Scientific Instruments* 88, 095007, 2017.

[55]B. N. Kommula and V. R. Kota, "Mathematical modeling and fuzzy logic control of a brushless DC motor employed in automobile and industrial applications," in *2016 IEEE First International Conference on Control*, Measurement and Instrumentation (CMI), IEEE, 2016.

[56]P. S. Chaudhari, S. L. Patil, S. K. Pandey and S. Sinha, "Performance analysis of BLDC motor on sinusoidal and square wave supply," *2016 IEEE International Conference on Power Electronics, Drives and Energy Systems (PEDES)*, Trivandrum, 2016, pp. 1-6.

[57]C.-m. Ong, Dynamic Simulation of Electric Machinery using Matlab/Simulink: Prentice Hall, 1998.

[58]J. S. Park and K. Lee, "Online Advanced Angle Adjustment Method for Sinusoidal BLDC Motors with Misaligned Hall Sensors," in IEEE Transactions on Power Electronics *IEEE Transactions on Power Electronics*, vol. 32, no. 11, pp. 8247-8253, Nov. 2017, doi: 10.1109/TPEL.2017.2694042.

[59]P. Beran, M. Stahl-Offergeld, V. Peters, D. Krause and H. Hohe, "Impact of Contact Misalignment on Magnetic Cross Sensitivity of Integrated Vertical Hall Sensors," in *IEEE Transactions on Magnetics*, vol. 55, no. 1, pp. 1-4, Jan. 2019, Art no. 4000904.

[60]M. Aqil and J. Hur, "A Direct Redundancy Approach to Fault-Tolerant Control of BLDC Motor With a Damaged Hall-Effect Sensor," in *IEEE Transactions on Power Electronics*, vol. 35, no. 2, pp. 1732-1741, Feb. 2020.

[61]O. Zandi and J. Poshtan, "Fault Diagnosis of Brushless DC Motors Using Built-In Hall Sensors," in *IEEE Sensors Journal*, vol. 19, no. 18, pp. 8183-8190, 15 Sept.15, 2019, doi: 10.1109/JSEN.2019.2917847.

[62]C. Miguel-Espinar, D. Heredero-Peris, G. Igor-Gross, M. Llonch-Masachs, and D. Montesinos-Miracle, "An Enhanced Electrical Angle Representation in PMSM Control with Misplaced Hall-Effect Switch Sensors," in *Proceedings of the 23rd International Conference on Electrical Machines and Systems (ICEMS)*, Hamamatsu, Japan, 2020, doi: 10.23919/ICEMS50442.2020.9291194.

[63]Toshiba Electronic Devices & Storage Corporation, "120° Square-Wave Commutation for Brushless DC Motors," Application Note, Aug. 3, 2018.

[64]Darba, Araz, et al. "Improved dynamic behavior in BLDC drives using model predictive speed and current control." *IEEE transactions on Industrial Electronics* 63.2 (2015): 728-740.

[65]X. Zhang and W. Zhang, "An improved rotor position estimation in PMSM with low-resolution hall-effect sensors," *2014 17th International Conference on Electrical Machines and Systems (ICEMS)*, 2014, pp. 2722-2727, doi: 10.1109/ICEMS.2014.7013961.

[66]D. S. Nair, G. Jagadanand and S. George, "Modified switching scheme-based explicit torque control of brushless direct current motor drive," in *IET Electric Power Applications*, vol. 13, no. 7, pp. 1051-1060, 7 2019, doi: 10.1049/iet-epa.2018.5662.

[67]C. K. Lad and R. Chudamani, "Simple overlap angle control strategy for commutation torque ripple minimisation in BLDC motor drive," in *IET Electric Power Applications*, vol. 12, no. 6, pp. 797-807, 7 2018, doi: 10.1049/iet-epa.2017.0644.

[68]S. S. Bharatkar, R. Yanamshetti, D. Chatterjee and A. K. Ganguli, "Dual-mode switching technique for reduction of commutation torque ripple of brushless dc motor," in *IET Electric Power Applications*, vol. 5, no. 1, pp. 193-202, January 2011, doi: 10.1049/iet-epa.2010.0015.

[69]Y. Cao, T. Shi, X. Niu, X. Li and C. Xia, "A Smooth Torque Control Strategy for Brushless DC Motor in Braking Operation," in *IEEE Transactions on Energy Conversion*, vol. 33, no. 3, pp. 1443-1452, Sept. 2018, doi: 10.1109/TEC.2018.2800750.

[70]Pratikanta Mishra, Atanu Banerjee, Hari Charan Nannam, Mousam Ghosh, "A Novel Modified Digital PWM Control Technique to Reduce Speed Ripples in BLDC Motors",

Power Electronics Conference (SPEC) 2018 IEEE 4th Southern, pp. 1-8, 2018.

[71]J. Gamazo-Real, E. Vzquez-Snchez, and J. Gmez-Gil, “Position and speed control of brushless dc motors using sensorless techniques and application trends," *Sensors*, vol. 10, no. 7, pp. 6901{6947, 2010.

[72]Jianwen Shao, D. Nolan and T. Hopkins, "A novel direct back EMF detection for sensorless brushless DC (BLDC) motor drives," APEC. *Seventeenth Annual IEEE Applied Power Electronics Conference and Exposition (Cat. No.02CH37335)*, Dallas, TX, USA, 2002, pp. 33-37 vol.1, doi: 10.1109/APEC.2002.989224.

[73]T.-H. Kim and M. Ehsani, “Sensorless control of the bldc motors from near-zero to high speeds,” *IEEE Transactions on Power Electronics*, vol. 19, no. 6, pp. 1635–1645, 2004.

[74]Park, Joon Sung, et al. "Unbalanced ZCP compensation method for position sensorless BLDC motor." *IEEE Transactions on Power Electronics* 34.4 (2018): 3020-3024.

[75] K. D. Carey, N. Zimmerman and C. Ababei, "Hybrid field oriented and direct torque control for sensorless BLDC motors used in aerial drones," in *IET Power Electronics*, vol. 12, no. 3, pp. 438-449, 20 3 2019, doi: 10.1049/iet-pel.2018.5231.

[76]A. Tashakori and M. Ektesabi, "A simple fault tolerant control system for Hall Effect sensors failure of BLDC motor," *2013 IEEE 8th Conference on Industrial Electronics and Applications (ICIEA)*, Melbourne, VIC, 2013, pp. 1011-1016, doi: 10.1109/ICIEA.2013.6566515.

[77]S. -Y. Kim, C. Choi, K. Lee and W. Lee, "An Improved Rotor Position Estimation With Vector-Tracking Observer in PMSM Drives With Low-Resolution Hall-Effect Sensors," in *IEEE Transactions on Industrial Electronics*, vol. 58, no. 9, pp. 4078-4086, Sept. 2011.

[78]A. Azarudeen and D. Mary, "Performance analysis of conventional and digital PWM control scheme for speed control of BLDC motor drives," *2017 International Conference on Advances in Electrical Technology for Green Energy (ICAETGT)*, Coimbatore, 2017, pp. 69-75.

[79]Mehmet Cihat Ozgenel, “Increasing power and torque capability of brushless direct current motor by employing 150-degree conduction mode controlled three-phase voltage source inverter,” *Review of Scientific Instruments* 89, 085002,2018.

[80]Y. Lee, "A New Method to Minimize Overall Torque Ripple in the Presence of Phase Current Shift Error for Three-Phase BLDC Motor Drive," in *Canadian Journal of Electrical and Computer Engineering*, vol. 42, no. 4, pp. 225-231, Fall 2019.

[81]T.J.E. Miller, Brushless PM and Reluctance Motor Drives. Oxford: Clarendon Press,

1989.

[82]Wei, Yanyu, et al. "Analytic investigation on commutation angle of brushless DC motors with 120 voltage source inverter." *International Journal of Applied Electromagnetics and Mechanics* 45.1-4 (2014): 219-225.

[83]I. Kim, N. Nakazawa, S. Kim, C. Park, and C. Yu, "Compensation of torque ripple in high performance BLDC motor drives," *Control Eng. Pract*., vol. 18, pp. 1166-1172, 2010.

[84]J.R. Hendershot and T.H.E. Miller, Design of Brushless Permanent Magnet Motors. Oxford: Magna Physics, 1994.

[85]H. Le-Huy, R. Perret, and R. Feuillet, "Minimization of torque ripple in brushless DC motor drives," *IEEE Trans. Ind. Electron*., vol. 1-22, pp. 748-755, 1986.

[86]R. Carlson, M. Lajoie-Mazenc and J. C. d. S. Fagundes, "Analysis of torque ripple due to phase commutation in brushless DC machines," in *IEEE Transactions on Industry Applications*, vol. 28, no. 3, pp. 632-638, May-June 1992, doi: 10.1109/28.137450.

[87]B.H. Kang, C.J. Kim, and G.H. Choe, "Analysis of torque ripple in BLDC motor with commutation time," in *Proc. ISIE Conference*, vol. 32, pp. 1044-1048, 2001.

[88]S. Park, T. Kim, S. Ahn, and D. Hyun, "A new current control algorithm for torque ripple reduction of BLDC motors," *in Proc. of IECON'01*, vol. 2, pp. 1521-1526, 2001.

[89]X. Xiao, Y. Li, M. Zhang, and M. Li, "A novel control strategy for BLDC motor with low torque ripples," in *Proc. of IECON'01*, pp. 1660-1664, 2001.

[90]J. Song and I. Choy, "Commutation torque ripple reduction in brushless DC motor drives using a single DC current sensor," *IEEE Trans. Power Electron*., vol. 19, pp. 312-319, 2004.

[91]S. Bharatkar and R. Yanamashetti, "Reduction of commutation torque ripple in permanent magnet motors," in *Proc. of ECTI-CON*, pp. 1-3, 2008.

[92]K.Y. Nam, W.T. Lee, C.M. Lee, and J.P. Hong, "Reducing torque ripple of brushless DC motor by varying input voltage," *IEEE Trans. Magn*., vol. 42, pp. 1307-1310, 2006.

[93]Y. Liu, Z.Q. Zhu, and D. Howe, "Commutation torque ripple minimization in direct controlled PM brushless DC motors," in *IAS 2006 Conference*, pp. 1642-1648, 2006.

[94]X. Changliang, Y. Wei, and L. Zhiqiang, "Toque ripple reduction of PM brushless DC motors based on auto disturbances-rejection controller," in *Proc. CSEEE 26*, pp. 137-142, 2006.

[95]C.G. Kim and J.H. Lee, "A commutation torque minimization method for brushless DC motors with trapezoidal electromotive force," in *Proc. ICPE 1*, pp. 476-481, 1998.

[96]ATMEL, "AVR435: BLDC motor control using a sine modulated PWM algorithm," Application Note AVR435, 2006. [Online]. Available: https://ww1.microchip.com/downloads/aemDocuments/documents/OTH/ApplicationNotes/ApplicationNotes/doc7671.pdf.

[97]H. Lu, L. Zhang and W. Qu, "A New Torque Control Method for Torque Ripple Minimization of BLDC Motors With Un-Ideal Back EMF," in *IEEE Transactions on Power Electronics*, vol. 23, no. 2, pp. 950-958, March 2008, doi: 10.1109/TPEL.2007.915667.

[98]Jorge Zambada and Microchip Technology Inc., "Driving a BLDC with Sinusoidal Voltages Using dsPIC30F," Code Examples, Microchip Technology Inc., CE003, DS92003A, 2005.

[99]M. N. Gujjar and P. Kumar, "Comparative analysis of field oriented control of BLDC motor using SPWM and SVPWM techniques," *2017 2nd IEEE International Conference on Recent Trends in Electronics, Information & Communication Technology (RTEICT)*, Bangalore, 2017, pp. 924-929, doi: 10.1109/RTEICT.2017.8256733.

[100] Prashant Kumar, Ranjan Kumar Behera, Devara Vijaya Bhaskar, "Novel closed loop speed control of permanent magnet brushless DC motor drive", *Technologies for Smart-City Energy Security and Power (ICSESP) 2018*, pp. 1-6, 2018.

[101] Wei-Feng Zhang and Yue-Hui Yu, "Comparison of Three SVPWM Strategies," 2007, *Journal of Electronic Science and Technology of China*, Vol. 5, No. 3, September.

[102] K. C. L. J. Kim, T., "A new sensorless drive scheme for a bldc motor based on the terminal voltage difference," in *Proceeding of the 37th Annual Conference of the IEEE Industrial Electronics Society, IECON 2011*, (Melbourne, VIC), pp. 1710{1715, Nov 2011. Conference of 37th Annual Conference of the IEEE Industrial Electronics Society, IECON 2011.

[103] ST Microelectronics, " Low cost sinusoidal control of BLDC motors with Hall sensors using ST7FMC," 2006. [Online]. Available: https://www.st.com/resource/en/application_note/an2372-low-cost-sinusoidal-control-of-bldc-motors-with-hall-sensors-using-st7fmc-stmicroelectronics.pdf.

[104] K. Kolano, "Improved Sensor Control Method for BLDC Motors," in *IEEE Access*, vol. 7, pp. 186158-186166, 2019. doi: 10.1109/ACCESS.2019.2960580.

[105] Do-Hyeon Park, Anh Tan Nguyen, D. -C. Lee and Hyong-Gun Lee, "Compensation of misalignment effect of hall sensors for BLDC motor drives," *2017 IEEE 3rd International Future Energy Electronics Conference and ECCE Asia (IFEEC 2017 - ECCE Asia)*, Kaohsiung, Taiwan, 2017, pp. 1659-1664, doi:

10.1109/IFEEC.2017.7992296.

[106] Behera, Ranjan K., et al. "Analysis of electric vehicle stability effectiveness on wheel force with BLDC motor drive." *2018 IEEE International Conference on Industrial Electronics for Sustainable Energy Systems (IESES)*. IEEE, 2018.

[107] Perotti, Michele. "On the Influence of the Load Parasitics on the CM Conducted EMI of BLDC Motor Drives." *IEEE Proceedings*. 2020.

[108] Ming, Yue, and Jian-Xin Shen. "Research on conducted EMI and vibration characteristics of PM BLDC motors with different stator structures." *2011 International Conference on Electrical Machines and Systems*. IEEE, 2011.

[109] H. F. Prasetyo A. S. Rohman F. I. Hariadi H. Hindersah "Controls of BLDC motors in electric vehicle Testing Simulator" *2016 6th International Conference on System Engineering and Technology (ICSET)* pp. 173-178 2016.

[110] A. Tashakori, M. Ektesabi, and N. Hosseinzadeh, “Characteristics of suitable drive train for electric vehicle,” in *Proceeding of the International Conference on Instrumentation, Measurement, Circuits and Systems (ICIMCS 2011)*, (Hong Kong,China.), pp. 535–541, Dec 2011. 1, 8, 10, 13, 14, 24, 25.

[111] Wang, L., Zhu, Z. Q., Bin, H., and Gong, L., "A Commutation Optimization Strategy for High-Speed Brushless DC Drives with Voltage Source Inverter," *IEEE Trans. Ind. Appl.*, vol. 58, no. 4, pp. 4722-4732, 2022.

[112] Z. Q. Zhu and J. H. Leong, "Analysis and Mitigation of Torsional Vibration of PM Brushless AC/DC Drives With Direct Torque Controller," in *IEEE Transactions on Industry Applications*, vol. 48, no. 4, pp. 1296-1306, July-Aug. 2012, doi: 10.1109/TIA.2012.2199452.

[113] F. Yang et al., "Design of a High-Efficiency Minimum-Torque-Ripple 12-V/1-kW Three-Phase BLDC Motor Drive System for Diesel Engine Emission Reductions," in *IEEE Transactions on Vehicular Technology*, vol. 63, no. 7, pp. 3107-3115, Sept. 2014, doi: 10.1109/TVT.2014.2300931.

[114] R. Sreejith K. R. Rajagopal "An insight into motor and battery selections for three-wheeler electric vehicle" *2016 IEEE 1st International Conference on Power Electronics Intelligent Control and Energy Systems (ICPEICES)* pp. 1-6 2016.

[115] J. Wei, P. Liu and W. Tao, "An Incorporated Control Strategy of Commutation and Conduction Torque Ripples Mitigation for BLDCM Drives in Household Appliances," in *IEEE Access*, vol. 7, pp. 108137-108151, 2019, doi: 10.1109/ACCESS.2019.2932837.

[116] ST Microelectronics, "How to use the 1 kW traction controller reference design for 3-phase BLDC motors for light electric vehicles," 2019. [Online]. Available: https://www.st.com/resource/en/user_manual/um2647-how-to-use-the-1-kw-traction-controller-reference-design-for-3phase-bldc-motors-for-light-electric-vehicles-stmicroelectronics.pdf.

[117] Texas Instruments, "Automotive 1-kW 48-V BLDC Motor Drive Reference Design," 2015. [Online]. Available: https://www.ti.com/lit/pdf/tiduay9. Accessed: Jan. 26, 2022.

[118] ST Microelectronics. (2019, November). 1 kW traction controller reference design for 3-phase BLDC motors for light electric vehicles, DB4061, STDES-EVT001V1, Rev. 1, Data Brief. [Online]. Available: https://www.st.com/resource/en/data_brief/stdesevt001v1.pdf. Accessed: Feb. 2020.

[119] J. S. Park, J.-H. Choi, and J. Lee, “Compensation Method of Position Signal Error with Misaligned Hall-Effect Sensors of BLDC Motor,” *Journal of Electrical Engineering and Technology*, vol. 11, no. 4. The Korean Institute of Electrical Engineers, pp. 889–897, 01-Jul-2016.

[120] X. Zhou, X. Chen, M. Lu, and F. Zeng, "Rapid Self-Compensation Method of Commutation Phase Error for Low-Inductance BLDC Motor," *IEEE Transactions on Industrial Informatics*, vol. 13, no. 4, pp. 1833-1842, 2017.

[121] C.-H. Chen and M.-Y. Cheng, "A New Cost-Effective Sensorless Commutation Method for Brushless DC Motors Without Phase Shift Circuit and Neutral Voltage," *IEEE Transactions on Power Electronics*, vol. 22, no. 2, pp. 644-653, 2007.

[122] J. Shi and T. Li, "New Method to Eliminate Commutation Torque Ripple of Brushless DC Motor With Minimum Commutation Time," in *IEEE Transactions on Industrial Electronics*, vol. 60, no. 6, pp. 2139-2146, June 2013, doi: 10.1109/TIE.2012.2191756.

[123] M. Masmoudi, B. E. Badsi and A. Masmoudi, "DTC of B4-Inverter-Fed BLDC Motor Drives With Reduced Torque Ripple During Sector-to-Sector Commutations," in *IEEE Transactions on Power Electronics*, vol. 29, no. 9, pp. 4855-4865, Sept. 2014, doi: 10.1109/TPEL.2013.2284111.

[124] D. Zhao, X. Wang, L. Xu, L. Xia, and Y. Huangfu, "A New Phase-Delay-Free Commutation Method for BLDC Motors Based on Terminal Voltage," *IEEE Transactions on Power Electronics*, vol. 36, no. 5, pp. 4971-4976, 2021.

[125] L. Kreindler, I. Iacob, G. Casaru, A. Sarca, R. Olteanu and D. Matianu,"PMSM drive using digital hall position sensors for light EV applications," *2015 9th International Symposium on Advanced Topics in Electrical Engineering (ATEE)*, Bucharest, Romania,

2015, pp. 199-204. doi: 10.1109/ATEE.2015.7133764.

[126] G. Scelba, G. De Donato, M. Pulvirenti, F. Giulii Capponi and G. Scarcella,"Hall-Effect Sensor Fault Detection, Identification, and Compensation in Brushless DC Drives," in *IEEE Transactions on Industry Applications*, vol. 52, no. 2, pp. 1542-1554, March-April 2016, doi: 10.1109/TIA.2015.2506139.

[127] Yao, X., Ma, C., Zhao, J., & De Belie, F., "Rapid estimation and compensation method of commutation error caused by Hall sensor installation error for BLDC motors," in *IET Electric Power Applications*, 14(3), August 2019, https://doi.org/10.1049/iet-epa.2018.5941.

[128] P. Alaeinovin and J. Jatskevich, "Filtering of Hall-Sensor Signals for Improved Operation of Brushless DC Motors," *IEEE Trans. Energy Convers.*, vol. 27, no. 2, pp. 547-549, 2012.

[129] Y.K.Lin and Y. Lai, "Pulsewidth Modulation Technique for BLDCM Drives to Reduce Commutation Torque Ripple Without Calculation of Commutation Time," in *IEEE Transactions on Industry Applications*, vol. 47, no. 4, pp. 1786-1793, July-Aug. 2011, doi: 10.1109/TIA.2011.2155612.

[130] B.N. Kommula and V.R. Kota, "Direct instantaneous torque control of Brushless DC motor using firefly Algorithm based fractional order PID controller," *J. King Saud Univ. - Eng. Sci.*, vol. 32, no. 2, pp. 133-140, 2020. [Online]. Available: https://doi.org/10.1016/j.jksues.2018.04.007.

[131] Lee, Sun-Kwon, et al. "Stator and rotor shape designs of interior permanent magnet type brushless DC motor for reducing torque fluctuation." *IEEE Transactions on Magnetics* 48.11 (2012): 4662-4665.

[132] Zilog Incorporation, "Self-calibrating Phase-angle Adjustment for Sinusoidal Commutation using Hall Sensors," Application Note AN039801-0916, Accessed: Oct. 2021. [Online]. Available: http://www.zilog.com/docs/appnotes/AN0398.pdf.

[133] ST Microelectronics, STM32F103x8 STM32F103xB, Datasheet, DS5319 Rev 19. [Online]. Available: https://www.st.com/resource/en/datasheet/cd00161566.pdf. Accessed: Oct. 19, 2019.

[134] M. M. Rahman and T. J. Hua, "Controller cooling of an electric vehicle (EV): An analytical and CFD simulation study," 5th Brunei International Conference on Engineering and Technology (BICET 2014), Bandar Seri Begawan, 2014, pp. 1-4.

[135] M. Azri et al., "A Review on BLDC Motor Application in Electric Vehicle (EV) using

Battery, Supercapacitor and Hybrid Energy Storage System: Efficiency and Future Prospects," *Journal of Advanced Research in Applied Sciences and Engineering Technology*, vol. 30, pp. 41-59, 2023, doi: 10.37934/araset.30.2.4159.

[136] P. Millett, "Brushless DC (BLDC) Motor Phase Undershoot," Monolithic Power Systems, Application Note AN216, Rev. 1.0, 2019.

[137] Monolithic Power Systems. (2024, June). MP9486A Datasheet (Document ID 3749). [Online]. Available:https://www.monolithicpower.com/en/documentview/productdocument/index/version/2/document_type/Datasheet/lang/en/sku/MP9486A/document_id/3749

[138] Toshiba Corporation, (2014-06-30, Rev.6.0). TK100E10N1, Datasheet. [Online]. Available: https://semiconductors.es/datasheet/TK100E10N1.html

[139] ROHM Semiconductor. (n.d.). BD2320UEFJ-LA Datasheet. [Online]. Available: https://pdf1.alldatasheet.com/datasheet-pdf/download/1423446/ROHM/BD2320UEFJ-LA.html

[140] Texas Instruments. INA181 Datasheet. [Online]. Available: https://www.ti.com/lit/ds/symlink/ina181.pdf

[141] Texas Instruments. LM2903B Low-Power, Dual-Voltage Comparator. Retrieved June 21, 2024, from https://www.ti.com/lit/gpn/lm2903b

[142] ETC2. (n.d.). 334-NTC103-RC Datasheet. [Online]. Available: https://pdf1.alldatasheet.com/datasheet-pdf/view/227635/ETC2/334-NTC103-RC.html

[143] S., Tsotoulidis, A., "Side-effects of Hall sensors misplacement on BLDC motor drive operation," in 2014 International Conference on Electrical Machines (ICEM), 2014, pp. 1825-1830. doi: 10.1109/ICELMACH.2014.6960431.

[144] D. A. Papathanasopoulos, D. V. Spyropoulos, E. D. Mitronikas, "Fault Diagnosis of Misaligned Hall-effect Position Sensors in Brushless DC Motor Drives Using a Goertzel Algorithm," in 2019 IEEE 12th International Symposium on Diagnostics for Electrical Machines, Power Electronics and Drives (SDEMPED), 2019, pp. 167-173.

[145] T. Nama, A. K. Gogoi, P. Tripathy, "Application of a smart Hall effect sensor system for 3-phase BLDC drives," in 2017 IEEE International Symposium on Robotics and Intelligent Sensors (IRIS), Ottawa, ON, Canada, IEEE, 2017, pp. 208-212. https://doi.org/10.1109/IRIS.2017.8250123

[146] P. Saiteja, B. Ashok, B. Mason and P. S. Kumar, "Assessment of Adaptive Self-Learning-Based BLDC Motor Energy Management Controller in Electric Vehicles Under Real-World Driving Conditions for Performance Characteristics," in *IEEE Access*, vol. 12, pp. 40325-40349, 2024, doi: 10.1109/ACCESS.2024.3375753.

[147] A. K. Kasyap and M. Balakrishnan, "Comparison of electromagnetic torque ripple in square wave and sine wave permanent magnet motor drives," *2014 IEEE International Conference on Power Electronics, Drives and Energy Systems (PEDES)*, Mumbai, 2014, pp. 1-5.

[148] B. Tan, X. Wang, D. Zhao, K. Shen, J. Zhao, and X. Ding, "A Lag Angle Compensation Strategy of Phase Current for High-Speed BLDC Motors," in *IEEE Access*, vol. 7, pp. 9566-9574, 2019.

[149] Faulhaber, "Equivalent DC-current in FAULHABER SC and MC," Application Note 183, 2020. [Online]. Available: https://www.faulhaber.com/fileadmin/Import/Media/AN183_EN.pdf.

[150] Y. Wei, Y. Xu, J. Zou and Y. Li, "Current Limit Strategy for BLDC Motor Drive With Minimized DC-Link Capacitor," in *IEEE Transactions on Industry Applications*, vol. 51, no. 5, pp. 3907-3913, Sept.-Oct. 2015, doi: 10.1109/TIA.2015.2427285.

[151] Wei, Kun, et al. "A novel commutation torque ripple suppression scheme in BLDCM by sensing the DC current." *2005 IEEE 36th Power Electronics Specialists Conference*. IEEE, 2005.

[152] Dixon, Juan W., and L. A. Leal. "Current control strategy for brushless DC motors based on a common DC signal." *IEEE Transactions on Power Electronics* 17.2 (2002): 232-240.

[153] Murali, M., and Sreekanth, P. K., "A Novel Method for the Torque and Current Ripple Minimization of BLDC Motor Using Phase Voltage Method," in *Proceedings of the International Conference on Control, Power, Communication and Computing Technologies*, India, pp. 273-277, 2018.

LIST OF PUBLICATIONS FROM THE RSEARCH WORK

Publications in SCI/SCIE Journals:

1. Goswami, A., Sreejeth, M. & Singh, M., “Investigation and mitigation of unbalanced hall sensor signal faults in sensored brushless DC motor drives,” in *Electrical Engineering*, 2024, Sringer. https://doi.org/10.1007/s00202-024-02245-7.

2. Goswami, A., Sreejeth, M. and Singh, M., “DC link current based commutation delay compensation method for sensored brushless DC motor drives,” in *Journal of Power Electronics*, 2024, Springer. https://doi.org/10.1007/s43236-024-00781-w.

Publications in International Conferences:

1. A. Goswami, M. Sreejeth, R. Upadhyay and S. Indu, "Brushless DC Motor Based E-Rickshaw Controller Design," *2021 International Conference on Recent Trends on Electronics, Information, Communication & Technology (RTEICT)*, Bangalore, India, 2021, pp. 196-200, https://doi.org/10.1109/RTEICT52294.2021.9573560.

2. A. Goswami, M. Sreejeth and M. Singh, "Simulation and Analysis of Hall Sensor Misalignment in BLDC Motor Drive," *2022 IEEE Delhi Section Conference (DELCON)*, New Delhi, India, 2022, pp. 1-6, https://doi.org/10.1109/DELCON54057.2022.9753351.

3. Goswami, A., Sreejeth, M., Singh, M. (2023). Analysis and Mitigation of Hall Sensor Glitch Effects in Brushless DC Motor Based E-Vehicle Controller. In: Rani, A., Kumar, B., Shrivastava, V., Bansal, R.C. (eds) *Signals, Machines and Automation. SIGMA 2022. Lecture Notes in Electrical Engineering*, vol 1023. Springer, Singapore. https://doi.org/10.1007/978-981-99-0969-8_8.

4. A. Goswami, M. S. Eth and M. Singh, "Automatic Phase Sequence Detection in BLDC Motor Drives with Hall Sensors," *2024 IEEE Third International Conference on Power Electronics, Intelligent Control and Energy Systems (ICPEICES)*, Delhi, India, 2024, pp. 78-83, https://ieeexplore.ieee.org/document/10719169.

CURRICULUM VITAE

Orcid iD: https://orcid.org/0000-0002-2918-7695

Email: goswamiarvind_elect@rediffmail.com

Profile Summary:

Mr. Arvind Goswami was born and brought up in Punjab, India. He has got nearly 13 years of professional experience in both academia and industry in different sectors including research, industrial training, project management and embedded system development, He is currently working to contribute to bridging the gap between the academic sector and real-world engineering challenges and problems. His current research interests include electric vehicle control systems, embedded systems, power electronics and drives.

His educational qualifications include:

- B.E. in Electrical Engineering from Punjab Engineering College, Chandigarh, India
- M.E. from PEC University of Technology (Deemed University), Chandigarh, India
- Ph.D. on Design and Implementation of BLDC Motor Drive Controller for Electric Vehicle Applications from Department of Electrical Engineering, Delhi Technological University (DTU), Delhi, India.

Some of his major professional stints include:

- Centre for Development of Advanced Computing (C-DAC), Mohali, India. (Ministry of Electronics and Information Technology, Govt. of India)
- TCIL IT Chandigarh, India (ICS Group)
- Electrical Engineering Department, Chandigarh University (Deemed Univ.), India.
- Inductis (India) Pvt. Ltd., India Office (Now EXL Services Pvt. Ltd.).
- AamzToFaamz Technosolutions Pvt. Ltd., Mohali, Punjab.
- Other experiences sectors include stints with tech start-up ventures.